GOLD-BEARING GRANITOIDS OF SOUTHERN GHANA, WEST AFRICA

by

Brad E. Yonaka

Submitted to the Faculty of the Graduate School of

The New Mexico Institute of Mining and Technology

in partial fulfillment of the requirements for the degree of

Master of Science in Geochemistry

Department of Earth and Environmental Sciences

May 1996

ABSTRACT

Gold-bearing granitoids are a recently recognized deposit type in southern Ghana. Several mineralized intrusive bodies were studied from three districts; the Amansie mine, the Obuasi mines, and the Ayanfuri project. Methods used were field mapping, thin and polished section petrography, trace and major element geochemistry, fluid inclusion microthermometry, and bulk gas analysis of fluid inclusions. The Amansie mine was studied in the greatest detail.

The igneous bodies intrude Lower Proterozoic folded and metamorphosed sedimentary rocks. They are localized by NE-SW striking shear zones associated with the first transcurrent tectonic phase of the Eburnean event (~2.1 Ga). The intrusive bodies are dike-like to elliptical in shape, elongate along the NE-SW shear axis, and do not exceed 600 meters in length. They range in composition from tonalite to granite, and display little or no foliation. Primary biotite and muscovite of all intrusives have been at least partially replaced by clay minerals, quartz, and calcite. Plagioclase and potassic feldspar have been affected by sericitization and albitization. The most extensive alteration within the intrusives occurs along microfractures. Modeling indicates the principal changes in major element composition due to alteration are loss of K, Ca, and addition of Na, except in the Anyankyerim intrusive, where the opposite change has occurred. In many of the intrusive bodies, two types of quartz veins are observed. Vertical quartz veins strike along the NE-SW shear zone, and horizontal quartz veins occur within the intrusive bodies.

Gold mineralization occurs within the intrusives, in quartz veins, and in the surrounding phyllites and metagreywackes. The distribution of gold and grade varies from intrusive to intrusive. The Amansie mine shows the highest gold enrichment in quartz veins and country rocks, the latter of which are carbonaceous. Ore reserves of the Amansie mine are estimated at 10.1 mt at 2.2 g/t. The South Esuajah pit at the Ayanfuri project has the highest grade mineralization within the intrusive body. Ore reserves of the

Ayanfuri project are estimated at 4.89 mt at 1.82 g/t. Gold does not correlate with intensity of alteration, or with intrusive lithology. Geochemical sampling of the intrusives shows an average gold grade of 0.5 ppm and gold shows positive correlations with As and Mo, and W. Intrusives show anomalous concentrations of As (1411 ± 40 ppm), Mo (18.7 ± 4.5 ppm), W (14.7 ± 5 ppm), and Cr (148.6 ± 7 ppm).

Vertical, horizontal, and sub-vertical quartz veins at the Amansie mine contain fluid inclusions that were measured to establish fluid compositions during mineralization. Microthermometric data indicates three types of fluid inclusions; an aqueous type that forms a second liquid phase upon cooling (type 1), an aqueous type that forms no second liquid phase (type 2), and a vapor-dominant type (type 3). Type 1 inclusions exhibit average $Tm(CO_2)$ = -62° C (±5.5^o C), $Tm(H_2O)$ = -4° C (±2° C), Tm(clathrate) = 11° C (±4° C), and homogenization to both liquid and vapor over a range of 210° to 350° C. Type 2 inclusions exhibit average $Tm(H_2O)$ = -3.6^o C (±3.2^o C), homogenize to a liquid over a range of 130° to 326° C, and three show Tm(clathrate) = 11.8^o C (±0.55^o C). Type 3 inclusions exhibit average $Tm(CO_2)$ = -64.3^o C (±5° C), and homogenize to both a liquid and a vapor over a range of -35° C to 21° C. Some type 1 and type 2 inclusions contain small solid phases. Depression of $Tm(CO_2)$ below -56.6^o C indicates the presence of additional gaseous species such as CH_4 or N_2 in type 1 and type 3 inclusions. In addition, a few two-phase inclusions exhibit behavior typical of CH_4-rich inclusions (Tm(first liquid phase) ~ -81° C) and a few one-phase inclusions exhibit behavior typical of N_2-rich inclusions (Th(vapor) ~ -140° C). Ranges of $Tm(CO_2)$ vary by quartz vein type for type 1 inclusions; $Tm(CO_2)$ for inclusions in horizontal quartz veins ranges from -64° to -57° C, and in inclusions from vertical quartz veins $Tm(CO_2)$ ranges from -68° to -58° C. Depression of $Tm(H_2O)$ below 0° C in type 1 and type 2 inclusions indicates the presence of NaCl. The range of salinity for both inclusion types is calculated as 0.7 to 12.1 eq wt % NaCl. Ranges in homogenization temperatures of type 1 and type 2 inclusions are similar for all quartz vein types. Type 1 inclusions homogenize to both a

liquid and vapor phase at similar temperatures, indicating that the system was boiling. Calculations based on the densities and homogenization temperatures of type 1 and type 3 inclusions indicate depths of formation averaging 4.2 km (±1.5 km) assuming a lithostatic overburden. Calculations for type 2 inclusions indicate depths of formation of 1.4 km (± 0.3 km) assuming a lithostatic overburden, or 3.8 km (±0.9 km) assuming a hydrostatic overburden.

Bulk fluid inclusion gas analyses of quartz vein and sulfide mineral samples show significant amounts of CO_2, CH_4, N_2, and H_2O. Analyses of vertical quartz veins show higher concentrations of CH_4, N_2 and n-alkane hydrocarbon species. Horizontal quartz veins show higher concentrations of CO_2 and n-alkene hydrocarbon species. The distribution of data plotted on ternary plots indicates two distinct fluid compositions. Each fluid exhibits a range of composition, which is demonstrated by calculation to be an effect of breaking mostly type 1 or type 3 inclusions during each analysis. Thus, the ranges represent phase separation, or fluid boiling, assumed to occur at about 300° C.

The data indicate that the main mineralizing fluid at the Amansie mine was a CO_2-CH_4-N_2-rich fluid during formation of vertical quartz veins. Mineralization closely followed emplacement of the intrusives at Nkran Hill. Solubility of Au as $Au(HS)_2^-$ was facilitated by reactions between H_2O and organic-rich metasediments in the wall rocks. Enrichment of the fluids in CH_4, N_2, and organic species is related to these reactions. Subsequent boiling of fluids and loss of H_2S to sulfidization of the wall rocks caused a decrease in gold solubility and precipitation of gold. The second mineralizing phase at the Amansie mine occurred after emplacement of horizontal quartz veins in the intrusive at Nkran Hill. The lower amount of organic species in this fluid is attributed to the gradual depletion of organic material in wall rocks along the shear zone. Limited data suggest that all intrusives of the study were subject to a similar manner of gold mineralization as the Amansie mine.

Models are proposed for the sources of mineralizing fluids and gold in the mineralized intrusives. Low salinity fluids initially dominated by CO_2 and H_2O were probably derived from metamorphic sources. Granitoid emplacement triggered activity of the geothermal system responsible for gold mineralization. These igneous bodies intruded preferentially along shear zones and may be part of much larger plutons at depth. Though they provided heat, it is unlikely that the granitoids were a source of gold. Organic-rich metasediments already enriched in gold may have been the source of mineralization. Low gold solubilities calculated from bulk gas analysis data suggest that mineralization took place over a long period of time.

ACKNOWLEDGMENTS

I would like to thank Amansie Resources, Ltd., for permission to conduct field work on the Amansie concession, and the on-site staff for their support throughout the project. In particular I thank Al Perry for making the journey to Ghana possible. I acknowledge the cooperation of Cluff Resources for collection of samples from intrusive bodies at the Ayanfuri project. I also thank the Ashanti Goldfields Corporation for their information on the mineralized intrusives of Obuasi. Special thanks to my advisor, Dr. Dave Norman, for his enthusiasm, advice, and hours of instruction in the laboratory, and to my other committee members Dr. Andrew Campbell and Dr. Kent Condie for their support. Partial funding of this project was received from the Institute of International Education grant # 1006. Support is also acknowledged from the Charles and Eula Park Fellowship and the Tech Graduate Student Research Project Scholarship.

I extend personal thanks to my mother and father, who have provided moral support since day one, and my fellow sufferers in MSEC, who made my confinement in the building bearable. Special thanks goes to my girlfriend Emily, who withstood the terrors of Nicaraguan spiders, and who went through much sympathetic labor during the more stressful parts of my thesis work.

TABLE OF CONTENTS

LIST OF FIGURES

LIST OF TABLES

Table **Page**

INTRODUCTION

Scope and Objectives of Present Study

Gold-bearing intrusives in southern Ghana occur at the Amansie mine, the Obuasi mines, and the Ayanfuri project (Fig. 1). They are a recently recognized type of gold mineralization in Lower Proterozoic (Birimian aged) rocks that have no history of production prior to 1985 (Kesse, 1985). Today, however, gold-bearing granitoids are actively being sought out and developed; ore reserves of the Amansie mine approach 10.1 million tons at a grade of 2.2 g/t Au and oxidized ore at the Ayanfuri project is estimated at 4.89 million tons grading 1.8 g/t Au. Gold production at the Obuasi mines, which includes the Nhyiaso and Anyankyerim intrusives, exceeds 800,000 kg Au (Dzigbodi-Adjimah, 1992).

Though these intrusives constitute an important gold resource in Ghana, they have not been studied systematically. Of particular interest is whether the granitoids are accidental to gold mineralization or if they are instrumental in forming the ore deposits. The objectives of this study are to describe the deposits and determine if there is a genetic link between the granitoids and ore mineralization.

Previous Studies of Granitoid-Related Gold Deposits

Felsic intrusions are associated with many Precambrian gold deposits (Hodgson and MacGeehan, 1982). Two schools of thought exist concerning the source of ore fluids:

1. One group of researchers suggests that ore-bearing fluids are magmatic or associated directly with fractionation processes of the intrusive (Hattori, 1987; Burrows, et al., 1986; Ishihara, 1981; Cameron and Hattori, 1987; Burrows and Spooner, 1987). Magnetite-rich felsic intrusives, formed from a more oxidized magma, are reported to be

naturally anomalous in gold (Hattori, 1987; Ishihara, 1981). For several gold deposits in the Archean rocks of the Canadian Shield, Hattori (1987) concludes that oxidized magmas are responsible for separating gold from sulfides and transporting it to upper levels of the crust in the free oxidized form Au^{+} or Au^{+3}. This association between gold ions and oxidized magmas is also postulated by Khitrunov and Mel'tser (1979). Ishihara (1981) concludes that magnetite-series granitoids, originating at deep crustal levels, concentrates high amounts of sulfur through extensive fractionation of immiscible melt material. Gold then complexes with sulfur and is carried to the highest levels of the intrusive to form metallic sulfide deposits.

2. The second group of researchers suggest that the fluids originate from deep crustal metamorphism with possible mixing of meteoric waters (Cameron, 1988; Feng et al., 1993; Schreiber et al., 1990; Zweng et al., 1993). The fluids may result from dehydration reactions during granulite formation in the lower crust (Cameron, 1988; Feng at al., 1993). Schreiber et al. (1990), Olson et al. (1992), and Hirdes and Leube (1989) postulate that heat from an intrusion is necessary to facilitate fluid movement. It is thought that these high temperature fluids are of low salinity and high in CO_2 due to phase separation within the $NaCl$-CO_2-H_2O system (Cameron, 1988; Cameron and Hattori, 1987). Cameron (1988) and Zweng et al. (1993) state that low concentrations of Cl^- inhibit formation of base metal complexes, while S levels are sufficient to allow complexing and transport of Au, As, and Sb. Corfu (1993) summarizes U-Pb dates for deposits in the Abitibi greenstone belt in Canada and concludes that there is a genetic link between Au mineralization and metamorphic fluids. It is thought that these fluids are derived from lower crustal dewatering and possibly metamorphism promoted by CO_2 fluxing and heat injected from the mantle (Fyon et al., 1989).

Evidence cited in support of mineralizing fluids with no link to intrusive bodies is found in Barnes (1967), Brown (1948), Beattie and Barton (1992), and Harris (1980). Barnes (1967) points out that similar gold deposits occur both near and far from felsic

intrusives. Brown (1948) concludes that the weak, sheared country rock surrounding many intrusives can be used by fluids as channel ways to concentrate metals. Gold is thought to have been deposited in areas of maximum alteration within the Salave gold-bearing granitoid, Spain. The source of the gold is thought to be from the surrounding metasediments (Harris, 1980). Gold mineralization in the granitoids of the Roodepoort Goldfield, South Africa is thought to be the result of CO_2-rich fluid flow from gold enriched country rocks (Beattie and Barton, 1992). They postulate that this mineralizing fluid concentrated gold along shear zones within the centrally located plutons.

A recent study to resolve fluid sources in granitoid-related ore deposits was undertaken in the Abitibi greenstone belt gold deposits, Canada. Precise U-Pb age dates by Carignan and Gariépy (1993) reveal a difference in ages between mineralization and intrusive activity. They conclude that mineralization can only be explained by invoking both magmatic and deep-seated metamorphic fluid sources.

Previous Studies of West African Gold Deposits

Gold deposits associated with felsic intrusives occur throughout West Africa. These include: Poura in Burkina Faso (Wright et al., 1985), Kalana in Mali (Blagonadezhdin, 1975), and Syama in Mali (Olson et al., 1992). It is postulated by the authors that the associated intrusions supplied heat to the mineralizing fluids. The three West African gold occurrences differ in their paragenesis, host rocks, and timing of the deposit in relation to regional tectonic events. Junner (1932) suggests a genetic relationship between nearby granitic intrusions and the gold-bearing quartz veins located at Obuasi. Kesse (1985) concurs with a magmatic fluid origin and adds that gold mineralization was structurally controlled along NE-SW trending shear zones. Ntiamoah-Agyakwa (1979), Leube et al. (1990), and Hirdes and Leube (1989) state that shear zones are merely a local control for

concentrating gold from chemical sediments already rich in metals. Leube et al. (1990) conclude that the sulfide-gold occurrences of southern Ghana are regionally controlled by the occurrence of gold-rich chemical sediments. They use as an argument the occurrence of NE-SW trending shear zones that do not pass through chemical sediments and that are barren of mineralization.

Hirdes and Leube (1989) point out that granitoids occurring in areas far from gold-bearing chemical sediments are barren of gold mineralization. The Amansie mine is located in a region not mapped as having chemical sediments, yet gold mineralization does exist and is of economic significance. Kesse (1985) concludes that the gold mineralization of granitoid bodies is purely structural, as gold follows the intrusive margins in cases where deep-seated shearing is present, but is absent from intrusives having no association with deep-seated shearing. This suggestion does not take into account the presence of granitoid bodies with elevated gold grades completely within their margins, such as the South Esuajah intrusive of the Ayanfuri project.

Steps of Present Study

This paper presents the following steps that were taken to resolve the source of mineralization in felsic intrusives of southern Ghana:

1. A description is made of the gold-bearing granitoids of the Amansie mine, the Obuasi mines, the Ayanfuri project, and an unmineralized granitoid north of the Amansie mine. Sources of information include field mapping, petrography of thin and polished sections, and whole rock and trace element geochemistry. Ore distribution and mineralogy are compared to rock type and degree of alteration in each intrusive.

2. Fluid inclusion microthermometry and bulk gas analyses are used to establish composition, depth, gold solubility characteristics, and number of mineralizing fluids. Fluids are then related to episodes of quartz veining mapped during the field study.

3. A chronological relationship is established between intrusion of granitoids, episodes of quartz veining, and mineralizing fluids.

4. The results from the above steps are used to constrain hypotheses on the source of mineralizing fluids and genesis of the ore.

REGIONAL GEOLOGY

Stratigraphy

The rocks of southwestern Ghana are part of the Man Shield (Bessoles, 1977), which comprises the southernmost third of the West African craton. The craton consists of Archean rocks of Liberian age (3.0-2.5 Ga) in its western domain, and of early Proterozoic metamorphosed rocks in its eastern domain (Leube et al., 1990). The early Proterozoic rocks are underlain by a Archean basement complex of migmatites and gneisses over most of the craton (Wright et al., 1985). This basement is not exposed in southwestern Ghana, but limited isotopic evidence from a granitoid complex near Winneba suggests an underlying Archean basement (Taylor et al., 1992). The early Proterozoic rocks, labeled the Birimian Supergroup, are a series of basic volcanic and sedimentary units. One member, called 'Lower Birimian' by Junner (1935) is mostly sedimentary, composed of phyllites, tuffs, and greywackes. The other member, called 'Upper Birimian' by Junner (1935) is composed mainly of volcanic and pyroclastic rocks. Kesse (1985) notes the presence of conglomerates, quartzites, and tuffaceous sediments in this second unit. Dating of Birimian rocks by Taylor et al. (1988), give ages ranging from 2.195 to 2.166 Ga (Sm/Nd model ages).

There are two hypotheses concerning the stratigraphy of Birimian rocks: (1) the sediments were deposited before the volcanics (Milési et al., 1990; Junner, 1935), or (2) the two rock types were deposited contemporaneously as lateral time equivalent facies (Leube et al., 1990). It was originally thought by Junner (1935) and Kesse (1985) that the Lower and Upper Birimian occurred separately during the development of an intra-continental basin.

The Birimian volcanic and sedimentary rocks underwent changes during active tectonics, and in some places are overlain by later sediments. The rocks are folded,

metamorphosed, and intruded by granitoids emplaced during the Eburnean event between 2150 and 1850 Ma (Caen-Vachette, 1986). Overlying the Birimian volcanic rocks are the Tarkwaian sediments (Whitelaw, 1929), consisting of arkoses, shales, and conglomerates. The youngest rocks in the region are Cretaceous to Eocene sediments overlying Birimian units on the southern coast and continental shelf of Ghana (Wright et al., 1985).

Tectonic Events

The tectonic episodes of the Eburnean event are responsible for the structure in the Birimian Supergroup. The beginnings of the Eburnean are still not fully understood. This is partly due to the lack of basement rocks to provide evidence of the underlying materials upon which the first Birimian rocks were emplaced (Leube et al., 1990). Wright et al. (1985) postulate that either (1) the sediments were formed in basins developed during re-activation of Archean continental crust, or (2) the sediments were deposited in an intra-continental marine basin floored by oceanic crust. Leube et al. (1990) propose that the crust was continental, and during an episode of increased mantle convection, this crust became highly fractured as a result of continental rifting. Five fractures in all were formed, each evenly spaced and several hundred kilometers long (Leube et al., 1990), and continued attenuation of the basin floors all but destroyed the underlying sialic crust. Wright et al. (1985) postulate that basin fill initially entered the basins from the nearby stable Liberian crust and later from rift-related volcanics. Leube et al. (1990) suggest that sediment was derived from the activity of newly formed volcanic arcs at the basin edges, based on the occurrence of volcaniclastic rocks in the basins. Though these volcanoes may originally have been subaqueous, they eventually attained subarial exposures (Leube et al., 1990). This led to the contribution of younger units of Birimian-aged volcaniclastic sediments noted by Kesse (1985).

The first regional deformational phase occurred after the formation of sedimentary and volcanic rocks, and during the intrusion of syn-tectonic granitoids (Leube et al., 1990). The phase is characterized by roughly E-W compression, and labeled the D1 collisional tectonic phase by Milési et al. (1990). This episode of crustal shortening closed the basins and folded the Birimian rocks (Leube et al., 1990). Milési et al. (1990) conclude, however, that this deformational phase occurred between the deposition of 'Lower Birimian' sedimentary rocks and 'Upper Birimian' volcanic rocks, and was due to the collision of the Proterozoic block with the stable Liberian craton. Schnetzler et al. (1966) and Kolbe et al. (1967) obtain an Rb/Sr date of 2100 Ma from the Lake Bosumtwi gneiss. This is interpreted by Milési et al. (1990) as indicating the date of metamorphism associated with the D1 tectonic phase in Ghana.

In order to explain the characteristics of the Tarkwaian Group of clastic sediments, some researchers invoke the occurrence of a second rifting phase. Leube et al. (1990) propose this phase opened intermontane grabens in volcanic belts. The basins were filled with eroded Birimian rocks, resulting in the formation of the Tarkwaian Group. Other authors (Milési et al., 1990) conclude that the Tarkwaian was formed during the same time as the other Birimian rocks and thus subject to the D1 collisional tectonic phase.

A second deformational phase (D2) is proposed by Milési et al. (1990) during which NE-SW strike-slip faults developed. The phase is associated with sub-vertical cleavage and is synchronous with greenschist metamorphism (Milési et al., 1990). In Ghana the strike-slip faulting trends N 030 E to N 060 E, is generally sinistral, and locally led to overthrusted sheets. Deformation corresponding to the D2 phase in northwest Côte D'Ivoire occurred between 2096 and 2073 Ma (Feybesse et al., 1989). The date of 2096 Ma corresponds to clasts unaffected by the D2 phase (Milési et al., 1990).

The sinistral NE-SW shearing of the D2 deformational phase is generally correlated with the occurrence of large-scale shear zones in southern Ghana. Due to the concentration of gold and manganese mineralization along these zones, they have been

labeled as mineralized 'belts' by Bates (1955). They are named, in order from SE to NW, the Kibi-Minneba Belt, Ashanti Belt, Asankrangwa Belt, Sefwi Belt, Bui Belt, and Bole-Navrongo Belt. They correspond to contact zones between the Lower and Upper Birimian lithologies, except for the Asankrangwa Belt (Fig. 1). The latter is thought to be an embryonic volcanic belt developed and aborted early in the history of the basin, later to be buried under volcaniclastic sediments originating at the basin edges (Leube et al., 1990).

A last deformational event is proposed by Milési et al. (1990) in which the previous faults were offset by dextral shearing. It is labeled the D3 transcurrent deformational phase by Milési et al. (1990), and occurred some time after 2073 Ma. The effects of this phase are not nearly as pronounced as with the D2 phase.

Magmatic Events

The Birimian Supergroup is intruded by three phases of felsic intrusives emplaced during and after the Eburnean event. The sedimentary rocks of the Birimian are intruded by granitic batholiths apparently coeval with a high temperature and low- to medium-pressure metamorphic event (Junner, 1935). These granitoids, named Cape Coast granitoids by Kesse (1985), and later as 'basin granitoids' (Leube et al., 1990) are thought to be syn-tectonic intrusions due to the presence of well developed foliation (Milési et al., 1990; Kesse, 1985). Recent U-Pb of zircons in basin granitoids by Hirdes et al. (1992) places them at 2116.2±2.3 Ma. The Birimian volcanic rocks have been intruded by what are termed Dixcove granitoids (Kesse, 1985), also termed 'belt granitoids' by Leube et al. (1990). Milési et al. (1990) conclude that these granitoids are characterized by post-tectonic intrusion, due to the absence of foliation. However, U-Pb dating by Hirdes et al. (1993) places them at 2170 to 2160 Ma, hence syn-tectonic. A third phase of felsic

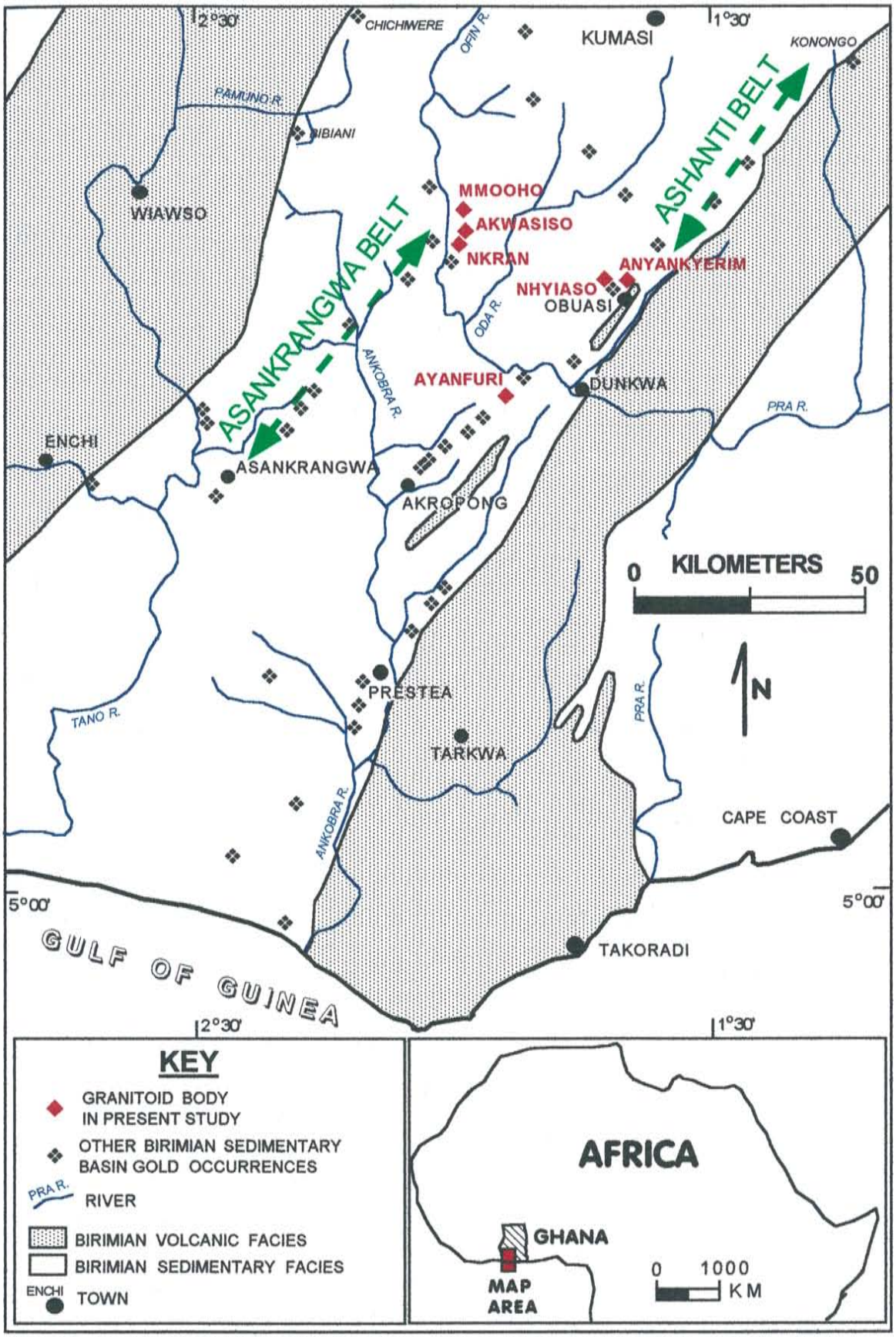

Figure 1. Geological map of southwestern Ghana showing locations of intrusive bodies in the study. Map modified after a compilation by Haude (1987).

intrusives within the metasedimentary basins post-dates the Eburnean and consists of K-rich granitoids (Leube et al., 1990; Hirdes et al., 1993).

Regional Controls on Gold Mineralization

Vein-type gold deposits are the most important gold sources in Ghana, and these deposits occur most commonly along the contacts between Birimian metasedimentary and metavolcanic rocks (Kesse, 1985). The largest single gold occurrence in Ghana is along the Ashanti Belt, at the Ashanti Goldfields Corporation mines located around the town of Obuasi (Fig. 1). Most of the gold mineralization in this area is directly related to fissures reflecting the larger scale structural trends (Dzigbodi-Adjimah, 1992). The deposits are characterized by lode Au mineralization associated with pyrite and arsenopyrite (Milési et al., 1990). Junner (1935) believed that gold mineralization was regionally controlled by the formation of deep-seated shear zones. However, Leube et al. (1990) conclude that regional mineralization is controlled by the presence of metal-rich chemical sediments. They postulate that gold-rich chemical sediments formed during gold complex destabilization reactions after fluid discharge on the ocean floor.

Anomalous gold values are ubiquitous in the Birimian rocks of southern Ghana. Hirdes and Leube (1989) report anomalous concentrations of gold in many igneous and metasedimentary rock types. In particular they report an average of 22 ppb Au in carbonaceous schists, ranging from 1 to 120 ppb (n = 25).

METHODS

Field work

A total of five months were spent mapping and collecting data at the Amansie mine in southern Ghana (Fig. 2). I participated in exploration work by Amansie Resources Limited during the course of the field study. Samples of intrusives, country rocks, and quartz veins were collected from trenches, drill core, and drill chips.

Trenches consisted of excavations roughly 1 m wide and 1 to 4 m deep. Careful mapping and sampling was conducted in areas where trenching intersected surface exposures of weathered granitoid. Trenches exposed quartz veining and highly silicified zones. Quartz veins were sampled for fluid inclusion microthermometry and bulk fluid inclusion gas analysis. Reverse circulation (RC) drill chips and sections of diamond drill core were sampled. Seventeen RC holes and six diamond drill holes intersected the granitoid on Nkran Hill. Three RC holes on Akwasiso Hill intersected the granitoid. Detailed logging and sampling was made of the diamond drill core that intersected the granitoid. Results of drill core and trench sample gold assays conducted by Amansie Resources Limited were recorded. Some samples were taken from RC core in areas where no diamond drilling had taken place. The material was described and samples sent to New Mexico.

Excursions were made to four other mineralized felsic intrusive bodies in Ghana. The granitoid-hosted gold deposits at Obuasi (the Nhyiaso and Anyankyerim intrusive), and the intrusives of the Ayanfuri project were visited. During these visits samples were collected and discussions held with resident geologists. Samples were also taken at the unmineralized granitic exposure of Mmooho Hill a few kilometers north of the Amansie mine (Fig. 2).

Maps

All geologic maps were drawn on site, or taken from survey maps of trenching and drill hole locations. No previous geologic maps had been made of the Amansie mine. The mapping done was limited by poor exposure in thick vegetation. Detailed observations of surface geology were made only in areas where exploration was taking place.

On-site maps and a topographic map of the Amansie mine area prepared by the Ghanaian Survey Department were scanned into a graphics manipulation program at NMIMT. A map of southwestern Ghana gold occurrences compiled by Haude (1987) and presented in Hirdes and Leube (1989) was used as a regional geologic map (Fig. 1).

Petrographic analysis

Twenty-six thin sections were made of the unweathered rock types and a description of petrology and alteration was conducted at New Mexico Institute of Mining and Technology (NMIMT). Samples were chosen to provide a range of depth, degree of alteration, degree of mineralization, and rock type. Cutting and mounting of thin sections was done by Gold Hill Geological Research based in Albuquerque, NM. The petrographic descriptions made at NMIMT are shown in Appendix A. Polished sections were produced at NMIMT from the same billets. Sections were examined using an Olympus BH2 polarizing binocular microscope, and criteria for distinguishing sulfide minerals in polished section were taken from Uytenbogaardt and Burke (1971).

Geochemical analysis

Thirty samples from diamond drill core and RC chips were used for geochemical analysis. The samples were taken from areas immediately adjacent to material used for

thin section study when ever possible. Trace elements Cr, V, Ba, Nb, Zr, Y Sr, Rb, Th, Pb, Ga, Zn, Cu, and Ni were analyzed by the X-Ray Fluorescence (XRF) facility located at the New Mexico Bureau of Mines and Mineral Resources in Socorro, NM. ACME Analytical Laboratories Ltd., Vancouver B.C., Canada, analyzed major elements and trace elements by ICP, rare earth elements and gold by INAA (neutron activation), and the Leco method was used to measure carbon and sulfur.

Microthermometric and Raman microprobe study

Fluid inclusion sections were prepared from ten samples of quartz veins at the Amansie mine. The material was taken from quartz veins exposed by trenching and in diamond drill core. Sections were broken into small chips, sketched, and described according to clarity, fracturing, and inclusion orientation.

Microthermometry was conducted with a Linkham Th600 stage linked to a Linkham TP91 temperature control unit. This control unit was fed by a Linkham CS 196 nitrogen cooling system. A LEITZ microscope was used, and viewing was done with an Olympus 80X lens. Inclusions were projected to a TV screen and the outlines of the inclusions and phases within them were traced on to a clear sheet of paper. Inclusion volumes were calculated from these traces, assuming the inclusion to be the volume of rotation and the vapor phase to be spherical. The degree of fill (F) was calculated by subtraction of bubble volume from inclusion volume. The Linkham microthermometric stage was calibrated at regular intervals. Standards with melting temperatures of -56.6^{o}, 0°, 51.5^{o}, 149.9^{o}, 205.9^{o}, 258°, and 398° C were measured every two weeks to check the calibration of the instrument. Calibration curves were constructed to adjust the recorded data in the event that the standards did not melt at the appropriate temperatures.

Measurements below room temperature were conducted first. The temperature was cycled two times at rates of 5° to 10° C per minute in order to determine the approximate

temperature of a phase change. Final measurements of phase changes were made using a heating rate of 0.2° to 0.4° C per minute. The melting temperature of clathrate was the most difficult to observe. Measurements were made by temperature cycling:

1. The stage was heated to a temperature at which the vapor phase was spherical and free of restrictions.
2. This stage temperature was maintained for one minute to ensure that clathrate was as fully melted as possible.
3. The stage temperature was then reduced 5° to 10° C. If the vapor phase became distorted, then it was assumed that clathrate had not all melted in step 2. If no changes occurred in the vapor bubble, then clathrate was assumed to be melted.
4. If step 3 showed clathrate still present, then step 1 was repeated at 0.2° C higher than before.

In most inclusions, melting occurred at a higher temperature than indicated by rounding of the vapor phase.

Inclusion homogenization (Th) above room temperature was measured using a heating rate of 1° C per minute. After this initial measurement, the temperature was cycled several times to duplicate the event. This was done to ensure that leaking was not occurring, which results in errors of Th measurement. Decrepitation occurred in about 84 % of the inclusions heated.

Four fluid inclusion sections were sent to the Department of Geology and Geochemistry at Stockholm University, Stockholm, Sweden, for Raman microprobe analysis. Ten inclusions were analyzed for proportions of CO_2 and CH_4 in the vapor phase. Limited microthermometric work was also conducted in Sweden.

Bulk Gas Analysis

Fragments were taken from 14 samples of quartz and three samples of sulfide minerals for bulk fluid inclusion gas analysis. The quartz fragments were broken to < 4 mm, cleaned in a hot HCl solution for one hour, then set in boiling water for an additional hour. The sulfide fragments were carefully extracted from rock matrix and any remaining silicate mineral was dissolved by HF acid. Samples were loaded between the crushing plates on a vacuum line leading into a Balzers® QMS 112 quadrupole mass spectrometer located at NMIMT. A number of standard gases were used to calibrate the sensitivity of the machine. These sensitivity factors were used in reduction of the raw data. The gas emissions from the crushed samples were recorded on a computer attached to the QMS 112 unit by the Quadstar® program.

Principle gaseous species and organic gas species were measured and peak interferences were calculated. Principle gaseous species were measured at m/e peaks of 4 (He), 15 (CH_4), 18 (H_2O), 28 (N_2), 40 (Ar), 34 (H_2S), 44 (CO_2), 26 (C_mH_n), and 48 (SO_2). A second crush measured organic gases, at m/e peaks of 26, 27, 29, 30, 39, 41, 44, 56, 57, 58, and 78. The peak area was calculated by a BASIC program developed by Dr. D. Norman at NMIMT. Some peaks represent the contribution of more than one gaseous species. Therefore, it was necessary to subtract the contribution of these other species from the peak height. The peak for He is close to that of hydrogen gas, but is a fraction of the value. For that reason, a control measurement was made at the m/e peak of 3.7. The peak of hydrogen was assumed to mask the He peak if this value was greater than the He m/e peak of 4.0. Organic gases were reduced in a similar way by another BASIC program developed by Dr. D. Norman at NMIMT. No further reduction was used to change the values to mole percent.

LOCAL GEOLOGY

The Amansie Mine

I. General

The three granitoid bodies of the Amansie mine area occur along the Asankrangwa Belt (Fig. 1). They form low-lying hills in an area of undulating topography, and are each separated by approximately three kilometers. In order from the southwest to the northeast, they are called Nkran Hill, Akwasiso Hill, and Mmooho Hill (Fig. 2). The intrusives have been classified as basin granitoids (Senger, oral commun., 1993), and intrude Birimian metasedimentary rocks. U/Pb dating of zircons by Hirdes et al. (1992) of a basin granitoid approximately 20 km west of Nkran shows an intrusive age of 2116.2± 2.3 Ma. The metasediments of Nkran Hill are cut by thick, vertical quartz veins striking N 036 E, while Akwasiso Hill has flat lying quartz veins within the intrusion that now act as a weathering resistant cap. Both intrusives are highly weathered in surface exposures. Mmooho Hill is a roughly circular intrusion that has not undergone significant weathering, and contains no observable quartz veining. It is, however, cut by roughly vertical veins of aplite that strike a different direction to the quartz veining on Nkran Hill or Akwasiso Hill. The mine area is affected by a tropical climate, which causes rapid chemical weathering rates of the rocks and development of laterite. The rainy season lasts six months of the year, and the total average rainfall is 200 to 500 mm. As a consequence, the weathering profile is extreme; it extends 40 to 60 m below surface on the hills. An adit ending at a depth of 42 meters under Nkran Hill reveals completely oxidized and friable rock. The water table varies from 50 to 70 meters below ground surface. Lateritic soils are greater than 3 meters thick in low-lying zones and 0.4 to 3 meters thick on hills. Cross sections show a ten centimeter thick A horizon followed by a B horizon containing Fe nodules and

pyrite replaced by either goethite or limonite. Under this is a mottled red and white saprolite with interfingering of in-situ minor quartz veins and metasediments. There is evidence for minor colluvial movement of the saprolite. The area around Nkran Hill and Akwasiso Hill is characterized by gold and arsenic anomalies (Fig. 2). This was established during geochemical soil sampling between the two ore bodies. The halo of arsenic enrichment in soils is more extensive than the gold enrichment.

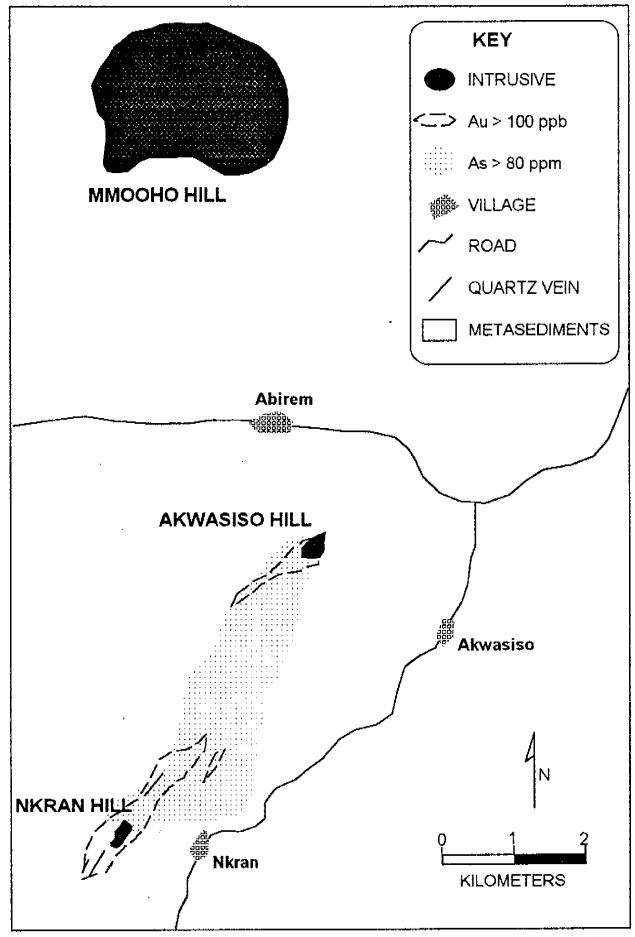

Figure 2. Map of the Amansie mine and Mmooho Hill. Nkran Hill and Akwasiso Hill are oriented along a NE-SW shear zone that is not visible beyond or between the ore bodies.

II. Country Rocks

The country rocks of the area are composed of metagreywackes, phyllites, and schists. Foliation is well developed and runs parallel to the larger-scale vein systems, striking NE-SW and dipping at 85° to 90°. At the surface, metasediments exhibit intense weathering that precludes rock description. Presence of sulfide minerals prior to weathering is indicated by abundant angular voids and Fe-hydroxide grains. At depths exceeding 50 meters, sulfide minerals such as pyrite and arsenopyrite are abundant in proximity to the quartz veins and intrusives. Some of the metasediments immediately adjacent to quartz veins and intrusives are highly carbonaceous. Highly carbonaceous

metasedimentary rocks have been described as occurring along the centerline of the metasedimentary basin by Leube et al. (1990).

Thin sections of metasediments (Fig. 3) show strong foliations of phyllosilicates, and have an abundance of sulfide minerals. Most quartz crystals are stretched, and micas are altered to finely-grained clay minerals. Calcite is present throughout the matrix as both euhedral and anhedral crystals, and the latter are elongate in the direction of foliation. Some sulfide minerals display 'pressure shadows', or overgrowth of chlorite and quartz (Fig. 3), and in two thin sections sulfide minerals are partially replaced. Sulfide concentration also increases in samples close to the intrusive margins, and in samples closer to the major shear zone at Nkran Hill. Some sections display quartz veins in various states of deformation, and in one case the quartz contains albite.

Two polished sections were made of metasedimentary rock at the intrusive margins. The sulfide minerals present in one section are almost exclusively pyrrhotite. The one arsenopyrite crystal observed is partially replaced by both pyrite and pyrrhotite. The other section shows euhedral arsenopyrite crystals rimmed by pyrite and the cores replaced by pyrrhotite and chalcopyrite.

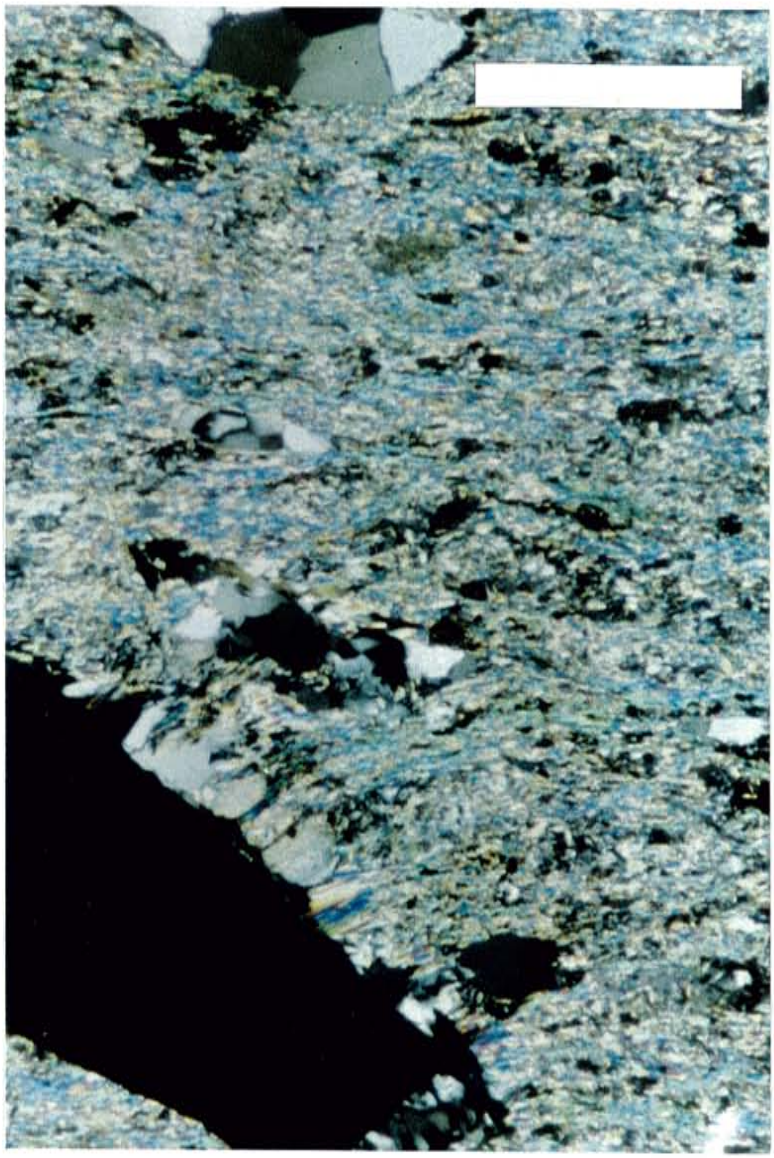

Figure 3. Microphotograph of metagreywacke near metasediment-intrusive contact zone. Scale bar is 0.5 mm. Matrix is micaceous material with some elongated quartz grains. Large opaque mineral is arsenopyrite, with overgrowth of quartz and clay minerals.

IIIa. Intrusives - Nkran Hill

The intrusives of Nkran Hill occur as dike-like to elliptical bodies with the long axis striking N 036 E. The intrusive outcrops in two places; the larger exposure is 120 m long by 50 m wide, the smaller less than 40 m long and 10 m wide (Fig. 4). The intrusive is less than three meters wide in all diamond drill intersections except one case where it is greater than 20 meters wide. In several RC drill holes the intrusive is up to 10 meters wide (Appendix A). In diamond drill core, it has a porphyritic texture where it is thin, and along the one borehole where the intrusive is much wider, the texture is decidedly hypidiomorphic-granular. Due to the limited information provided by these drill hole intersections, it is not possible to establish a cross cutting relationship between the two intrusive types.

Petrography of thin sections from Nkran Hill confirms the textural division of the intrusive; moderately altered, hypidiomorphic-granular granitoid, and moderately altered, porphyritic-aphanitic granitoid. Primary minerals in both types are quartz, plagioclase, muscovite, biotite, and minor potassic feldspar. Plagioclase is albite to andesine in composition, as determined by Michel-Lévy extinction angle measurements, and secondary albite occurs both interstitial to plagioclase and as overgrowths. Plagioclase has undergone sericitization, though the alteration is incomplete. In many sections secondary albite is free of sericite, though in some sections it has undergone sericitization along with plagioclase. Most primary biotite and muscovite is completely replaced by secondary muscovite, calcite, quartz, chlorite, and opaques. In many cases secondary muscovite appears interstitial to quartz and feldspar crystals. Calcite occurs in varying amounts, as solitary euhedral crystals and as masses interstitial to other minerals. Primary potassic feldspar is uncommon. Some sections show what appear to be potassic feldspar crystals that have been partially destroyed. Rutile is a common secondary mineral in

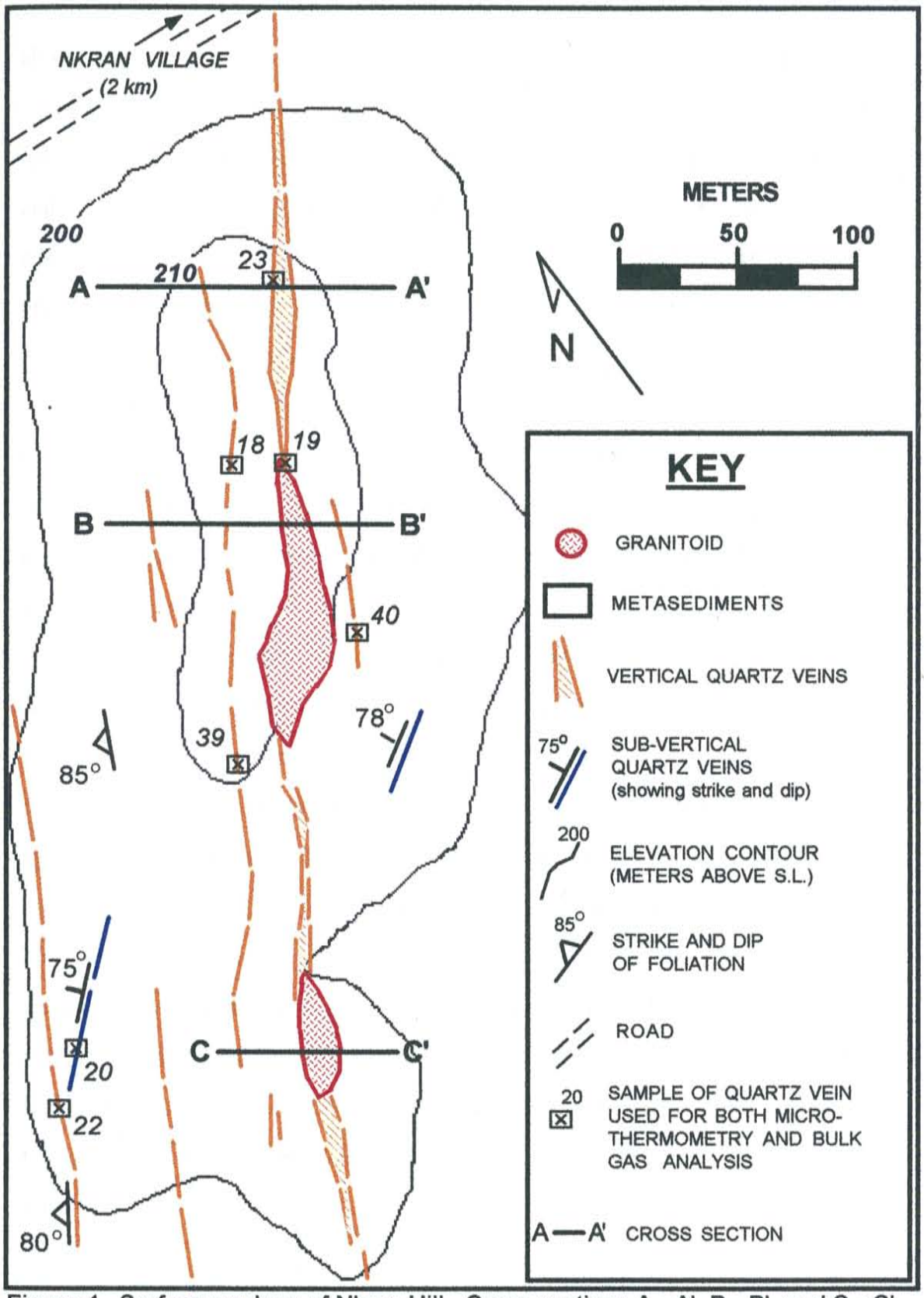

Figure 4. Surface geology of Nkran Hill. Cross sections A - A', B - B', and C - C' are shown in Appendix A.

all sections. It occurs in the remnants of primary biotite and muscovite crystals.

Polished sections of both intrusive types display similar features. They reveal sub- to euhedral arsenopyrite with anhedral pyrite overgrowths. In a few sections euhedral pyrite and arsenopyrite are intergrown. Euhedral arsenopyrite occurs on both sides of the contact of porphyritic intrusive and wall rock in section #6A. Blebs of pyrrhotite are present in these sulfide minerals, and the occurrence chalcopyrite is uncommon both outside and in the cores of arsenopyrite crystals.

There are several features in which the two intrusive types differ in thin section. Sections of porphyritic intrusive display more characteristics of metamorphic change. Mechanical changes of a ductile nature are indicated by undulatory extinction of quartz grains. One sample of drill core shows development of mylonite within the intrusive. There is profuse embayment of small matrix quartz crystals in phenocrysts of feldspar and quartz (Fig. 5). Some plagioclase grains have secondary twins that suggest brittle deformation. Foliation is present, noticeable by the alignment of clay minerals in the matrix. Sericite in feldspars is aligned along crystal cleavages (Fig. 5), and sericite in the matrix is random or faintly aligned with clay minerals. Thin sections of the hypidiomorphic-granular rocks show no development of foliation, though sutured margins between the various crystals is ubiquitous (Fig. 6). Undulatory extinction of quartz is less intense than in thin sections of the porphyritic rocks. It is common in the hypidiomorphic-granular sections to find sericite, calcite, and opaques forming preferentially along microfractures running both between and through mineral grains. In several thin sections, there is a matrix composed of fine grained quartz, though this matrix does not occur throughout the section. One thin section shows graphitic intergrowth of quartz and feldspar.

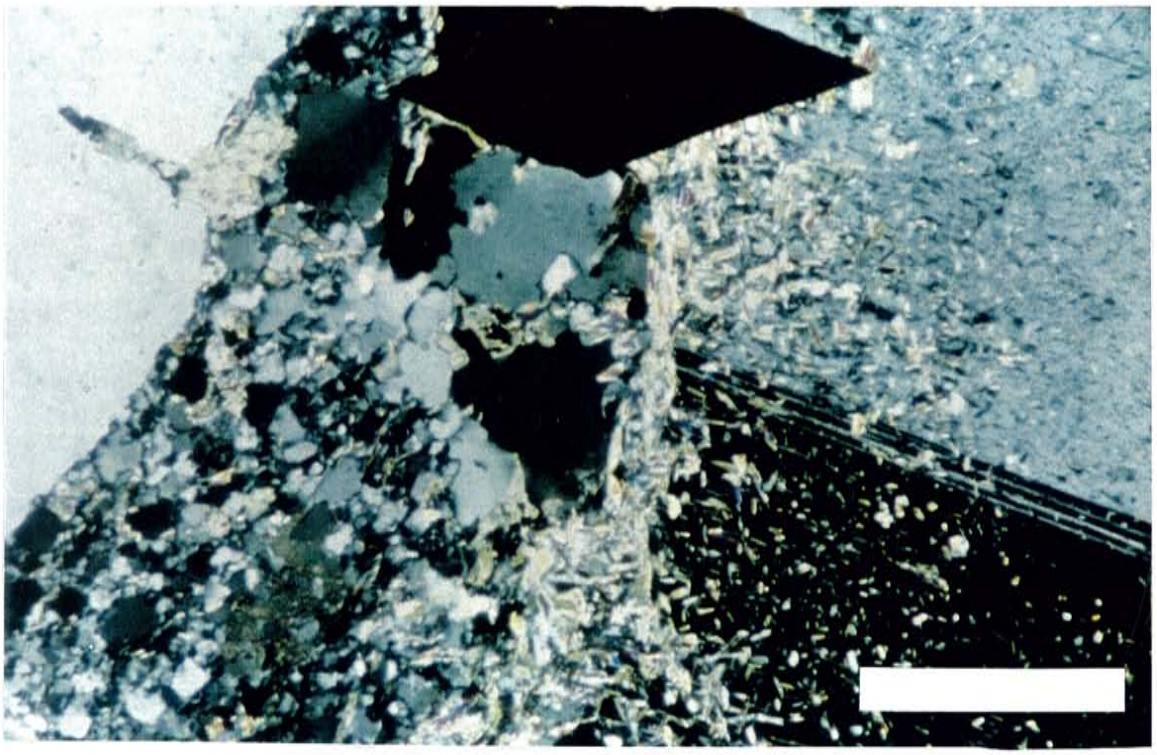

Figure 5. Microphotograph of the porphyritic intrusive, Nkran Hill. Scale bar is 0.5 mm. Phenocrysts are oligoclase (right), quartz (left), and arsenopyrite (top). Matrix is quartz, clay minerals, and calcite. Quartz phenocryst shows embayment of smaller quartz crystals. Sericite and arsenopyrite have developed along a microfracture bordering the oligoclase crystal.

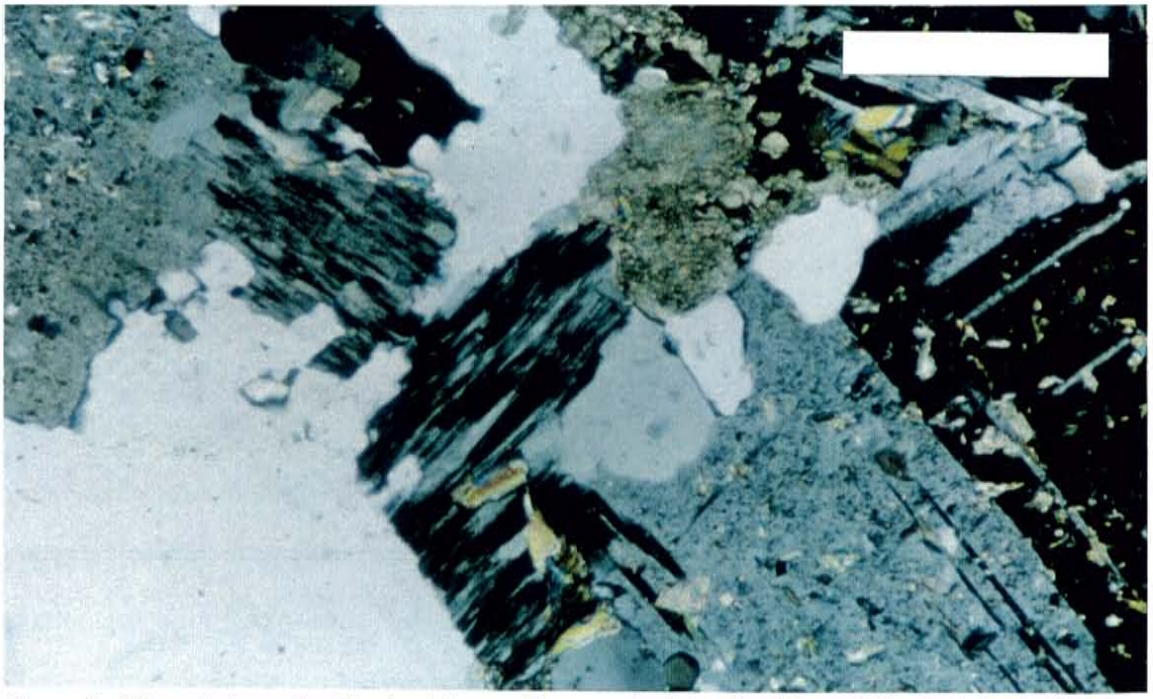

Figure 6. Microphotograph of the hypidiomorphic-granular intrusive, Nkran Hill. Scale bar is 0.5 mm. Large crystal on right is oligoclase with sericite. White mineral is quartz. Anhedral calcite at center top. Plagioclase crystals show overgrowth of albite (center).

quartz veins occur both within the intrusive and in metasediments immediately adjacent. The veins within the intrusive appear to be vertical and horizontal, and there is no indication that the intrusive material has been forced into position during faulting. In other drill intersections of the shear zone, no brecciation is present between intrusive and wall rock. Thin section #6A, taken across the intrusive-metasediment boundary, indicates no small-scale faulting along the contact.

The quartz veining at the Amansie mine falls into three categories:

1. Vertical veins, dipping 85° to 90° and oriented N 036 E, occur either along the main shear or running roughly parallel to it (Fig. 4). These veins display varying degrees of deformation, and commonly contain fragments of metasediments. In thin section some of these veins display fractured, ribbon-like patterns. A few exposures of vertical veins contain sulfide minerals and visible gold.

2. Horizontal veins occur within the hypidiomorphic-granular intrusive and can extend for short distances past the margins of the intrusive. Field evidence indicates that they are much more pronounced within the intrusive (Fig. 8). No crosscutting relationships were found between horizontal and vertical veining. No visible sulfide minerals or gold are found within the veins, and there is no increase in alteration of the intrusive rock near the contacts.

3. Sub-vertical quartz veins, dipping 75° to 85°, are oriented 10° to 20° from the main shear orientation. They form blocky exposures and contain no fragments of wall rock. An abundance of fracturing and inclusions containing microscopic specks of dark material have given the quartz a cloudy blue tint. No crosscutting relationships were observed between these veins and the other two types.

V. Gold Mineralization

Gold mineralization at the Amansie mine is found both in quartz veins and disseminated throughout the intrusives and metasediments. Analysis of gold was conducted by Amansie Resources, Limited, during field study. Gold grades of the quartz veins vary by vein type. Grades of vertical quartz veins range from 7 to 13.8 g/t Au, an analysis of a sub-vertical quartz vein grades 5.1 g/t Au, and grades of horizontal quartz veins range from 0.34 to 1.21 g/t Au. Gold assays from drill core indicate that the highest gold grades occur in metasediments surrounding the intrusive bodies (see cross sections, Appendix A).

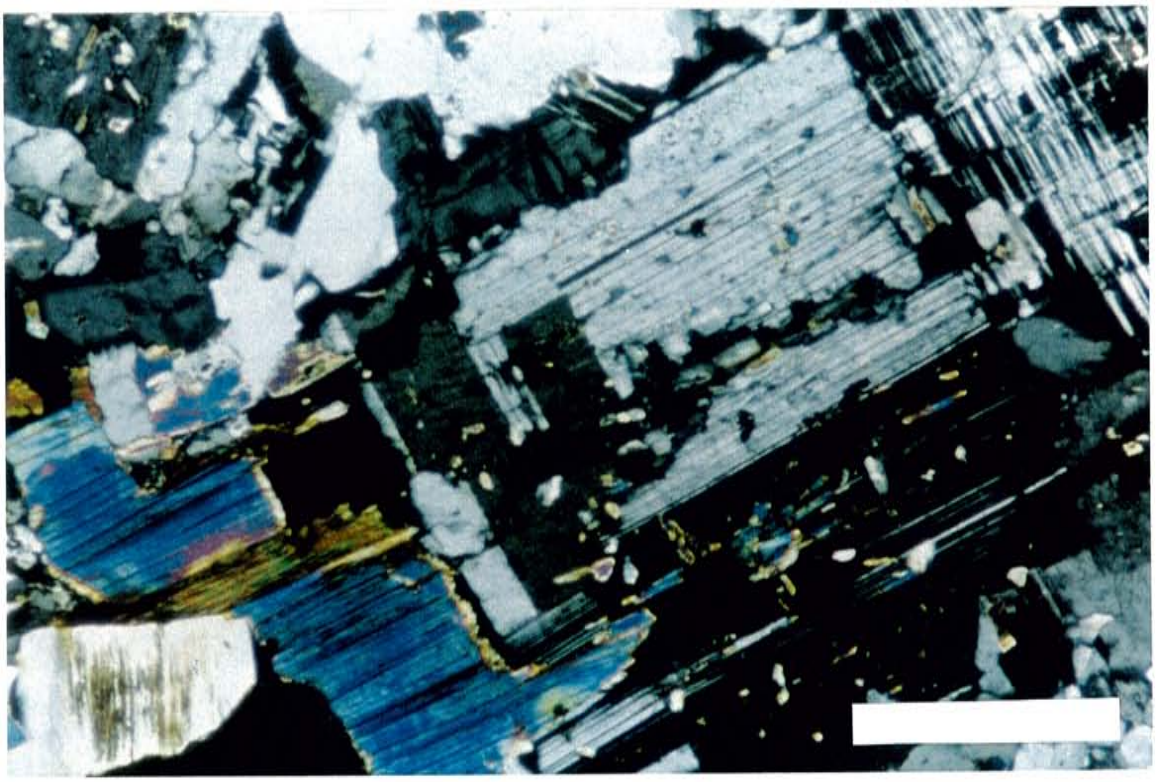

Figure 7. Microphotograph of the Mmooho Hill unmineralized intrusive. Scale is 0.5 mm. Center is andesine. One muscovite crystal (far right) has been altered to white mica, while others have slight alteration at the margins.

Figure 8. Underground exposure of intrusive/metasediment contact zone, Nkran Hill. Depth of 40 m. Rocks are highly weathered. Intrusive (right) shows greater development of horizontal quartz veins (dark color). From pivot (steel circle) to end of scale is 50 cm.

The Obuasi Intrusives

The Nhyiaso and Anyankyerim intrusives were emplaced along the Ashanti Belt (Fig. 1), near the contact between the metasedimentary and volcanic Birimian rocks. The Nhyiaso intrusive occurs along a subsidiary shear zone to the west of the main Obuasi shear. Junner (1932) classifies intrusives of this area as Dixcove granites. Both intrusives occur as single granitoid bodies with some association to regional shearing. The Nhyiaso intrusive is bordered on one side by a well-developed shear zone, and the highest gold grades occur near the intrusive margins. Quartz veins outside the intrusive, however, show very low degrees of mineralization. Both horizontal and vertical quartz veins occur within the intrusives (N. Bailie, pers. commun., 1994). The horizontal veins extend only short distances past the intrusive margins.

The two thin sections of the Nhyiaso intrusive differ greatly from each other. One section is allotriomorphic-granular and shows primary plagioclase (andesine), muscovite, and quartz. Plagioclase shows little development of sericite. Secondary albite and quartz are common interstitial to primary crystals. Primary quartz crystals display strong undulatory extinction, but no foliation is evident. There is a notable absence of calcite. The other thin section is from a deeper location and has a porphyritic texture. It shows a higher degree of alteration. Feldspars have undergone complete sericitization, and a faint foliation is visible. All primary micas are altered to clay minerals, quartz, and calcite. Calcite is abundant throughout the matrix. Polished sections display sub- to anhedral pyrite, isolated patches of subhedral arsenopyrite, and minor occurrences of chalcopyrite.

Thin sections of the Anyankyerim intrusive show a relatively unaltered hypidiomorphic-granular rock. The major constituents are quartz, andesine, primary muscovite, and potassic feldspar, all finer grained than the same minerals in thin sections

of Nkran Hill. These minerals show only minor alteration. Quartz and feldspar have strong graphitic intergrowths in one sample. The edges of some mica grains are altered to clay minerals and some calcite is present. Of all the mineralized granitoids studied, the Anyankyerim intrusive appears to be the least altered or deformed. A polished section of the Anyankyerim intrusive shows only tiny, isolated, subhedral arsenopyrite crystals.

The Ayanfuri Project

The Ayanfuri project refers to a group of intrusive bodies concentrated within an area of 7000 m^2. At least 14 granitoids have been recognized on the mine property, but only two were sampled for the study. The granitoids are related to shearing but do not occur along the same shear. Each of the intrusive bodies is elongate striking NE-SW, parallel to regional shearing. Hand samples of the intrusives appear similar to those collected from the Nhyiaso intrusive and the Anyankyerim intrusive. Some of the intrusives of the Ayanfuri project (i.e., South Esuajah), show elevated gold grades completely within the intrusive itself with no enriched halo of wall rocks. Both vertical and horizontal quartz veins occur in association with the intrusives. Gold grades are higher within these veins than in the surrounding igneous body (G. Amamkwa, pers. commun., 1994). One granitoid, the Chirwewa intrusive body, appears in many respects similar to Nkran Hill, having lower gold grades in the center than at the margins. However, no drilling has taken place on this hill and consequently no samples could be collected for analysis.

Thin sections were taken from the South Esuajah and Fetish Pit ore bodies. Sections show an altered allotriomorphic-granular rock. In one thin section, intense alteration has almost completely converted feldspars to sericite, and primary micas are absent. Calcite and rutile are abundant in the matrix. In the other thin section, very little sericite is present in feldspars. In both thin sections, quartz displays highly undulatory extinction and there

are sutured margins between crystals. One polished section shows euhedral arsenopyrite being overgrown by pyrite, and both contain small pyrrhotite blebs. There are euhedral pyrite grains present that show no apparent paragenetic relationship to the arsenopyrite. No chalcopyrite was observed.

Metamorphism and Alteration

The mineralized intrusive bodies show minor evidence of metamorphism, and metamorphic textures are well developed in the surrounding metasediments. Both rock types show evidence of alteration. Foliation does not cross the contact between the two rock types at the Amansie mine, indicating that regional metamorphism was ending during intrusive emplacement. Undulatory extinction of quartz grains, observed in most thin sections, and development of mylonite in the porphyritic intrusive of Nkran Hill, are indicative of mechanical metamorphism. Sericitized feldspar crystals are weaker than quartz crystals, and lack of such ductile deformation in sericitized feldspar crystals suggest that sericitization occurred after metamorphism. The concentration of sericite and sulfide minerals along microfractures within the intrusives suggest hydrothermal processes are responsible for their occurrence. Proximity of the intrusives to a shear zone suggests that subsequent brittle deformation induced the secondary twinning in plagioclase at the Amansie mine. The porphyritic intrusive of Nkran Hill has undergone a higher degree of metamorphic change than the hypidiomorphic-granular intrusive.

Sulfide Paragenesis and Gold

Paragenesis of sulfide minerals is most easily interpreted from evidence at Nkran Hill. The occurrence of euhedral arsenopyrite in the metasediments and intrusives indicates that the sulfide minerals phase post-date emplacement of the intrusives and metamorphism.

Similar observations have been made of arsenopyrite crystals at Prestea, and are classed as initial arsenopyrite-gold (type 4) mineralization common to the Birimian rocks of Ghana (Milési et al., 1992). Pyrite forms both with and subsequent to the formation of arsenopyrite. Both chalcopyrite and pyrrhotite occur subsequent to the formation of arsenopyrite and pyrite, but show a poor degree of development. Limited data suggests that all other intrusives studied have a similar paragenesis.

The one polished section containing visible gold comes from a vertical quartz vein. The occurrence is in a fracture that is near the surface, thus most sulfide minerals have been weathered out. One pyrite crystal remains, and it does not enclose the gold grains. Metallurgical testing done by Amansie Resources Limited indicate that samples of drill core contain gold that occurs interstitial to sulfide minerals (D. Bertram, pers. commun., 1996).

Table 1b
Major element abundances of Akwasiso and Mmooho Hill

	Mmooho	Akwasiso #1	Akwasiso #2	Akwasiso #3
SiO_2	72.21	75.11	73.1	70.92
TiO_2	0.21	0.18	0.13	0.18
Al_2O_3	15.13	12.52	13.93	14.49
Fe_2O_3	1.76	1.49	1.38	1.49
MnO	0.009	0.034	0.023	0.016
MgO	0.33	0.39	0.39	0.45
CaO	0.37	1.3	1.06	1.56
Na_2O	3.72	5.25	6.64	6.14
K_2O	4.86	1.01	0.85	1.23
Cr_2O_3	0.039	0.018	0.02	0.02
LOI	1.2	2.1	1.7	2.8
C	0.05	0.41	0.39	0.54
S	0.01	0.16	0.27	0.1

Table 1c
Major element abundances of SB and VB Averages

SB (ave of 25)	VB (ave of 51)
69.24	67.46
0.32	0.36
15.05	14.86
2.73	3.95
0.04	0.07
0.97	1.33
2.19	3.24
4.37	4.53
2.58	2.13
0.77	1.36

Table 1d
Major element abundances of the Ayanfuri and Obuasi intrusives

	Ayanfuri #1	Ayanfuri #2	Nhyiaso	Anyankyerim #1	Anyankyerim #2
SiO_2	68.13	67.3	77.04	70.76	69.69
TiO_2	0.34	0.47	0.05	0.23	0.25
Al_2O_3	14.69	13.78	13.38	14.78	14.81
Fe_2O_3	4.3	4.32	1.47	3.64	4.03
MnO	0.031	0.035	0.01	0.033	0.032
MgO	0.84	1.06	0.07	0.52	0.55
CaO	1.97	2.63	0.08	1.66	1.61
Na_2O	4.44	4.48	5.69	2.49	3.32
K_2O	2.35	1.83	1.22	3.55	3.29
Cr_2O_3	0.029	0.034	0.016	0.034	0.028
LOI	3.1	4.2	1.0	2.1	2.1
C	0.8	1.1	0.03	0.54	0.52
S	0.63	0.73	0.50	0.19	0.32

Tables 1a-d. Major element abundances of intrusives at Mmooho Hill, Nkran Hill, Akwasiso Hill, Anyankyerim, Nhyiaso, and Ayanfuri in % weight of whole rock, as determined by geochemical analysis. The SB and VB averages are taken from Leube et al. (1990). Nkran (pr) indicates analyses of the porphyritic dike at Nkran Hill, and Nkran (hg) indicates analyses of the hypidiomorphic-granular intrusive. C is total carbon and S is total sulfur.

Table 2a
Trace element abundances from the Nkran Hill intrusives

Element	Nkran (pr) #1	Nkran (pr) #2	Nkran (pr) #3	Nkran (hg) #1	Nkran (hg) #2	Nkran (hg) #3	Nkran (hg) #4	Nkran (hg) #5
As	5470	305.3	242.3	4021	531.9	3183	2121	1701
Au*	1080	57	62	324.5	472	391	448	511.5
Ba	424	386	407	238	267	399	351	448
Ce	14	28	26	13	9	9	14	13
Cr	139	148	122	92	106	175	203	169
Cu	60	27.8	29.4	16.2	40.6	24.3	37.5	39
Ga	28	17	21	25	20	22	22	22
Mo	17.2	12.2	8.8	96.75	14.4	21.6	12.3	12.7
Nb	1.7	1.83	0.42	tr	tr	1.51	tr	tr
Ni	19	72	19	7	9	10	9	9
Pb	5.84	8.46	8.08	34.49	9.69	10.36	14.7	5.1
Rb	61	53	60	21	19	41	30	43
Sb	tr	tr	tr	tr	tr	tr	tr	tr
Sc	6.1	7.7	6.2	2	2.4	2.5	2.5	2.1
Sr	508	382	455	482	305	333	434	363
W	9	6	5	7	tr	tr	tr	tr
Y	7.47	10	7.49	3.06	3.51	3.77	3.6	3.6
Zn	57	131	58	39	31	32	38	35
Zr	99.7	106.8	101.4	80.6	76.2	80.7	75.5	85.2

Table 2b
Trace element abundances of Akwasiso and Mmooho Hill

Element	Mmooho	Akwasiso #1	Akwasiso #2	Akwasiso #3
As	t	301.2	2136	676.4
Au*	40	140	1450	34
Ba	441	295.2	253.4	378.2
Ce	54	13	7	8
Cr	161	95.4	97.4	102.5
Cu	19.6	19.5	22.9	9
Ga	27.29	15.32	17.93	18.29
Mo	17.8	10	19.7	15.1
Nb	1.8	0.37	1.42	tr
Ni	2.7	7.5	6.72	10.88
Pb	18.8	9.12	17.34	6.57
Rb	426	26.96	23.56	34.43
Sb	0.5	tr	tr	tr
Sc	1.6	2.1	1.7	2.3
Sr	132	457.5	333.9	681.4
W	4	8	81	5
Y	9.9	4.01	2.81	2.5
Zn	59	25.85	32.84	32.15
Zr	101	61.7	53.19	76.8

Table 2c
Trace element abundances of SB and VB averages and average granites

SB (25)	VB (51)	High-Ca Granite	Low-Ca Granite
nd	nd	1.9	1.5
1	2.6	4	4
706	770	420	840
nd	nd	81	92
20	32	22	4.1
9	19	30	10
nd	nd	17	17
nd	nd	1	1.3
4.8	5.3	20	21
6.3	17	15	4.5
29	15	15	19
152	53	110	170
nd	nd	0.2	0.2
7.6	11	14	7
374	487	440	100
nd	nd	1.3	2.2
7.4	28	35	40
63	55	60	39
116	151	140	175

Table 2d
Trace element abundances of the Ayanfuri and Obuasi intrusives

Element	Ayanfuri #1	Ayanfuri #2	Nhyiaso	Anyankyerim #1	Anyankyerim #2
As	539.3	83.2	324	352.9	594
Au*	686	174	163	764	1340
Ba	422.8	342.1	468	823.4	897.7
Ce	18	15	16	43	49
Cr	152.5	160.3	132	262.7	223
Cu	31.7	41.9	24.5	24	21.4
Ga	23.35	20.01	26.9	21.2	23.5
Mo	15.1	14	7.6	15.7	13.7
Nb	1.44	0.99	20	4.4	4.5
Ni	14.24	18.01	6.6	13	11.1
Pb	8.04	9.71	26.9	17.9	16.2
Rb	70.38	59.45	33.6	121	113.8
Sb	7.1	2.8	tr	0.2	0.6
Sc	4.5	4.2	2.7	2.3	2.7
Sr	338	457.4	119	449	488
W	5	6	tr	tr	tr
Y	5.42	4.7	6.3	5.5	6.6
Zn	48.57	57.83	24.8	44.9	49.9
Zr	108.3	144.3	42	131.6	140.9

Tables 2a-d. Trace element abundances of the intrusives at Mmooho Hill, Nkran Hill, Akwasiso Hill, Anyankyerim, Nhyiaso, and Ayanfuri, in ppm (the asterisk * denotes ppb). Gold values from Mmooho Hill are trace from INAA results, but fire assay results of five samples yields 40 ppb, s = 0.009. Values for SB and VB are taken from Leube et al. (1990) except for Au, which is from Hides and Leube (1989). The average high-Ca granites and low-Ca granites represent intermediate and highly felsic end members, respectively, for the general class of 'granitoids' (Turekian and Wedepohl, 1961). nd = not determined, tr = trace values.

There are differences between the major element analyses of the studied intrusives and the VB and SB averages (Tables 1a-d). Detailed comparison is misleading because the intrusives of this study are altered and the VB and SB averages are assumed to be unaltered. One pattern, however, is clear from the averages. The Na_2O values for most studied intrusives are higher than the VB and SB averages and the K_2O values are lower. The exceptions are the samples from Mmooho Hill and the Anyankyerim intrusive, both of which show the opposite trend.

The trace element concentrations of the intrusives differ from average granites and from VB and SB averages (Tables 2a-d). Elements that occur in clearly anomalous concentrations are Au, Cr, W, Sb, Mo, and As. Gold is variably enriched above

background values in all samples of granitoids. Molybdenum is at least ten times higher, As is 100 to 1000 times higher, and Cr is 10 to 50 times higher than the range for average granites. The SB and VB averages are similar to the average high-Ca granite end member for these three elements. Tungsten and Sb are anomalous in some of the intrusives studied. Rubidium is depleted in most samples, showing values less than Rb values for average high-Ca granites. The exceptions are the samples from the Anyankyerim intrusive, which show Rb values similar to average high-Ca granites, and the samples from Mmooho Hill, which shows Rb values more than two times higher than average low-Ca granites. Most samples show Ba values similar to or slightly less than average high-Ca granites. The exceptions are the samples from the Anyankyerim intrusive, which show Ba values similar to average low-Ca granites. All Sr values are similar to the average VB, SB, and average high-Ca granites, except for the samples from the Nhyiaso intrusive. The latter shows a Sr value similar to that of average low-Ca granites. Zirconium values in samples from Nkran Hill, Akwasiso Hill, Mmooho Hill, and the Nhyiaso intrusive are lower than VB, SB, or the range of high-Ca to low-Ca granites. Niobium values in all samples are slightly lower than the VB and SB averages, but are much lower than the range in average high-Ca to low-Ca granites.

Correlations

Trace element abundances are correlated with each other using Spearman's method (Appendix C). Gold shows a strong positive correlation with W, a moderate positive correlation with As and Mo, and a strong negative correlation with Sb. All other elements show no correlation with Au. Lead shows a moderate negative correlation with Cu and Ni. Zinc shows a moderate positive correlation with Cu and Ni. Scandium shows a very strong positive correlation with Sb.

Major element abundances are correlated with each other and with Au, Sr, Rb, Ba, C, and S, using the Spearman's method (Appendix C). Gold shows a weak positive correlation with CaO. Silica shows strong negative correlation with TiO_2, Zr, CaO, Fe_2O_3, MgO, and MnO, and the latter three show strong positive correlations with each other. K_2O shows a strong negative correlation with Na_2O, and a strong positive correlation with Cr_2O_3, Ba, and Rb. CaO shows a strong positive correlation with Sr, Zr, and a moderate positive correlation with Rb and TiO_2.

Rock Type Classifications

Major Element Classification Diagrams

A CaO-Na_2O-K_2O ternary diagram (Fig. 9) shows a dominance of tonalite and trondhjemite compositions at Nkran Hill, Akwasiso Hill, the Nhyiaso intrusive, and the Ayanfuri intrusives. The SB and VB averages plot on the granodiorite/tonalite boundary, and data from the Anyankyerim intrusive and Mmooho Hill plot as quartz monzonites. The more Na_2O-rich samples follow a tonalite-trondhjemite trend, while data from the Anyankyerim intrusive and Mmooho Hill follow a calc-alkaline trend (Fig. 9).

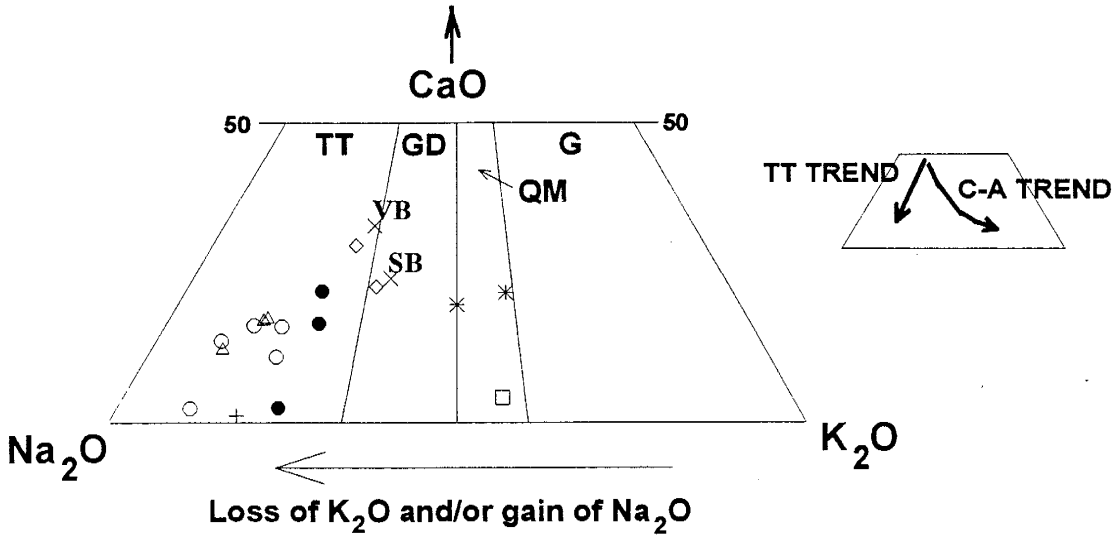

Figure 9. CaO-Na_2O-K_2O ternary diagram for major element classification of igneous rocks. Field labels are: TT = tonalite-trondhjemite, GD = granodiorite, QM = quartz monzonite, G = granite. The symbol × = an average abundance of sedimentary basin granitoids (SB) and volcanic belt granitoids (VB) (Leube et al., 1990). Remaining symbols as follows: □ = Mmooho Hill, ◊ = Ayanfuri intrusives, Δ = Akwasiso Hill, o = hypidiomorphic-granular Nkran Hill intrusive, ● = porphyritic Nkran Hill intrusive, + = Nhyiaso intrusive, star = Anyankyerim intrusive. Arrow under diagram indicates the shift in classification resulting from loss of K_2O and/or gain of Na_2O. Diagram to right illustrates the evolution of rock compositions following a tonalite-trondhjemite trend (TT) and a calc-alkaline trend (C-A).

The La Roche (1978) diagram classifies samples according to the abundances of Al_2O_3, SiO_2, K_2O, Na_2O, and CaO (Fig. 10). It is a ternary diagram with quartz, K-feldspar, and Na + Ca feldspar at the apices. Figure 10 illustrates only the applicable portion of this ternary diagram. Data plot in similar fields in both Figures 9 and 10. Data from Nkran Hill, Akwasiso Hill, and the Nhyiaso intrusive plot within the tonalite field. One set of data from the Ayanfuri intrusives plots as a tonalite and the other plots as a granodiorite. Data from the Anyankyerim intrusive plot as adamellites. The term 'adamellite' covers a range of compositions straddling the granodiorite-granite boundary (O'Connor, 1965), and is synonymous to the quartz monzonite field in Figure 9. The data set from Mmooho Hill plots as a granite.

The majority of data plot in the peraluminous domain in the Debon and Le Fort (1983) characteristic minerals diagram (Fig. 11a). Data from two Nkran Hill samples and

one data set from the Ayanfuri intrusives plot within the metaluminous domain. Some data plot in the leucogranite field. Data that plot in the peraluminous domain are scattered across both biotite- and muscovite-dominant fields.

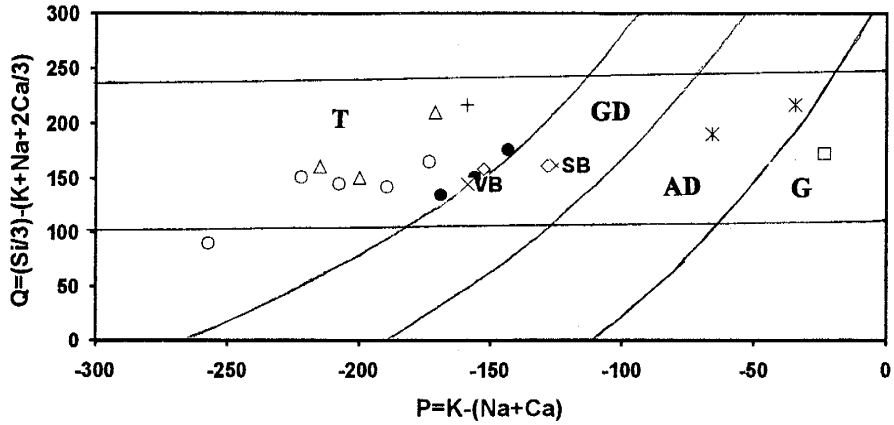

Figure 10. The La Roche (1978) nomenclature diagram using major element abundances. Symbols and field labels as in Figure 9. AD = adamellite.

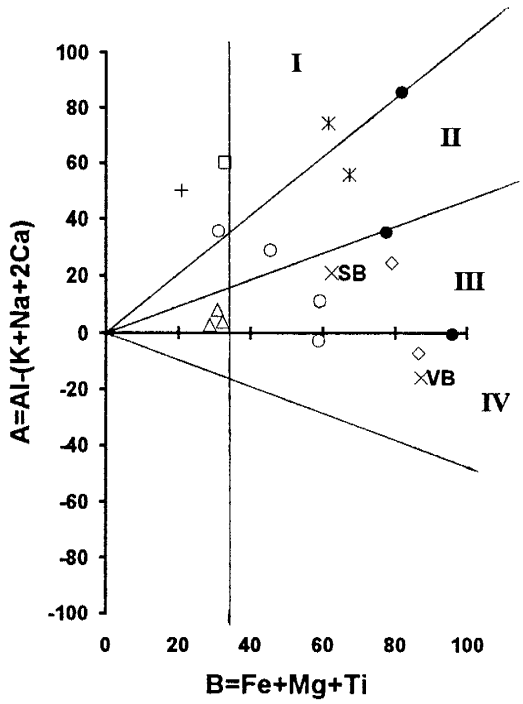

Figure 11a. Characteristic minerals diagram using major element abundances (Debon and Le Fort, 1983). The diagram is divided into four sectors numbered I to IV. I = muscovite alone or muscovite > biotite. II = biotite > muscovite. III = biotite alone. IV = biotite with amphiboles. All positive A values indicate peraluminous domain, and all negative A values indicate a metaluminous domain. Leucogranitic compositions occur at a B value less than 38.8. Symbols as in Fig. 9.

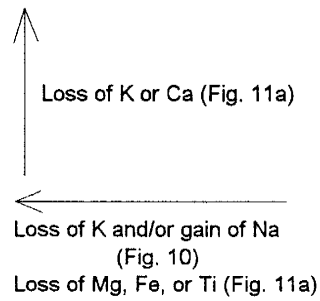

Figure 11b. Expected shifts in composition in Figures 10 and 11a during losses and gains of the indicated elements.

Alteration, as observed in thin sections, complicates the determination of rock types in Figures 9, 10, and 11a. If significant addition or subtraction of SiO_2, K_2O, Na_2O, or CaO has occurred, the rock classification will not be correct. Arrows shown in Figure 9 and Figure 11b illustrate the shift expected from addition of Na_2O or loss of K_2O. In both cases the points move to the left. Figure 11a has the same weakness. The parameter A=Al-(K+Na+2*Ca) is very sensitive to alteration (Debon and Le Fort, 1983). Arrows (Fig. 11b) also illustrate the shifts that would be expected during losses of Fe_2O_3, MgO, TiO_2, K_2O, and CaO. Minerals such as hornblende and primary biotite are rarely seen in thin section except for in the case of Mmooho Hill. The sample from Mmooho Hill is Al-rich, which agrees with thin section observations showing an abundance of muscovite.

Trace Element Classification Diagrams

Figure 12 is a Ce-Zr/TiO_2 trace element classification diagram (Winchester and Floyd, 1977) showing the distribution of data from the intrusives. Trace elements and TiO_2 are generally less mobile than major oxides such as Na_2O, K_2O, and CaO during hydrothermal alteration. Hence, they are better to classify altered igneous rocks. The Winchester diagram was created for classification of volcanic rocks, and it was adapted to plutonic rocks by relabeling the fields with plutonic rock equivalents. The Zr/TiO_2 value is generally an index of alkalinity, the more alkaline rocks tending to have higher concentrations of Zr (Winchester and Floyd, 1977). Diagrams that include Nb were not used because this element was detected in only a few samples.

The samples plot over a range of rock types as with Figures 9 and 10. The data from Nkran Hill, Akwasiso Hill, Mmooho Hill, and the Ayanfuri intrusives plot as tonalites (Figure 12). Data from the Anyankyerim intrusive plot as granodiorites. The data set from the Nhyiaso intrusive plots as a granite. Data from the hypidiomorphic-granular intrusive at Nkran Hill plot as more felsic rocks than data from the porphyritic dike.

There is general agreement between Figure 12 and the major element classification diagrams. All three diagrams indicate a dominance of tonalites in the samples. The exceptions are data from the Anyankyerim intrusive and Mmooho Hill, which plot as more felsic rocks on Figure 9 and 10 than in Figure 12, and the Nhyiaso intrusive, which plots as a granite on Figure 12.

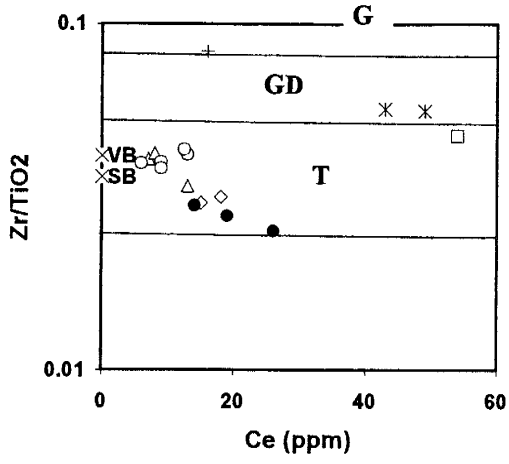

Figure 12. Zr/TiO_2 - Ce trace element classification diagram modified after Winchester and Floyd (1977). Symbols and field symbols same as Fig. 10. Averages for SB and VB give values for Zr and TiO_2, but do not include abundance of Ce. This element is set equal to zero, as it does not affect the indicated degree of alkalinity.

Intrusive Origin

A tectonic classification of the intrusives was determined by use of a discrimination diagram (Pearce et al., 1984) (Fig. 13). The diagram applies to granitic rocks, classified by Pearce et al. (1984) as any plutonic igneous rock containing more than 5% of modal quartz. The x-coordinate of this diagram is Y+Nb. Many of the Nb values in this study are below the detection limit of 2 ppm, but the error in plotting these points is minor. For example, adding a value of 1 ppm Nb rather than 2 ppm Nb to a yttrium value of 8 ppm will not significantly shift the analysis in the x-direction, and the VAG/syn-COLG boundary is overwhelmingly dependent on the y-component (Rb). All data points plot within volcanic arc granites (VAG) field with the exception of Mmooho Hill; it plots as a syn-collisional granite (syn-COLG). Pearce et al. (1984) state that data points straddling

the VAG/syn-COLG boundary can also be interpreted as being characteristic of post-collisional granites.

The diagram was originally intended for Phanerozoic rocks, and adapting them to Precambrian rocks may not be suitable. Pearce et al. (1984) state, that in the case of Precambrian rocks, the VAG/syn-COLG boundary may not be as well defined. A blurring of this boundary would affect the classification of the intrusives in the study.

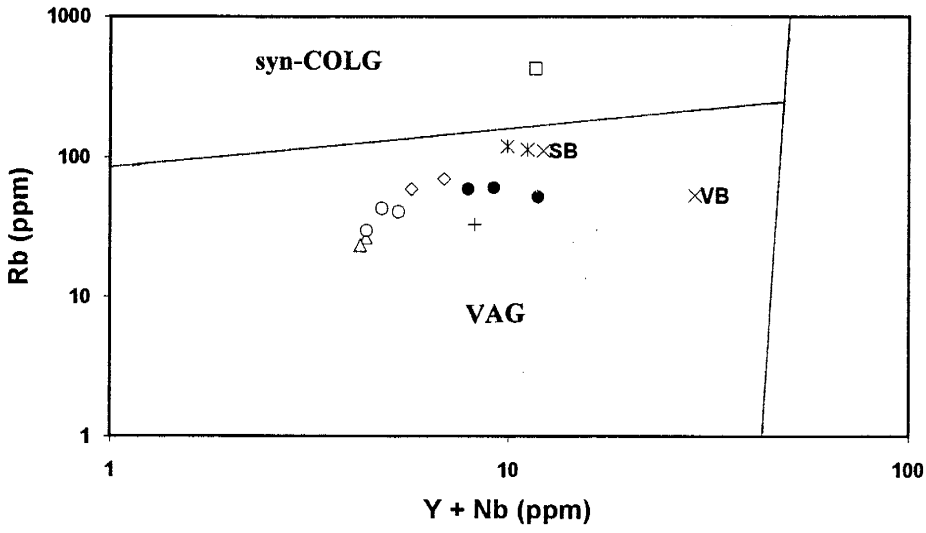

Figure 13. Rb versus Y+Nb tectonic discrimination diagram (Pearce et al., 1984). Field labels are VAG = volcanic arc granitoid, syn-COLG = syn-collisional granitoid. Symbols as on Fig. 9.

Adjustments for Alteration

Three approaches were taken in order to determine the manner and degree of alteration experienced by the intrusive bodies. These approaches include petrographic description, a mathematical reconstruction model (Renault, 1986), and a comparison of element changes relative to TiO_2 abundance. It is not feasible to use the method of analyzing alteration presented by Gresens (1967), which requires analyses of unaltered rocks adjacent to altered rocks.

Petrographic study (detailed in Appendix A, summarized in Table 3) determines the alteration minerals, and provides a sense of relative alteration intensity. It has limited use in quantitative determination of elemental losses or gains. Rock for geochemical analyses came from the same pieces of drill core as rock used for thin sections.

Two methods were used to determine likely protolith compositions. Only samples unaffected by weathering were chosen. The first method uses the computer modeling program Deltas written by J. Renault (1986). This model determines the protoliths of altered volcanic rocks, but is adapted here to classify plutonic igneous rocks. The second method compares the abundances of various elements against TiO_2 abundance. Results of the two methods and the petrographic observations are summarized in Table 3.

Model 1 - The Deltas Program

Deltas is a program that uses equations to calculate hypothetical igneous precursor compositions (Appendix E). It is based on equations by Smith (1963) and linear relationships among major element oxides in the compositions of average igneous rocks as presented by Daly (1933). The model assumes that the $Al_2O_3/(Al_2O_3 + Fe_2O_3)$ ratio is unchanged by alteration. Silica, FeO, and TiO_2 are determined by formulas based on the $Al_2O_3/(Fe_2O_3 + Al_2O_3)$ ratio. Values for the sum of CaO, MgO, MnO, and FeO are determined from the above abundances along with a sum of the alkalis, and an iterative process recalculates all values until silica agrees to within 0.1%. Various formulas solve for MgO, MnO, CaO, Na_2O, and K_2O once the iteration is complete. Table 3 qualitatively summarizes the changes in major element abundances for all data as shown by the model.

The model 'forces' assemblages of the altered rocks into a very limited range of compositions. To do this, the program subtracts all of the magnesium from some data sets. The VB and SB averages were modeled as a test of the procedure, and it was found

that both compositions changed slightly. In theory, neither of these average analyses should undergo any change, unless some altered rocks were included in the averages.

The adjusted data are plotted on Figures 14a and 14b. Both diagrams show a spread of points from granodiorites to granites, defining a calc-alkaline trend. Data from the Ayanfuri intrusives, the Anyankyerim intrusive, and most data from Nkran Hill plot as granodiorites. Data from Akwasiso Hill, Mmooho Hill, the Nhyiaso intrusive, and the remaining data from Nkran Hill plot as adamellites (quartz monzonites) or granites.

The classifications differ from the original data plotted in Figures 9 and 10. The adjusted data show increases in K_2O and decreases in Na_2O. This shift agrees with the effects of K_2O depletion and Na_2O enrichment as indicted by arrows (Figs. 9, 11b). This occurs in every case except in the Anyankyerim intrusive, which shows the opposite shift, and Mmooho Hill, which does not change significantly. The points VB and SB shown on Figures 14a-b are the original averages, not the averages adjusted by the Deltas model.

Figures 14a and 14b do not agree in most cases with rock type determinations using trace elements (Fig. 12). Figures 14a and 14b indicate more felsic rock compositions in the case of the data from Nkran Hill, Akwasiso Hill, and Mmooho Hill. Data from the Anyankyerim intrusive plot as less felsic rocks. However, there is agreement with data from the Ayanfuri intrusives and the Nhyiaso intrusive, which plot as tonalites and a granite, respectively.

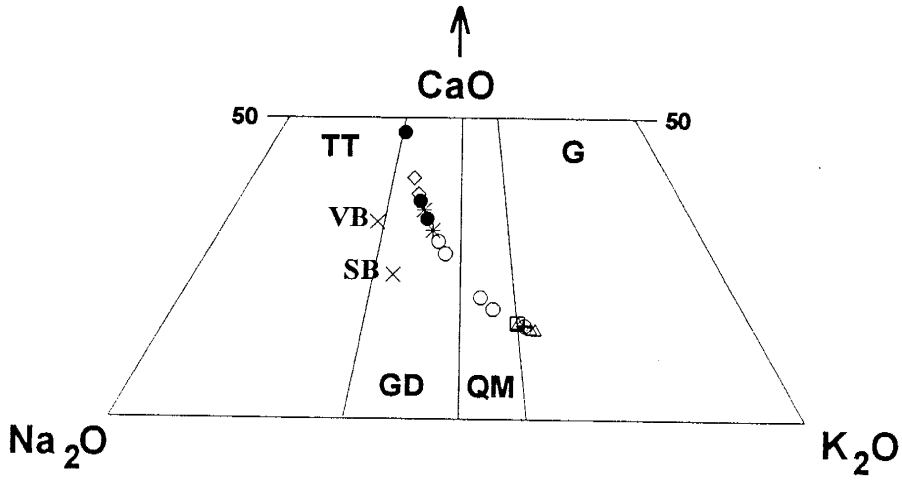

Figure 14a. The CaO-Na_2O-K_2O ternary classification diagram, with analyses plotted after adjustment by the Deltas model. The VB and SB averages have not been adjusted by the model. Symbols and field labels as in Figure 9.

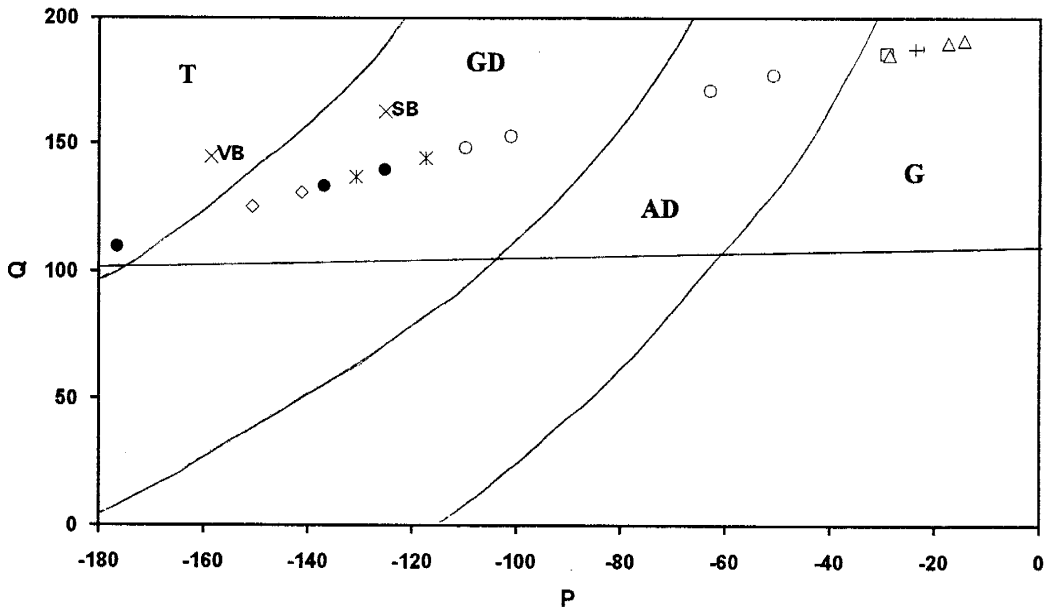

Figure 14b. Major element nomenclature diagram (La Roche, 1978) for the analysis results adjusted by the Deltas program (Renault, 1986). Symbols, field labels, and axis labels Q and P same as Fig. 10. The VB and SB averages have not been adjusted.

Model 2 - Changes of Major Elements Relative to TiO_2

Abundance of CaO, Na_2O, and K_2O were plotted relative to TiO_2 abundance (Figs. 15a-c). The procedure expands on a graph of log CaO/TiO_2 vs. log TiO_2 (Hynes, 1980). This graph was created to establish possible relationships between carbonate- and Ti-enrichment of metasomatised rocks. Titanium oxide is assumed to be immobile relative to CaO, Na_2O, and K_2O. The value of TiO_2 changes very little in samples taken along drill holes through the intrusives at the Amansie mine (Appendix D). This is an indication, at least at the Amansie mine, that TiO_2 does not change with the degree of alteration along these drill holes. A second assumption is that the VB and SB averages, and the data from the Anyankyerim intrusive represent unaltered rocks. A line drawn through these points, therefore, constitutes an 'ideal' ratio of an alkali oxide to TiO_2. Points falling off of this 'ideal' line are either depleted or enriched in the oxide.

Figures 15a-c show two relationships: (1) the VB and SB averages, along with data from the Anyankyerim intrusive and the Ayanfuri intrusives, tend to fall on or near a straight line, and (2) all other data plot off this line this line in at least two of the diagrams. The Mmooho Hill data set plots off the 'ideal' line in one diagram (Fig. 15a).

The changes in major element abundances, illustrated by the distances each point falls from the unaltered locus of points, are summarized qualitatively in Table 3. The results are in general agreement with losses and gains of Na, K, and Ca as shown in the Deltas model.

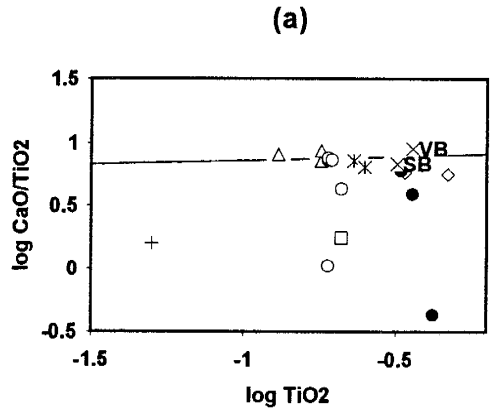

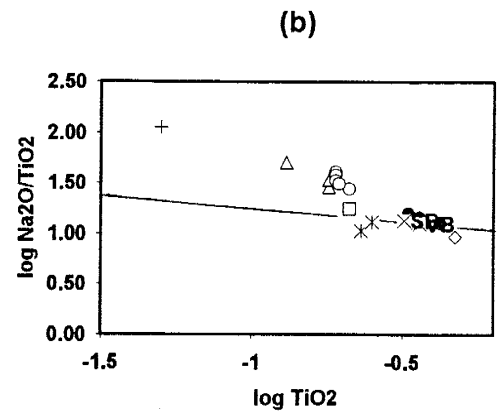

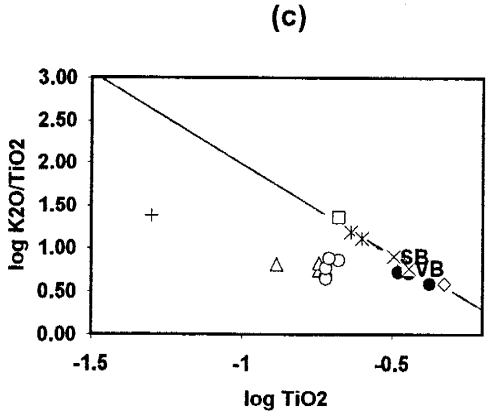

Figures 15a-c. Changes in major element abundances as a function of TiO_2 abundance. Points plotting off the line indicate relative depletion or enrichment of the oxide relative to TiO_2. In almost all cases the data from Mmooho Hill, the Anyankyerim intrusive, and the SB and VB averages fall near or on the locus of unaltered rocks. Symbols as on Fig. 9.

The absolute changes in CaO, Na_2O, and K_2O abundances were determined from Figures 15a-c and adjusted data were plotted on Figure 16. The adjusted data show a calc-alkaline trend as in Figure 14a, but span a wider range of compositions. Data from the Ayanfuri intrusives and the porphyritic intrusive at Nkran Hill plot as tonalites. Data from the Anyankyerim intrusive plot as quartz monzonites, and the reminder of the data plot as granites.

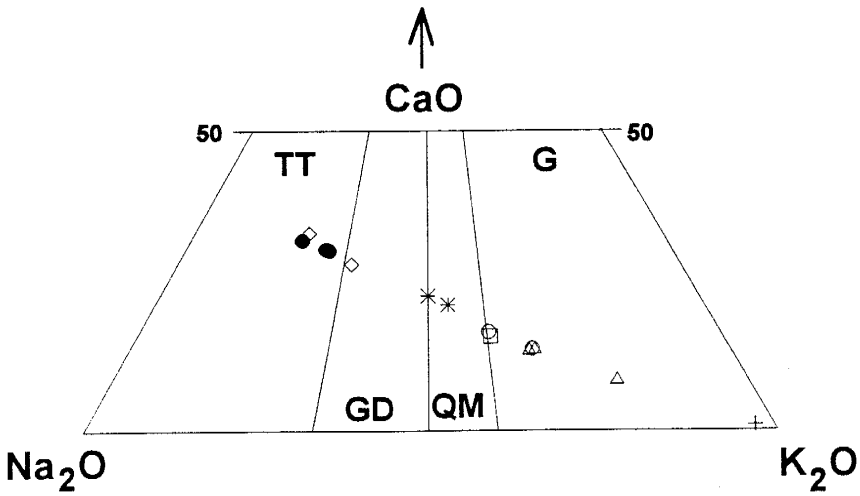

Figure 16. CaO-Na_2O-K_2O plot of data sets adjusted after comparison with TiO_2 in Figures 15a-c. Symbols and field labels same as in Figure 9.

The results show similarities and contrasts with Figure 9. Data from the Anyankyerim intrusive, the porphyritic intrusive of Nkran Hill, the Ayanfuri intrusives, and Mmooho Hill plot as the same rock types on both diagrams. Major differences are shown by the data from the hypidiomorphic-granular intrusive of Nkran Hill, Akwasiso Hill, and the Nhyiaso intrusive, which show a strong depletion of K_2O and addition of Na_2O.

Table 3 - Summary of rock alteration

Intrusive (x), (y)	Petrographic Observation	Deltas Program	Changes relative to TiO_2
Mmooho Hill (1), (1)	Slight alteration of primary muscovite No sericitization of feldspars Calcite absent	Moderate loss of Ca	Moderate loss of Ca
Ayanfuri intrusives (2), (2)	Complete alteration of primary micas One section shows complete sericitization of feldspars, other shows almost no sericite Addition of SiO_2 to matrix Calcite present	Moderate loss of K, Mg, Ca, moderate gain of Na High gain of SiO_2	Slight changes in Ca, K, and Na
Akwasiso Hill (0), (2)		High loss of K, high gain of Na	Slight loss of Ca High loss of K High gain f Na
Nkran Hill (hypidio-morphic granular) (5), (5)	Partial to complete alteration of primary micas Alteration of potassic feldspar Partial sericitization of feldspars, strong development of albite at edges of plagioclase and in matrix Addition of SiO_2 to matrix Calcite present in most sections	High loss of K Moderate loss of Ca High gain of Na Variable change in SiO_2	Variable loss of Ca High loss of K Moderate gain of Na
Nkran Hill (porphyritic) (6), (3)	Complete alteration of primary micas and amphiboles Sericitization of feldspars almost complete Formation of secondary albite in matrix Addition of SiO_2 to matrix Calcite present in most sections	High loss of Ca and Mg Moderate loss of K High gain of Na, SiO_2	Variable loss of Ca Moderate loss of K Moderate gain of Na
Nhyiaso intrusive (2), (1)	One section shows alteration of primary micas with no sericitization of feldspars, though strong development of albite interstitial to quartz crystals Other section has complete alteration of primary micas, complete sericitization Calcite present in one section, absent in the other	High loss of K, Ca High gain of Na	High loss of Ca and K High gain of Na
Anyankyerim Intrusive (2), (2)	Micas are large but localized in feldspars, indicating secondary development Addition of SiO_2 to matrix Calcite present	High loss of Ca, Mg Slight loss of Na Gain of SiO_2	Slight loss of Na, K, Ca

Table 3. Comparison of petrographic observations to changes in rock chemistry shown by the two models. (x) = number of thin sections studied, (y) = number of geochemical analyses.

Interpretations

Intensity of Alteration

All of the intrusives of the study are altered to some degree. This is reflected chemically in most analyses by a calculated loss of K, Ca and Mg and a gain of Na (Table 3). Thus, most intrusives have been affected by sodic alteration. The exceptions are analyses from the Anyankyerim intrusive, which show loss of Na and gain of K, and the analysis from Mmooho Hill, which shows only a loss of Ca. The correlation between Na enrichment and K and Ca depletion is illustrated on Figure 17. The data plot roughly along a line indicating a 1:1 relationship between gain of Na and loss of K + Ca. Two alteration reactions that support this trend are the alteration of potassic feldspar to albite, and the alteration of plagioclase to albite. A high Na/K in hydrothermal fluids would favor the first reaction (Moore et al., 1981). There are several points of evidence that support loss of K. Petrographic study reveals partial destruction of potassic feldspar in some thin sections. Figure 11a indicates that most samples are of peraluminous character, a rare condition for tonalites. A metaluminous rock acquires peraluminous character with sufficient loss of K as indicated in Figure 11b. In Figure 13, data from samples showing the most alteration in thin section (Nkran Hill and the Nhyiaso intrusive) have the lowest Rb values. This suggests that alteration has depleted Rb, which is proportional to loss of K. This depletion could have shifted the data points from syn-COLG to VAG origins (Fig. 13). There is even stronger evidence from petrographic observation for the alteration of plagioclase to albite. Plagioclase is much more abundant than potassic feldspar in most thin sections and is clearly associated with albite (Appendix A). Albite is common as overgrowths on plagioclase crystals in thin sections of the hypidiomorphic-granular intrusive at Nkran Hill and the Nhyiaso intrusive. Data from these intrusives show the largest shifts toward Na-enrichment and K + Ca depletion (Fig. 17). Loss of Ca

will shift the data points from metaluminous to peraluminous domains on Figure 11a in the same manner as loss of K (Fig 11b).

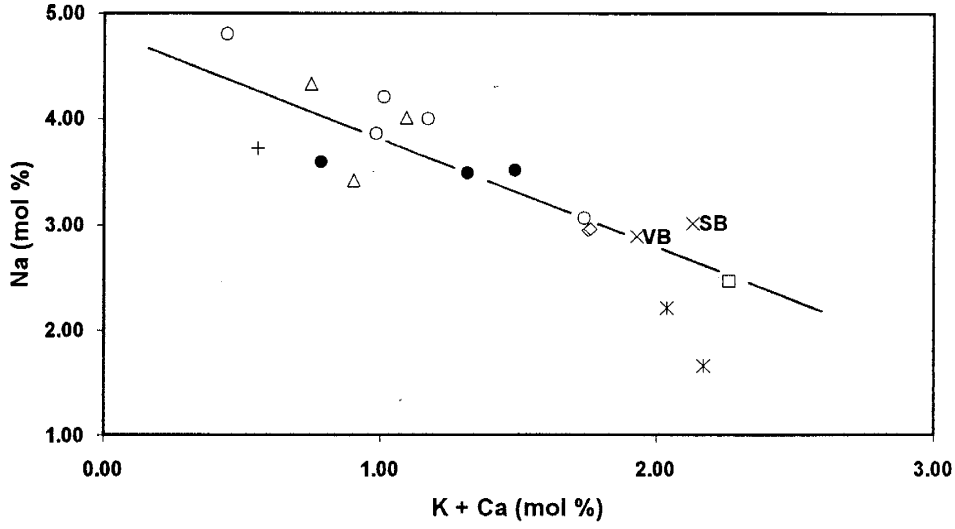

Figure 17. Graph of Na versus K + Ca abundances as determined by geochemical analyses. The data from all samples show loss of K and/or Ca and gain of Na during alteration except Mmooho Hill and the Anyankyerim intrusive. Symbols same as Figure 9. The data roughly plot along the line indicating a 1:1 inverse relationship between Na and K + Ca. The location of the VB and SB averages are assumed to indicate unaltered compositions.

The trace element classification diagram (Fig. 12) is in closer agreement with Figures 9 and 10 than it is with major element classification diagrams using adjusted data (Figs. 14a-b). There are two possible explanations for this: (1) the changes in Na and K abundance are overestimated by the alteration models, particularly for the hypidiomorphic-granular intrusive of Nkran Hill, Akwasiso Hill, and the Nhyiaso intrusive, or (2) the intrusives have been depleted in Zr relative to TiO_2, shifting the data points downward on Figure 12. Depletion of TiO_2 will exaggerate the indicated alteration in Figure 16, and this is likely to be the case for the adjusted data from Nkran Hill and the Nhyiaso intrusive. Positive correlation between CaO, Ti, and Zr suggests that a chemical relationship exists between the three. Hynes (1980) observed this correlation in metabasalts of low carbonate content, and attributed it to mobility of Ti and Zr in CO_2-rich metamorphic

fluids. If depletion of Zr and Ti are related, the net effect may not change the results of Figure 12, but will substantially change the results in Figure 16.

Classification of Intrusives

The intrusives of this study fall into the general classification of 'granitoids'. Classification diagrams of both original data and data adjusted by modeling of protoliths do not agree on more specific determination of rock types. If the reaction altering potassic feldspar to albite is favored in the hypidiomorphic-granular Nkran Hill intrusive, Akwasiso Hill, and the Nhyiaso intrusive, then the protoliths are granites. If the reaction altering plagioclase to albite is favored, then the protoliths of the Anyankyerim intrusive and Mmooho Hill range from tonalites to granodiorites. A clear relationship between plagioclase and albite, and a dominance of primary plagioclase over potassic feldspar in thin section supports the second case. The thin section of Mmooho Hill displays only slight alteration, and most diagrams indicate that it is a granodiorite or granite. Data from the Anyankyerim intrusive consistently plot as granodiorites or adamellites.

Evidence for Two Intrusive Events at Nkran Hill

Rock classification diagrams indicate that samples from Nkran Hill cover a wide range of compositions, and data tend to cluster according to texture observed in thin section. However, lack of a cross-cutting relationship between rocks with hypidiomorphic-granular textures and rocks with porphyritic textures precludes clear evidence of two separate intrusive episodes. Development of weak foliation and the occurrence of mylonite in samples of the porphyritic intrusive, and lack of foliation or mylonite in the hypidiomorphic-granular intrusive samples suggests either: (1) the porphyritic intrusive was emplaced syn-tectonically and hypidiomorphic-granular material

was emplaced post-tectonically, or (2) porphyritic intrusive material, invariably occurring as a thin dike, was subject to higher stress from waning regional tectonism or continued movement along the shear zone, while hypidiomorphic-granular intrusive material, invariably occurring as a thicker body, was less subject to these stresses.

Indicators of Gold Mineralization

The presence of alteration, but not the intensity, can be correlated with the occurrence of gold mineralization. The Anyankyerim intrusive shows a different manner of alteration than the other intrusives, yet does not exhibit different mineralization. The presence of alteration, however, does indicate gold mineralization. Mmooho Hill is the least altered of all the intrusions in thin section, and exhibits the lowest concentrations of gold (Table 2b).

Anomalous concentrations of trace elements are related to the occurrence of gold mineralization. The intrusive bodies occurring near the deep-seated Obuasi shear zone show anomalous Sb. Antimony may therefore be associated with such basin-edge gold deposits. This study shows Sb negatively correlated with gold, but this may be an artifact of the small data base (four analyses detected Sb). Dzigbodi-Adjimah (1992) concludes that Sb was added during formation of shear-related gold occurrences along the Ashanti Belt. Strong correlation of gold with W has been reported for Au-rich metavolcanics along the Sefwi Belt (west of the Asankrangwa Belt) that are associated with a granitic intrusion (Hirdes and Leube, 1989). The porphyritic Nkran Hill intrusive, the Ayanfuri intrusives, and Akwasiso Hill yielded anomalous values for W (Tables 2a, b, d). However, the detection limit of W in these analyses is 4 ppm, indicating that the other intrusives could also be anomalous (between 1.5 and 4 ppm). Enrichment in W appears to not be a function of lithology. Data from the porphyritic Nkran Hill intrusive plot as less felsic rocks than data from the Anyankyerim intrusive, yet the latter has lower concentrations of

W. Enrichment of As is related to gold mineralization. This is concluded by other studies of Birimian gold deposits (Leube et al., 1990; Dzigbodi-Adjimah, 1992). Molybdenum and chromium are anomalous in all intrusives including Mmooho Hill. Enrichment in Mo and Cr therefore appear to be a characteristics of all granitoids in the study (Table 2a-d). Hirdes and Leube (1989) report a weak correlation between Cr and Au in gold-mineralized zones at Obuasi, and attribute anomalous Cr to the presence of hydrothermal fluids. Kerrich (1986) reports anomalous Cr in hydrothermal fluids passing through volcanic rocks. The strong correlation between Cr_2O_3 and K_2O could be a result of alteration. Breakdown of both potassic feldspar and of mafic minerals containing Cr occurs in the initial stages of alteration, thus K and Cr could be lost in similar proportions.

FLUID INCLUSION STUDY

Petrography of Samples

Samples used for fluid inclusion study were taken from quartz veins in and around the intrusive bodies on Nkran Hill and Akwasiso Hill. Over 130 inclusions in twelve samples were studied petrographically and measured by microthermometry. Sufficient microthermometric data to determine inclusion compositions were obtained from 92 inclusions, the others are not clear or large enough to make all necessary measurements. Locations of quartz vein samples are illustrated on Figure 4.

One group of samples were obtained from cloudy quartz veins with a blue tint striking 10° to 20° to the main shear orientation. The quartz is moderately sheared with abundant inclusions throughout that show no orientation. Inclusions range from 10 to 25 μ in size. Irregularly-shaped inclusions contain opaque material. This type of quartz vein is represented by samples #20 and #29.

Vertical quartz veins in the main shear zone and nearby parallel veining are highly sheared. In thin section this shearing gives the appearance of a ribbon-like texture. In samples #18 and #19, abundant inclusions occur throughout the sample. Many inclusions are aligned parallel to shear directions and have negative crystal shapes. Inclusions range from 10 to 20 μ in size. A few fracture planes host larger irregular inclusions that contain opaque material (Fig. 18). Inclusions can only be observed in about 10% of the quartz. The remaining 90% is cloudy because of the many fracture planes. Samples #22, #39, and #23 display much less ribbon-like texture. The inclusions are clustered along highly deformed planes. In sample #39, inclusions are extremely small (< 10 μ).

Horizontal quartz veins within the granitoid body are moderately sheared and host fewer inclusions than other vein types. Inclusions are concentrated near sheared planes and tend to be aligned. Most inclusions range from 10 to 30 μ in size. Some

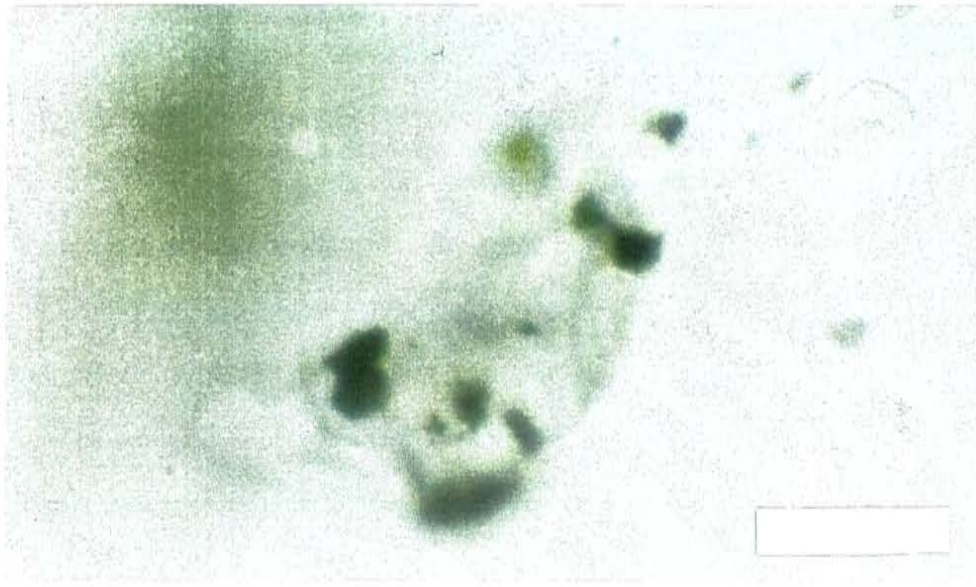

Figure 18. Inclusion hosting amorphous opaque material, from sample of vertical quartz vein. Scale bar is 10 μ.

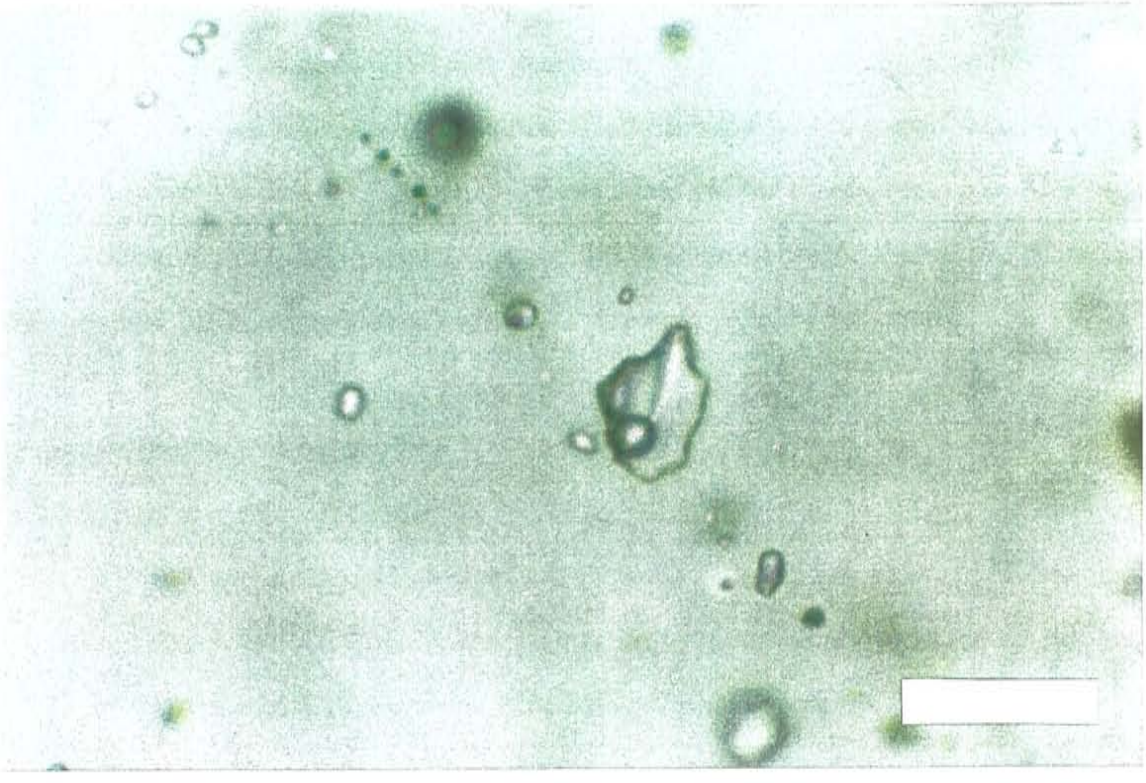

Figure 19. A type 2 inclusion occurring in a sample of sub-vertical quartz vein. Scale bar is 20 μ.

fracture planes host inclusions smaller than 5 μ along clearly secondary fractures. Irregularly-shaped inclusions filled by opaque material occur along an irregular fracture pattern. This vein type is represented by samples #25, #27, #38, #31, and #26. The inclusions in #26 are smaller than those in the other samples, typically < 15 μ in size.

Inclusions are classified as primary, pseudosecondary, and secondary after criteria set by Shepherd et al. (1985). Void-filling quartz crystals were not found in any quartz vein sample. The anhedral nature of the quartz precludes definitive identification of primary inclusions occurring along growth planes in quartz crystals. The classification of primary or pseudosecondary inclusions is based on pervasive alignment of negative crystal and regular inclusion shapes. Secondary inclusions concentrate along partially annealed fractures and are too small for microthermometric measurements.

Inclusions suspected of having undergone changes after trapping were not used for microthermometric measurement. Some inclusions form aligned series of elongate forms and have possibly been affected by the phenomenon known as necking down (Shepherd et al., 1985). Inclusions that have highly irregular shapes and have traces of radiating fractures were avoided, as were groups of inclusions packed closely together. As shown by Shepherd et al. (1985), even close groupings of negative crystal shaped inclusions can be the result of 'necking down' of a large, amorphous cavity within quartz.

Classification of fluid inclusions

Four basic types of fluid inclusions are observed. Classification of fluid inclusions is based on the number and type of phases appearing at room temperature, and on changes in the number of phases during initial cooling below room temperature.

Type 1 inclusions are two phase, liquid-rich inclusions that form a second liquid phase upon initial cooling. They exhibit irregular to negative crystal shapes, the majority being

the latter. Generally they occur scattered throughout the sample and have no relationship to annealed fractures. A few type 1 inclusions contain minute solid phases of amorphous black material. This is best viewed near total homogenization when the vapor phase moves rapidly, because the solid phase is commonly attached to the vapor bubble. There is no apparent relationship between inclusion properties and presence of solid material.

Type 2 inclusions have two phases at room temperature, but do not develop a third phase when cooled. They exhibit regular to irregular shapes (Fig. 19), and typically occur in poorly defined planes within the crystal. Some type 2 inclusions contain small black solid phases like type 1 inclusions. Two inclusions displayed only a liquid phase at room temperature, and formed no vapor phase upon cooling. These were grouped as type 2L in Appendix F.

Type 3 inclusions exhibit one phase at room temperature. A subdivision is made for single phase liquid (type 3a), and single phase vapor (type 3b). The division of type 3a and 3b inclusions is based on homogenization to a liquid phase (type 3a) or to a vapor phase (type 3b) below room temperature.

Type 4 inclusions are primary, two phase inclusions at room temperature. The phases are either a liquid or a gas with a solid phase. The solid phase is black opaque material constituting 30% to 60% of the inclusion volume.

Microthermometric Results

Phase behavior over a temperature range of -190° to 400° C was recorded for all inclusions. The resulting temperatures were compiled by inclusion type. Salinity and gas composition are estimated according to these measurements. The following section summarizes these findings according to fluid inclusion type. Melting temperatures are labeled as Tm(*n*), homogenization temperatures are labeled as Th(*n*), and decrepitation temperatures are labeled as Td. Phase changes are listed in order of occurrence from the

lowest temperature upwards. All recorded phase changes for each inclusion are listed in Appendix F and summarized in Table 4.

Type 1 Inclusions

1. Melting and homogenization measurements

In type 1 inclusions, the following phase changes are identified; $Tm(l_0)$, $Tm(l_1)$, $Tm(l_2)$, $Tm(l_3)$, $Tm(l_4)$, $Th(l_1)$, $Th(l_2)$, and Td. Events such as $Tm(l_0)$ and $Tm(l_4)$ are observed in very few inclusions, while $Tm(l_1)$ is observed in nearly all inclusions.

$Tm(l_0)$ occurs between -140° and -145° C for two inclusions in sample #25 and one inclusion in sample #18. It is the most difficult of all melting phenomena to observe. It probably indicates a N_2-rich gas phase, as $Th(l_0)$ temperatures are near the critical point of N_2 at -147° C (Touret, 1982).

$Tm(l_1)$ occurs from -57° to -68° C, with the mode occurring at -61° C (Fig. 20b). The triple point of CO_2 is -56.6° C, and increasing molar fractions of CH_4 lowers $Tm(l_1)$ to the critical point of CH_4 at -82.1° C (Shepherd et al., 1985). Inclusions from vertical veins (Fig. 21b) and horizontal veins (Fig. 21c) have different ranges of $Tm(l_1)$. Inclusions from vertical veins show a complete range of $Tm(l_1)$ temperatures whereas inclusions from horizontal veins exhibit melting temperatures ranging from -64° to -56.6° C.

$Tm(l_2)$ occurs from -5° to -2° C, and is observable in ten type 1 inclusions (Fig. 20c). $Tm(l_2)$ corresponds to the melting point of H_2O. This measurement is difficult to make for type 1 inclusions. The growth of clathrate partially or completely masks the melting of H_2O-NaCl at the low heating rate required for accurate measurements (0.2 to 0.5 degrees per minute).

$Tm(l_3)$ occurs from 7° to 16° C with a mode at 10° C (Fig. 20e). Carbon dioxide clathrate melts at 10° C in pure H_2O (Collins, 1979). Salinity depresses $Tm(l_3)$ below

10° (Shepherd et al., 1985). Melting temperatures above 10° C may result from other components causing metastability in the clathrate. The most likely component is CH_4, which forms a clathrate present above 10° C (Thomas and Spooner, 1988).

$Tm(l_4)$ was observed in two inclusions in sample #20 during $Tm(l_3)$ measurements. The procedure followed to measure $Tm(l_3)$ was to hold the sample at the temperature where clathrate melting was thought to occur, then cool it to less than 5° C to see if tiny, invisible clathrate crystals still existed in the liquid phase. On rapid cooling, these tiny crystals would nucleate and quickly fill the inclusion with clathrate ice if melting was incomplete. The two inclusions in sample #20 underwent rapid freezing between 0° and -10° C after the first clathrate was clearly absent. At about 14° C, subsequent cooling to -10° C resulted in no further sudden freezing events. This indicated that the second clathrate had fully melted.

Homogenization ($Th(l_1)$) occurs between the vapor and second liquid phase at temperatures ranging from -30° to $+12^{o}$ C. Twenty-three inclusions homogenized to a CO_2-rich liquid phase, and 14 homogenized to a CO_2-rich vapor phase. These temperatures indicate gas densities below 0.15 g/cm^3 and above 0.85 g/cm^3, respectively. (Valakovich and Altunin, 1968).

$Th(l_2)$ and Td were measured in type 1 inclusions between 100° and 350° C (Figs. 20f, 20g). The critical point of pure H_2O is 373° C, hence $Th(l_2)$ values are for mixtures of H_2O, additional gaseous species, and salts. $Th(l_2)$ ranges from 257° to 350° C. About equal numbers of inclusions homogenize to liquid and to gas; a smaller number homogenize at critical conditions (Fig. 20f). Most type 1 inclusions decrepitated when heated. Decrepitation temperatures (Td) range from 100° to 280° C, and average 100° C less than $Th(l_2)$ (Fig. 20g). Relatively few of these decrepitations were the result of a single inclusion breaking, rather fracturing occurred on planes of inclusions. Therefore, Td measurements generally represent fracturing along planes of weakness in the crystal. There is no significant difference in average $Th(l_2)$ or Td between quartz vein types (Figs.

22a-c, 23a-c). Inclusions in vertical veins exhibit the most $Th(l_2)$ events of the three types of quartz veins.

2. Estimation of salinity

Type 1 inclusions have salinities ranging from 0.7 to 5.4 eq wt % NaCl, averaging 2.8 eq wt % NaCl. Only inclusions exhibiting both $Tm(l_2)$ and $Tm(l_3)$ were used in calculations. Salinity was estimated from a graph by Collins (1979) using melting of CO_2-clathrate ($Tm(l_3)$) rather than $Tm(l_2)$. The procedure assumes that only CO_2, H_2O, and NaCl are present in the inclusion. It is impossible to calculate salinity from $Tm(l_2)$ because CO_2 is present. However, salinity calculations based on the melting of clathrate (Collins, 1979; Bozzo et al., 1973) are not accurate due to the presence of CH_4. Methane elevates CO_2-clathrate melting temperatures above 10° C, because CH_4 forms the same hydrates as CO_2 (Davidson, 1972). Therefore, CH_4-clathrate counters the effect of $T(l_2)$ depression caused by CO_2-clathrate (Shepherd et al., 1985). Both CH_4 and CO_2 exclude NaCl from the clathrate lattice, and the cumulative effect leaves the residual liquid with a higher salinity (Thomas and Spooner, 1988). However, the opposing effects of CO_2 and CH_4 on salinity estimations have not been quantified (Shepherd et al., 1985). Salinity measurements based only on $Tm(l_2)$ yield salinities ranging from 3.5 to 8.4 eq wt % NaCl. This is only an estimate of maximum salinity. No significant difference in salinity could be detected between types of quartz veining.

3. Estimation of gas composition and density

Evidence of other gas species besides CO_2 is shown by $Tm(l_0)$, $Tm(l_1)$, $Tm(l_3)$, $Tm(l_4)$, and $Th(l_1)$, all of which differ from that of pure CO_2. $Tm(l_1)$ and $Th(l_1)$ values were used to estimate mole percentage CH_4 in the vapor phase using procedures by Heyen

et al. (1982). The vapor phase averages 29 mole % CH_4 for all type 1 inclusions, with a range of 2 to 76 mole % CH_4. Sub-vertical veins show 44 mole % CH_4, ranging from 28 to 57 mole % CH_4. Vertical veins average 32 mole % CH_4, but over a higher range of 8 to 76 mole % CH_4. Horizontal veins average 19 mole % CH_4, with a range of 2 to 44 mole % CH_4. These values were not determined for all inclusions, as some $Tm(l_1)$ and $Th(l_1)$ values do not plot on the graph. This indicates the presence of a third gaseous specie, such as N_2 or H_2S (Shepherd et al., 1985). It is possible that many of the estimations made for the mole % CH_4 have been influenced by the presence of additional gaseous species. The levels of these species, however, are low enough that points can still be plotted. In these cases, the mole % CH_4 estimated must be considered a maximum value. $Tm(l_0)$ provides clear evidence of N_2 in some inclusions, making it a likely component in inclusions where direct evidence is lacking.

An extra set of measurements were taken on four inclusions to test the results of the procedure presented in Seitz et al. (1987). In this procedure, CH_4 content of the whole inclusion is calculated from measurements of $Th(l_1)$ without the presence of clathrate. The average value obtained is 22.5 mole % CH_4. This value is 10 mole % CH_4 less than what is shown by the same inclusions using the graph by Heyen et al. (1982). In some cases the values did not plot on the graph, indicating the presence of unknown gaseous species. The values that were plotted probably indicate maximum mole % CH_4.

Densities of type 1 inclusions average 0.92 g/cm^3, ranging from 0.79 to 0.98 g/cm^3. Density of the liquid phase was assumed to be equal to one because the estimated salinities are low. Density of the CO_2 in the vapor phase was estimated using $Th(l_1)$ and a graph of $Th(CO_2)$ versus density of CO_2 by Valakovich and Altunin (1968). The resulting density of the vapor phase was multiplied by the proportion of the vapor phase present. This was added to the density of the liquid multiplied by the proportion of the liquid phase.

Type 2 inclusions

1. Melting and homogenization measurements

$Tm(l_2)$, $Th(l_2)$, and Td were measured in type 2 inclusions, and three inclusions exhibit $Tm(l_3)$. $Tm(l_2)$ occurs in all type 2 inclusions over a temperature range of -8° to 0° C (Fig. 20c), and corresponds to the melting point of H_2O-ice. Two type 2 inclusions exhibit no vapor phase at any temperature, and yield an average $Tm(l_2)$ of -4.4° (Fig. 20c). $Tm(1_3)$ occurs from 10° to 12° C, and corresponds to melting of CO_2 clathrate (Fig. 20e). All examples of these inclusions occur in sub-vertical quartz veins. $Th(l_2)$ occurs to the liquid phase for most type 2 inclusions, and temperatures range from 130° to 326° C. One type 2 inclusion homogenizes to a vapor phase at 308° C, and this inclusion also exhibits $Tm(l_3)$. The highest $Th(l_2)$ of type 2 inclusions were measured in samples of horizontal quartz veins, ranging from 157° to 326° C (Fig. 22c). The lowest $Th(l_2)$ of type 2 inclusions were measured samples of sub-vertical quartz veins, ranging from 130° to 218° C (Fig 22a). Td occurs in some inclusions, but much less frequently than for type 1 inclusions. The range of decrepitation temperatures is similar to Td for type 1 inclusions in all three vein types (Figs. 23a-c).

2. Estimation of salinity

Salinities were estimated directly from the melting point of water (Fig 20c), using figures by Collins (1979). Salinities for inclusions displaying $Tm(l_3)$ were estimated using graphs by Heyen et al. (1982). The average salinity of 2 inclusions is 5 eq wt % NaCl, ranging from 0 to 12.1 eq wt % NaCl. Inclusions from the horizontal veins show the highest salinities, averaging 6.5 eq wt % NaCl. Inclusions from the sub-vertical veins

show the lowest salinities, averaging 3.3 eq wt % NaCl. Salinities for the two type 2 inclusions having no vapor phase (type 2L) average 7 eq wt % NaCl.

3. Estimations of gas composition and density

The vapor phases of type 2 inclusions are almost entirely H_2O vapor. The three type 2 inclusions displaying $Tm(l_3)$ contain additional gaseous species. Absence of $Tm(l_1)$ in these inclusions indicates <3 mole % CO_2 (Norman and Sawkins, 1987). It is assumed that CH_4 (or N_2) is present in addition to CO_2 because $Tm(l_3)$ occurs above 10° C (Fig. 20e). The remaining type 2 inclusions show no evidence of clathrate. According to Hedenquist and Henley (1985), absence of clathrate indicates less than 1 mole % CO_2.

The densities of type 2 inclusions average 0.97 g/cm^3, with a range of 0.88 to 1.02 g/cm^3. The salinity was taken into account for the liquid phase during density calculations. Type 2 inclusions exhibiting only $Tm(l_2)$ yield an average density of 1.07 g/cm^3.

Type 3 inclusions

1. Melting and homogenization measurements

Type 3 inclusions are subdivided by differences in the melting and homogenization temperatures and behavior. $Tm(l_1)$ ranges from -56° to -70° for both all type 3 inclusions, averaging -65° for each type (Fig. 20b). $Th(l_1)$ occurs to the liquid phase for type 3a inclusions, and to the vapor phase for type 3b inclusions. The range is -35° to 10° for type 3a inclusions, and -10° to 20° for type 3b inclusions (Fig. 20d). One type 3b inclusion is of an irregular geometry. It was possible to get an accurate estimation of

$Th(l_1)$ because small amounts of liquid could be seen disappearing in a corner of the inclusion. This avoided the occurrence of the apparent homogenization phenomenon as described by Sterner (1992). In inclusions of regular shape, small volumes of liquid can remain at the inclusion edges after an apparent $Th(l_1)$ has been estimated.

2. Estimation of gas composition and density

Liquid/gas ratios of type 3a and 3b inclusions were estimated from temperatures below $Th(l_1)$ where two phases are visible. The liquid phase appearing around the vapor bubble was assumed to be entirely H_2O. $Tm(l_1)$ of type 3a and 3b inclusions indicate highly variable mixtures of CO_2 with other gaseous species. $Tm(l_1)$ of type 3a inclusions yield an average of 43 mole % CH_4 in the vapor phase. $Tm(l_1)$ of type 3b inclusions yield an average of 70 mole % CH_4 in the vapor phase. The occurrence of type 3 inclusions is too sporadic to distinguish the vein types based on type 3 inclusion composition (Figs. 21a-c).

The gas-rich mixtures of type 3b inclusions yield densities averaging 0.68 g/cm^3, ranging from 0.61 to 0.75 g/cm^3. Type 3b inclusions are almost completely vapor and densities range from 0.5 to 0.55 g/cm^3.

Type 4 inclusions

Almost all type 4 inclusions were encountered in sample #29, located at Akwasiso Hill. Microthermometry was ineffective on most type 4 inclusions. The presence of opaque material believed to be carbon obscures melting phenomena. One inclusion of this type exhibits a $Tm(l_1)$ of -57° C, indicating the vapor phase is mostly CO_2. Over 50% of this inclusion is opaque solid.

Unclassified inclusions

Other inclusions yield microthermometric data that are impossible to interpret. Sample #39 contains two inclusions that display unusual freezing behavior. A globular solid forms at -46° C. This solid melts at the same temperature as H_2O-ice in nearby inclusions. Another inclusion displays formation of globular solid at -70°. This solid melts at -57.8^{o} C and total homogenization occurs at 35.8^{o} C. Sample #29 contains two inclusions that exhibit unusual behavior. On slow warming to about -26° C, a reddish liquid appeared and grew, apparently at the expense of the vapor phase. Eventually the reddish phase grew large and the vapor phase disappeared. Immediately after this point the vapor reappeared and grew rapidly in size in another part of the inclusion. The reddish phase shrank and disappeared at -3° C. Repeated cooling and warming produced the same phenomena, though the temperatures of the phenomenon varied over a few degrees.

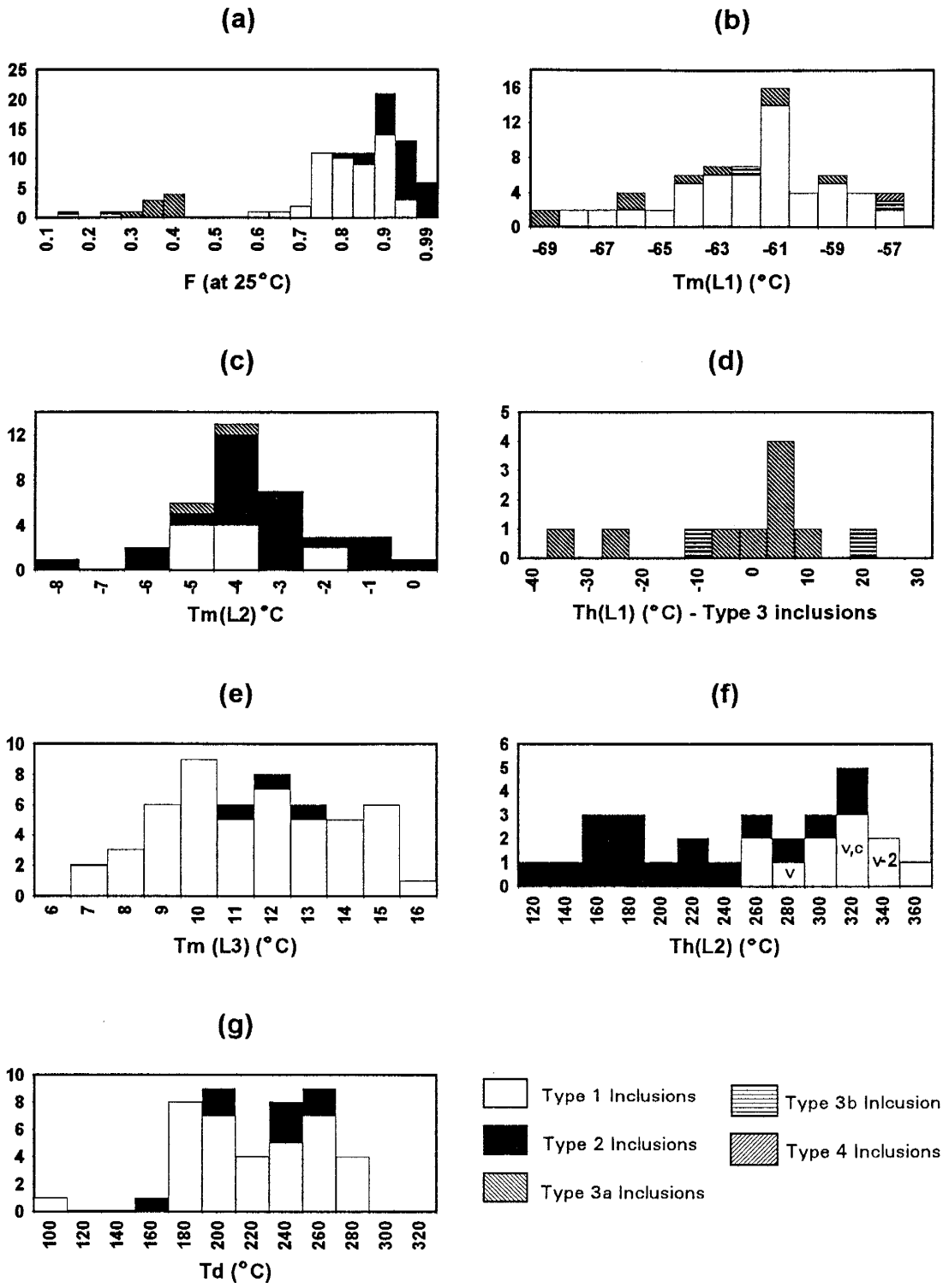

Figures 20a-g. Melting and homogenization temperatures for all inclusion types. The references L1, L2, L3 are equivalent to l_1, l_2, l_3 of text. In Fig. 20f, v = homogenization to the vapor phase, and c = homogenization at the critical point. Unlabeled phenomena in Fig. 20f are homogenization to the liquid phase.

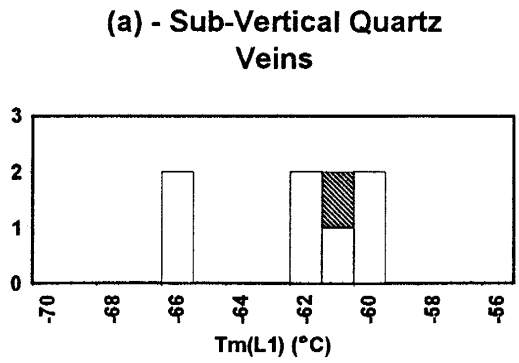

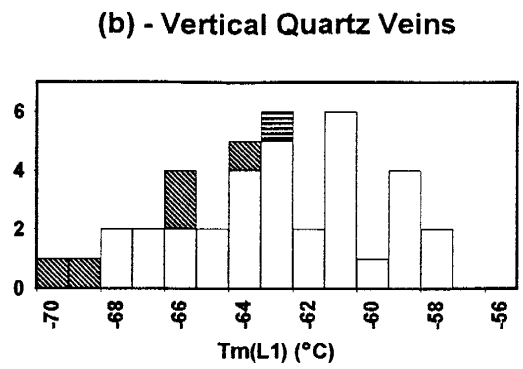

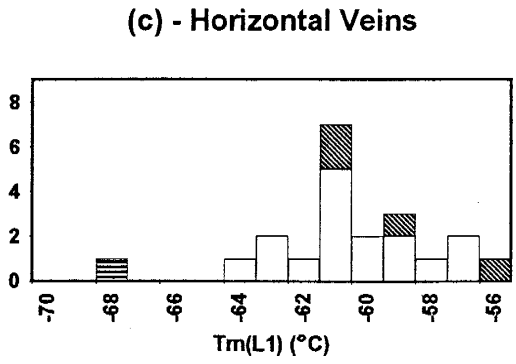

Figures 21a-c. Melting temperatures for the CO_2 gas mixture in inclusions from the three types of quartz veining at the Amansie mine. Tm(L1) is equivalent to $Tm(l_1)$ in text. Fill symbols same as Figures 20a-g.

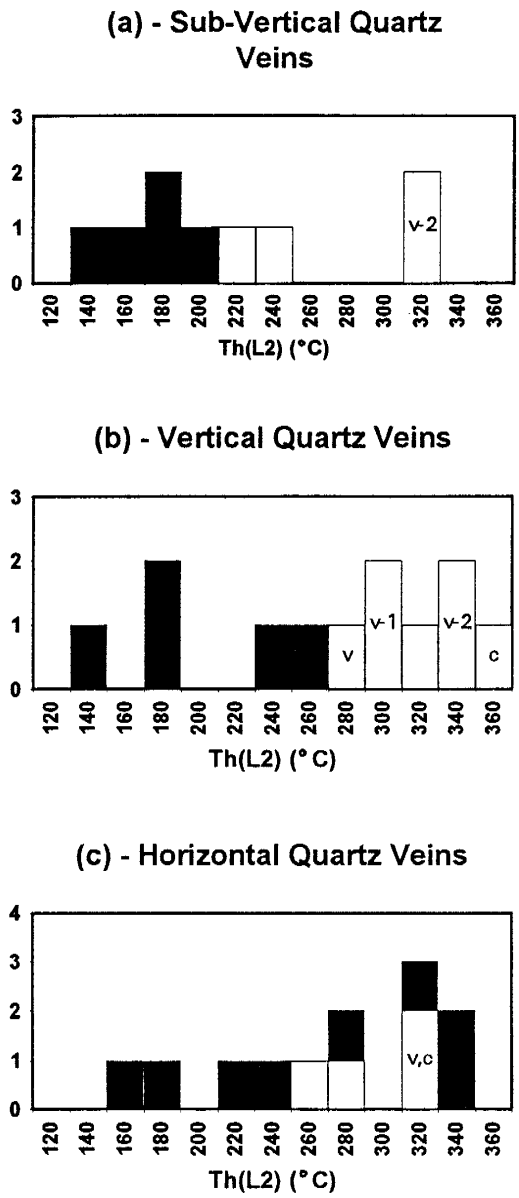

Figures 22a-c. Homogenization temperatures (Th(L2)) for the three types of quartz veins at Amansie mine. Th(L2) is equivalent to Th(l_2) from text. Fill symbols same as Figures 20a-g. The symbol v = homogenization to the vapor phase. In cases where more than one measurement is represented, the number of occurrences are indicated. The symbol c = homogenization at the critical point.

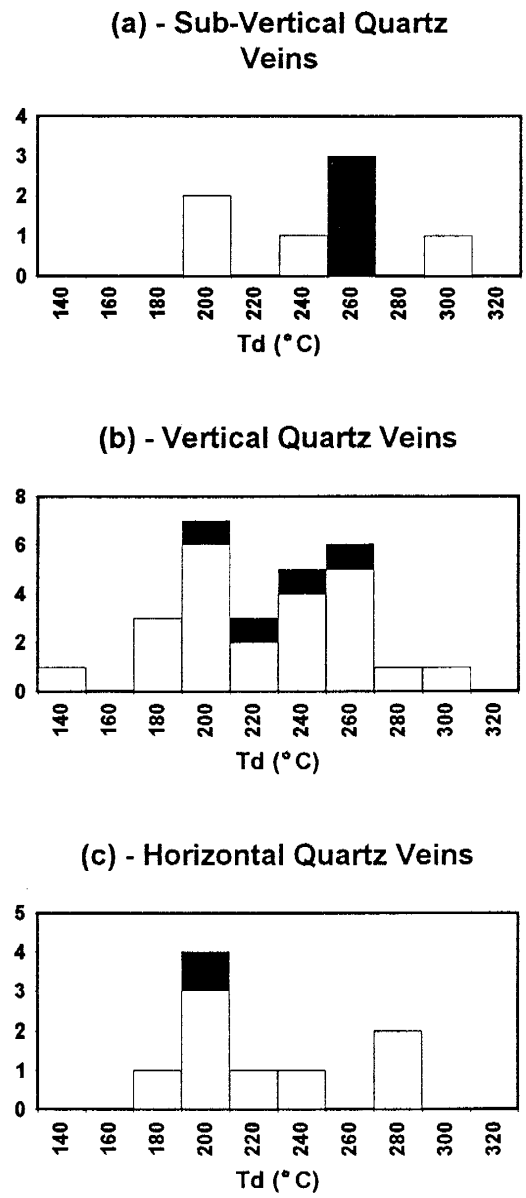

Figures 23a-c. Decrepitation temperatures (Td) for the three types of quartz veins at Amansie mine. Fill symbols same as Figures 20a-g.

Table 4 - Summary of microthermometric data by inclusion type

Type 1:	Two-phase, CH_4 ($+N_2$?) < CO_2, liquid-rich
Mole Fractions:	H_2O = 0.79, CH_4 ($+N_2$?) = 0.07, CO_2 = 0.13, NaCl = 0.01
Th(l_2) (to l):	Avg = 286°, range = 58°
Th(l_2) (to v):	Avg = 320°, range = 76°
Th(l_1) (to l):	Avg = 6°, range = 32°
Th(l_1) (to v):	Avg = -9°, range = 55°
Tm(l_2):	Avg = -4°, range = 4°
Tm(l_3):	Avg = 11°, range = 8°
Tm(l_1):	Avg = -62°, range = 11°
D bulk (g/cm^3):	0.92 (0.89 - 0.96)
Type 2:	Two phase, H_2O-NaCl liquid rich
Mole fractions:	H_2O = 0.96, CO_2 + CH_4 = 0.01, NaCl = 0.02
Th(l_2) (to l):	Avg = 215°, range = 197°
Tm(l_3):	Avg = 11.8°, range = 1.1° (observed in three inclusions)
Tm(l_2):	Avg = -3.6°, range = 8.4°
D bulk (g/cm^3):	0.97 (0.94 - 1.02)
Type 3a	One phase, CO_2 + CH_4 rich
Mole fractions:	H_2O = 0.40, CO_2 = 0.30, CH_4 ($+N_2$) = 0.30
Tm(l_1):	Avg = -64°, range = 10°
Th(l_2 to liquid):	Avg = -5°, range 44°
D bulk (g/cm^3):	0.68 (0.63 - 0.73)
Type 3b:	One phase, CO_2 + CH_4 rich
Mole fractions:	H_2O = 0.20, CO_2 = 0.30, CH_4 ($+N_2$) = 0.45
Tm(l_1):	Avg = -65°, range = 5°
Th(l_2 to vapor):	Avg = 7°, range = 30°
D bulk (g/cm^3):	0.55 (0.51 - 0.59)

Table 4. Summary of heating and freezing events for inclusion types 1 to 3 (as discussed in text). D bulk = bulk density, MV = molar volume, Tm(l_1) = $Tm_{(CO2)}$, Tm(l_2) = $Tm_{(H2O)}$, Tm(l_3) = $Tm_{(clathrate)}$, Th(l_1) = $Th_{(CO2)}$, Th(l_2) = Temperature of total inclusion homogenization.

Estimation of Pressure and Depth

Estimates of trapping pressure and trapping depth were calculated from microthermometric data for each type of inclusion (Table 5). Calculations are based on programs developed by Holloway (1981). Boiling conditions were assumed, which allows $Th(l_2)$ values to be equal to trapping temperatures. Criteria for immiscibility were taken from a summary by Ramboz et al. (1982). The primary evidence is occurrence of homogenization temperatures to gas, liquid, and critical conditions in the range 280° to 350° C. However, conclusive evidence is sparse as homogenization phenomena were rare, and in only one case were homogenization to liquid and to critical conditions observed in inclusions less than 30 μ apart.

Trapping pressures were determined using isochores for supercritical fluids. Vapor-filled type 3 inclusions (type 3b) were used for this determination. Molar volumes of the liquid were assumed to be 18, and molar volumes of gaseous species in the vapor phase were estimated using the graph by Heyen et al. (1982). This graph accounts for the percentage of CH_4 present in the vapor phase, assuming the remainder is CO_2. It was assumed that N_2 has similar behavior to CH_4. This assumption was tested by isochore calculations. Calculated isochores fluctuate only slightly when the proportions of N_2 and CH_4 are interchanged. Trapping temperatures were assumed to be 300° C. Over the density range specified in Table 4 for type 3b inclusions, pressures average 1200 bar, ranging from 1060 to 1450 bar. This corresponds to depth of 4.6 km, ranging from 4 to 5.4 km, assuming a lithostatic overburden.

Pressure estimations for aqueous inclusions (type 1 and type 2) were calculated using fugacity equations that included salinity. Mole fractions of CO_2, $CH_4 + N_2$, and salinities were taken from Table 4. Type 1 inclusions were assumed to have been trapped at 300° C under lithostatic pressure conditions. Trapping pressures average 1030 bar, ranging from 750 to 1300 bar. This corresponds to a depth of 4.2 km, ranging from 2.8 to 4.9

km. Type 2 inclusions are H_2O-NaCl liquid-rich, with levels of CO_2 and $CH_4 + N_2$ totaling less than 3 mole %. The Th(l_2) values are close to those of type 1 inclusions, which suggests they may have been trapped under similar conditions as type 1 inclusions. Trapping temperatures of type 2 inclusions exhibiting $CO_2 + CH_4 + N_2$ in the vapor phase are assumed to be 280° C, and 170° C for type 2 inclusions exhibiting only H_2O in the vapor phase. Ranges in pressures for type 2 inclusions are calculated from minimum and maximum salinities. The range shown in Table 5 is a composite range of both high temperature (280° C) and low temperature (170° C) type 2 inclusions. Trapping pressures average 370 bar, ranging from 300 to 490 bar. This corresponds to an average depth of 1.4 km, ranging from 1.1 to 1.8 km assuming a lithostatic overburden. Assuming a hydrostatic overburden, the trapping pressure corresponds to an average depth of 3.8 km, ranging from 3 to 5 km.

Table 5 - Pressure and depth calculations for fluid inclusion types

INCLUSION TYPE	3b	1	2
PRESSURE (bar)	1200 (1060 - 1450) [1]	1030 (600 - 1450) [2]	380 (300 - 490) [2]
DEPTH (km)	4.6 (4 - 5.4) (a)	3.8 (2.3 - 5.5) (a)	3.8 (3 - 5) (b) 1.4 (1.1 - 1.8) (a)

Table 5. Estimations of pressure and consequent depth relationships of fluid inclusion groupings from microthermometry. Pressures determined by isochore method [1], and by fugacity equations involving salinities [2]. Depth calculations assuming a lithostatic overburden (a), and assuming a hydrostatic overburden (b). All calculations use procedures by Holloway (1981).

BULK GAS ANALYSIS

Seventy-eight analyses were performed on 14 samples of quartz veins, two samples of rock-forming quartz, and three samples of sulfide minerals. Each sample was repeatedly crushed to yield several bulk gas analyses. Some crushes opened too many inclusions which overloaded the Quadrupole Mass Spectrometer (QMS). Others opened too few inclusions for precise measurement. The QMS system can measure only a limited number of peaks simultaneously. Hence, the QMS was set to measure trace organic species after measuring principal gaseous species. Sixty of the crushes measured m/e peaks 4, 15, 18, 26, 28, 34, 40, 44, and 48. These data were used to calculate the ratios of He, CH_4, H_2O, C*m*H*n*, N_2, H_2S, Ar, CO_2, and SO_2, respectively. Eighteen crushes measured the ratios of C_2H_4, C_2H_6, C_3H_6, C_3H_8, CO_2, C_4H_8, C_4H_{10}, and C_6H_6.

Abundance of Gases

Results indicate a wide range of fluid inclusion volatile compositions (see Appendix G). Principle gaseous species are H_2O, CO_2, N_2, and CH_4. The major component is H_2O that ranges from 40 to 90 mole %. Carbon dioxide ranges from <1 to 48 mole %; nitrogen ranges from 1 to 25 mole %; and methane ranges from 1 to 20 mole %. Nitrogen concentration is higher than CH_4 in all analyses except for those of rock-forming quartz and sulfide minerals. Argon, SO_2, H_2S, and C*m*H*n* together are less than 1 mole %. Helium was only detected in 14 analyses; they are from analyses of inclusions in two quartz vein samples, most analyses of rock-forming quartz, and analyses of sulfide minerals.

Organic species measurements indicate the presence of all organic compounds listed above. The m/e peak of 56 (butene), however, is below detection limits in five of the 14

analyses. The largest values occur at m/e peaks of 27, 29, and 39. These peaks indicate the abundance of ethane and propane.

Ternary Plots

Bulk gas analyses displayed on eight ternary plots illustrate differences among analyses (Figs. 24-31). Figure 25 does not show analyses of sulfide minerals because analysis of H_2S contained in sulfide minerals may not represent the H_2S content of the trapped fluid. There are three general patterns visible on the ternary plots:

1. An almost linear distribution of analyses is shown on the N_2-CO_2-Ar, N_2-CH_4-Ar, CO_2-N_2-CH_4, and N_2-He-Ar plots (Figs. 24, 28-30). The linear distribution indicates nearly identical ratios of N_2 to Ar in the case of Figures 28, 29, and 30.
2. A scatter of analyses is indicated by the CO_2-CH_4-H_2S, H_2O-CH_4-N_2, and CO_2-CH_4-H_2O plots (Figs. 25-27).
3. Analyses cluster in two groups on the organic m/e peak plot (Fig. 31).

The data for each sample, reduced to mole percent, appear in Appendix G.

The ternary plots show clusters of analyses that correlate with sample types. Analyses of sub-vertical veins and horizontal veins cluster in different areas of each plot. Some plots show a distinct cluster of analyses from vertical veins. Rock-forming quartz analyses group in different areas than quartz vein analyses in several ternary plots. Analyses of sulfide minerals typically fall near those of rock-forming quartz.

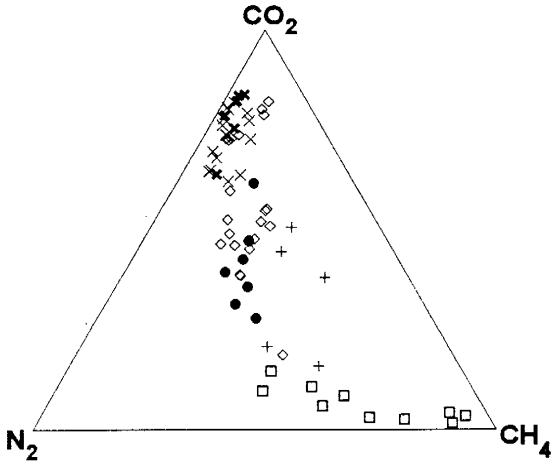

Figure 24. Ternary plot for the CO_2-N_2-CH_4 system. Sample types represented as follows: ◊= vertical veins, ●=sub-vertical veins, ×=horizontal veins, ✖=horizontal veins outside Amansie mine, +=rock-forming quartz, and □=sulfide minerals.

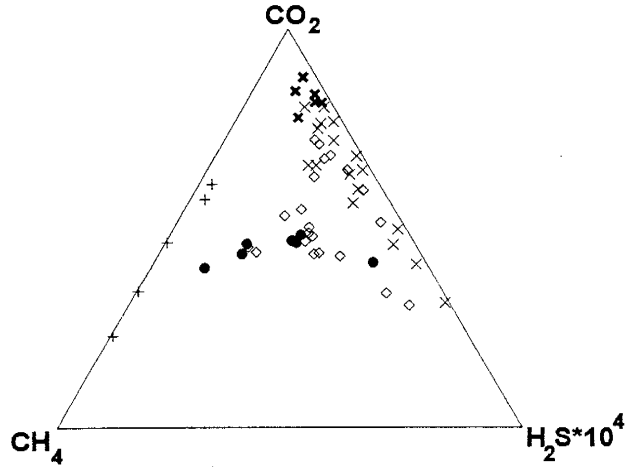

Figure 25. Ternary plot for the CO_2-CH_4-H_2S system. Symbols same as in Fig. 24.

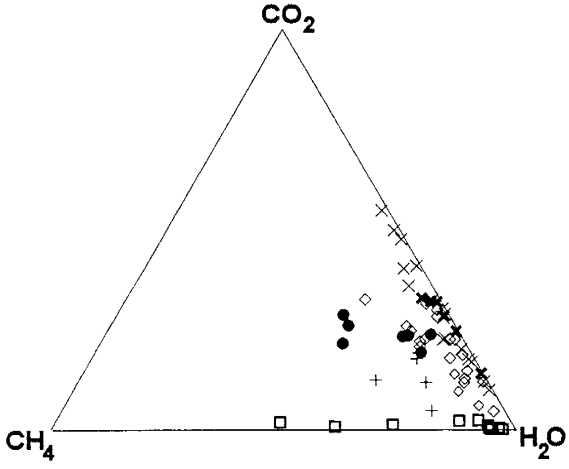

Figure 26. Ternary plot for the CO_2-CH_4-H_2O system. Symbols same as in Fig. 24.

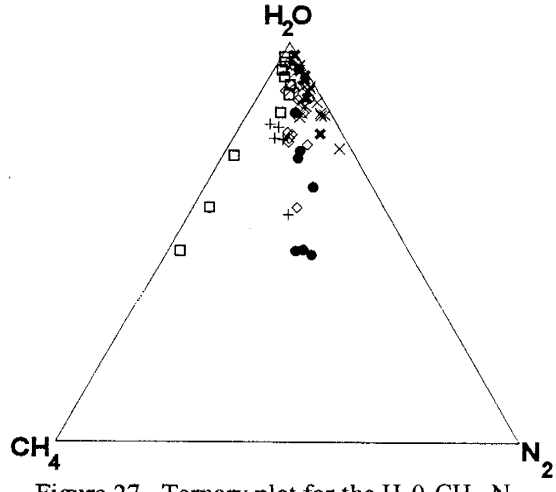

Figure 27. Ternary plot for the H_20-CH_4-N_2 system. Symbols same as in Fig. 24.

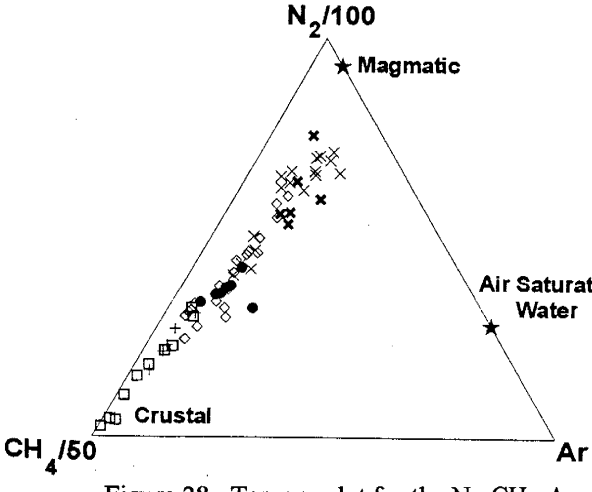

Figure 28. Ternary plot for the N_2-CH_4-Ar system. Symbols same as in Fig. 24.

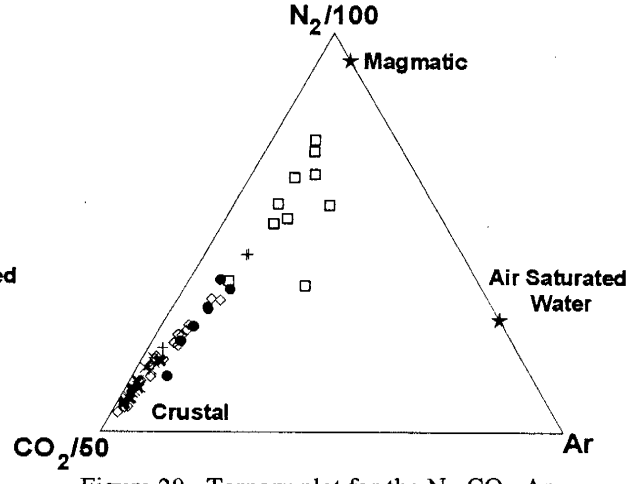

Figure 29. Ternary plot for the N_2-CO_2-Ar system. Symbols same as in Fig. 24.

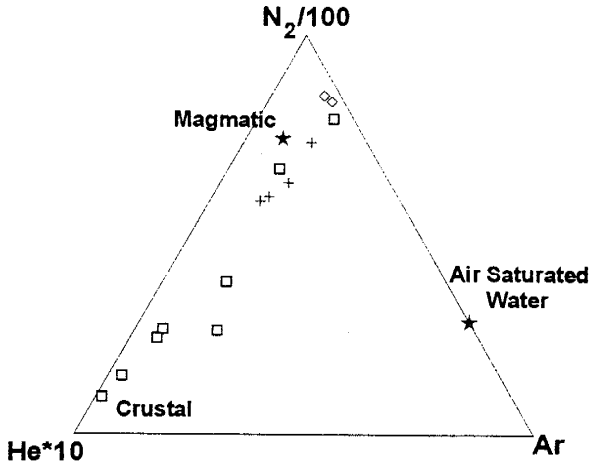

Figure 30. Ternary plot for the N_2-He-Ar system. Symbols same as in Fig. 24.

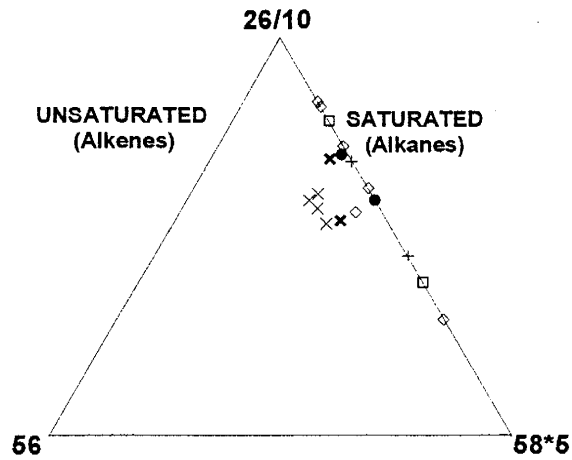

Figure 31. A ternary m/e peak plot of 26, 56, and 58 showing relative proportions of saturated versus unsaturated hydrocarbon species. Symbols same as in Fig. 24.

Modeling

The distributions of analyses on Figures 24-27 pose an important question about the fluids. Ideally, analyses of fluid inclusions in a sample will yield identical fluid compositions. Microthermometry, however, shows vapor and liquid-rich inclusions in the same sample. Measurement of a limited number of fluid inclusions during each bulk gas analysis reflect this heterogeneity. The microthermometric data exhibit a large range in gas/water ratios (Fig. 12a), indicating variable mixtures of type 1 (liquid-rich) and type 3 (vapor-rich) inclusions. The ratios of the gaseous species in type 1 and type 3 inclusions will differ if type 3 inclusions are derived by boiling a fluid trapped in type 1 inclusions, because the gas partitioning coefficient (B) is different for each gaseous species. Possible compositions of liquid and vapor phases were calculated by modeling the boiling process to determine if the bulk gas analyses are consistent with the heterogeneous trapping of liquid and vapor for a boiling fluid. Assumptions of the boiling model are:

1) Inclusions are either vapor or liquid from which the vapor was derived. The vapor phase was in equilibrium with the liquid phase.

2) Fluid boiling occurred in a closed system.

3) Fluid composition remained constant with time.

4) Only a few inclusions are broken during each bulk gas analysis, thus it is highly probable that the analysis will not measure an equal number of vapor and liquid-rich inclusions.

5) Boiling occurred at about 300° C.

The composition of a fluid containing dissolved gaseous species changes consistently as a result of boiling, and a boiling model quantifies these changes. The partitioning coefficient (B) is temperature dependent and equals the concentration of a gaseous species in vapor (C_V) divided by the concentration of that gaseous species in the liquid (C_l). Equations for B values of different gaseous species were taken from Henley et al. (1984) and Prini and Crovetto (1989). The model follows a format presented by Henley et al. (1984) (Appendix H). Each boiling step produces a unique C_V and C_l value for each component. There are limits on the extent of the boiling process; the value of the fraction of the original fluid converted to vapor (y) defines these limits. The results of the calculations are plotted on ternary plots in the same manner as the analyses. Figure 32 illustrates the modeling of two analyses. The starting compositions are from an analysis of a sub-vertical quartz vein (#20) and a horizontal quartz vein (#27). Each point represents the progressive change in vapor compositions (open circles) and liquid compositions (closed circles) resulting from $\Delta y=0.01$. The liquid composition moves away from the starting fluid composition toward the H_2S apex. Hence, a gaseous species such as CH_4 moves rapidly to the vapor phase, while CO_2/CH_4 and H_2S/CH_4 increase in the residual liquid, as shown by Giggenbach (1980) and Drummond and Ohmoto (1985). The vapor composition plots farthest from the starting fluid composition in the first step, and moves closer during each boiling step. The composition of the vapor will approximate the starting fluid composition if boiling continues indefinitely. For any value of y, a tie line connecting the vapor and liquid composition will pass through the starting fluid composition (Fig. 32).

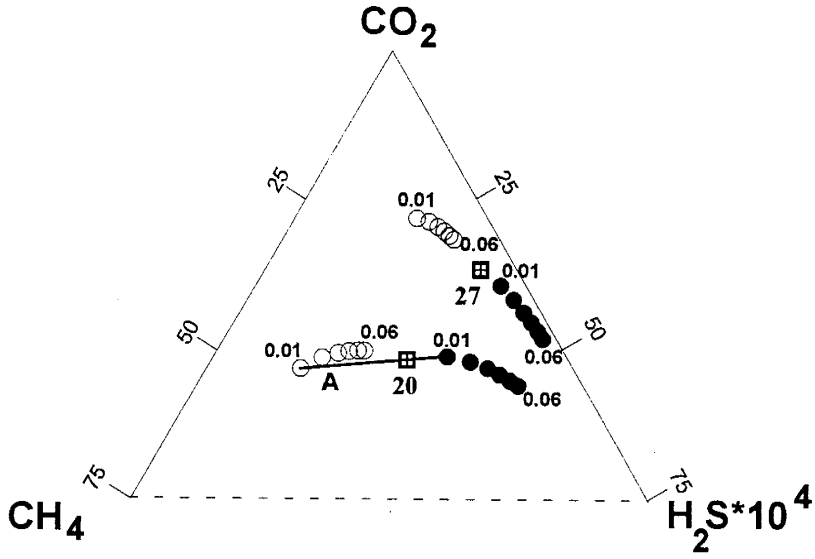

Figure 32. A CO_2-CH_4-H_2S ternary plot, showing determinations of liquid and vapor fraction compositions using the boiling model. The (⊠) symbols represent bulk gas analyses, chosen as compositions prior to boiling. Open circles denote vapor fraction compositions, and closed circles denote liquid fraction compositions, for a step of y=0.01. The value of y ranges from 0.01 to 0.06. Tie line A illustrates that the composition of the vapor and liquid fraction average the starting composition of the fluid for y=0.01 in sample #20.

Variations in bulk gas analyses for specific types of samples (Figs. 24-31) are similar to those calculated. Figures 33a-b show calculated distributions of bulk gas analyses using the above boiling model. Starting compositions for modeling were chosen from among the analyses. These analyses plot centrally in a cluster of analyses for particular sample types. For example, one analysis of sample #20 (Fig. 32) sits approximately at the center of the analyses of sub-vertical veins (Fig. 24). Vapor and liquid compositions are shown for y=0.01 to 0.06 at a step of y=0.01, with arrows indicating the direction of change. A final value of y=0.06 corresponds to a total temperature drop of 18° C, and a loss of about 80% of the total dissolved gaseous species. The resulting distribution, indicated by solid lines, agrees reasonably well with distribution exhibited by analyses (Figs. 24 and 25). There are several reasons for slight disagreement between calculated and the actual range of analyses: (1) the bulk gas analysis technique has a 20% analytical precision, (2) the source for fluid volatiles may not have been uniform over time, and (3) there may have been minor losses of volatile gases because the system was not entirely closed. The

modeling shows that boiling of initial fluid compositions in sub-vertical veins will not yield bulk inclusion compositions measured in horizontal veins. Hence, analyses of the vein types indicate the presence of two distinct fluids unrelated by boiling. On Figure 25, the rock-forming quartz analyses indicate a fluid unrelated to any other fluid by boiling, but can be related by boiling to analyses of sub-vertical quartz veins on Figure 24. Analyses of sulfide mineral inclusions do not lie along a boiling curve on Figure 24.

Closed system boiling to a value of y=0.06 (Fig. 33a) does not account for the total variation in analyses of horizontal vein inclusions (Fig. 25). However, the general distribution of the analyses is linear. Calculations indicate that the distribution can be modeled using open system boiling, or by using a lower starting temperature. This does not necessarily mean the system was completely open, but does indicate some degree of open system behavior. Starting fluid composition changes during open system boiling because gaseous species are lost from the system. The result is a greater change of liquid compositions over the same y interval. It is unlikely that the distribution can be explained by boiling to a higher value of y. Figures 33a-b show that at higher values of y, the stepwise change in liquid and vapor compositions diminishes rapidly.

There are some analyses plotting between boiling curves for horizontal veins and vertical veins (Fig. 25). These analyses are from two quartz vein samples, #39 and #31. They may represent an admixture of primary inclusions in vertical quartz veins and secondary inclusions trapped during mineralization of horizontal quartz veins. The analyses could also document that geothermal fluid gas chemistry varied with time.

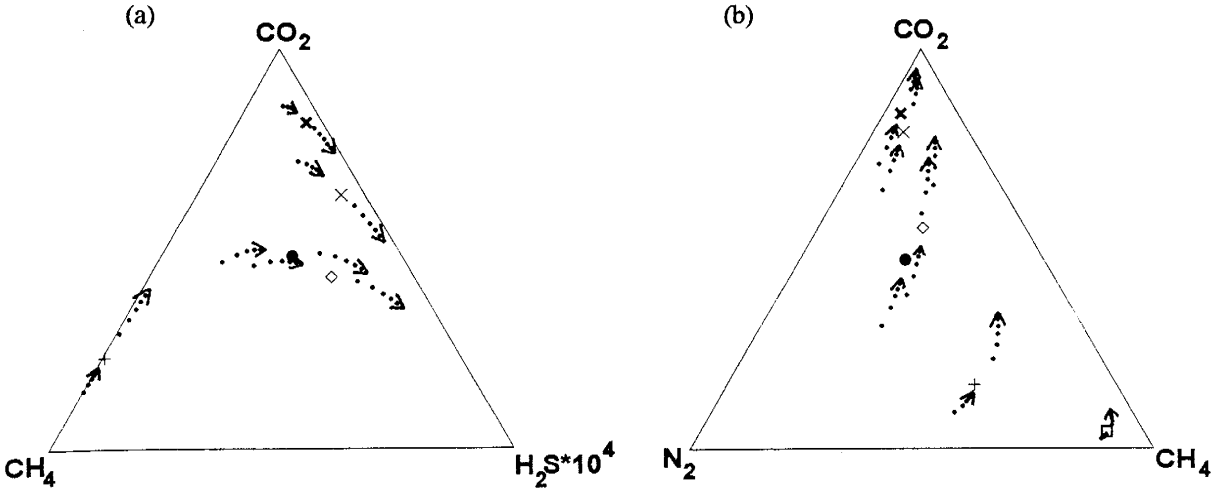

Figures 33a-b. Boiling curves on the CO_2-CH_4-H_2S and CO_2-N_2-CH_4 ternary plots. Boiling temperature starts at 300^0, and y steps from 0.01 to 0.06, at a Δy=0.01. Initial compositions from bulk gas analyses are indicated by symbols defining sample types as in Figure 24.

Classification of Fluid Types

Distributions of analyses and modeling of variations in C_V and C_l during boiling indicate three distinct fluid compositions (Table 6). The first two compositions correlate with analyses of quartz veins. The third corresponds to analyses of rock-forming quartz and most analyses of sulfide minerals.

Fluid A is rich in CH_4, N_2, and relatively poor in CO_2. Analyses of all sub-vertical and most vertical veins (samples #20 #29, #19, #18, #39, and #40) represent the range in fluid A composition. Analyses of vertical and sub-vertical veins indicate a dominance of saturated hydrocarbons on Figure 31.

Fluid B is rich in CO_2 and relatively poor in CH_4. Analyses of horizontal veins and some vertical veins (samples #22, #23, #26, #38, #31, #25, and #27) represent the range in fluid B compositions. The range of analyses exceeds the range indicated by closed system boiling on Figure 25, indicating that the hydrothermal system was subject to open system conditions. On the CO_2-N_2-CH_4 and N_2-CO_2-Ar plots, fluid A and B are in roughly linear trends. Horizontal veins from the Anyankyerim intrusive (#34) and the Ayanfuri

intrusives (#16) plot as CO_2-rich, H_2S-poor members of fluid B. Analyses representative of fluid B cluster together on Figure 31. The cluster shows a higher proportion of unsaturated hydrocarbons than that shown by fluid A.

Fluid C is rich in CH_4, poor in CO_2, and poor in H_2S. It shows slightly lower N_2 values than fluid A. Analyses of rock-forming quartz (samples #4 and #9A) and analyses of sulfide minerals (samples #20S and #6S) represent the range in fluid C compositions. On Figures 26-28 and 31 it is indistinguishable from fluid A. In Figures 24 and 25, it shifts from the range for fluid A due to high values of CH_4 and low values of H_2S, respectively. On Figure 25, analyses from rock-forming quartz and sulfide mineral inclusions cover a wide range of compositions that is impossible to model.

Table 6 - Starting compositions for each fluid type as indicated by the boiling model

FLUID	CH_4	H_2O	N_2	H_2S	Ar	CO_2	C_mH_n	SO_2
A	6	64	9	0.0013	0.021	20	0.16	0.0014
B	3	60	10	0.0022	0.025	26	0.07	0.008
C	10	78	5	0.00001	0.013	6	0.6	0.0003

Table 6. Starting fluid compositions as indicated by the boiling model (in mole %) for analyses from the Amansie mine, the Ayanfuri project, and the Anyankyerim intrusive, as determined by bulk gas analysis. Fluid A and B correlate with analyses of quartz veins, and fluid C correlates with analyses of rock-forming quartz and some analyses of sulfide minerals. Fluid B is only approximate, since boiling relationships indicate that the system was open and the starting composition of fluid B was changing over time.

RAMAN MICROPROBE ANALYSIS

Four polished sections of quartz veining at the Amansie mine were selected for Raman microprobe analysis. The objective was to compare the results with microthermometric data and bulk gas analyses. Curt Broman at the Department of Geology and Geochemistry at the Stockholm University in Stockholm, Sweden, conducted the study. The polished sections selected represent the three types of quartz veining. Sample #18 represents vertical veining, samples #20 and #29 are from sub-vertical veining, and sample #27 is from horizontal veining.

Analysis of nine inclusions shows CO_2, CH_4, some hydrocarbons (n-Alkenes), solid carbon, and an absence of N_2. The CO_2/CH_4 is greater than one in all analyses (Table 7, Figure 34). Inclusions from sub-vertical quartz veins show the greatest proportion of CH_4 in the vapor phase. Inclusions from horizontal quartz veins show the highest proportion of CO_2 in the vapor phase. The inclusion in sample #29 contains organic hydrocarbons (n-alkenes); no hydrocarbons were found in the other inclusions. An inclusion from sample #20 contains a small amount of solid carbon. Carbon is suspected in several other inclusions because of the high CO_2 background spectra (C. Broman, written commun., 1995). Nitrogen was not detected in any inclusion. However, limited microthermometric analyses conducted by C. Broman reports the presence of an inclusion displaying two phases at -150° C and homogenizing at -139° C. This phase behavior is consistent with an N_2-rich inclusion (Touret, 1982).

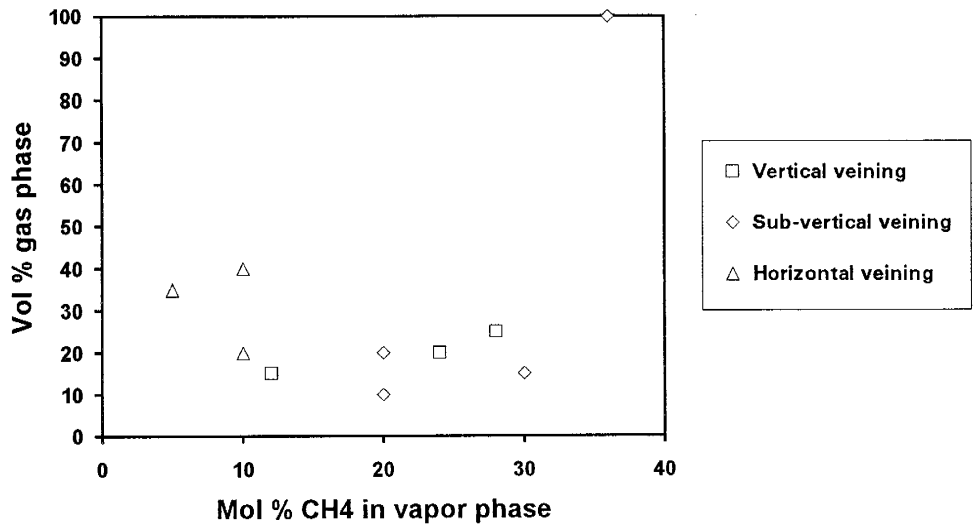

Figure 34. Raman microprobe analysis results for ten aqueous inclusions located in the three types of quartz veins at the Amansie mine.

Raman analysis may overestimate the amount of insoluble gases in an inclusion. The method measures only the species within the vapor phase of the inclusion. Carbon dioxide is more soluble than CH_4 in aqueous solutions. For example, at room temperature and 85 bars pressure, the solubility of CO_2 in pure water is 2 mole %, while the solubility of CH_4 is 0.2 mole % (Seitz et al., 1987). Thus, the CH_4/CO_2 in the vapor bubble is always higher than in the inclusion as a whole.

The microprobe analyses are similar to calculated inclusion compositions based on microthermometric data and bulk gas analyses. Inclusions from samples #20, #29, and #18 have $CO_2/CH_4 > 1$ in all three methods of analysis, and inclusions in sample #27 show higher CO_2/CH_4 values in all three methods of analysis. Overall, Raman analysis indicates lower CO_2/CH_4 than those obtained by calculations and bulk gas analyses. An explanation for lower CO_2/CH_4 determined by Raman microprobe is the inability of the microprobe to analyze dissolved CO_2 in the aqueous phase. However, in some cases the Raman microprobe gives higher CO_2/CH_4 values than analyses from microthermometry or

bulk gas analysis. Comparisons among results from the three analytical methods are only generally applicable (Table 7). The only direct comparisons are the two cases where specific inclusions measured during microthermometry were also analyzed by the Raman microprobe. In both cases the Raman microprobe has given a lower CO_2/CH_4 than the ratio calculated from microthermometric data. Bulk gas analysis detects organic hydrocarbon species, though it indicates the presence of both alkene and alkane species.

Raman microprobe analysis shows an absence of N_2; this conflicts with findings from the other two analytical methods. Calculations of microthermometric data suggest concentrations of N_2 similar to CH_4. Bulk gas analysis shows N_2, typically in excess of CH_4. This discrepancy of Raman microprobe findings with other analytical methods may be due to the inclusions selected for Raman microprobe work. High N_2 may occur in only certain types of inclusions, none of which were chosen for Raman microprobe analysis. Inclusions found during microthermometry conducted both by C. Broman and by this researcher exhibited N_2-rich behavior, confirming that such inclusions do exist. Still unexplained is the behavior of an inclusion in sample #20 (Table 7), which exhibited Tm(CO_2) and Tm(clathrate) that would not plot on the diagram for determining mole % CH_4. The presence of N_2 indicates this behavior, but N_2 cannot be quantified by calculations of microthermometric data. However, Raman microprobe analysis revealed no such N_2 component. It is possible that nitrogen in many inclusions occurs as NH_3, dissolved in the liquid fraction where the Raman microprobe fails to detect it. This means that a high fraction of NH_3 would have to convert to N_2 upon crushing for bulk gas analysis, and in the process release H_2 at slightly greater levels. However, this possibility cannot be assessed, as H_2 was not analyzed during bulk gas analysis.

Table 7 - Comparison of CO_2/CH_4 values from Raman microprobe results, bulk gas analysis, and microthermometric data

SAMPLE	CO_2/CH_4 (r. m.)	CO_2/CH_4 (g. a.)	CO_2/CH_4 (f. i.)
18a	3.17	2.5	1.4
18b	7.33	"	1.4
18c	2.57	"	1.4
20a	2.33	2.2	2 [<2.5]
20b	4	"	2
20c	4	"	2
29	1.8	1.1	3.8
27a	9	8.8	[14.2]
27b	9	"	
27c	19	"	

Table 7. CO_2/CH_4 values from Raman microprobe (r.m.), bulk gas analysis (g.a.), and microthermometric data (f.i.). Both Raman microprobe and microthermometric data are restricted to type 1 inclusions, while bulk gas analyses account for all fluid inclusion types. Ratio determinations from microthermometric measurements taken on two of the four inclusions sent for Raman microprobe work are shown in brackets [ ]. The microthermometric results of sample 20a did not define an exact value for CH_4 content, as the intersection of Tm(CO_2) and Tm(clathrate) could not be plotted on the applicable graph.

INTERPRETATION OF FLUID TYPES

Comparison of Results from the Three Methods of Analyzing Fluid Inclusions

Many relationships exist between the bulk gas analyses, microthermometric data, and Raman microprobe analyses. These correlations exist even though the methods measure fluid inclusion compositions at entirely different scales. Bulk gas analyses and microthermometric data confirm the presence of the gaseous species CO_2, CH_4, and N_2 in many inclusions. Microthermometric data also indicate these gaseous species, and the Raman microprobe confirms the presence of CH_4. All three methods also confirm that fluid compositions of sub-vertical and vertical veins are richer in CH_4 than compositions determined for horizontal veins. The fluid compositions of horizontal veins show the highest proportions of CO_2. Figures 35a and 35b compare the bulk gas analyses and microthermometric data for the CO_2-CH_4-H_2O system. The distribution of analyses of sub-vertical and horizontal veins is similar in both plots, with the microthermometric data yielding liquid or gas-rich end members. Microthermometric data indicate fluid boiling, and boiling models explain the distribution of analyses from bulk gas analysis.

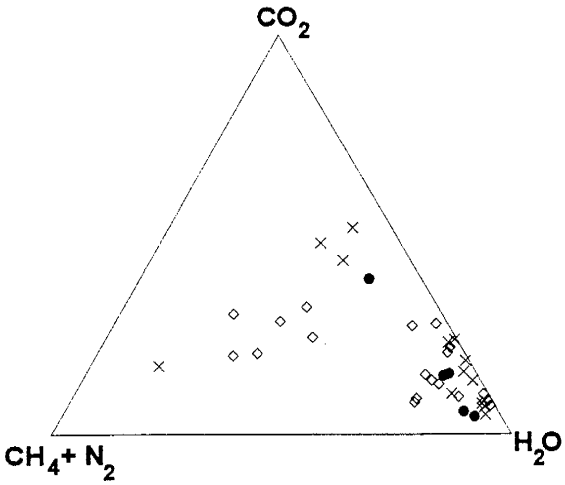

Figure 35a. Ternary plot of the CO_2-CH_4-H_2O system, using data from applicable microthermometric calculations. Symbols same as in Fig. 24.

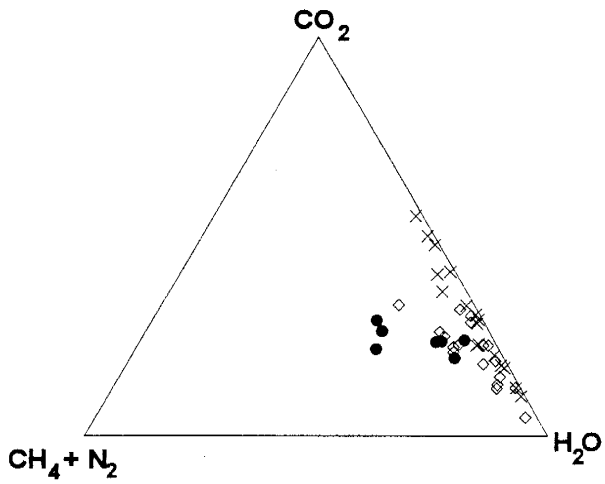

Figure 35b. Ternary plot of the CO_2-CH_4-H_2O system, using bulk gas analyses from the same samples as Fig. 34. Symbols same as in Fig. 24.

Some differences exist between microthermometric data and bulk gas analyses. The average percentage of water is lower in gas analyses (Table 6) than an average of all inclusion types (Table 4). This discrepancy shows a bias toward measurement of liquid-rich inclusions during microthermometric study. Bulk gas analysis measured N_2 at levels consistently higher than CH_4. Microthermometric data confirm the presence of N_2 in few inclusions, but it is suspected in many others. Nitrogen may exist in inclusions yielding microthermometric data for which the CH_4/CO_2 cannot be determined on the applicable graphs. The Raman microprobe found no evidence of N_2.

Classification of Fluid Types

Combination of bulk gas analyses and microthermometric data indicate two distinct fluid compositions. These fluid compositions roughly correspond to quartz vein types present at the Amansie mine. Limited data from the Raman microprobe analysis confirm these findings (Fig. 34). Though bulk gas analyses define clear differences in fluids from different types of quartz veins (Figs. 24-31), microthermometric data only suggest a

dominance of particular fluid inclusion compositions in different types of quartz veins (Figs 21a-c).

Fluid A, determined from bulk gas analysis, and CH_4-rich type 1 and type 3 inclusions measured during microthermometry represent fluid A. It is a gas-rich, low-salinity fluid, and fluid inclusions exhibit homogenization temperatures of 280° to 350° C. Microthermometric data indicate that fluid A was subject to boiling. Bulk gas analyses of samples #29, #20, #19, #18, #40, and to some degree #39 represent fluid A, and the distribution of these analyses on ternary plots indicates closed system boiling conditions. These samples are from sub-vertical and vertical veining outside the intrusive or in the case of #19, within the main shear zone. Analyses of sub-vertical veins show the highest CH_4 levels within the range of fluid A compositions. Dominance of alkanes such as propane and butane indicate highly reducing fluid conditions (Norman et al., 1996). Fluid C from bulk gas analysis is similar to fluid A in most respects, and may represent a vapor-rich component of that fluid.

Fluid B, determined from bulk gas analysis, and CH_4-poor type 1 inclusions and higher temperature type 2 inclusions measured during microthermometry represent fluid B. The average estimated salinity is greater than the average salinity determined for fluid A. Bulk gas analyses of horizontal quartz veins within the Ayanfuri intrusives and the Anyankyerim intrusive fall within the range of fluid B compositions. Analyses of samples #22 and #23 from vertical veins at the Amansie mine also fall within this range of compositions. These samples are petrographically different from other vertical quartz vein samples and similar to horizontal quartz vein samples. They may constitute zones within vertical veins that were re-fractured and contaminated by later fluids. Fluid temperatures based on microthermometric data from horizontal veins indicate a broad range from 220° to 340° C. Fluid B shows a higher proportion of alkene to alkane organic species than fluid A. This indicates a higher oxidation state for fluid B than that indicated by fluid A (Norman et al., 1996).

Data Sets Not Used In Classification

There are some analyses that do not fit with the fluid classification. Bulk gas analyses of sulfide minerals (i. e., samples #10S and #6S) do not fit a boiling curve on some plots (Figs. 24, 33b). It is possible that the distributions of these analyses show the effects of fluid-rock interactions. Trapping of this fluid occurred before equilibrium was achieved. Enrichment of CH_4 resulting from such reactions can oppose or obscure the effects of phase separation (Channer and Spooner, 1994). Fluid mixing also confuses boiling trends, and explains the distribution of analyses from samples #39 and #31. Some type 2 inclusions (gas-poor, low salinity H_2O) exhibit homogenization temperatures from 120° to 240° C, and do not fit into the classification of fluid A or B. They may represent the liquid fraction from extensive boiling of the above fluids, or the occurrence of a minor post-mineralization fluid at lower temperatures.

DISCUSSION

Classification of the Ore Bodies

Several points of evidence indicate that the Amansie mine is a mesothermal gold deposit, and some of these points can be applied to the remaining gold deposits of this study. The supporting evidence includes: (1) the gold deposits have a spatial association to major faulting, (2) mineralizing fluids are of low salinity and CO_2 contents range from 5-30 mole %, (3) the mineral paragenesis includes quartz, mica, pyrite, and carbonate, and (4) there is a high Au, As, W, Mo and low Cu, Pb, and Zn element budget (Kerrich and Wyman, 1990). Mineralizing depths of 4-6 km place the deposit below levels commonly cited for epithermal gold occurrences. The vertical extents of the gold deposits in this study are unknown. If they are vertically extensive (up to 2 km), then this point would support the mesothermal classification.

Timing of Ore-Bearing Fluids at the Amansie Mine

Cross-cutting relationships and fluid characteristics indicate that the first stage of mineralization at the Amansie mine occurred during and shortly after the emplacement of the intrusives. Fluid inclusions with fluid A compositions occur in sub-vertical and vertical quartz veins, and some fluid inclusions showing fluid A compositions occur in horizontal quartz veins. It is similar in most respects to the fluid associated with formation of arsenopyrite and pyrite throughout the ore body. Development of euhedral arsenopyrite crystals both within the porphyritic dike and in the surrounding wall-rock indicates that sulfide mineralization follows emplacement of the intrusive and metamorphism of the wall rocks. Presence of 'pressure shadows' around sulfide minerals in rocks adjacent to the main shear zone, however, suggest that some mechanical stresses still existed in this zone

during and after mineralization. Temperatures of greenschist metamorphism indicate a depth of 12 to 20 km, using an average geothermal gradient of 25°/km. The depth of mineralization is estimated at 4 to 6 km. This would require a sufficient time interval to remove at least 7 km of overburden. These points of evidence indicate that ore-bearing fluids occurred after regional metamorphism. Cross-cutting relationships indicate that the hypidiomorphic-granular intrusive body post-dates vertical quartz veins. Pressures higher than lithostatic pressures were necessary for formation of horizontal quartz veins within this second intrusive body.

Cross-cutting relationships of quartz veins suggest that the second pulse of mineralizing fluids proceeds the above events. It has a composition that cannot be related to fluid A by the boiling model, thus fluid composition must have changed since the occurrence of fluid A. This indicates that some period of time must have passed, during which inflow of fluids through the shear zone was minor. Fluid B is the dominant component in horizontal veins that crosscut all other features of the deposit. Pressure estimations from microthermometric data indicate depths of about 1.2 km (lithostatic pressures) or 4 km (hydrostatic pressures). It is thought that the latter depth is more likely. However, this means hydrostatic pressures were necessary for fluid B to exist at the same depth as fluid A. It is possible that initially this fluid entered the system under lithostatic pressures, but fracturing opened the system to hydrostatic pressures. During this sudden decompression, fluid B boiled and Au precipitated in the horizontal quartz veins and along microfractures within the intrusive body. Samples of vertical quartz veins yielding fluid compositions typical of fluid B may have been fractured and contaminated with this later fluid. Assuming lithostatic pressures throughout the time of fluid B, over 60% of the overburden must have been removed between the first and second mineralization event. However, bulk gas analysis data do not indicate the contribution of air saturated ground waters to fluid B (Figs. 28, 29) as observed in geothermal systems at depths <2 km (Norman et al., 1996).

Enrichment of Fluids with Organic Compounds

Fluid A is the primary source of gold mineralization at the Amansie mine, and the composition of this fluid was altered by organic material. The fluid is organic-rich, of low salinity, and ubiquitous in auriferous quartz veins. Many type 1 fluid inclusions exhibit specks of graphite. It is hypothesized that the carbonaceous metasediments surrounding the intrusives at the Amansie mine are also present at depth. These points suggest an association between this organic-rich material and the occurrence of gold. This association is shown by comparing CH_4/CO_2 to the gold grade of quartz veins (Fig. 36). Organic material is also rich in N_2. A comparison of N_2 to m/e peak 26 values (C*m*H*n*, a general indicator of organic species), also results in a positive correlation (Fig. 37).

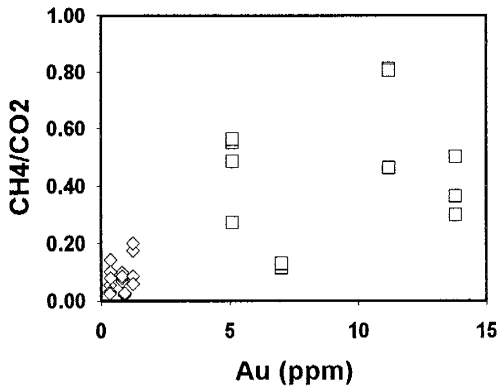

Figure 36. Relationship between CH_4/CO_2 and gold grade in quartz vein samples. □ = analyses of sub-vertical and vertical quarz veins; ◊ = analyses of horizontal quartz veins.

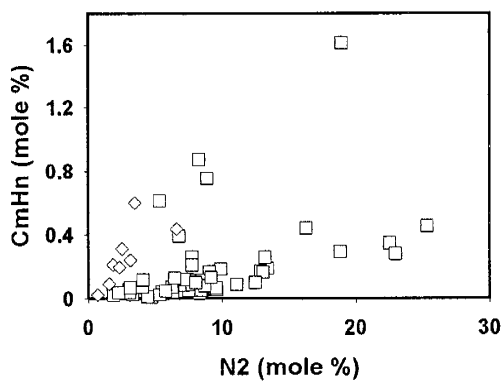

Figure 37. Comparison of N_2 and C*m*H*n* values (at m/e peak 26) from bulk analyses. □ = analyses of quartz veins, ◊ = analyses of sulfide minerals.

The enrichment of CH_4, N_2, and organic species in fluid A could be explained by reactions of hot fluids with organic-rich metasediments. Olson et al. (1992) proposes this explanation for CH_4-rich fluids occurring at the Syama gold deposit in Mali. Association between graphitic shales and enrichment of fluids in CH_4 and N_2 has been shown by Shepherd et al. (1991) for black shale-hosted gold deposits. The following reaction;

$$2C_{(graphite)} + 2H_2O === CO_2 + CH_4, \qquad (1)$$

occurs as hot fluids pass through carbonaceous rocks. This reaction favors temperatures above ~300° C.

Gold Solubility and System Equilibrium

Reactions of fluids with organic-rich metasediments could increase gold solubility through production of H_2S. It is thought that gold-bearing solutions of low salinity transport gold as sulfide complexes rather than as chloride complexes (Cameron, 1988). This is further suggested by the absence of anomalous base metals at the Amansie mine. Organic-rich metasediments may have been previously enriched in pyrite, and addition of hot fluids could cause the following reaction;

$$3FeS_2 + 6H_2O + C_{(graphite)} === Fe_3O_4 + CO_2 + 6H_2S, \qquad (2)$$

which favors higher temperatures. Increased levels of H_2S result in an increase in gold the solubility as $Au(HS)_2^-$ by the reaction

$$Au_{(s)} + 2H_2S === Au(HS)_2^- + H^+ + 1/2H_2. \qquad (3)$$

This sulfide complex is preferred at moderate pH conditions and low fO_2, as shown by Shenberger and Barnes (1989), and originally by Seward (1973).

A stability diagram (Fig. 38) illustrates a possible location for an Au-bearing solution associated with this mineralizing episode, calculated for 300°. The largest constraints on pH are the stability fields for the observed alteration minerals. Measured salinities yield estimates for Na^+ in solution and consequently for K^+ using the NaK geothermometer. Equilibrium between potassic feldspar and sericite indicate a pH ~ 5. Equilibrium of arsenopyrite and pyrite indicate a narrow field at $\log fO_2 = -35$ (Fig. 38). Carbon dioxide and CH_4 are also at equilibrium at this oxygen fugacity. It is expected, therefore, that the measured levels of H_2S in these fluids allow the solubility of between 0.01 and 0.05 ppb of gold.

Low levels of H_2S measured by bulk gas analyses of quartz veins indicate gold solubilities not exceeding 0.1 ppb. Shenberger (1985) calculates that a hydrothermal fluid with a concentration of at least 1 to 10 ppb Au in solution is necessary for the formation of an ore deposit. However, the solubility of gold indicated in the Amansie mine fluids are similar to the average of 0.101 ppb measured in natural waters in areas presently undergoing Au mineralization (McHugh, 1988).

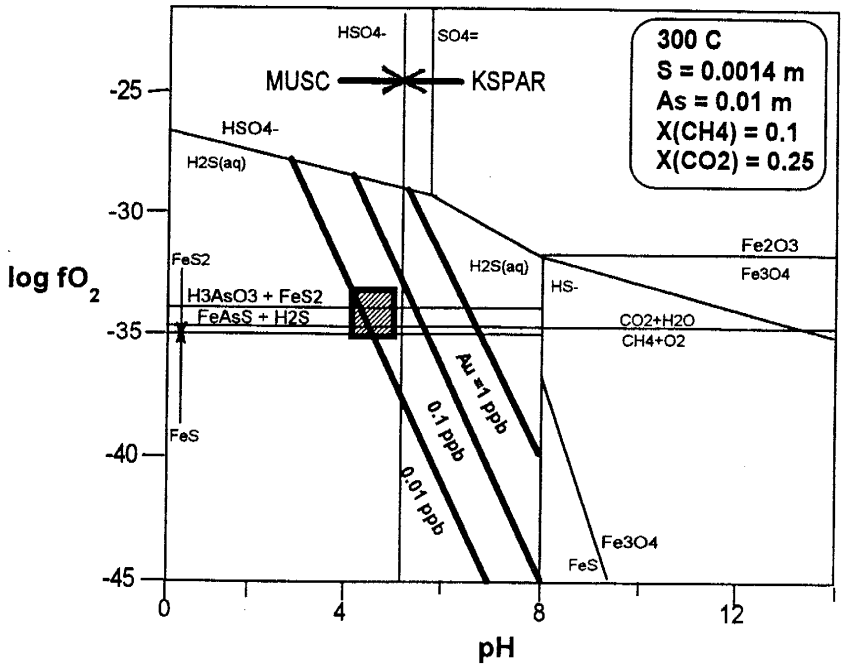

Figure 38. Stability fields for sulfide species, iron species, alteration minerals, methane, and arsenopyrite. Calculations for various phase boundaries are presented in Appendix I and Appendix K. The hatched box indicates the expected position of mineralizing fluids. Gold solubility from Shenberger and Barnes (1989). Feldspar, muscovite, and kaolinite equilibria from Henley et al. (1984). Arsenopyrite stability from data by Pal'yanova and Kolonin (1991). $m_{(Na+)} = 0.51$, $m_{(K+)} = 0.07$.

Stability of arsenopyrite is strongly temperature dependent, and if the above temperatures are coupled with high arsenic ion concentrations in solution, there is general agreement with arsenopyrite equilibrium. Arsenopyrite stability diagrams are shown in Figure 39 (Pal'yanova and Kolonin, 1991). At measured levels of H_2S, arsenopyrite is at equilibrium at 260° to 280° C, just below predicted solution temperatures of about 300° C. The anticipated reaction is:

$$FeS_2 + H_3AsO_3 + 5/2H_2 = FeAsS + H_2S + 3H_2O, \qquad (4)$$

where H_3AsO_3 is the dissolved arsenic species (Pal'yanova and Kolonin, 1991). This equilibrium indicates H_3AsO_3 concentrations of 0.001 to 0.006 m.

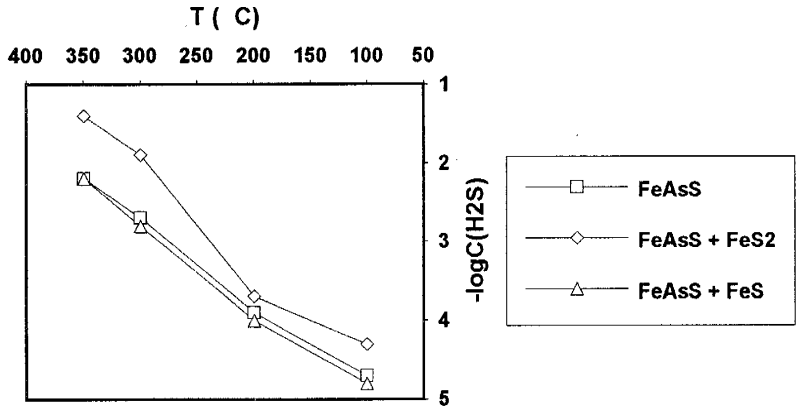

Figure 39. Stability diagram of arsenopyrite (◊), arsenopyrite + pyrite (□), and arsenopyrite + pyrrhotite (Δ) (Pal'yanova and Kolonin, 1991). Bulk gas analyses representative of fluid A yield $-\log C_{(H2S)} = 3.1$.

Deposition of Gold

Gold deposition occurs upon changing the system equilibrium. Important mechanisms for altering fluid chemistry are boiling and the precipitation of mineral phases. Boiling systems undergo rapid chemical changes and thus deposit minerals more readily than non-boiling systems (Drummond and Ohmoto, 1985). Fluid boiling is shown by both microthermometric data and the bulk gas analysis boiling model. There is a substantial loss of CH_4 to the vapor phase during this process in the mineralizing fluids of the Amansie mine. Naden and Shepherd (1989) conclude that CH_4 assists the precipitation of Au by increasing fluid immiscibility at depths where CO_2-H_2O-H_2S solutions will not unmix. However, H_2S is only weakly partitioned into the vapor phase relative to the other gaseous species. Therefore, this process alone will not cause sufficient instability of the gold sulfur complex in equation (3) to precipitate Au. An additional mechanism is necessary to deplete H_2S. Bowers (1991) shows the importance of precipitating associated mineral phases in causing deposition of gold in high P-T solutions. These reactions oppose changes in pH that would inhibit precipitation. Drummond and Ohmoto

(1985) state that changes in pH are not as pronounced in closed systems at high pressures as they are in open, epithermal-type systems. The precipitation of arsenopyrite and pyrite, by reactions (2) and (4), deplete fluids in H_2S and drive reaction (3) toward the left. Low levels of H_2S at the Amansie mine may reflect the loss of this component to such sulfidization of the wall rocks. Extremely low levels of H_2S measured in the fluid inclusions of sulfide minerals suggest that H_2S has been lost to reactions on the inclusion walls.

On a larger scale, depletion of H_2S in fluids at the Amansie mine may be a function of the deposit level that is presently exposed. The range in depth for mesothermal gold deposits is 4 km down to the brittle/ductile transition boundary at 10-15 km (Cameron, 1988). Fluid inclusions from the present surface show formation depths of 4-6 km, suggesting that the Amansie mine is near the top of a typical mesothermal gold system. The lowest levels of H_2S might be expected at the top of the ore body, where depletion due to sulfidization is the most pronounced. Groff (1996) measured H_2S levels in the Getchell and Twin Creeks Carlin-type gold deposits, and reports the lowest H_2S/Ar at the top of the deposits. This ratio was found to increase 5-fold over a depth of 1000 m for Getchell mine, and over 10-fold over a depth of 400 m at Twin Creeks mine.

Depletion of Organics and the Second Pulse of Mineralization

Evidence of gold solubility indicates that fluid B is responsible for a second mineralizing event at the Amansie mine. This event is thought to have resulted in less gold mineralization, and this may be related to the depletion of the organic-rich metasediments at depth. Fluid B is relatively depleted in CH_4 and organic species (Table 6). This suggests that organic enrichment processes dominate only in the initial stages of wall rocks heating, evolving much of the available N_2 and CH_4. This would leave later stage fluids relatively depleted in those gases (Norman and Musgrave, 1993). Fluid B, however, is not

completely depleted in these gaseous species, and the same chemistry of gold solubility and deposition could apply at a smaller scale. Equilibrium calculations were made for gold solubility as a sulfide complex. Results indicate that up to 0.1 ppb gold could have been transported by fluid B. During this time gold may have been remobilized and deposited in areas within or immediately surrounding the second intrusive. Preferential deposition of gold within the intrusive itself could be related to high porosity of the intrusive material. This effect could have been much more pronounced at ore bodies such as the South Esuajah intrusive of the Ayanfuri project.

Sources of Mineralizing Fluids

In mesothermal gold deposits, there are three commonly debated end-member sources for mineralizing fluids; magmatic, metamorphic, and meteoric (Elder and Cashman, 1992). The evidence presented by this study can only definitively exclude meteoric fluid sources. Various points of evidence for and against different fluid origins are discussed below.

Metamorphic Sources

Metamorphic fluids are concluded as being the origin of quartz gold-bearing vein deposits by many researchers (e.g., Phillips et al., 1987; Cameron, 1988; Kerrich and Fyfe, 1981; Powell et al., 1991; Studemeister and Kilias, 1987). At the Amansie mine, low salinity CO_2-H_2O fluids (assuming the organic gaseous species are a later addition) are in agreement with such a source. These fluids would have been focused along the NE-SW striking shear zone. The intrusives of the Amansie mine could have provided heat, provided that they are part of a much larger plutonic body at depth. However, a critical factor in the above argument is timing of metamorphism and mineralization. The intrusive bodies at the Amansie mine do not show pronounced metamorphism. It is possible that

fluids were derived from high-grade metamorphic reactions occurring at deeper crustal levels, long after peak metamorphism at the level of the Amansie mine. The 'deeper-later' model presented by Powell et al. (1991) may be applicable, in which retrograde metamorphism occurs at shallow depths while prograde metamorphism continues at intermediate depths and melting of crust occurs at deep levels. The model gives a broad time association between mineralizing fluids and felsic intrusives without requiring a genetic association. However, a long time may have elapsed since this metamorphism, and it may have ceased even at deeper levels. Such a conclusion was reached for a similar situation at the Barberton greenstone gold deposits (de Ronde et al., 1992).

Magmatic Sources

Magmatic hydrothermal processes are thought to be the source of mineralizing fluids by many researchers (e.g., Cameron and Hattori, 1987; Burrows and Spooner, 1987; Ishihara, 1981), and there are aspects of fluids and mineralization at the Amansie mine that support this idea. Bulk gas analyses of quartz veins corroborate with a magmatic source on Figure 30. Several points of evidence indicate that the main mineralizing fluid follows the emplacement of the intrusives, and thus makes a more compelling source than metamorphic fluids that do not have a clear time association with mineralization. Geochemical analyses indicate enrichment of Mo and W, and Au is strongly correlated with W. These three elements are partitioned into hydrothermal fluids derived from an felsic intrusive (Burrows and Spooner, 1987) and are anomalous in associated ore deposits.

There are several points, however, that conflict with the magmatic association. High values of N_2 do not necessarily imply a magmatic source for fluids as shown on Figure 30 (nitrogen sources are discussed below). A magmatic fluid might be expected to be rich in K and NaCl (Schreiber et al., 1990), and the fluids at the Amansie mine show no

enrichment in either component. The association between Au and W anomalies could indicate the dominance of sulfide complexes over chloride complexes in mineralizing fluids (Barnes, 1979). It may also be possible to reject a magmatic fluid source based on the estimated oxidation state of fluids at the Amansie mine. The important association between highly oxidizing fluids and magmatic sources for gold is discussed by Hattori (1987). Thomas and Spooner (1988) state that high fO_2 values are expected in fluids from pegmatites, lying somewhere between the QFM and HM buffer. However, a plot of organic species in fluids at the Amansie mine (Fig. 31) indicate highly reduced fluid conditions during the main phase of gold mineralization. Calculations of oxygen fugacity from equilibrium relationships and stability fields for sulfide minerals (Fig. 38) also indicate highly reduced conditions.

Meteoric Influences

The influence of unevolved meteoric fluids on the mineralizing fluids is either non-existent or minor. Figures 28 and 29 show no bulk fluid inclusion gas analyses giving the composition of air saturated ground water, or of fluid mixing with such ground waters. This indicates that the fluids occurred at deep levels in the crust. Any convection that may have been occurring could not have included near-surface waters. Depth estimations from microthermometric data give further evidence of mineralization at depth.

Combination of Sources and Organic Enrichment

Difficulty in resolving a fluid source suggests that fluids have been influenced by more than one source. Metamorphic (labeled as crustal) and magmatic fluid compositions are marked on Figs. 28-30. Bulk gas analyses tend to fall between these end members, spread out in what could be interpreted as a mixing line. Analyses in Figure 30 falling outside of

this range could be the result of N_2 contamination by organic-rich sediments. Interpretation, however, is confused by lack of agreement between the ternary plots. Analyses of rock-forming quartz indicate a magmatic fluid source as would be expected on Figure 30, but yield compositions suggesting crustal sources on Figures 28 and 29. The most probable explanation for fluid source is that fluids initially from metamorphic reactions in the lower crust were present in the shear zone. Intrusion of the granitoids triggered activity of the geothermal system through introduction of heat, assuming that the intrusives are part of much larger plutons at depth. This is suggested by the enrichment of organic species, since the emplacement of the intrusives is well timed with the occurrence of reduced, organic-rich fluids. The intrusives could have remobilized reduced fluids already present in the metasediments. Thomas and Spooner (1988) suggest that CH_4-rich fluids associated with the Tanco pegmatite could have been metamorphic, present and at equilibrium with graphite before pegmatite emplacement. These fluids would then have been remobilized by the intrusion.

Source of Gold

Metasediments underlying the Amansie mine are the most likely sources for gold mineralization within the ore bodies. Organic-rich sediments could have acquired anomalous levels of gold prior to intrusive activity at the Amansie mine. This gold could have been contained by diagenetic pyrites, or by carbonaceous material. Activated carbon is a general name for a group of randomly oriented fragments of graphite (Mattson and Mark, 1971). It occurs when hot fluids pass through carbonaceous material. These particles could adsorb gold on to their surfaces, as suggested by Springer (1985). This could, over time, result in anomalous concentrations of gold at depth. Such gold concentrations would act as a source for subsequent remobilization during the hydrothermal processes hypothesized in this study. Remobilization would result from

reactions (1) and (2) moving to the right, dissolving graphite and increasing H_2S concentration. Previous geochemical analyses of Birimian rocks confirm anomalous gold concentrations, particularly in carbonaceous schists (Hirdes and Leube, 1989). In this study, anomalous gold on the edge of the unmineralized Mmooho Hill intrusive suggests that the pluton passed through gold-enriched metasediments during ascent.

The quantity of gold now present at the Amansie mine does not necessarily imply a gold-rich fluid source. The low levels of gold solubility shown in equilibria relationships (Fig 38) could indicate an efficient hydrothermal system acting over a long period of time. This is the suggested explanation for gold deposits at the Pataz region gold mineralized quartz veins (Schreiber et al., 1990). Phillips et al. (1987) suggest that neither high Au concentrations in source rocks or large volumes of source rock are required to produce economic Au deposits. A more important factor is a suitable focusing mechanism for fluids (i.e., deep shearing) and Fe-rich rocks to ensure efficient Au deposition.

The estimated amount of gold at the Amansie mine is about 2.2×10^7 grams (D. Bertram, pers. commun., 1996). Assuming a 50% efficient leaching (Buisson and Leblanc, 1987), this amount of gold requires on the order of 20 km^3 of source rocks having 1 ppb Au. Though this amount of source rock is not excessive, the amount of fluid required to move the Au is considerable. Given a maximum Au solubility of 0.1 ppb, a deposit of 2.2×10^7 grams requires 2.2×10^{11} metric tons of H_2O, or 220 km^3 of H_2O. This assumes 100% efficiency in gold-bearing capacity of the H_2O. If mineralizing fluids were discharged through the Amansie mine shear zone at 1×10^4 kg/hr, the present reserves would have taken 250,000 years to form. By comparison, fluid discharge from the Ohaaki Pool in Broadlands, New Zealand, is 1.6×10^6 kg/hr (Weissberg et al., 1979).

The above figures assume that H_2S levels are as measured from bulk gas analyses. However, as previously discussed, these levels may be low due to fluid-rock interactions. Higher levels of H_2S in the original mineralizing fluids would increase gold solubility.

This would substantially reduce discharge requirements for mineralizing fluids at the Amansie mine.

GUIDES TO EXPLORATION

This study provides some information relevant to gold exploration in Lower Proterozoic metasedimentary rocks covering portions of West Africa and in similar geologic settings throughout the world. The study emphasizes the relationship between NE-SW trending shear zones, late syn- to post-tectonic felsic intrusives, and gold mineralization of possibly economic potential. It associates carbonaceous material in metasediments and anomalous Mo, As, and W values with ore-bearing zones. A major point of interest provided by the study involves the method of bulk fluid inclusion gas analysis in determining fluid signatures in quartz veins. These signatures could, as in the case of the Amansie mine, indicate the onset of fluids rich in CH_4 or organic species derived from possible gold source areas at depth. Surface rocks are highly weathered in tropical environments. Geochemical sampling of soils or rock exposures may give limited information about mineralization at depth. Quartz veins encountered on surface, however, are in essentially an 'unweathered' state, and preserve information about possible mineralizing fluids. Sampling and analysis of quartz veins with a knowledge of cross-cutting relationships could be used to reconstruct the fluid history of a potential deposit, and indicate the likelihood of gold-bearing fluids.

CONCLUSIONS

1. Gold-bearing intrusives are late syn- to post-tectonic occurrences in Birimian metasedimentary rocks. They vary in composition from tonalites to granites. Alteration is ubiquitous; most commonly it is sodic alteration accompanied by loss of K and Ca. All intrusives can be associated with NE-SW trending shear zones that are manifestations of a transcurrent shearing phase of the Eburnean event. They occur in a metasedimentary basin but do not fit the classification of 'basin granitoid' (Leube et al., 1990; Kesse, 1985). The timing of emplacement is probably similar to that shown by Hirdes et al. (1993).

2. The Amansie mine is a mesothermal gold deposit that formed at 4 to 6 km depth. Gold mineralization occurred in two phases, roughly synchronizing with the emplacement of the intrusive bodies. The first fluid phase is rich in CH_4 and is of low salinity. The second mineralizing fluid is depleted in CH_4, enriched in CO_2, and is of slightly higher salinity. Organic-rich metasediments at depth have enriched the fluid in CH_4 and N_2, and the second fluid shows lower levels of CH_4 because this source has become depleted over time.

3. Ternary plots of bulk fluid inclusion gas analyses can be used to determine the possibility of fluid phase separation (i.e., boiling) by using the differences in gas solubilities to construct a 'boiling curve'. Clusters of data points on the ternary plots that cannot be linked by a 'boiling curve' may represent distinct fluid phases, separated by either origin or time or both.

4. Low concentrations of H_2S in the Amansie mine fluid inclusions indicate that gold mineralization must have occurred over an extended period of time. It may imply that the present Amansie mine is situated at the top of the mineralized system and that H_2S levels reflect substantial losses to sulfidization of wall rocks. It may also suggest that there was an efficient hydrothermal system leaching gold from its source at depth. Reactions of

organic-rich metasediments with mineralizing fluids may have facilitated Au solubility and transport along the shear zone.

5. Numerous points of evidence can be given for and against metamorphic and magmatic fluid sources. Fluids are most likely to have been metamorphic in origin, and the geothermal system responsible for gold mineralization was triggered by the intrusion of the granitoid bodies. One conclusive point is that fluids were not influenced by air saturated water.

6. A possible gold source is from organic-rich metasediments at depth. Geochemical analyses of unmineralized areas in this study and by previous researchers confirms anomalous gold present in many Birimian rocks. However, adequate levels of gold could be acquired from the lower crust during metamorphic reactions. The reduced state of the mineralizing fluid precludes a gold source from within the intrusive bodies.

7. Limited data reveal similarities between mineralizing fluid, alteration, and structure of the Amansie mine and the gold-bearing intrusives of the Ayanfuri project and the Obuasi intrusives. The intrusive displaying the greatest overall differences from the others is the unmineralized pluton of Mmooho Hill.

REFERENCES

Barnes, H. L., 1967, Geochemistry of Hydrothermal Ore Deposits: New York, Holt, Rinehart and Winston, Inc., 670 p.

Barnes, H. L., 1979, Solubilities of ore minerals, *in* H. L. Barnes, ed., Geochemistry of Hydrothermal Ore Deposits (second edition): New York, John Wiley & Sons, p. 404-460.

Bates, D. A., 1955, Geological map of the Gold Coast and Togoland under British trusteeship (1:1 000 000): Gold Coast Geol. Surv., Accra.

Beattie, M., and Barton Jr., J. M., 1992, Alteration and occurrence of gold mineralization in the Roodepoort Goldfield, Pietersburg granite-greenstone terrane: South Af. J. of Geology, v. 95 (3/4), p. 131-140.

Bessoles, B., 1977, Géologie de l'Afrique. Vol 1. Craton de l'Ouest Africain: Bur. de Rech. Géol. Min. Mem., v. 88, 402 p.

Blagonadezhdin, B. I., 1975, Gold mineralization in relation to tectonics and magmatism, as in the northwestern margin of Birrim gold belt, West Africa: Internat. Geology Rev., v. 17 (9), p. 1080-1090.

Bowers, T. S., 1991, The deposition of gold and other metals: pressure-induced immiscibility and associated stable isotope signatures: Geochim. Cosmochim. Acta, v. 55, p. 2417-2434.

Bozzo, A. T., Chen, J. R., and Barduhn, A. J., 1973, The properties of the hydrates of chlorine and carbon dioxide, *in* Delyanni, A., and Delyanni, E., eds., Internat. Symposium on Fresh Water from the Sea, 4th: v. 3, p. 437-451.

Brown, J. S., 1948, Ore Genesis: New Jersey, Hopewell Press.

Buisson, G., and Leblanc, M., 1987, Gold in mantle peridotites from Upper Proterozoic ophiolites in Arabia, Mali, and Morocco: Econ. Geol., v. 82, p. 2091-2097.

Burrows, D. R., and Spooner, E. T. C., 1987, Generation of a magmatic H_2O-CO_2 fluid enriched in Au and W within an Archean sodic granodiorite stock, Mink Lake, northwestern Ontario: Econ. Geol., v. 82, p. 1931-1957.

Burrows, D. R., Wood, P. C., and Spooner, E. T. C., 1986, Carbon isotope evidence for a magmatic origin for Archean gold-quartz vein ore deposits: Nature, v. 321, p. 851-854.

Caen-Vachette, M., 1986, Apport de la géochronologie isotopique à la connaissance du Protérozoïque inférieur de l'Afrique de l'Ouest: CIFEG publication occasionnelle, n° 10, p. 25-44.

Cameron, E. M., 1988, Archean gold: Relation to granulite formation and redox zoning in the crust: Geology, v. 16, p. 109-112.

Cameron, E. M., and Hattori, K., 1987, Archean gold mineralization and oxidized hydrothermal fluids: Econ. Geol., v. 82, p. 1177-1191.

Carignan, J., and Gariépy, C., 1993, Pb isotope geochemistry of the Silidor and Launay gold Deposits: Implication for the source of Archean Au in the Abitibi Subprovince: Econ. Geol., v. 88, p. 1722-1730.

Channer, D. M., and Spooner, E. T. C., 1994, Combined gas and ion chromatographic analysis of fluid inclusions: Applications to Archean granite pegmatite and gold-quartz vein fluids: Geochim. Cosmochim. Acta., v. 58, p. 1101-1118.

Collins, P. L. F., 1979, Gas hydrates in CO_2-bearing fluid inclusions and the use of freezing data for estimation of salinity: Econ. Geol., v. 74, p. 1435-1444.

Corfu, F., 1993, The evolution of the southern Abitibi greenstone belt in light of precise U-Pb geochronology: Econ. Geol., v. 88, p. 1323-1340.

Daly, R. A., 1933, Igneous Rocks and the Depths of the Earth: New York, McGraw-Hill, 598 p.

Davidson, D. W., 1972, Clathrate hydrates, *in* F. Franks, ed., Water a Comprehensive Treatise: Vol. 2, Plenum Press, p. 115-234.

de Ronde, C. E. J., Spooner, E. T. C., de Wit, M. J., and Bray, C. J., 1992, Shear zone-related, Au quartz vein deposits in the Barberton greenstone belt, South Africa: Field and petrographic characteristics, fluid properties, and light stable isotope geochemistry: Econ. Geol., v. 87, p. 366-402.

Debon, F. and Le Fort, P., 1983, A chemical-mineralogical classification of common plutonic rocks and associations: Trans. R. Soc. Edinburgh, Earth Sci., v. 73, p. 135-149.

Drever, J. I., 1988, The geochemistry of natural waters, second edition: New Jersey, Prentice Hall, 437 p.

Drummond, S. E., and Ohmoto, H., 1985, Chemical evolution and mineral deposition in boiling hydrothermal systems: Econ. Geol., v. 80, p. 126-147.

Dzigbodi-Adjimah, K., 1992, Geology and geochemical patterns of the Birimian gold deposits, Ghana, West Africa: J. of Geochem. Exploration, v. 47, p. 305-320.

Elder, D., and Cashman, S. M., 1992, Tectonic control and fluid evolution in the Quartz Hill, California, lode gold deposits: Econ. Geol., v. 87, p. 1795-1812.

Feng, R., Fan, J., and Kerrich, R., 1993, Noble metal abundances and characteristics of six granitic magma series, Archean Abitibi Belt, Pontiac Subprovince: Relationships of metallogeny and overprinting of mesothermal gold deposits: Econ. Geol., v. 88, p. 1376-1401.

Feybesse, J. L., Milési, J. P., Verhaeghe, Ph., and Johan, V., 1989, Le domaine de Toulepleu-Ity (Côte-d'Ivoire): une unité "birrimienne" charrieé sur les gneiss archéens du domaine de Kénéma-Man lors des premiers stades de l'orogène éburnéen: C. R. Acad. Sci., Fr. (in press).

Fyon, J. A., Troop, D. G., Marmont, S., and Macdonald, A. J., 1989, Introduction of gold into Archean crust, Superior province, Ontario---coupling between mantle-initiated magmatism and lower crustal thermal maturation: Econ. Geol. Mon. 6, p. 479-490.

Garrels, R. M., and Christ, C. L., 1965, Solutions, Minerals and Equilibria: New York, Harper and Row, 450 p.

Giggenbach, W. F., 1980, Geothermal gas equilibria: Geochim. Cosmochim. Acta, v. 44, p. 2021-2032.

Gresens, R. L., 1967, Composition-volume relationships of metasomatism: Chem. Geol., v. 2, p. 47-65.

Groff, J., 1996, $^{40}Ar/^{39}Ar$ Geochronology of gold mineralization and origin of auriferous fluids for the Getchell and Twin Creeks mines, Humboldt County, Nevada: Unpub. Ph. D. thesis, New Mexico Institute of Mining and Technology, 291 p.

Harris, M., 1980, Hydrothermal alteration at Salave gold prospect, northwest Spain: Institution of Mining and Metallurgy Transactions, v. 89, p. 5-15.

Hattori, K., 1987, Magnetic felsic intrusions associated with Canadian Archean gold deposits: Geology, v. 15, p. 1107-1111.

Haude, H., 1987, Placer gold prospecting in the Mensin, Chira, Pamunu, Bensupata, Bonsa and Totua rivers, SW Ghana: Rep. Arch. BGR, Hannover, 144 p. (unpubl.)

Hedenquist, J. W., and Henley, R. W., 1985, The importance of CO_2 on freezing point measurements of fluid inclusions: Evidence from active geothermal systems and implications for epithermal ore deposition: Econ. Geol., v. 80, p. 1379-1406.

Henley, R. W., Truesdell, A. H., and Barton, P. B., 1984. Fluid-Mineral Equilibria in Hydrothermal Systems, *in* J. Robertson, ed., Reviews in Economic Geology, Volume I: Society of Economic Geologists, 264 p.

Heyen, G., Ramboz, C., and Dubessy, J., 1982, Simulation des equilibres de phases dans le systeme CO_2-CH_4 en dessous de 50° C et de 100 bar. Application aux inclusions fluides: C. R. Acad. Sci. Paris 294, série II, p. 203-206.

Hirdes, W., and Leube, A., 1989, On gold mineralization of the Proterozoic Birimian Supergroup in Ghana/West Africa: Technical Cooperation Project No. 80.2040.6: Hannover, Bundsanstalt für Geowissenschaften und Rohstoffe, 179 p.

Hirdes, W., Davis, D. W., and Eisenlohr, B. N., 1992, Reassessment of Proterozoic granitoid ages in Ghana on the basis of U/Pb zircon and monazite dating: Prec. Res., v. 56 p. 89-96.

Hirdes, W., Senger, R., Adjei, J., Efa, E., Loh, G., and Tettey, A., 1993, Explanatory notes for the geological map of southwest Ghana 1 : 100,000: Geologisches Jahrbuch Reihe B, Heft 83: Hannover, Bundsanstalt für Geowissenschaften und Rohstoffe, 139 p.

Hodgson, C. J., and MacGeehan, P. J., 1982, A review of the geological characteristics of "gold-only" deposits in the Superior Province of the Canadian Shield: Canadian Inst. of Mining and Metallogy Spec. Vol. 24, p. 211-229.

Holloway, J. R., 1981, Compositions and volumes of supercritical fluids in the earth's crust, *in* L. S. Hollister and M. L. Crawford. eds., Fluid Inclusions: Applications to Petrology, Mineralogical Association of Canada Shortcourse Handbook 6: p. 13-38.

Hynes, A., 1980, Carbonatization and mobility of Ti, Y, and Zr in Ascot Formation metabasalts, SE Quebec: Contrib. Mineral. Petrol., v. 75, p. 79-87.

Ishihara, S., 1981, The granitoid series and mineralization: Econ. Geol., 75th Anniversary Volume, p. 458-484.

Junner, N. R., 1932, The geology of Obuasi Goldfield with coloured geological map and section: Gold Coast Geol. Surv. Mem., No. 2, 71 p.

-------, 1935, Gold in the Gold Coast: Ghana Geol. Surv. Mem., No. 4, 67 p.

Kerrich, R., 1986, Fluid transport in lineaments: Phil. Trans. Roy. Soc. London, v. A 317, P. 219-251.

Kerrich, R., and Fyfe, W. S., 1981, The gold-carbonate association: Source of CO_2, and CO_2 fixation reactions in Archean lode deposits: Chem. Geol., v. 33, p. 265-294.

Kerrich, R., and Wyman, D., 1990, Geodynamic setting of mesothermal gold deposits: An association with accretionary tectonic regimes: Geology, v. 18, p. 882-885.

Kesse, G. O., 1985, The mineral and rock resources of Ghana: Rotterdam/Boston, Balkema, 610 p.

Khitrunov, A. T. and Mel'tser, M. L., 1979, Geochemistry of gold in the granitoid process: Geochemistry International, v. 16 (5), p. 37-42.

Kolbe P., Rinson, W. H., Saul, J. M., Miller, E. W., 1967, Rb/Sr studies on country rocks of the Bosumtwi Crater, Ghana: Geochim. Cosmochim. Acta, GB, v. 31, p. 869-875.

Kolonin, G. R., Pal'yanova, G. A., and Shironosova, G. P., 1988, Arsenopyrite stability and solubility in hydrothermal solutions: Geokhimiya, no. 6, p. 843-856.

La Roche, 1978, La chimie des roches présentée et interprétée d'après la structure de leur faciès minéral dans l'espace des variables chimiques: fonctions spécifiques et diagrammes qui s'en déduisent. Application aux roches ignées: Chem. Geol., v. 21, p. 63-87.

Leube, A., Hirdes, W., Mauer, R. and Kesse, G. O., 1990, The early Proterozoic Birimian supergroup of Ghana and some aspects of its associated gold mineralization: Prec. Res., v. 46, p. 139-165.

Mattson, J. S. and Mark, H. B., 1971, Activated Carbon: New York, Mancel Dekkerr, 125 p.

McHugh, J. B., 1988, Concentration of gold in natural waters: Jour. Geochem. Explor., v. 30, p. 85-94.

Milési, J. P., Feybesse, J. L., Ledru, P., Dommanget, A., Ouedraogo, M. F., Marcoux, E., Prost, A., Vinchon, C., Sylvain, J. P., Johan, V., Tegyey, M., Calvez, J. Y., and Langy, P., 1990, West African gold deposits in their lower Proterozoic lithostructural setting: Chron. rech. min., v. 497, p. 3-98.

Milési, J. P., Ledru, P. Feybesse, J. L., Dommanget, A., and Marcoux, E., 1992, Early Proterozoic ore deposits and tectonics of the Birimian orogenic belt, West Africa: Prec. Res., v. 58, p. 305-344.

Moore, D. E., Liou, J. G., and King, B., 1981, Chemical modifications accompanying blueschist facies metamorphism of Franciscan conglomerates, Diablo Range, California: Chem. Geol., v. 33, p. 237-263.

Naden, J., and Shepherd, T., 1989, Role of methane and carbon dioxide in gold deposition: Nature, v. 342, p. 793-796.

Norman, D. I., and Musgrave, J. A., 1993, N_2-Ar-He compositions in fluid inclusions: Indicators of fluid source: Geochim. Cosmochim. Acta, v. 58 (3), p. 1119-1131.

Norman, D. I., and Sawkins, F. J., 1987, Analysis of gases in fluid inclusions by mass spectrometer: Chem. Geol., v. 61, p. 1-10.

Norman, D. I., Moore, J. N., Yonaka, B., and Musgrave, J., 1996, Gaseous species in fluid inclusions: A tracer of fluids and indicator of fluid processes. Proceedings: Twenty-first Workshop on Geothermal Reservoir Engineering, Stanford University, Stanford, California, January 22-24.

Ntiamoah-Agyakwa, Y., 1979, Relationship between gold and manganese mineralizations in the Birimian of Ghana: West Africa Geol. Mag., v. 116 (5), p. 345-352.

O'Connor, J. T., 1965, A classification for quartz-rich igneous rocks based on feldspar ratios: U.S. Geol. Survey Prof. Paper 525-B, p. B79-B84.

Olson, S. F., Diakite, K., Ott, L., Guindo, A., Ford, C. R. B., Winer, N., Hanssen, E., Lay, N., Bradley, R., and Pohl, D., 1992, Regional setting, structure, and descriptive geology of the middle Proterozoic Syama gold deposit, Mali, West Africa: Econ. Geol., v. 87, p. 310-331.

Pal'yanova, G. A., and Kolonin, G. R., 1989, Arsenopyrite-bearing mineral assemblages as indicators of conditions of hydrothermal mineralization: Geochemistry International, v. 26, p. 120-131.

Pearce, J. A., Harris, N. B., and Tindle, A. G., 1984, Trace element discrimination diagrams for the tectonic interpretation of granitic rocks: Jour. of Petrology, v. 25, Part 4, p. 956-983.

Phillips, G. N., Groves, D. I., and Brown, I. S., 1987, Source requirements for the Golden Mile, Kalgoorlie: Significance to the metamorphic replacement model for Archean gold deposits: Canadian Jour. Earth Sci., v. 24, p. 1643-1651.

Powell, R., Will, T. M., and Phillips, G. N., 1991, Metamorphism in Archean greenstone belts: Calculated fluid compositions and implications for gold mineralization: Jour. Metamorphic Geology, v. 9, p 141-150.

Prini, R. F., and Crovetto, R., 1989, Evaluation of data on solubility of simple apolar gases in light and heavy water at high temperature: J. Phys. Chem. Ref. Data., v. 18 (3), p. 1231-1243.

Ramboz, C., Pichavant, M., and Weisbrod, A., 1982, Fluid immiscibility in natural processes: use and misuse of fluid inclusion data. II. Interpretation of fluid inclusion data in terms of immiscibility: Chem. Geol., v. 37, p. 29-48.

Renault, J., 1986, Mass balance calculation based on hypothetical igneous precursor compositions: Abstracts with Programs, Geological Society of America, v. 18, p. 405.

Schnetzler, C. C., Pinson, W. H., Hurley, P. M., 1966, Rb/Sr age of the Bosumtwi Crater area, Ghana, compared with the age of the Ivory Coast tectites: Science USA, v. 151, p. 816-819.

Schreiber, D. W., Fontboté, L., and Lochmann, D., 1990, Geologic setting, paragenesis, and physicochemistry of gold quartz veins hosted by plutonic rocks in the Pataz Region: Econ. Geol., v. 85, p. 1328-1347.

Seitz, J. C., Pasteris, J. D., and Wopenka, B., 1987, Characterization of CO_2-CH_4-H_2O fluid inclusions by microthermometry and laser Raman microprobe spectroscopy: Inferences for clathrate and fluid equilibria: Geochim. Cosmochim. Acta, v. 51, p. 1652-1664.

Seward, T. M., 1973, Thio complexes of gold and the transport of gold in hydrothermal ore solutions: Geochim. Cosmochim. Acta, v. 37, p. 370-399.

Shenberger, D. M., 1985, Gold solubility in aqueous sulfide solutions: Unpub M. Sc. thesis, Pennsylvania State Univ., 102 p.

Shenberger, D. M., and Barnes, H. L., 1989, Solubility of gold in aqueous sulfide solutions from 150 to 350° C: Geochim Cosmochim. Acta, v. 53, p. 269-278.

Shepherd, T. J., Bottrell, S. H., and Miller, M. F., 1991, Fluid inclusions volatiles as an exploration guide to black shale-hosted gold deposits, Dolgellau gold belt, North Wales, UK: J. Geochem. Explor., v. 43, p. 5-24.

Shepherd, T. J., Rankin, A. H., and Alderton, D. H. M., 1985, A practical guide to fluid inclusion studies: Glasgow, Blackie Sons Ltd., 293 p.

Smith, F. G., 1963, Physical Geochemistry: Reading, Massachusetts, Addison-Wesley Publishing Company, Inc, p. 624.

Springer, J., 1985, Carbon in Archaean rocks of the Abitibi belt (Ontario-Quebec) and its relation to gold distribution: Can. J. Earth Sci., v. 22, p. 1945-1951.

Sterner, S. M., 1992, Homogenization of fluid inclusions to the vapor phase: The apparent homogenization phenomenon: Econ. Geol., v. 87, p. 1616-1623.

Studemeister, P. A., and Kilias, S., 1987, Alteration pattern and fluid inclusions of gold-bearing quartz veins in Archean trondhjemite near Wawa, Ontario, Canada: Econ. Geol., v. 82, p. 429-439.

Taylor, P. N., Moorbath, S., Leube, A., and Hirdes, W., 1988, Geochronology and crustal evolution of Early Proterozoic granite-greenstone terrains in Ghana/West Africa: Abstr., International Conference on the Geology of Ghana with Special Emphasis on Gold Comm. 75th Anniversary of Ghana Geol. Surv. Dept., Accra, p. 43-45.

Taylor, P. N., Moorbath, S., Leube, A., and Hirdes, W., 1992, Early Proterozoic crustal evolution in the Birimian of Ghana: constraints from geochronology and isotope geochemistry: Prec. Res., v. 56, p. 97-111.

Thomas, A. V., and Spooner, E. T. C., 1988, Fluid inclusions in the system H_2O-CH_4-NaCl-CO_2 from metasomatic tourmaline within the border unit of the Tanco zoned granitic pegmatite, S. E. Manitoba: Geochim. Cosmochim. Acta., v. 52, p. 1065-1075.

Touret, J., 1982, An empirical phase diagram for a part of the N_2-CO_2 system at low temperature: Chem. Geol., v. 37, p. 49-58.

Turekian, K. K., and Wedepohl, K. H., 1961, Distribution of the elements in some major units of the Earth's crust: Geol. Soc. Amer. Bull.., 72, p. 175-192.

Uytenbogaardt, W., and Burke, E. A. J., 1971, Tables for Microscopic Identification of Ore Minerals: New York, Dover Publications, Inc., 430 p.

Valakovich, M. P., and Altunin, U. V., 1968, Thermophysical Properties of Carbon Dioxide: London, Collets.

Weissberg, B. G., Browne, P. R. L., and Seward, T. M., 1979, Ore metals in active geothermal systems, in Barnes, H. L., ed., Geochemistry of hydrothermal ore deposits: New York, John Wiley and Sons, p. 738-780.

Whitelaw, O. A. L., 1929, The geology and mining features of the Tarkwa-Abosso goldfield: Gold Coast Geol. Surv. Mem., No. 1, 46 p.

Winchester, J. A. and Floyd, P. A., 1977, Geochemical discrimination of different magma series and their differentiation products using immobile elements: Chem. Geol., v. 20, p. 325-343.

Wright, J. and Hastings, D., 1985, Geology and Mineral Resources of West Africa: London, Allen & Unwin, 189 p.

Zweng, P. L., Mortensen, J. K., and Dalrymple, G. B., 1993, Thermochronology of the Camflo Gold Deposit, Malartic, Quebec: implications for magmatic underplating and the formation of gold-bearing quartz veins: Econ. Geol., v. 88, p. 1700-1721.

APPENDIX A

Petrographic Descriptions of Thin and Polished Sections

Cross Sections from Fig. 4: (A - A'), (B - B'), (C - C')

Locations Index of All Samples

THIN SECTION DESCRIPTIONS

#1] MMOOHO HILL - GRANITOID

30% kspar, 30% quartz, 25% plagioclase (An 37 -andesine), 10% muscovite
Minor rutile, hematite
Hypidiomorphic granular, med./course grained, all crystals subhedral to euhedral. Muscovite forms books.

Alteration: Slight oxidation, development of clay minerals in some micas, and some muscovite is completely clay minerals. Only slight development of sericite.
Metamorphic indicators: none
Notes: Microcline noted much more abundantly than is present in other sections. Crystal sizes are larger than other intrusives.

#2] NKRAN HILL - GRANITOID

20% plagioclase, 75% matrix (70% quartz, 30% clay minerals)
Minor calcite, hematite, rutile, chlorite (blue)
Porphyritic aphanitic, quartz and plagioclase subhedral

Alteration: Almost complete sericitization of plagioclase and overgrowth of albite (w/ sericite), fine opaque cement throughout. Hornblends crystals present, now completely replaced by calcite, chlorite (blue), rutile, quartz
Metamorphic indicators: Possible greenschist (shown by intragranular boundaries in quartz. Embayment of small crystals in large quartz crystals (product of recrystalization)
Notes: Alignment of sericite is function of plagioclase cleavage. Somewhat deformed, uncertain to be same material as [#8]. However, it is possible that here, at a narrow intrusion width, strain has been much greater than thick [#8] area. Could be in a shear zone but not a fault zone, it was is shown is cataclastically deformed, then must be less than 10 km depth. Given fresh rock, quartz and micas are weaker than feldspar and will deformed first. However, if feldspar has been sericitized, will be the weaker component.

POLISHED SECTION: Few sulfides, mostly euhedral arsenopyrite with overgrowths of anhedral pyrite. Outer edges of sulfides heavily oxidized.

#3] NKRAN HILL - GRANITOID

25% plagioclase, 20% quartz, 5% kspar, 50% matrix (60% quartz, 20% feldspar, 20% clay minerals)
Minor opaques, chlorite, hematite (slight oxidation of opaques)
Porphyritic aphanitic, subhedral quartz and plagioclase

Alteration: plagioclase sericitized, some plagioclase crystals have overgrowths which are not altered. muscovite completely replaced by chlorite (blue), very high chlorite in matrix.
Metamorphic indicators: Slight alignment of clay minerals
Notes: calcite absent

#4] NKRAN HILL - GRANITOID

25% plagioclase, 20% quartz, 5% kspar, 50% matrix (70% quartz, 20% clay minerals, 10% calcite + plagioclase)
Minor opaques and opaque cement, chlorite, hematite, rutile
Porphyritic aphanitic, phenocrysts are rounded

Alteration: Plagioclase mostly altered to sericite. Matrix is recrystallized fine grained quartz and micas (which show crystallographic lineation). Primary micas completely replaced by quartz, chlorite, and some rutile. Much alteration has occurred along microfractures, which preferentially host calcite, opaques.
Metamorphic indicators: Possible slight alignment of clay minerals
Notes: Numerous opaques along large crystal boundaries

POLISHED SECTION: Anhedral pyrite, sub/euhedral arsenopyrite, no clear relationship between the two.

#5] NKRAN HILL - METAGREYWACKE

40% quartz, 40% clay minerals, 20% calcite
Minor opaques, chlorite (blue), albite
Fine grained metasedimentary rock, calcite is anhedral and elongate in direction of foliation

Metamorphic indicators: Greenschist, one direction of foliation. Opaques show pressure shadows at edges (syn-tectonic ?)

#6] NKRAN HILL - GRANITOID

30% plagioclase (An 7 or An 28 - albite or oligoclase), 5% kspar, 25% quartz, 40% matrix (65% quartz, 10% calcite, 25% clay minerals)
Minor rutile, opaques
Porphyritic aphanitic, quartz and plagioclase crystals are subhedral

Alteration: plagioclase has med./high sericitic alteration, unaltered albite overgrowths. All micas are replaced in grains along boundaries along with opaques. Possible amphiboles present, now replaced. Quartz is recrystallized, showing embayment of fine quartz in larger crystals
Metamorphic indicators: none
Notes: Section is very similar in many respects to [#2], [#3], [#4]

POLISHED SECTION: Mostly arsenopyrite with secondary sub/anhedral pyrite, possibly mixed with pyrrhotite. Some isolated euhedral pyrite

6A] NKRAN HILL - GRANITOID/METASEDIMENT CONTACT ZONE

(Granitoid)
35% plagioclase (An 44 - andesine), 5% kspar, 15% quartz, 45% matrix (20% calcite, 60% quartz, 20% clay minerals)
Minor opaques
Porphyritic aphanitic with very large, subhedral quartz and plagioclase

Alteration: Moderate clay alteration as micaceous needles along cleavage planes. One large muscovite, heavily altered to calcite

Metamorphic indicators: Faint lineation of micas

POLISHED SECTION: Euhedral arsenopyrite is first, pyrite later and forming subhedral around arsenopyrite crystals. Both have inclusions of possibly pyrrhotite (tiny). chalcopyrite later forming either outside other sulfides or in degrading cores (and usually rimmed by pyrrhotite).

(Phyllite)

60% micas, 5% opaques, 5% calcite, 25% quartz, 5% plagioclase (An 7 or An 29 - albite or oligoclase)

Minor chlorite

Fine grained metasedimentary rock, foliated micas, quartz and calcite aligned along foliation

Metamorphic indicators: Greenschist, one direction of foliation. quartz elongated.

Notes: Some quartz veining, impregnated with cc. Some cc in matrix is also sheared. Opaques are very large, and finer, amorphous opaques in matrix. Large opaques sometimes with chlorite (blue) overgrowths and quartz. Also seen in [#33].

POLISHED SECTION: See above.

#7] NKRAN HILL - GRANITOID

50% plagioclase (An 7 or An 28 - albite or oligoclase), 25% quartz, 5% kspar, 20% clay minerals + calcite + opaques

Minor chlorite

Hypidiomorphic granular, very large grains of mostly plagioclase with minor anhedral quartz

Alteration: Primary micas replaced mostly with calcite (some euhedral) and some opaques. Sericite tends to concentrate along microfractures with calcite and opaques.

Metamorphic indicators: none

Notes: Microvein present (slightly deformed) that preserves crystal boundaries but has NO sericite.

#8] NKRAN HILL - GRANITOID

50% plagioclase (An 36 - andesine), 25% quartz, 10% kspar, 10% muscovite, 5% matrix (quartz + chlorite)

Minor kpsar, opaques, unidentate gray/brown, mica-like mineral

Hypidiomorphic granular, large grained overall, sub- to euhedral crystals

Alteration: Some primary muscovite with many opaques surrounding (mostly hosted in micas), but NO cc replacement evident. Plagioclase moderately sericitized, chlorite abundant in micas. Quartz recrystallized.

Metamorphic indicators: none

Notes: Albite showing exsolution lamellae?

POLISHED SECTION: Euhedral arsenopyrite with overgrowths of pyrite. Some euhedral pyrite present with no paragenetic relationship.

#8A] NKRAN HILL - GRANITOID

55% plagioclase (An - andesine), 20% quartz, 10% kspar, 10% micas + clay minerals, 5% matrix (quartz + clay minerals + calcite)

Minor rutile, opaques, chlorite (brown)

Hypidiomorphic granular, large interlocking crystals of plagioclase and quartz

Alteration: plagioclase has moderate degree of sericite alteration. Sec. micas form 'fans' between other crystals in the matrix. These micas are being altered in some cases to clays, chlorite (brown), and cc.

Metamorphic indicators: Deformation of quartz indicated clear metamorphic effects (undulatory extinction)

#9] NKRAN HILL - GRANITOID

60% plagioclase (An 6 or An 29 - albite or oligoclase), 20% quartz, 10% kspar, 10% mica (replaced by clay minerals, quartz, opaques, calcite)

Minor rutile, chlorite

Hypidiomorphic granular, large grained plagioclase, mod interstitial quartz, some muscovite are primary

Alteration: One mica shows deformation, many micas are replaced by chlorite. Opaques are surrounded by chlorite. Matrix shows later stage albite. Alteration products more prevalent along microfractures.

Metamorphic indicators: Shows less deformation than [#3], which in turn shows less than [#2]. Some quartz shows near-euhedral boundaries, otherwise slightly recrystallized.

Notes: Exsolution lamellae of albite?

#9A] NKRAN HILL - GRANITOID

45% plagioclase (An 5 or An 30 - albite or oligoclase), 25% quartz, 5% kspar, 5% muscovite, 5% matrix (quartz + clay minerals + calcite)

Minor rutile, opaques, chlorite (brown)

Hypidiomorphic granular, large plagioclase and quartz with more frequent interstitial matrix than [#8A]. Prominence of large primary micas as in [#1]

Alteration: K-spar occur only as remnants. Micas altered in most cases to pervasive surrounding calcite, fine grained opaques, and in some cases completely by rutile. Usually present in these muscovite crystals are large opaques, randomly oriented. Plagioclase crystals mod altered to sericite. Most albite is sericitized but some is unaltered. Addition of quartz to matrix.

Metamorphic indicators: Muscovite shows some deformation. Moderate deformation shown by embayment of quartz crystals.

POLISHED SECTION: Euhedral arsenopyrite, partially replaced by subhedral pyrite. Slight replacement of that by strips of anisotropic gray sulfide. Chalcopyrite in patches isolated from other sulfides.

#9B] NKRAN - GRANITOID

POLISHED SECTION: Arsenopyrite first as euhedral crystals, with overgrowths of euhedral to subhedral pyrite. One crystal shows euhedral interfingering of the two, indicating possible similar formation times. Minor chalcopyrite at margins

#10] NKRAN HILL - GRANITOID

55% plagioclase (An 36 - andesine), 25% quartz, 5% kspar, 15% secondary muscovite + calcite + quartz matrix

Minor opaques, calcite, chlorite

Hypidiomorphic granular, plagioclase with some primary micas. Large anhedral quartz.

Alteration: Some altered k-spar visible. Edges of micas partially altered to cc and chlorite. Secondary micas show radiating growth patterns interstitially, some kspar associated with this? Graphic intergrowth of plagioclase and quartz. The primary micas remaining are heavily dusted with f. g. opaques. Addition of quartz to matrix.

Metamorphic indicators: none

POLISHED SECTION: Isolated subhedral/euhedral arsenopyrite.

#11] NKRAN HILL - METAGREYWACKE

40% quartz, 10% plagioclase, 30% micaceous material, 5% chlorite, 5% quartz vein, 5% opaques

Minor tourmaline, calcite

Fine grained micaceous, medium grained quartz.

Alteration: Abundant calcite is subhedral. One opaque cube is 25% replaced with quartz, clay minerals, chlorite. Chlorite is brown and in random orientation.

Metamorphic indicators: Greenschist, one direction of foliation

Notes: Numerous opaques are pyrite or pyrrhotite with embayment of chlorite, quartz, and calcite. Quartz veins running through section has a core of sericitically altered plagioclase, plagioclase is An 5 or An 30 (albite or oligoclase)

POLISHED SECTION: Anhedral pyrrhotite. One large arsenopyrite with pyrite overgrowth and tiny core replacement by pyrrhotite.

#12] NKRAN HILL - PHYLLITE

20% quartz, 60% micaceous material, 10% chlorite (blue), 5% quartz vein, 5% opaques

Minor calcite, plagioclase

Fine grained

Metamorphic indicators: Micaceous material shows well developed lineation fabric many quartz grains aligned. Calcite occurs both as euhdral crystals and as anhedral crystals aligned with foliation. At least greenschist metamorphism (elongated quartz). Dextral shearing?

Notes: UID mineral, when axis N-S in plane light, colour is dark gray

#13] NKRAN HILL - PHYLLITE

30% quartz, 60% micaceous material, 2% tourmaline

Fine grained opaques, hematite (or Fe hydroxide?)

Fine grained

Alteration: Opaques heavily oxidized

Metamorphic indicators: Well aligned matrix of micaceous material and some quartz. There appears to once have been very large crystals now only visible in outline and replaced by clay minerals and tourmaline.
Matrix very dark with opaques, and some highly deformed quartz veins have fine grained, almost orange amorphous mineral interstitially along quartz microshears.

#14] NKRAN HILL - ? (Material disintegrated during creation of slide. Only recognizable features are recrystallized quartz and foliated micaceous material)

75% micaceous material, 20% quartz
Minor opaques
Fine grained

Notes: Intergrown quartz grains, equigranular, flooding some previous micaceous fabric. Thin section is full of holes. Highly strained? Could be quartz mica schist

#15] NKRAN HILL - GRANITOID

60% plagioclase (An 7 or An 28 - albite or oligoclase), 15% quartz, 25% matrix (70% quartz, 20% plagioclase, 5% Fe oxides?)
Minor calcite, rutile
Porphyritic aphanitic, subhedral quartz and plagioclase grains

Alteration: Large plagioclase grains (recrystallization on boundaries, moderately to highly sericitized) with some large quartz grains. Secondary growth on plagioclase seem to show no less alteration than original crystals. No remaining primary micas.
Metamorphic indicators: Moderate metamorphic effects, evidence of brittle deformation from secondary twinning in plagioclase (see sketch):

Notes: One corner of this section is solid micaceous matrix, well aligned, with abundant granular brown mineral. Small quartz veins run along fractures. UID granular amorphous brown crystals present as in [#2], [#33] (possible Fe oxide or ankerite)

#16] AYANFURI - GRANITOID

40% quartz, 30% plagioclase (An 5 or An 30 - albite or oligoclase), 20% secondary micas, 10% clay minerals + calcite
Minor rutile, occurs in clusters, opaques, kspar
Allotriomorphic granular, quartz rich rock with highly sutured margins on the grains. Some calcite is euhedral.

Alteration: Plagioclase shows little sericitization, replacing grains are much larger than in [#17]. Addition of quartz to matrix.
Metamorphic indicators: none

POLISHED SECTION: Subhedral pyrite with replacing anisotropic gray sulfides.

#17] AYANFURI - GRANITOID

50% plagioclase, 30% quartz, 10% muscovite, 10% clay minerals + calcite
Minor rutile, opaques, kspar
Allotriomorphic granular, quartz-rich rock, quartz grains have sutured margins, all crystals anhedral.

Alteration: plagioclase heavily sericitized (though some are notably clear of alteration) with several crystals homogenized by the alteration. All micas appear secondary, as in [#16]. Calcite forms in micaceous area along with small abundant rutile as in previously described, and in sercitized plagioclase.
Metamorphic indicators: Quartz grains have highly undulatory extinction

#32] NKRAN HILL - PHYLLITE

70% micaceous material, 10% quartz, 10% opaques, 10% albite vein (follows foliation)
Minor calcite
fine grained

Metamorphic indicators: Few larger elongated grains (quartz, opaques, plagioclase) in well lineated matrix of micas and dark brown granular masses (see [#2]), which are also elongate. Highly developed foliation (one direction). Opaques have pressure shadows.
Notes: Slide very thick, all quartz is yellow in colour.

#33] NKRAN HILL - PHYLLITE

70% micaceous material, 20% quartz, 10% opaques
Minor UID mineral as in [#2], opaque 'dust', chlorite (blue), Fe oxides
Medium grained with some larger crystals of quartz

Metamorphic indicators: High degree of foliation. Matrix lineated, large opaques show overgrowths of quartz and chlorite (blue) as in [6A], and are sometimes bordered by masses of both light brown and hematite. These are possible pressure shadows around sulfides, shown below:

Notes: Possibly slide too thick, as quartz is yellow colour.

#34] NHYIASO - GRANITOID

50% plagioclase (An 0 or An 33 - albite or andesine), 25% quartz, 20% secondary muscovite, 10% clay minerals + calcite
Minor opaques, opaque 'dust'
Porphyritic (?) or allotriomorphic granular, anhedral grains

Alteration: Large scale alteration and recrystallization. Only remaining large phenocrysts are quartz, which has been heavily recrystallized in matrix with serrated boundaries. Plagioclase has been completely sericitized, most micas are now clays and calcite.
Metamorphic indicators: Weak shear fabric.
Notes: Overall similar to [#17]

POLISHED SECTION: Subhedral pyrite with inclusions of anisotropic gray mineral and some chalcopyrite.

#35] NHYIASO - GRANITOID

40% quartz, 40% plagioclase (An 2 or An 32 - albite or andesine), 15% secondary micas
Minor opaques
Allotriomorphic granular, equigranular.

Alteration: Only secondary micas are present. Matrix looks as though it may be completely recrystallized. No development of sericite in plagioclase. No calcite present. Albite crystals forming interstitial to quartz grains.

Metamorphic indicators: Rock has been deformed, evidenced by crystal intergrowth, especially with quartz, which has strong undulatory extinction

POLISHED SECTION: Patches of subhedral/anhedral pyrite, arsenopyrite also subhedral but isolated from former. Aniso-gray mineral as replacement. Chalcopyrite minor and outside other sulfides.

#36] ANYANKYERIM - GRANITOID

50% quartz, 40% plagioclase (An 39 - andesine), 15% muscovite
Minor rutile, opaques, calcite
Hypidiomorphic granular. Largest crystals are quartz with smaller micas and plagioclase.

Alteration: Feldspars host large secondary muscovite, unlike sericite seen in other intrusives. Some recrystallization has occurred, though micas appear primary. Micas are 20% altered to clay minerals, occasionally patches of calcite are present. Quartz and plagioclase show strong graphic intergrowths, which are sites for greatest sericite development.

Metamorphic indicators: Micas and quartz show slight deformation, but no undulatory extinction in quartz

Notes: Overall similar to [#37] except more altered

#37] ANYANKYERIM - GRANITOID

40% quartz, 10% plagioclase (An 0 or An 33 - albite or andesine), 40% muscovite, 10% calcite
Minor rutile, opaques
Hypidiomorphic granular

Alteration: Feldspars host large secondary muscovites, unlike sericite seen in other intrusives. Some micas have altered to clay in large, isolated patches. Moderate calcite has developed in plagioclase and micas, sometimes as cement. Some micas, otherwise unaltered, show rims of clay. Addition of quartz to matrix.

Metamorphic indicators: Low degree of serration along quartz boundaries

POLISHED SECTION: Tiny, isolated subhedral arsenopyrite.

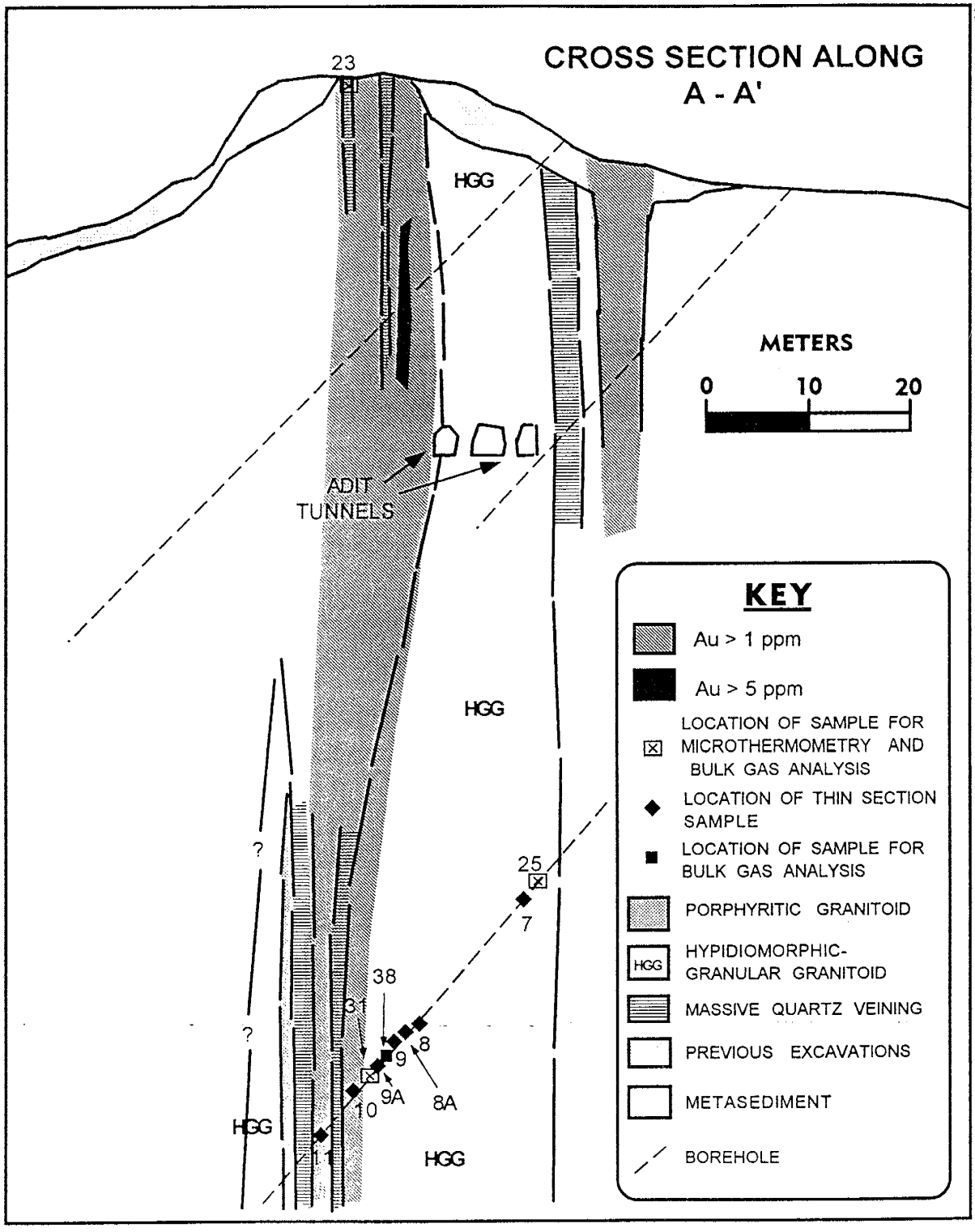
CROSS SECTION ALONG
A - A'
23
HGG
METERS
0
10
20
ADIT
TUNNELS
HGG
?
25
7
38
31
?
9
8
9A
8A
10
HGG
11
HGG
KEY
Au > 1 ppm
Au > 5 ppm
LOCATION OF SAMPLE FOR MICROTHERMOMETRY AND BULK GAS ANALYSIS
LOCATION OF THIN SECTION SAMPLE
LOCATION OF SAMPLE FOR BULK GAS ANALYSIS
PORPHYRITIC GRANITOID
HGG
HYPIDIOMORPHIC-GRANULAR GRANITOID
MASSIVE QUARTZ VEINING
PREVIOUS EXCAVATIONS
METASEDIMENT
BOREHOLE

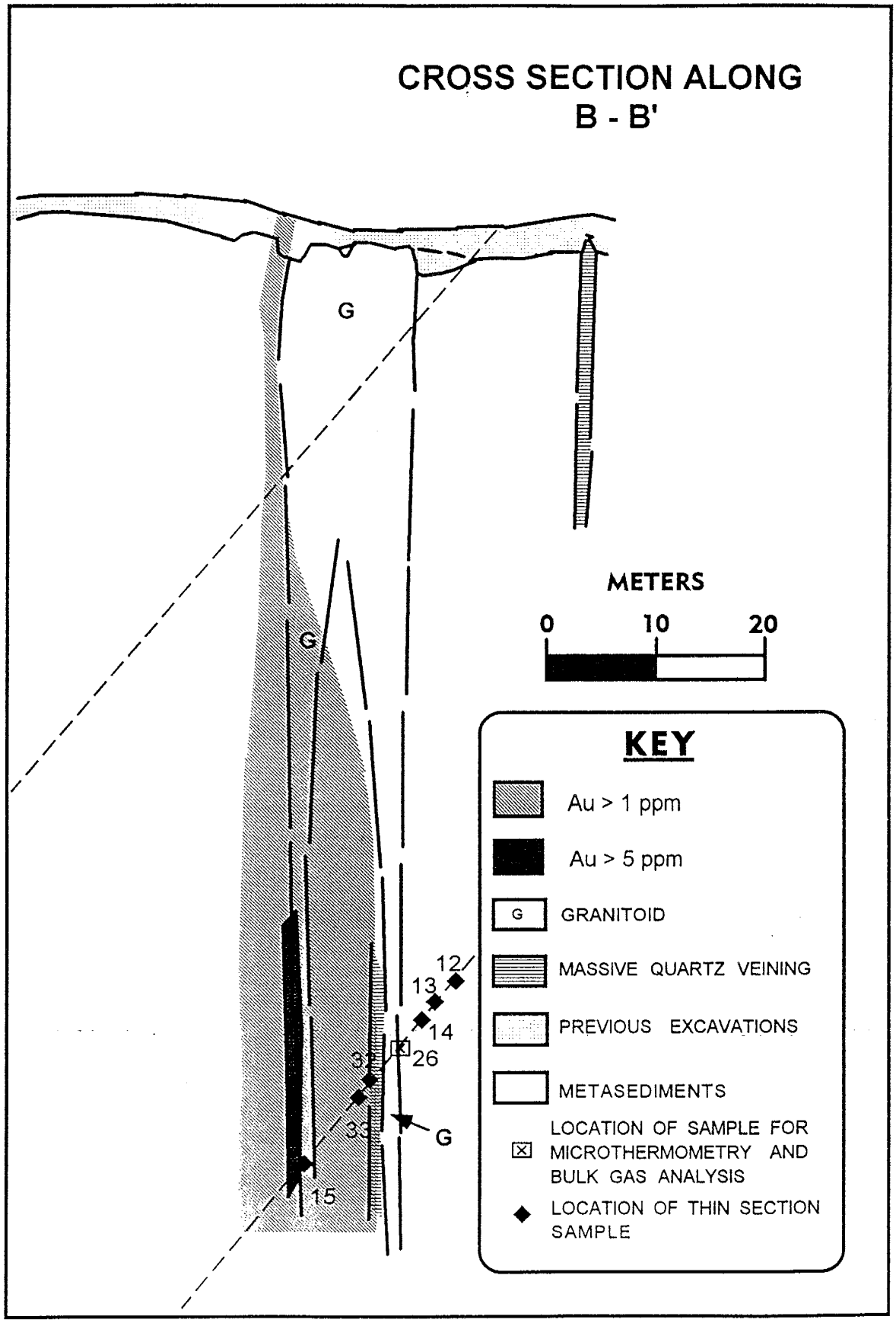
CROSS SECTION ALONG
B - B'
G
G
G
METERS
0
10
20
KEY
Au > 1 ppm
Au > 5 ppm
G
GRANITOID
MASSIVE QUARTZ VEINING
PREVIOUS EXCAVATIONS
METASEDIMENTS
LOCATION OF SAMPLE FOR MICROTHERMOMETRY AND BULK GAS ANALYSIS
LOCATION OF THIN SECTION SAMPLE
12
13
14
26
32
33
15

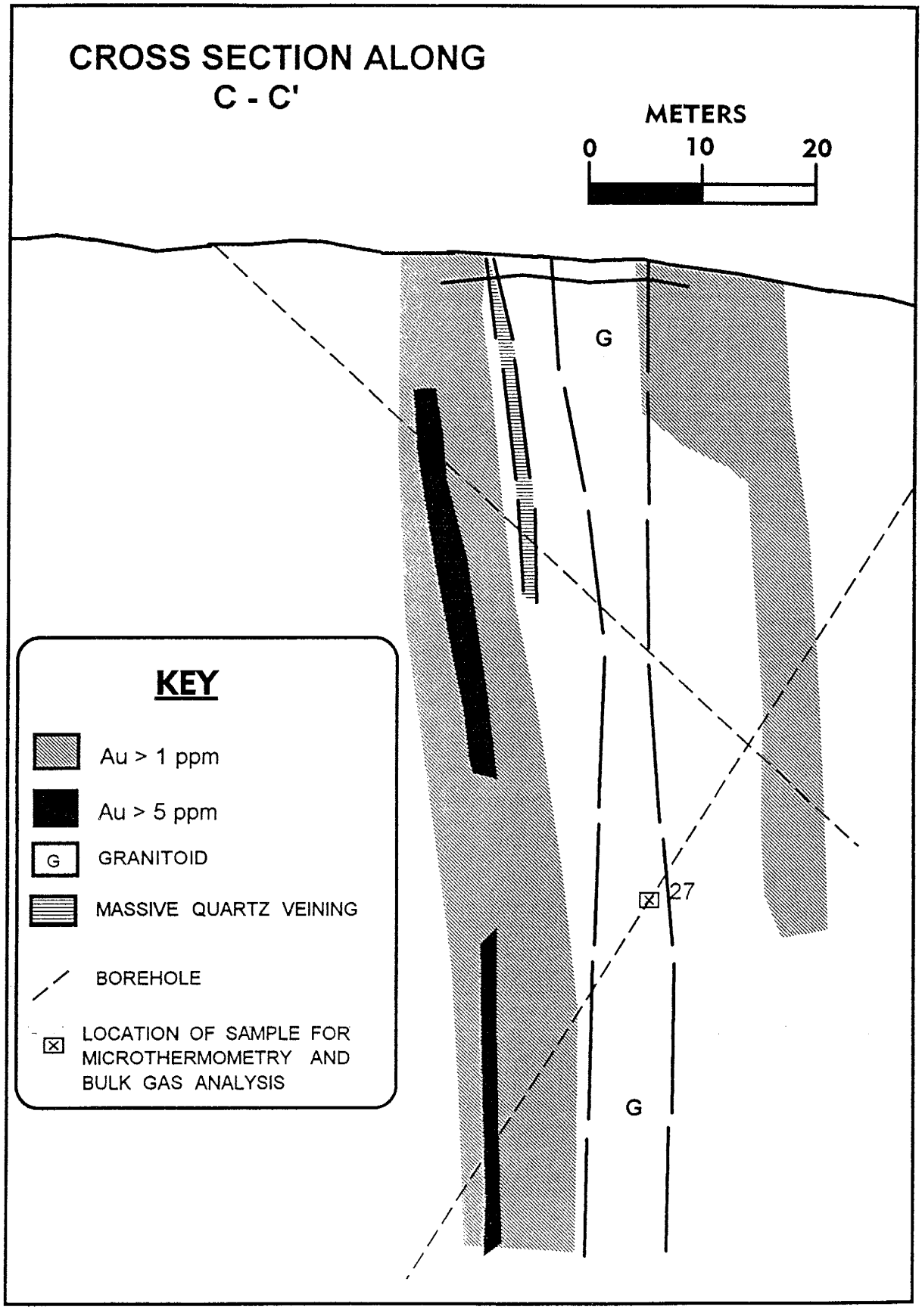
CROSS SECTION ALONG
C - C'
METERS
0
10
20
G
G
27
KEY
Au > 1 ppm
Au > 5 ppm
G
GRANITOID
MASSIVE QUARTZ VEINING
BOREHOLE
LOCATION OF SAMPLE FOR MICROTHERMOMETRY AND BULK GAS ANALYSIS

		CORRELATION LIST FOR ALL SAMPLES								
						polish	original	lab qtz	lab sulfide	
site	location	depth (m)	geochem #	f. i. #	thinsec #	sec #	gas an #	gas an #	gas an #	notes
Mmooho	Outcrop 6	0	90101	30	1					
Ayanfuri	S Esuajah	140	90102	16	16	16	16	5098		
Ayanfuri	Fetish pit	111	90103		17					
Nkran	RC 62	64	90105							
Nkran	RC 62	74	90106							
Nkran	DC 68	52		27			27	5020		qv
Nkran	DC 68	55	90107							wthrd ton
Nkran	DC 68	58		28						horz qv
Nkran	DC 25	71.5	90108		12					phyllite
Nkran	DC 25	76.3			13					defm phyllite
Nkran	DC 25	78.4	[NS 7]		14					defm mgwke
Nkran	DC 25	80.22	[NS 8]							
Nkran	DC 25	80.55	90109							wthrd ton
Nkran	DC 25	82.5		26			26	5026		qv
Nkran	DC 25	83.7			32					
Nkran	DC 25	87.7			33					
Nkran	DC 25	97			15					defm mgwke
Nkran	DC 6	158.25	90110		5					
Nkran	DC 6	158.9	90112	6	6	6	6S		5220	
Nkran	DC 6	159			6A	6A				contact zone
Nkran	DC 2	110.4	[NT 12]							
Nkran	DC 2	110.95	90113	2	2	2				
Nkran	DC 2	111.6	90114		3					
Nkran	DC 2	112.1	[NT 15]							
Nkran	DC 2	112.75	90115	4	4	4	4	5124		
Nkran	DC 22	81		25			25	5019		qv
Nkran	DC 22	81.5	90111A		7		7S			
Nkran	DC 22	98.05	90117	8	8	8				
Nkran	DC 22	101.9			8A					
Nkran	DC 22	103.9			9					
Nkran	DC 22	104.5					38	5097		8 g/ton Au
Nkran	DC 22	104.8	90131			9B				8 g/ton Au
Nkran	DC 22	106.2	90130	9A	9A	9A	9A	5125		
Nkran	DC 22	106.5		31			31	5096		qv in tonalite
Nkran	DC 22	108.7	90118	10	10	10	10S		5221	
Nkran	DC 22	111.5		11	11	11				
Nkran	T1A	trench		18			18	5092		
Nkran	T1B	trench		19			19	5093		
Nkran	T4A	trench		20			20,20S	5025	5099	20S - py in qv
Nkran	T9A	trench		21						
Nkran	T10A	trench		22			22	5100		
Nkran	T12A	trench		23			23	5094		
Nkran	T18A	trench		24						
Nkran	T3	trench		39			39	5027		Visible Au
Nkran	T9B	trench					40	5255		
Akwasiso	RC 74	25	90119							
Akwasiso	RC 74	39	90120							
Akwasiso	RC 74	79	90121							
Akwasiso	RC 74	119	90122							
Akwasiso	RC 75	82	[AK 8]							
Akwasiso	RC 76	132	90123							
Akwasiso	RC 76	133	[AK 10]							
Akwasiso	RC 76	134	90104A							
Akwasiso	T74	trench		29			29	5095		
Nhyiaso		61.66	90127		35	35				
Nhyiaso		130			34	34	34	5021		
Anyankyerim		24	90128		36	36				
Anyankyerim		236	90129		37	37				
* Note: Most drill holes are at 50 degrees, thus true depths are 1.4X less than shown										

APPENDIX B

Geochemical Analyses

SAMPLES BY LOCATION (Rejects excluded)

Sample	SiO2	Al2O3	Fe2O3	MgO	CaO	Na2O	K2O	TiO2	P2O5 (.01)	MnO(xrf)	Cr2O3	LOI %	C %	S %	Au (5)	As(xrf)	Mo(xrf)	Sb (.02)	La	Ce	Nd (5)	Sm	Eu (.2)	Yb (.2)	Lu (.05)	Sc	W (4)	Hf (1)	U (.5)	Zr
90101	72.21	15.13	1.76	0.33	0.37	3.72	4.86	0.21	0.24	0.009	0.039	1.2	0.05	0.01	t	t	17.8	0.5	25	54	28	3.9	0.5	t	t	1.6	4	3	5.1	100.6
Intrusive (Ayanfuri)																														
90102	68.13	14.69	4.3	0.84	1.97	4.44	2.35	0.34	0.1	0.031	0.029	3.1	0.8	0.63	686	539.3	15.1	7.1	10	18	10	1.4	0.5	0.2	t	4.5	5	3	t	108.3
90103	67.3	13.78	4.32	1.06	2.63	4.48	1.83	0.47	0.11	0.036	0.034	4.2	1.1	0.73	174	83.2	14	2.8	7	15	10	1.2	0.5	0.3	0.07	4.2	6	3	t	144.3
AVE	67.72	14.24	4.31	0.95	2.3	4.46	2.09	0.41	0.105	0.033	0.032	3.65	0.95	0.68	430	311.3	14.55	4.95	8.5	17	10	1.3	0.5	0.25	na	4.4	5.5	3	na	126.3
Intrusive (Akwasiso-unweathered)																														
90121	75.11	12.52	1.49	0.39	1.3	5.25	1.01	0.18	0.06	0.034	0.018	2.1	0.41	0.16	140	301.2	10	t	9	13	9	1.6	0.5	0.3	t	2.1	8	2	t	61.7
90122	73.1	13.93	1.38	0.39	1.06	6.64	0.85	0.13	0.02	0.023	0.02	1.7	0.39	0.27	1450	2136	19.7	t	6	7	6	0.9	t	0.3	t	1.7	81	t	t	53.19
90123	70.92	14.49	1.49	0.45	1.56	6.14	1.23	0.18	0.09	0.016	0.02	2.8	0.54	0.1	34	676.4	15.1	t	5	8	t	0.9	0.4	t	t	2.3	5	2	t	76.8
AVE	73.04	13.65	1.453	0.41	1.31	6.01	1.03	0.16	0.05667	0.024	0.019	2.2	0.45	0.18	541.33	1038	14.93	na	6.7	9.3	na	1.1	0.45	na	na	2	31	na	na	63.9
Intrusive (Nkran-unweathered)																														
90111A	68.13	16.06	2.28	0.58	1.38	7.82	0.92	0.19	0.08	0.024	0.02	2.25	0.53	0.39	324.5	4021	96.75	t	6.5	13	na	1	t	t	t	2	7	2.5	t	80.55
90112	66.06	14.18	5.35	0.89	1.97	5.3	1.75	0.33	0.06	0.056	0.027	3.1	0.88	0.73	1080	5470	17.2	t	11	14	7	1.6	0.6	0.8	0.1	6.1	9	3	t	99.72
90114	70.09	15.41	4.37	0.88	0.18	5.43	1.65	0.42	0.03	0.057	0.029	1.8	0.17	0.37	57	305.3	12.2	t	12	26	13	2.1	t	0.9	0.1	7.7	6	3	t	106.8
90115	68.05	15.04	3.93	0.96	1.4	5.28	1.85	0.36	0.04	0.041	0.022	3.4	0.59	0.61	62	242.3	8.8	t	10	19	6	1.7	0.6	0.8	0.12	6.2	5	2	1.7	101.4
90117	73.59	15.19	1.66	0.32	0.2	7.34	0.86	0.19	0.07	0.004	0.022	0.9	0.05	0.26	472	531.9	14.4	t	6	9	t	1	0.3	t	t	2.4	t	2	t	76.21
90118	71.68	14.43	2.33	0.55	0.9	5.88	1.52	0.21	0.05	0.019	0.039	1.5	0.36	0.3	391	3183	21.6	t	6	9	7	0.9	t	t	t	2.5	t	2	t	80.71
90130	70.67	14.19	3.31	0.6	1.44	6.38	1.12	0.19	0.1	0.027	0.029	1.9	0.58	0.32	448	2121	12.3	t	6	14	9	1	t	t	t	2.5	t	3	t	75.5
90131A	69.76	14.79	3.225	0.65	1.43	6.07	1.5	0.2	0.075	0.029	0.022	2.05	0.59	0.36	511.5	1701	12.7	t	7.5	13	8.5	1.3	t	t	t	3.1	t	2.5	t	85.15
AVE	69.75	14.91	3.307	0.69	1.11	6.19	1.4	0.26	0.06313	0.032	0.026	2.11	0.47	0.42	418.25	2197	24.49	na	8.1	15	na	1.3	na	na	na	4.1	na	2.5	na	88.25
Intrusive (Akwasiso-oxidized)																														
90119	68.15	19.6	2.9	0.29	0.01	0.12	2.19	0.37	0.05	0.012	0.018	6.4	0.05	0.01	108	533	8.4	t	17	35	33	6.1	1.5	1.5	0.23	8.5	6	4	1.8	107.7
90120	71.79	14.36	2.18	0.5	1.24	4.5	1.45	0.22	0.05	0.032	0.031	3	0.49	0.22	160	1660	18.9	t	20	11	24	5.2	1.6	0.8	0.09	2.6	100	1	t	74.77
AVE	69.97	16.98	2.54	0.4	0.63	2.31	1.82	0.3	0.05	0.022	0.025	4.7	0.27	0.12	134	1096	13.65	na	19	23	29	5.7	1.55	1.15	0.16	5.6	53	2.5	na	91.22
Intrusive (Nkran-oxidized)																														
90105	74.28	14.69	2.01	0.26	0.1	3.19	1.68	0.31	0.03	0.012	0.034	3.4	0.04	0.1	631	434.4	14.8	t	11	23	9	1.8	0.5	0.6	0.08	6	5	3	1.7	93.08
90106	70.66	15.3	2.95	0.35	0.14	4.57	2.07	0.37	t	0.059	0.034	3.6	1.8	0.69	830	2430	18.4	t	12	22	12	2	0.5	0.7	0.12	6.7	5	3	t	101.9
90107	69.28	19.39	2.01	0.28	0.01	0.11	2.14	0.28	t	0.002	0.024	6.8	0.06	0.03	144	720.1	18.5	0.4	10	22	15	3.2	1.1	1.3	0.22	4.6	10	4	1.5	108.3
90109	70.9	16.65	2.04	0.3	0.25	5.3	1.73	0.28	0.04	0.011	0.026	2.8	0.07	0.02	221	1284	11.2	t	8	14	11	1.9	0.6	0.4	0.07	2.9	10	2	1.5	98.27
AVE	71.28	16.51	2.253	0.3	0.13	3.29	1.91	0.31	na	0.021	0.03	4.15	0.49	0.21	456.5	1217	15.73	na	10	20	12	2.2	0.68	0.75	0.123	5.1	7.5	3	na	100.4
Metagreywacke (Nkran)																														
90104A	58.83	16.37	7.205	2.44	2.25	4.48	2.09	0.73	0.15	0.069	0.021	5.15	0.91	0.77	1035.5	3387	9.95	t	19	32	17	3	0.9	1.75	0.29	14	t	2.5	t	142.2
90110	55.01	14.64	10.53	1.91	5.13	2.87	3.04	0.9	0.16	0.17	0.034	5.7	2.03	1.29	679	1446	10.2	t	27	50	25	4.2	1.5	1.5	0.23	17	8	4	t	141.3
AVE	56.92	15.5	8.868	2.18	3.69	3.68	2.57	0.82	0.155	0.12	0.027	5.43	1.47	1.03	857.25	2417	10.08	na	23	41	21	3.6	1.2	1.63	0.26	16	na	3.3	na	141.7
Phyllite (Nkran)																														
90108	58.26	16.05	8.43	2.52	2.59	4.73	1.71	0.73	0.19	0.074	0.034	5	1.35	0.09	29	137.1	8.1	1.2	22	42	21	3.8	1.1	1.6	0.28	16	7	3	1.4	130.1
Intrusive (Nhyiaso)																														
90127	77.04	13.38	1.47	0.07	0.08	5.69	1.22	0.05	0.05	0.009	0.016	1	0.03	0.5	163	324.3	7.6	t	9	16	8	2	t	0.5	0.1	2.7	t	3	1.8	41.7
Intrusive (Anyankerim)																														
90128	70.76	14.78	3.64	0.52	1.66	2.49	3.55	0.23	0.08	0.033	0.034	2.1	0.54	0.19	764	352.9	15.7	0.2	24	43	16	2.7	0.8	0.4	0.06	2.3	t	4	4	131.6
90129	69.69	14.81	4.03	0.55	1.61	3.32	3.29	0.25	0.08	0.032	0.028	2.1	0.52	0.32	1340	594	13.7	0.6	27	49	16	3	0.9	0.6	0.13	2.7	t	4	5	140.9
AVE	70.23	14.8	3.835	0.54	1.64	2.91	3.42	0.24	0.08	0.033	0.031	2.1	0.53	0.26	1052	473.5	14.7	0.4	26	46	16	2.9	0.85	0.5	0.095	2.5	t	4	4.5	136.3

PRECISION (PRC 1 is 90104 and 90124) (PRC2 is 90111, 90116, and 90126 when present) (PRC3 is 90131 and 90137)

Sample	SiO2	Al2O3	Fe2O3	MgO	CaO	Na2O	K2O	TiO2	P2O5 (.01)	MnO(xrf)	Cr2O3	LOI %	C %	S %	Au (5)	As	Mo (5)	Sb (.02)	La	Ce	Nd (5)	Sm	Eu (.2)	Yb (.2)	Lu (.05)	Sc	W (4)	Hf (1)	U (.5)	Zr
PRC1	0.034	4E-04	5E-05	0	0	0	0.01	0	0.0002	3E-05	5E-07	0.01	0	0	706861	109.5	0.605		0	18	2	0	0	0.04	2E-04	0		0.5		2.856
PRC2	0.007	0.008	0.005	0	0	0	0	0	0.0002	0.001	5E-07	0.13	0	0	2964.5	471.2	0.845		4.5	2		0				0	2	0.5		0.963
PRCtot	0.021	0.004	0.003	0	0	0	0	0	0.0002	7E-04	5E-07	0.07	0	0	354913	290.4	0.725		2.3	10		0				0		0.5		1.91
PRC3	0.162	0.018	5E-04	0	0	0	0	0	0.00045	5E-07	5E-07	0.01	0	0	25765	691.9	0		0.5	0.5	13	0				0.1		0.5		0.605

V	Y	Sr	Rb	Ba	Cr	Nb	Pb	Ga	Zn	Cu	Ni	Sample
30.4	9.86	131.7	426.2	441.4	161.3	1.81	18.84	27.29	58.95	19.6	5.65	90101
												Intrusive (Ayanfuri)
48.8	5.42	338	70.38	422.8	152.5	1.44	8.04	23.35	48.57	31.7	14.24	90102
59.7	4.7	457.4	59.45	342.1	160.3	0.99	9.71	20.01	57.83	41.9	18.01	90103
54.3	5.06	397.7	64.92	382.5	156.4	1.215	8.875	21.68	53.2	36.8	16.13	AVE
												Intrusive (Akwasiso-unweathered)
24.9	4.01	457.5	26.96	295.2	95.4	0.37	9.12	15.32	25.85	19.5	7.5	90121
25.2	2.81	333.9	23.56	253.4	97.4	1.42	17.34	17.93	32.84	22.9	6.72	90122
24.6	2.5	681.4	34.43	378.2	102.5	t	6.57	18.29	32.15	9	10.88	90123
24.9	3.11	490.9	28.32	308.9	98.43	na	11.01	17.18	30.28	17.1	8.367	AVE
												Intrusive (Nkran-unweathered)
28.4	3.06	481.5	21.33	238.2	91.93	t	34.49	24.82	39.1	16.2	6.883	90111A
64.5	7.47	508.4	60.54	423.6	139.2	1.7	5.84	27.68	57.23	60	18.79	90112
72.7	10	382	52.52	386.1	148.4	1.83	8.46	21.49	130.7	27.8	72.29	90114
64.5	7.49	454.5	59.56	407.2	121.8	0.42	8.08	21.73	58.29	29.4	18.81	90115
29.3	3.51	305.1	19.08	266.5	105.5	t	9.69	19.72	30.54	40.6	9.38	90117
43.3	3.77	333.1	40.85	398.6	175	1.51	10.36	22.35	31.81	24.3	10.13	90118
38.7	3.6	433.7	30.3	350.6	202.6	t	14.7	21.8	37.9	37.5	9	90130
44.1	3.6	363.1	43.15	448	168.9	t	5.1	22.2	35.1	39	8.65	90131A
48.2	5.31	407.7	40.92	364.8	144.2	na	12.09	22.72	52.58	34.3	19.24	AVE
												Intrusive (Akwasiso-oxidized)
58.3	14.7	56.2	75.63	758.9	102.7	3.32	21.34	27.67	31.15	28	25.01	90119
37.2	7.73	326.3	45.09	406.5	150.4	0.65	21.02	20.84	37.97	24.6	14.39	90120
47.8	11.2	191.3	60.36	582.7	126.6	1.985	21.18	24.26	34.56	26.3	19.7	AVE
												Intrusive (Nkran-oxidized)
55.5	6.71	266.3	51.02	340.3	160.9	0.78	14.19	20.6	15.54	40.4	15.75	90105
70	8.81	330.4	63.98	427	196.7	1.47	9.38	23.86	71.88	42	122.2	90106
51.8	12.1	50.54	65.8	566.8	115.3	1.84	32.97	28.67	30.31	24.4	20.25	90107
36.5	8.37	315.4	46.35	329.8	120	1.02	27.44	25.49	45.48	9.8	17.53	90109
53.5	8.99	240.7	56.79	416	148.2	1.278	21	24.66	40.8	29.2	43.93	AVE
												Metagreywacke (Nkran)
144	19.3	508.1	70.68	498.1	153.4	4.45	13.45	21.94	94.13	37.2	41.31	90104A
188	15.1	577.8	98.11	554.3	216	4.16	5.43	20.72	80.85	79	34.05	90110
166	17.2	542.9	84.4	526.2	184.7	4.305	9.438	21.33	87.49	58.1	37.68	AVE
												Phyllite (Nkran)
139	17.6	422.6	55.17	397.9	237.9	3.95	4.02	19.05	79.66	37.2	47.69	90108
												Intrusive (Nhyiaso)
19.8	6.3	119.1	33.6	468	132	t	19.9	26.9	24.8	24.5	6.6	90127
												Intrusive (Anyankerim)
34.5	5.5	449	121	823.4	262.7	4.4	17.9	21.2	44.9	24	13	90128
29.4	6.6	488	113.8	897.7	223	4.5	16.2	23.5	49.9	21.4	11.1	90129
32	6.05	468.5	117.4	860.6	242.9	4.45	17.05	22.35	47.4	22.7	12.05	AVE

PRECISION

V	Y	Sr	Rb	Ba	Cr	Nb	Pb	Ga	Zn	Cu	Ni	Sample
3.92	0.01	2.808	0.205	0.605	1.28	139.1	5E-05	0.572	17.23	0.01	2E-04	PRC1
0.42	0.05	1.105	0.081	16.84	1.203		0.074	0.012	0.09	1	0.156	PRC2
2.17	0.03	1.957	0.143	8.724	1.242		0.037	0.292	8.659	0.5	0.078	PRCtot
2.42	0.18	0.125	0.005	118.6	1.28		1.28	0	0.98	8.41	6.125	PRC3

APPENDIX C

Major and Trace Element Correlation Tables

(Spearman correlations using StatMost for Windows)

Graphs of Element Correlations

Symbols:

Nkran-hg = hypidiomorphic granular intrusive

Nkran-pr = porphyritic intrusive

Spearman Correlation Table

	C %	S %	Au	Zr	V	Y
C %		0.5446 (17) 0.0238	0.1561 (16) 0.5637	0.4690 (17) 0.0575	0.5301 (17) 0.0286	-0.0424 (17) 0.8717
S %	0.5446 (17) 0.0238		0.0383 (16) 0.8880	0.3227 (17) 0.2065	0.5752 (17) 0.0157	0.2965 (17) 0.2478
Au	0.1561 (16) 0.5637	0.0383 (16) 0.8880		0.1559 (16) 0.5643	0.0397 (16) 0.8838	-0.0559 (16) 0.8370
Zr	0.4690 (17) 0.0575	0.3227 (17) 0.2065	0.1559 (16) 0.5643		0.6646 (17) 0.0036	0.5408 (17) 0.0250
V	0.5301 (17) 0.0286	0.5752 (17) 0.0157	0.0397 (16) 0.8838	0.6646 (17) 0.0036		0.5362 (17) 0.0265
Y	-0.0424 (17) 0.8717	0.2965 (17) 0.2478	-0.0559 (16) 0.8370	0.5408 (17) 0.0250	0.5362 (17) 0.0265	

	CaO	Na2O	K2O	Sr	Rb	Ba
CaO		-0.3973 (17) 0.1143	0.4231 (17) 0.0907	0.6426 (17) 0.0054	0.4500 (17) 0.0699	0.1827 (17) 0.4827
Na2O	-0.3973 (17) 0.1143		-0.8750 (17) 4.280E-006	-0.1127 (17) 0.6666	-0.8701 (17) 5.627E-006	-0.6618 (17) 0.0038
K2O	0.4231 (17) 0.0907	-0.8750 (17) 4.280E-006		0.0882 (17) 0.7363	0.9828 (17) 2.001E-012	0.7353 (17) 0.0008
Sr	0.6426 (17) 0.0054	-0.1127 (17) 0.6666	0.0882 (17) 0.7363		0.1005 (17) 0.7012	-0.0907 (17) 0.7292
Rb	0.4500 (17) 0.0699	-0.8701 (17) 5.627E-006	0.9828 (17) 2.001E-012	0.1005 (17) 0.7012		0.7696 (17) 0.0003
Ba	0.1827 (17) 0.4827	-0.6618 (17) 0.0038	0.7353 (17) 0.0008	-0.0907 (17) 0.7292	0.7696 (17) 0.0003	

Note: the values in the table are listed as follows:

correlation value
(sample size)
probability

Spearman Correlation Table

	Au	Pb	Zn	Cu	Ni
Au		0.1735 (16) 0.5204	0.0500 (16) 0.8541	0.2059 (16) 0.4443	-0.1235 (16) 0.6485
Pb	0.1735 (16) 0.5204		-0.1103 (17) 0.6735	-0.4436 (17) 0.0745	-0.5662 (17) 0.0178
Zn	0.0500 (16) 0.8541	-0.1103 (17) 0.6735		0.2010 (17) 0.4392	0.5588 (17) 0.0197
Cu	0.2059 (16) 0.4443	-0.4436 (17) 0.0745	0.2010 (17) 0.4392		0.4485 (17) 0.0709
Ni	-0.1235 (16) 0.6485	-0.5662 (17) 0.0178	0.5588 (17) 0.0197	0.4485 (17) 0.0709	

	Au	As	Mo	Sb	Sc	W
Au		0.4941 (16) 0.0517	0.4695 (16) 0.0666	-0.6000 (4) 0.4000	-0.1518 (16) 0.5746	0.6384 (9) 0.0642
As	0.4941 (16) 0.0517		0.7035 (16) 0.0024	0.0000 (4) 1.0000	-0.3154 (16) 0.2341	0.4682 (9) 0.2037
Mo	0.4695 (16) 0.0666	0.7035 (16) 0.0024		-0.5000 (5) 0.3910	-0.4982 (17) 0.0418	0.2346 (10) 0.5142
Sb	-0.6000 (4) 0.4000	0.0000 (4) 1.0000	-0.5000 (5) 0.3910		0.9000 (5) 0.0374	0.5000 (3) 0.6667
Sc	-0.1518 (16) 0.5746	-0.3154 (16) 0.2341	-0.4982 (17) 0.0418	0.9000 (5) 0.0374		-0.0677 (10) 0.8526
W	0.6384 (9) 0.0642	0.4682 (9) 0.2037	0.2346 (10) 0.5142	0.5000 (3) 0.6667	-0.0677 (10) 0.8526	

Note: the values in the table are listed as follows:

correlation value
(sample size)
probability

Spearman Correlation Table

	CaO	Na2O	K2O	P2O5 (.01)	Cr2O3	Au
CaO		-0.3973 (17) 0.1143	0.4231 (17) 0.0907	0.5234 (17) 0.0311	0.2526 (17) 0.3280	0.3355 (16) 0.2039
Na2O	-0.3973 (17) 0.1143		-0.8750 (17) 4.280E-006	-0.2966 (17) 0.2476	-0.4914 (17) 0.0452	-0.1176 (16) 0.6643
K2O	0.4231 (17) 0.0907	-0.8750 (17) 4.280E-006		0.3877 (17) 0.1241	0.6761 (17) 0.0029	0.1324 (16) 0.6251
P2O5 (.01)	0.5234 (17) 0.0311	-0.2966 (17) 0.2476	0.3877 (17) 0.1241		0.3952 (17) 0.1164	0.0769 (16) 0.7772
Cr2O3	0.2526 (17) 0.3280	-0.4914 (17) 0.0452	0.6761 (17) 0.0029	0.3952 (17) 0.1164		0.2173 (16) 0.4189
Au	0.3355 (16) 0.2039	-0.1176 (16) 0.6643	0.1324 (16) 0.6251	0.0769 (16) 0.7772	0.2173 (16)	

	SiO2	Al2O3	Fe2O3	MgO	MnO	Au
SiO2		-0.2305 (17) 0.3734	-0.8319 (17) 3.462E-005	-0.9171 (17) 2.226E-007	-0.6589 (17) 0.0040	-0.1369 (16) 0.6132
Al2O3	-0.2305 (17) 0.3734		0.2195 (17) 0.3973	0.0834 (17) 0.7502	-0.0515 (17) 0.8444	-0.0353 (16) 0.8968
Fe2O3	-0.8319 (17) 3.462E-005	0.2195 (17) 0.3973		0.8613 (17) 8.974E-006	0.7669 (17) 0.0003	0.1221 (16) 0.6522
MgO	-0.9171 (17) 2.226E-007	0.0834 (17) 0.7502	0.8613 (17) 8.974E-006		0.7796 (17) 0.0002	-0.0398 (16) 0.8838
MnO	-0.6589 (17) 0.0040	-0.0515 (17) 0.8444	0.7669 (17) 0.0003	0.7796 (17) 0.0002		-0.0500 (16) 0.8541
Au	-0.1369 (16) 0.6132	-0.0353 (16) 0.8968	0.1221 (16) 0.6522	-0.0398 (16) 0.8838	-0.0500 (16) 0.8541	

Note: the values in the table are listed as follows:

correlation value
(sample size)
probability

Spearman Correlation Table

	SiO2	CaO	TiO2	Zr	Y
SiO2		-0.7110 (17) 0.0014	-0.7582 (17) 0.0004	-0.6879 (17) 0.0023	-0.2613 (17) 0.3109
CaO	-0.7110 (17) 0.0014		0.4542 (17) 0.0671	0.5665 (17) 0.0177	-0.0429 (17) 0.8700
TiO2	-0.7582 (17) 0.0004	0.4542 (17) 0.0671		0.9053 (17) 5.847E-007	0.6326 (17) 0.0064
Zr	-0.6879 (17) 0.0023	0.5665 (17) 0.0177	0.9053 (17) 5.847E-007		0.5408 (17) 0.0250
Y	-0.2613 (17) 0.3109	-0.0429 (17) 0.8700	0.6326 (17) 0.0064	0.5408 (17) 0.0250	

Note: the values in the table are listed as follows:

correlation value
(sample size)
probability

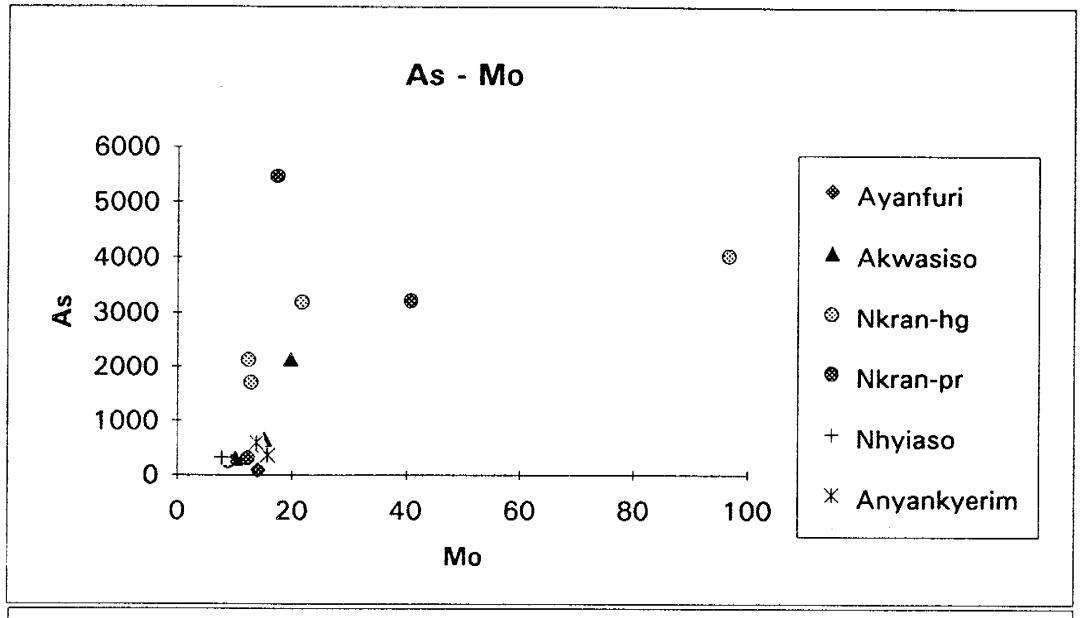
As - Mo
As
6000
5000
4000
3000
2000
1000
0
0
20
40
60
80
100
Mo
Ayanfuri
Akwasiso
Nkran-hg
Nkran-pr
Nhyiaso
Anyankyerim

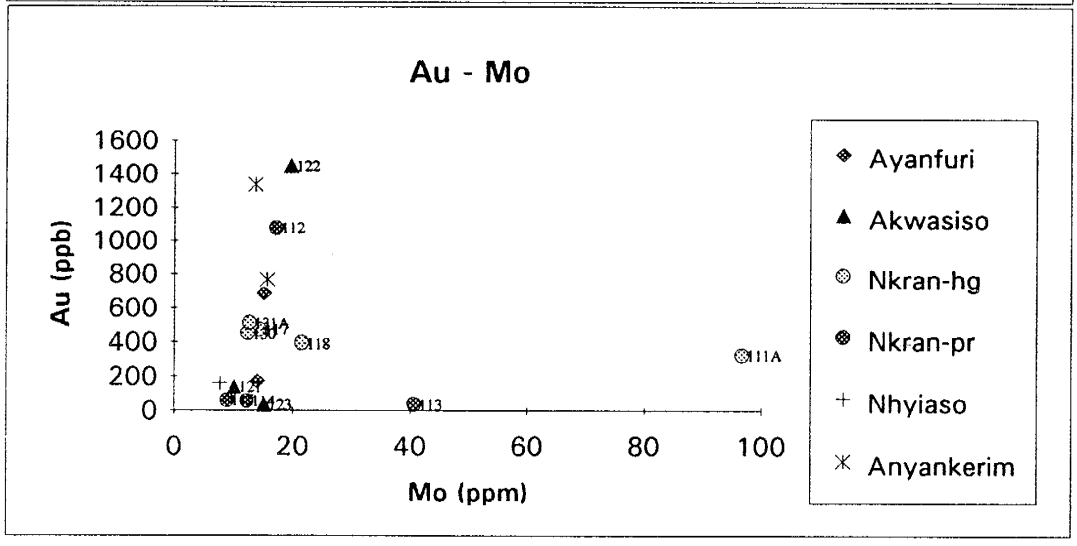
Au - Mo
Au (ppb)
1600
1400
1200
1000
800
600
400
200
0
0
20
40
60
80
100
Mo (ppm)
122
112
118
111A
113
123
Ayanfuri
Akwasiso
Nkran-hg
Nkran-pr
Nhyiaso
Anyankerim

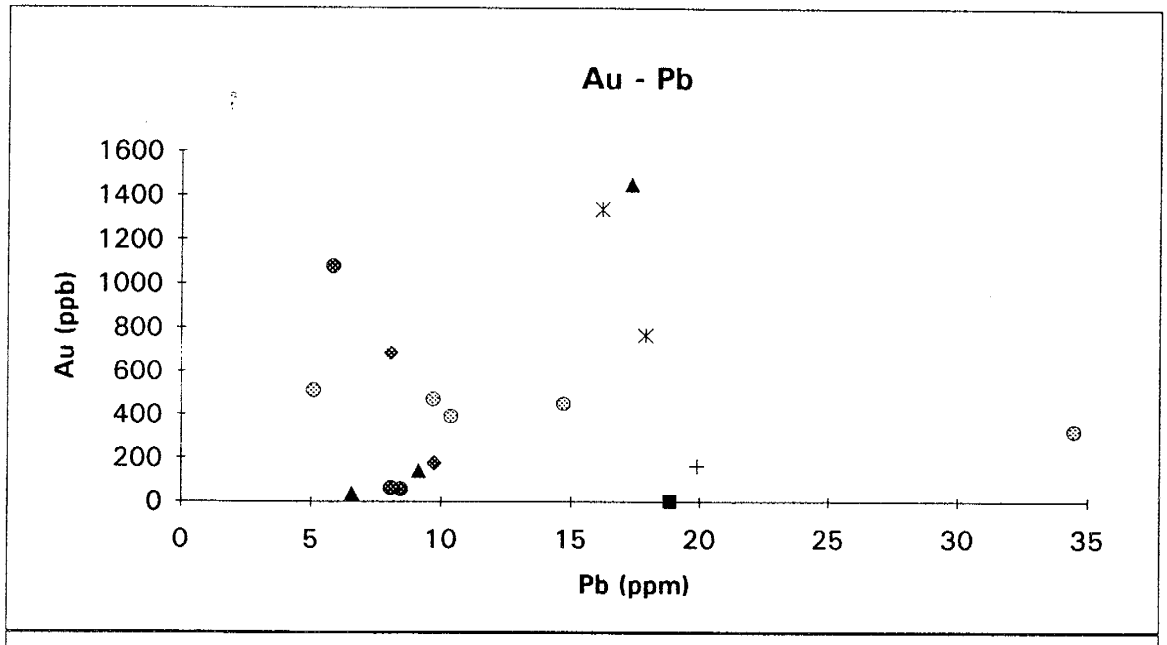
Au - Pb
Au (ppb)
1600
1400
1200
1000
800
600
400
200
0
0
5
10
15
20
25
30
35
Pb (ppm)

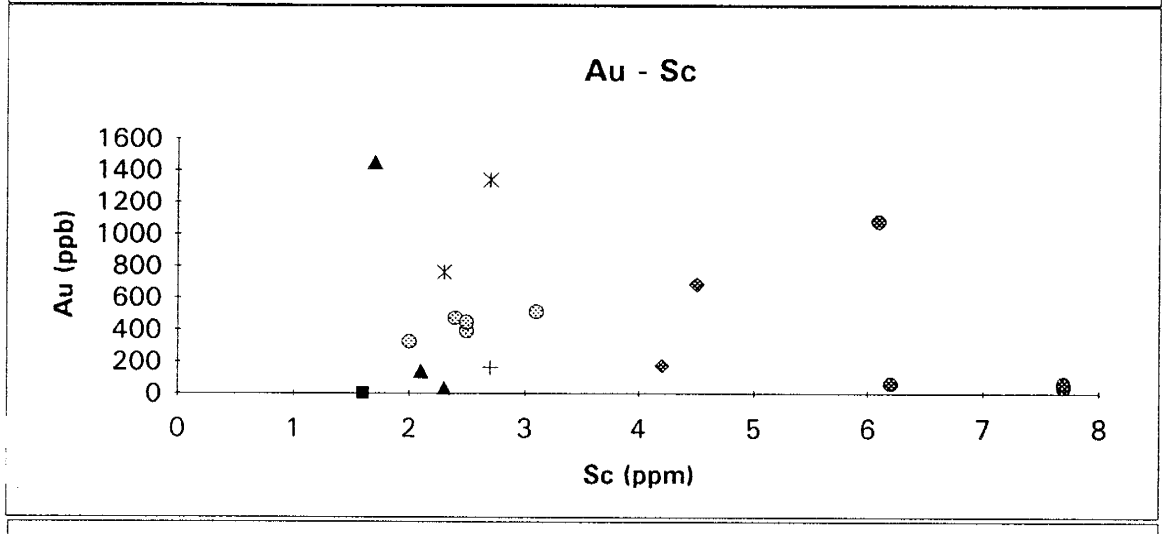
Au - Sc
Au (ppb)
1600
1400
1200
1000
800
600
400
200
0
0
1
2
3
4
5
6
7
8
Sc (ppm)

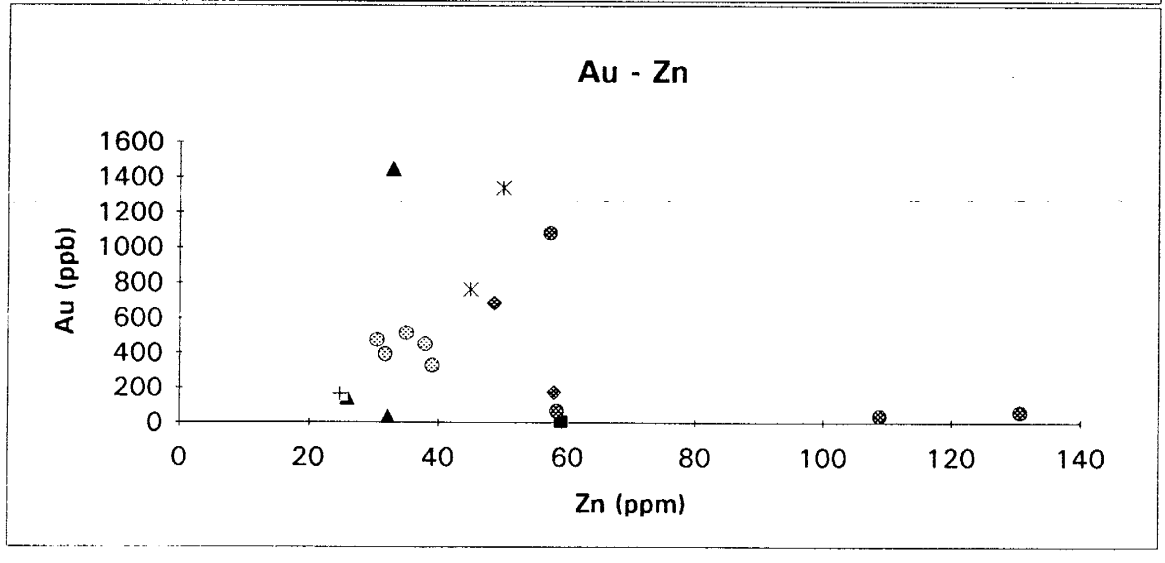
Au - Zn
Au (ppb)
1600
1400
1200
1000
800
600
400
200
0
0
20
40
60
80
100
120
140
Zn (ppm)

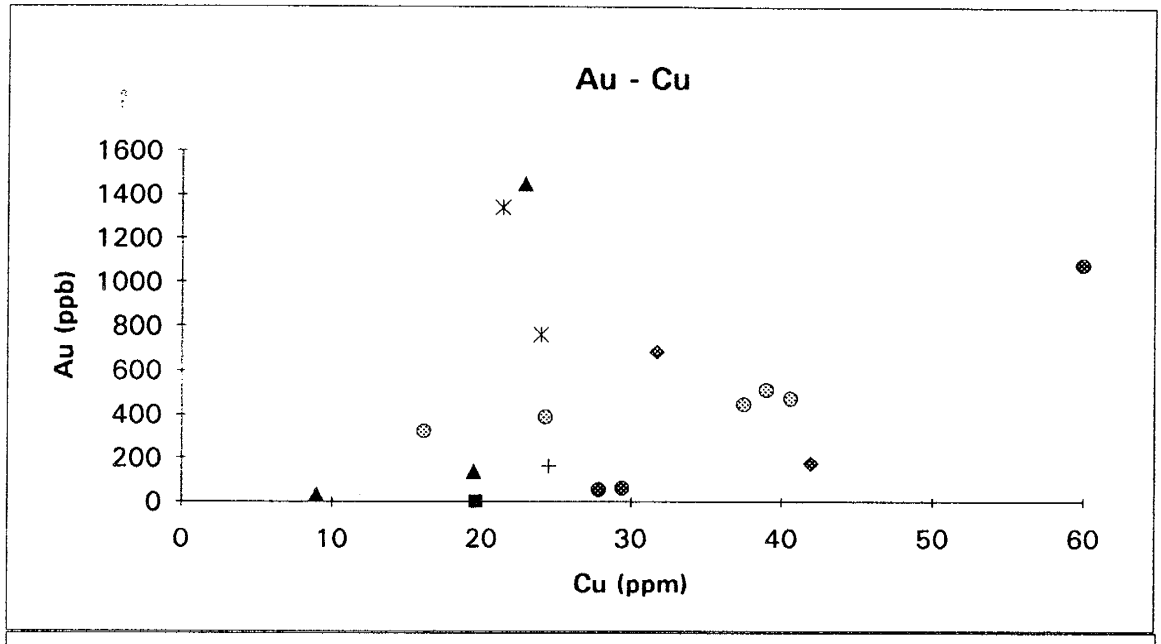
Au - Cu
Au (ppb)
1600
1400
1200
1000
800
600
400
200
0
0
10
20
30
40
50
60
Cu (ppm)

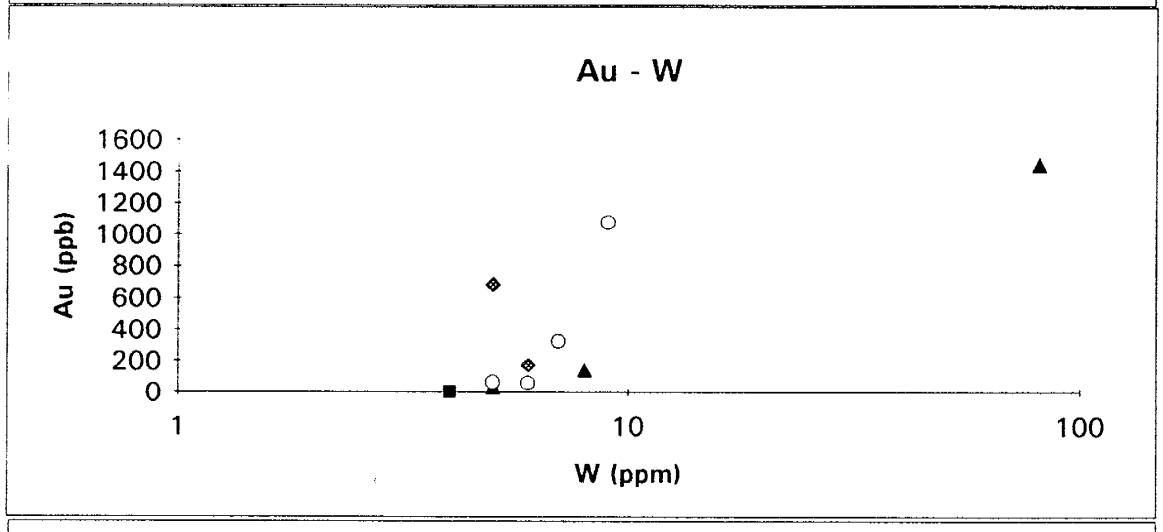
Au - W
Au (ppb)
1600
1400
1200
1000
800
600
400
200
0
1
10
100
W (ppm)

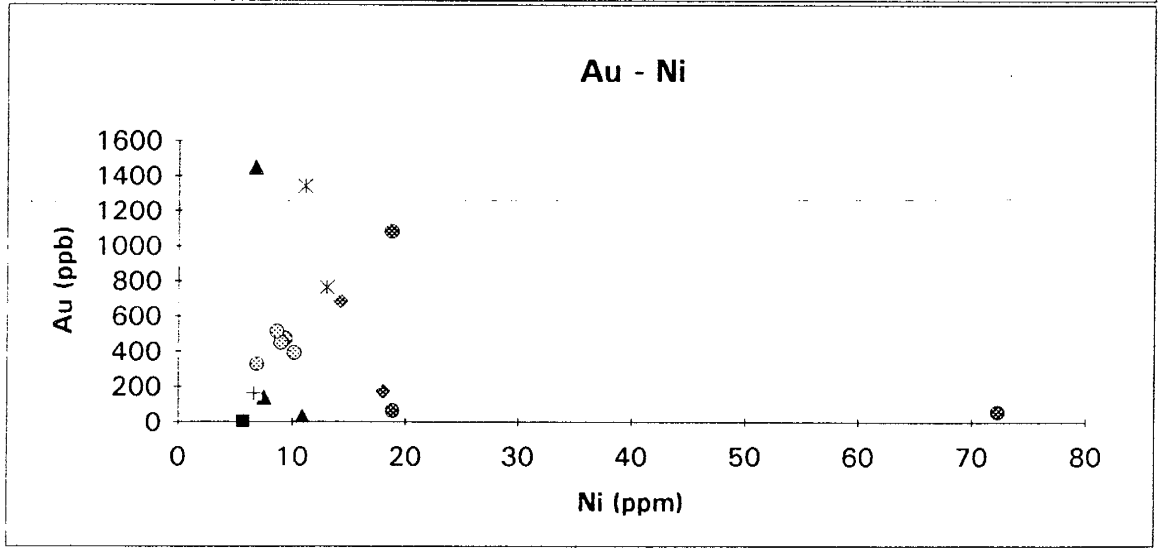
Au - Ni
Au (ppb)
1600
1400
1200
1000
800
600
400
200
0
0
10
20
30
40
50
60
70
80
Ni (ppm)

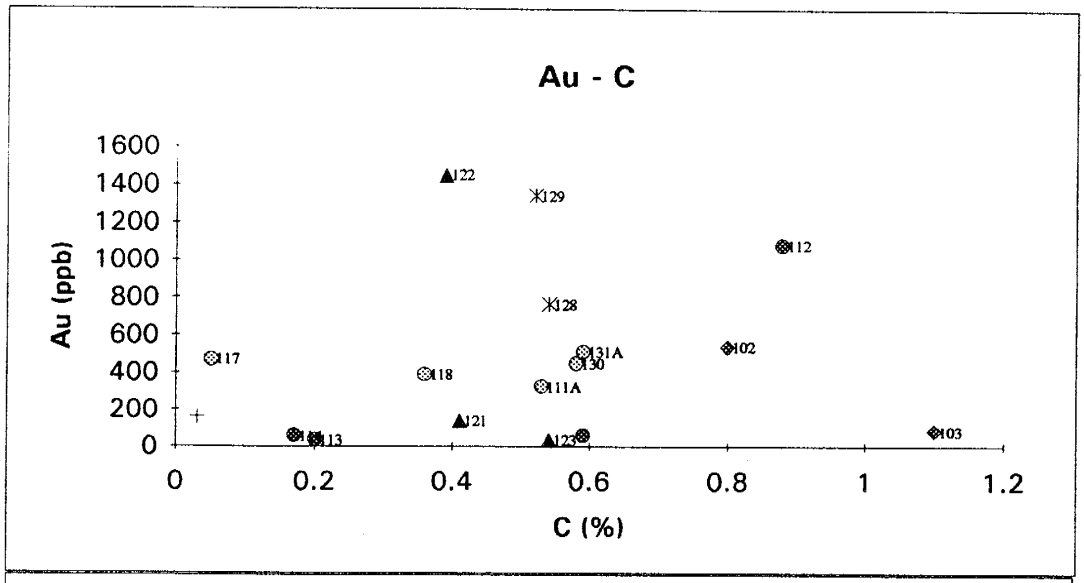
Au - C
Au (ppb)
C (%)
1600
1400
1200
1000
800
600
400
200
0
0
0.2
0.4
0.6
0.8
1
1.2
122
129
12
128
102
131A
130
111A
117
118
121
113
123
103

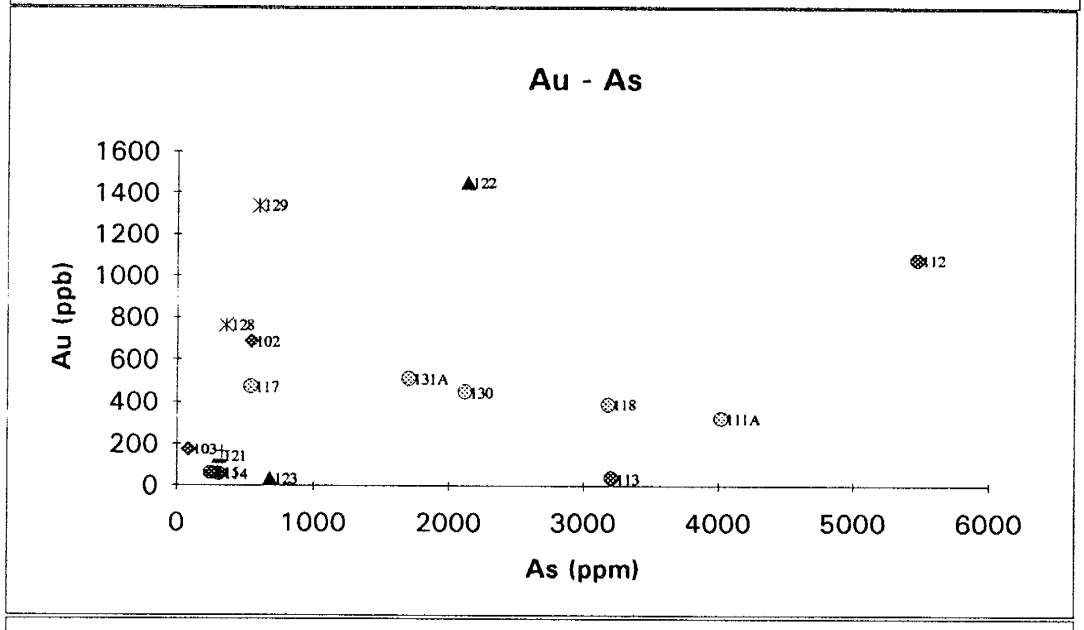
Au - As
Au (ppb)
As (ppm)
1600
1400
1200
1000
800
600
400
200
0
0
1000
2000
3000
4000
5000
6000
122
129
12
128
102
131A
130
117
118
111A
103
121
154
123
113

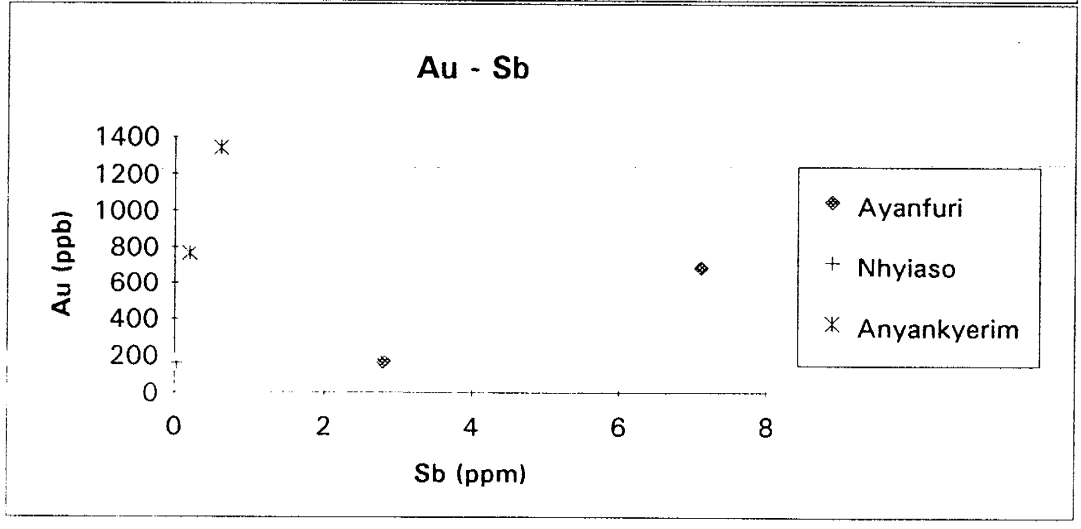
Au - Sb
Au (ppb)
Sb (ppm)
1400
1200
1000
800
600
400
200
0
0
2
4
6
8
Ayanfuri
Nhyiaso
Anyankyerim

APPENDIX D

Cross sections are shown for DC 22 (Nkran Hill) and RC 74 (Akwasiso Hill) with major element abundances with depth.

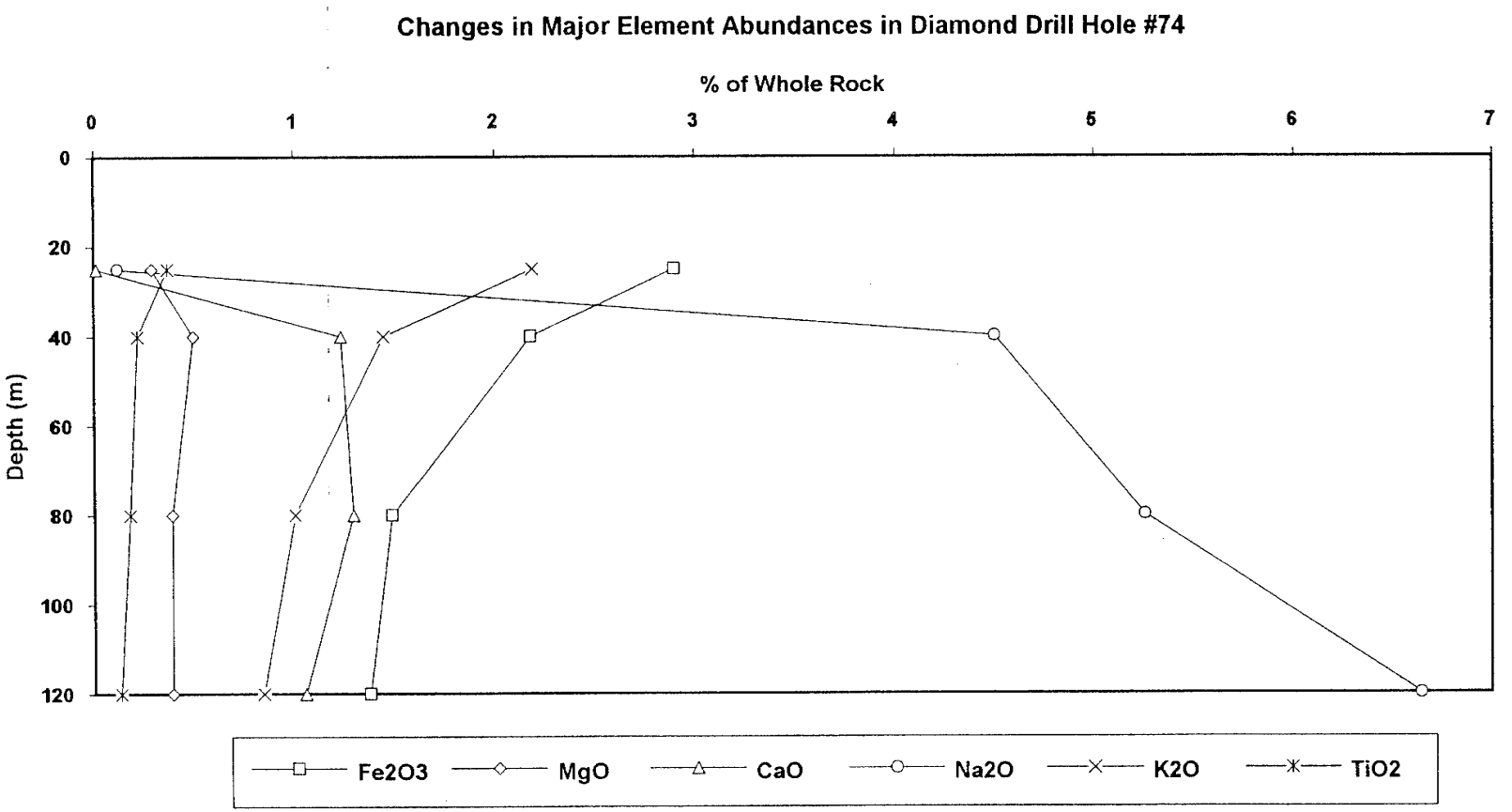
Changes in Major Element Abundances in Diamond Drill Hole #74
% of Whole Rock
0
1
2
3
4
5
6
7
Depth (m)
0
20
40
60
80
100
120
Fe2O3
MgO
CaO
Na2O
K2O
TiO2

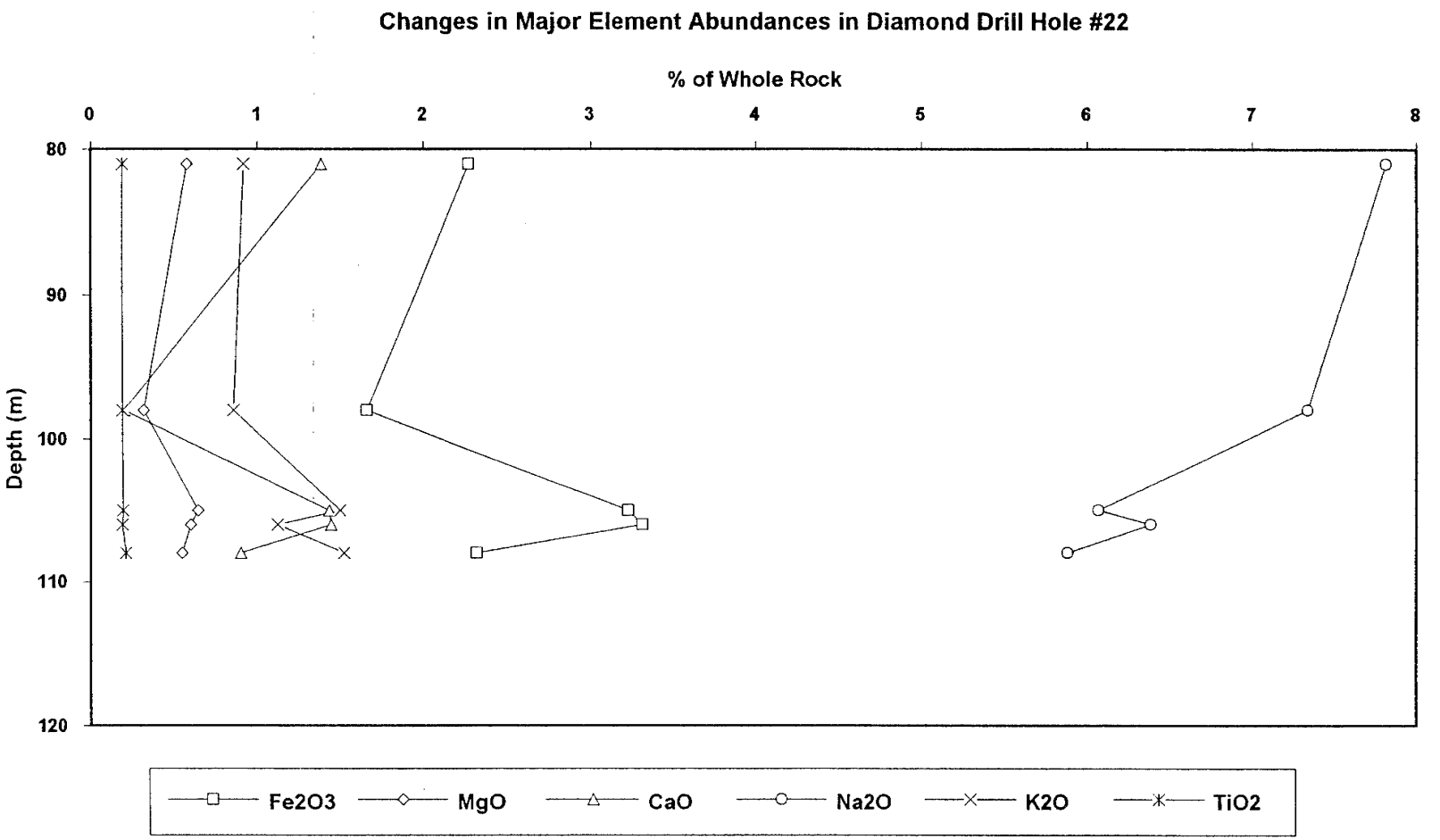
Changes in Major Element Abundances in Diamond Drill Hole #22
% of Whole Rock
0
1
2
3
4
5
6
7
8
Depth (m)
80
90
100
110
120
Fe2O3
MgO
CaO
Na2O
K2O
TiO2

APPENDIX E

Description and Output for the Deltas Model

(Renault, 1986)

This program calculates hypothetical igneous precursor compositions. It is based on the equations of F. G. Smith (1963) and linear relationships among the oxides of Daly (1933) average igneous rock compositions. First, the ratio of $Al_2O_3/(Al_2O_3 + Fe_2O_3t)$ is assumed to remain unchanged during transformations. Second, initial conditions are calculated from:

$$FeO = -0.7031 * Al_2O_3 + 0.6584 * (Al_2O_3 + Fe_2O_3t)$$
$$SiO_2 = e^{(1.247 * ratio + 3.264)}$$
$$TiO2 = e^{(3.59 + 5.482 * ratio)}$$

Second, iteration begins with calculation of cfm and alk:

$$cfm = 2.229 * (Al_2O_3 + Fe_2O_3t) - 2.383 * Al_2O_3$$
$$alk = 0.112 * (sil + cfm) - 0.1954 * cfm$$

where cfm is from a linear regression and alk is from Smith (1963).

FeO is calculated again from the equation above and then SiO_2, TiO_2, Al_2O_3, Fe_2O_3c, cfm, and alk are recalculated to the original sum.

Third, the iteration is repeated until successive values of SiO_2 are within a specified tolerance, usually 0.1%. When iteration is complete, the remaining oxides are calculated from:

$$MgO = -21.70 * ratio + 18.79$$
$$MnO = -3644 * ratio + 0.3846$$
$$CaO = cfm - FeO - MnO - MgO$$
$$Na_2O = 0.3727 * Al_2O_3 - 0.1111 * (Al_2O_3 + Fe_2O_3t)$$
$$K_2O = alk - Na_2O_3$$

The oxides are then recalculated to 100 % and mass balance is calculated by ratioing the hypothetical $Al_2O_3 + Fe_2O_3t$ to the analyzed concentrations and adjusting all the oxides by this ratio. Mass balance is calculated from Al + Fe when iteration is complete.

PROTOLITH BY SAMPLE NUMBER (by Deltas program, Renault, 1986)

	SiO2	Al2O3	Fe2O3	FeO	MgO	CaO	MnO	Na2O	K2O	TiO2
90101	75	13.33	1.08	0.43	0	1.57	0.06	3.31	4.96	0.26
90102	64.91	17.19	2.24	2.54	2	3.93	0.1	3.94	2.63	0.52
90103	63.94	17.32	2.35	2.8	2.27	4.27	0.11	3.93	2.46	0.56
90121	74.96	13.3	1.09	0.45	0	1.58	0.06	3.3	4.98	0.27
90122	76.08	12.49	0.95	0.26	0	1.48	0.05	3.13	5.31	0.24
90123	75.85	12.68	0.98	0.29	0	1.49	0.05	3.17	5.23	0.25
90111A	73.45	14.4	1.27	0.7	0	1.79	0.07	3.54	4.48	0.3
90117	75.43	13	1.03	0.36	0	1.53	0.06	3.24	5.1	0.26
90118	72.41	14.93	1.4	0.92	0.1	1.99	0.07	3.64	4.23	0.32
90130	68.01	16.51	1.88	1.8	1.19	2.97	0.09	3.89	3.23	0.43
90131A	68.86	16.27	1.78	1.61	0.98	2.75	0.09	3.86	3.41	0.4
90112	61.18	17.53	2.69	3.57	3.03	5.33	0.12	3.85	2.01	0.68
90113	59.81	17.54	2.87	3.98	3.43	5.91	0.13	3.78	1.8	0.75
90114	65.36	17.11	2.18	2.43	1.88	3.78	0.1	3.94	2.71	0.51
90115	66.5	16.89	2.05	2.15	1.58	3.41	0.1	3.93	2.93	0.47
90127	75.4	13.03	1.03	0.36	0	1.53	0.06	3.25	5.09	0.26
90128	67.29	16.7	1.96	1.96	1.38	3.18	0.09	3.91	3.08	0.45
90129	65.94	17.01	2.11	2.28	1.73	3.59	0.1	3.93	2.82	0.49
SB	71.11	15.47	1.54	1.13	0.42	2.23	0.08	3.74	3.92	0.35
VB	66.26	16.94	2.08	2.21	1.65	3.49	0.1	3.93	2.88	0.48

APPENDIX F

Fluid Inclusion Measurements

FLUID INCLUSION GROUPING BY INCLUSION TYPE									1) D and V of solid phase ignored						
(Excludes #29 Akwasiso sample)									2) D of gas phase in aqueous incl set = 0						
		Th(CO2)	Th(CO2)										Res	Bulk	
Type 1		l+v=l	l+v=l	Th(CO2)		Tm(clth)	incl					wt %	mol %	mol %	
	Tm(CO2)	w/ clth	w/o clth	l+v=v	Tm(H2O)	CO2	type	Th(to l)	Th(to v)	F	Td	NaCl	CH4	CH4	D gas
1B	-62.9			24.9		7.2	1(#31)		311	0.73		5.4	np		
2B	-61.2	8.4			-5.25	8.7	1(#31)			0.91	181.8	4.1	25		0.48
2C	-60.7			12.2	-5.15	8.7	1(#31)			0.87	267.4	4.1	np		
3D	-60.6	9.55			-4.1	10.35	1(#31)			0.90	187.7		24.3		0.44
1E	-60.5				-1.8	7.7	1(#23)			0.92					
2B	-61	-7.35				7.5	1(#23)			0.65	202		22.5		0.70
1E	-61.2					8.2	1(#26)			0.90					
2A	-60.4					8.7	1(#26)			0.76					
3C	-62.4		-9.85	-5.5		11.95	1(#27)			0.82	213		44		0.27
1A	-61.4			-24.5	-1.5	12.2	1(#20)			0.87	243		57		0.11
1B	-62	-15.1	-8.8			12.45	1s(#20)			0.79	203		28	?	0.71
1D	-62.1			-21.5		14.45	1(#20)			0.90	193		57		0.14
3B	-60.2		18.2	*0.1*		11	1(#20)			0.78	288		34		0.21
1A	-60.8	9.3				9.6	1(#22)		274	0.83					
1B	-61.2	8.6				10	1(#22)			0.82	192				
1C	-61.1	8.9				10	1(#22)			0.80	192				
1D	-60.7	8.9				9.2	1(#22)			0.84	192				
1E	-61	8.8				9.9	1(#22)			0.86	174				
2D	-61.4			-9.3		10.6	1(#22)			0.90	258.5		24.8		0.69
2A	-58.7	10.9			-4.25	8.9	1s(#25)			0.85	191.8	2.2	11.5		0.67
2C	-59.1	9.2			-4.55	9.6	1(#25)			0.82	234.2	0.7	13.5		0.71
2D	-58.2	9.7			-4.45	8.9	1(#25)	267.4		0.75		2.2	8.5		0.74
3C	-59.6	12.25			-4.7	9.65	1(#31)			0.90	187.7	0.7	17.4		0.55
3A	-58.8	10.1	4.55			10.5	1(#23)		343	0.92			11.6	17	0.70
3C	-58.5	9.6	-8.9			11.85	1(#23)		338	0.91			10	28	0.74
4A	-58.1	9.7	0.4			11.05	1(#23)			0.76	182		8	15	0.76
4B	-58.5	5.35	-7.7			12.05	1(#23)			0.76	187		10	23	0.78
4C	-58.4	9.6	-7.6			12.15	1(#23)			0.89	182		9.5	25	0.74
4D	-58.5	9	-10			12.35	1(#23)			0.70	190		8	27	0.76
4A	-56.8					10	1(#26)		323	0.76			*2*		0.87
2A	-61.2		-9.95			12.35	1(#27)			0.85	278				
3A	-57.2		20.1			11.15	1(#26)	257		0.81			*4*		0.86
5A	-62.7		13.45			9.65	1(#23)			0.92	251.5		np		
5D	-63	9.75				13.7	1(#23)			0.59	241.5		np		
3A	-63.2		-10.1	-6.3	-4.2	11.95	1(#27)			0.92	278		40		0.41
1A	-65.4		-10.1			13.15	1s(#18)			0.93	102				
1C	-64.1		-20.5			14.15	1(#18)		303	0.90					
1D	-63.7		-4.9			13.15	1(#18)			0.94	218				
2A	-63.4	-19.6				15.2	1(#18)			0.74	214		*43*		0.46
2B	-63.3			-9.7		15.2	1s(#18)			0.84	256		42		0.45
2C	-63.4		-11.9	-12.2		13.5	1(#18)			0.78	259		43		0.46
2F	-63.6					14.9	1(#18)			0.76	238		*44*		0.47
1A	-67			*1.5*		15.5	1(#19)		**349.8**	0.78					
1B	-66.5			-19.7		13.4	1(#19)			0.79	285		*76*		
1E	-66.4					15.8	1(#19)			0.76	227.4				
1G	-68.1					13.6	1(#19)	305.6		0.85					
2A	-64.7			-30.4		14	1(#19)			0.75	236.4		68		0.25
2D	-65.6					15.1	1(#19)			0.86	269.4				
2E	-63.7			-23.9		13.6	1(#19)	315.4		0.75			64		0.19
1A	-67.5	10.4	8.1			10.6	1(#39)			0.68	252				
1A	-64.4	7.25				10.5	1(#27)	>323		0.93					
Type 2p															
2B					*-0.7?*		2a(#20)	204		0.89		1.22			0
2A					-3.8	11.25	2a(#20)			0.91	248	*5.7*			0
2C					-3.7	*11.85*	2a(#20)			0.93	248	*5*			0
2D					-3.3	*12.35*	2a(#20)			0.86	253	*4.4*			0
1A					-6.15		2a(#31)			0.92	202	9.4			0
1D					-5.55		2a(#31)	222.1		0.88		8.6			0

1F					-4.3		2as(#39)	227		0.97		6.87			0
1G					-5.1		2as(#39)			0.95	198	8			0
2A					-3.1		2a(#39)			0.95	232	5			0
1B					-8.35		2a(#25)	no		0.96		12.1			0
3E					-4.1		2a(#31)	325.5		0.86		7.5			0
1C					-4.1		2a(#26)	326		0.96		6.58			0
1D							2a(#26)	308		0.95					0
2B					-2.8		2a(#27)	274		0.91		4.63			0
2A					-4.3		2a(#22)			0.95	258.5	6.87			0
1B					-2.8		2a(#39)	257.5		0.94		4.63			0
Type 2ps															
2B				*17.9?*	-3.95		2b(#25)	157.1		0.88		6.4	?		0
2A					-4.35		2b(#31)			0.94	151.6	6.9			0
3C					-1.35		2b(#26)	175		0.92		2.3			0
2B					-2.4		2b(#22)	130.3		0.97		4.01			0
1C					0		2bs(#20)	152		0.94		0			0
3A					-2.7		2bs(#20)	182		0.94		4.48			0
3D					-2.6		2b(#20)	167		0.99		4.32			0
3E					-1.35		2b(#20)	129		0.97		2.31			0
2A							2b(#23)	181		0.97					0
3B					-3.05	*9.6?*	2b(#26)	236		0.80		0.7			
Type 2L															
3C					-4.2		3c(#20)	na	na	1		6.72			0
2E					-4.5		3c(#18)	na	na	1		7.1			0
Type 3a															
3B	-59.3						3a(#31)	6.3		1			14		0.69
5B	-64						3a(#23)	9.75		1			*47*		
3B	-61.2						3a(#27)	-2.55		1			25		0.62
3D	-61.2						3a(#27)	2.85		1			26.6		0.51
1F	-66.1					na	3a(#19)	-34.7		1			*56*		
1H	-65.8					na	3a(#19)	-23.5		1			*56*		
3F	-60.5						3a(#20)	5.50		1			22.5		0.57
1C	-68.9						3a(#39)	5.5		1			*69*		
1D	-69.7						3a(#39)	1.3		1			*72*		
1B	close to -56.6				-5.3		3a(#26)	-21.60		1		8.27			
Type 3b															
1C	-67.6						3b(#31)		-7.9	1			*80*		
5C	-62.5						3b(#23)		21.4	1			*60*		
Type 4															
1B	-57.4						4(#26)			?					
Chip # 9A															
1A					-4.6		2a(#9A)			0.89	277	7.3			
1B					-4.6		2a(#9A)	296.8		0.83		7.3			
2A					-3.7		2a(#9A)	290.8		0.94		6			
2B					-4.2		2a(#9A)	297.8		0.98		6.7			
2D					-4.4		2a(#9A)	328.5				7			
2E					-2		2a(#9A)	292				3.4			
2F					-4.2		2a(#9A)				261	6.7			

FINAL STAT VALUES BY INCLUSION TYPE

TYP 1		Th(CO2) l+v=l	Th(CO2) l+v=l	Th(CO2)		Tm(clth)					wt %	Res mol %	Bulk mol %	
	Tm(CO2)	w/ clth	w/o clth	l+v=v	Tm(H2O)	CO2	Th(to l)	Th(to v)	F	Td	NaCl	CH4	CH4	D
AVG	-61.8	6.226	-3.075	-8.879	-3.995	11.481	286.3	320.2	0.82	220.8	2.77	29.33	22.5	0.92
SD	2.744	8.329	11.3448	15.22	1.2945	2.3246	28.58	26.58	0.08	40.45	1.81	21.14	5.36	0.05
REL SD	0.044	1.338	3.68937	1.715	0.324	0.2025	0.1	0.083	0.1	0.183	0.65	0.721	0.24	0.06
MEDIAN	-61.2	9.2	-8.25	-9.5	-4.35	11.15	286.5	322.9	0.83	215.8	2.2	24.8	24	0.94
MODE	-61.2	8.9	-10.05	#N/A	#N/A	8.7	#N/A	#N/A	0.85	192	4.1	44	#N/A	#N/A
RANGE	11.3	31.85	40.55	55.3	3.75	8.6	58.65	75.8	0.35	185.8	4.7	74	13	0.18
n	51	23	18	14	10	51	4	7	51	36	7	29	6	28

TYPE 2		Th(CO2) l+v=l	Th(CO2) l+v=l	Th(CO2)		Tm(clth)					wt %	Res mol %	Bulk mol %	
	Tm(CO2)	w/ clth	w/o clth	l+v=v	Tm(H2O)	CO2	Th(to l)	Th(to v)	F	Td	NaCl	CH4	CH4	D
AVG					-3.617	11.817	215		0.93	224	5			0.97
SD					1.7266	0.5508	64.76		0.04	37.05	2.84			0.04
REL SD					0.4773	0.0466	0.301		0.05	0.166	0.53			0.04
MEDIAN					-3.7	11.85	204		0.94	240	5			0.98
MODE					-4.3	#N/A	#N/A		0.94	247.8	5			1.00
RANGE					8.35	1.1	197		0	107	12			0
n					23	3	17		26	8	24			23

TYP 3a		Th(CO2) l+v=l	Th(CO2) l+v=l	Th(CO2)		Tm(clth)					wt %	Res mol %	Bulk mol %	
	Tm(CO2)	w/ clth	w/o clth	l+v=v	Tm(H2O)	CO2	Th(to l)	Th(to v)	F	Td	NaCl	CH4	CH4	D
AVG	-64.1				-5.3		-5		1		8	43		0.68
SD	3.777				0		15.54		0		0	21.58		0.06
REL SD	0.059				0		3.038		0		0	0.5		0.09
MEDIAN	-64				-5.3		2		1		8	47		0.68
MODE	-61.2				#N/A		5.5		1		#N/A	56		#N/A
RANGE	10.4				0		44		0		0	58		0.14
n	9				1		10		10		1	9		4

TYPE 3b		Th(CO2) l+v=l	Th(CO2) l+v=l	Th(CO2)		Tm(clth)					wt %	Res mol %	Bulk mol %	
	Tm(CO2)	w/ clth	w/o clth	l+v=v	Tm(H2O)	CO2	Th(to l)	Th(to v)	F	Td	NaCl	CH4	CH4	D
AVG	-65.1							7	1			70		
SD	3.606							20.72	0			14.14		
REL SD	0.055							3.069	0			0.202		
MEDIAN	-65.1							7	1			70		
MODE	#N/A							#N/A	1			#N/A		
RANGE	5.1							29	0			20		
n	2							2	2			2		

FLUID INCLUSION GROUPING BY VEIN TYPE															
		Th(CO2)	Th(CO2)										Res	Bulk	
SUB-V		l+v=l	l+v=l	Th(CO2)		Tm(clth)	incl					wt %	mol %	mol %	
Typ	Tm(CO2)	w/ clth	w/o clth	l+v=v	Tm(H2O)	CO2	type	Th(to l)	Th(to v)	F	Td	NaCl	CH4	CH4	D gas
1A	-61.4			-24.5	-1.5	12.2	1(#20)			0.87	243		57		0.11
1B	-62	-15.1	-8.8			12.45	1s(#20)			0.79	203		28	?	0.71
1D	-62.1			-21.5		14.45	1(#20)			0.90	193		57		0.14
3B	-60.2		18.2	*0.1*		11	1(#20)			0.78	288		34		0.21
1B	-66				-3.8	14.8	1(#29)	230.5		0.87					
3A	-65.5				-1.6	15.25	1(#29)	210.6		0.89					
4A	-60.2					12.55	1(#29)		318.9	0.58					
4B	-60.1					11.25	1(#29)		317.9	1					
Type 2p															
2B					*-0.77*		2a(#20)	204		0.89		1.22			0
2A					-3.8	11.25	2a(#20)			0.91	248	*5.7*			0
2C					-3.7	*11.85*	2a(#20)			0.93	248	*5*			0
2D					-3.3	*12.35*	2a(#20)			0.86	253	*4.4*			0
2A					-3		2a(#29)	218.4		0.92		4.94			
5C					-0.05		2a(#29)		307.9	0.7		0.09			
Type 2ps															
1C					0		2bs(#20)	152		0.94		0			0
3A					-2.7		2bs(#20)	182		0.94		4.48			0
3D					-2.6		2b(#20)	167		0.99		4.32			0
3E					-1.35		2b(#20)	129		0.97		2.31			0
Type 3a															
3F	-60.5						3a(#20)	5.50		1			22.5		0.57
Type 2L															
3C					-4.2		3c(#20)	na	na	1		6.72			0
		Th(CO2)	Th(CO2)										Res	Bulk	
V		l+v=l	l+v=l	Th(CO2)		Tm(clth)	incl					wt %	mol %	mol %	
Typ	Tm(CO2)	w/ clth	w/o clth	l+v=v	Tm(H2O)	CO2	type	Th(to l)	Th(to v)	F	Td	NaCl	CH4	CH4	D gas
1E	-60.5				-1.8	7.7	1(#23)			0.92					
2B	-61	-7.35				7.5	1(#23)			0.65	202		22.5		0.70
1A	-60.8	9.3				9.6	1(#22)		274	0.83					
1B	-61.2	8.6				10	1(#22)			0.82	192				
1C	-61.1	8.9				10	1(#22)			0.80	192				
1D	-60.7	8.9				9.2	1(#22)			0.84	192				
1E	-61	8.8				9.9	1(#22)			0.86	174				
2D	-61.4			-9.3		10.6	1(#22)			0.90	258.5		24.8		0.69
3A	-58.8	10.1	4.55			10.5	1(#23)		343	0.92			11.6	17	0.70
3C	-58.5	9.6	-8.9			11.85	1(#23)		338	0.91			10	28	0.74
4A	-58.1	9.7	0.4			11.05	1(#23)			0.76	182		8	15	0.76
4B	-58.5	5.35	-7.7			12.05	1(#23)			0.76	187		10	23	0.78
4C	-58.4	9.6	-7.6			12.15	1(#23)			0.89	182		9.5	25	0.74
4D	-58.5	9	-10			12.35	1(#23)			0.70	190		8	27	0.76
5A	-62.7		13.45			9.65	1(#23)			0.92	251.5		np		
5D	-63	9.75				13.7	1(#23)			0.59	241.5		np		
1A	-65.4		-10.1			13.15	1s(#18)			0.93	102				
1C	-64.1		-20.5			14.15	1(#18)		303	0.90					
1D	-63.7		-4.9			13.15	1(#18)			0.94	218				
2A	-63.4	-19.6				15.2	1(#18)			0.74	214		*43*		0.46
2B	-63.3			-9.7		15.2	1s(#18)			0.84	256		42		0.45
2C	-63.4		-11.9	-12.2		13.5	1(#18)			0.78	259		43		0.46
2F	-63.6					14.9	1(#18)			0.76	238		*44*		0.47
1A	-67			*1.5*		15.5	1(#19)		349.8	0.78					
1B	-66.5			-19.7		13.4	1(#19)			0.79	285		*76*		
1E	-66.4					15.8	1(#19)			0.76	227.4				
1G	-68.1					13.6	1(#19)	305.6		0.85					
2A	-64.7			-30.4		14	1(#19)			0.75	236.4		68		0.25
2D	-65.6					15.1	1(#19)			0.86	269.4				
2E	-63.7			-23.9		13.6	1(#19)	315.4		0.75			64		0.19
1A	-67.5	10.4	8.1			10.6	1(#39)			0.68	252				
Type 2p															
1F					-4.3		2as(#39)	227		0.97		6.87			0
1G					-5.1		2as(#39)			0.95	198	8			0

2A					-3.1		2a(#39)			0.95	232	5			0
2A					-4.3		2a(#22)			0.95	258.5	6.87			0
1B					-2.8		2a(#39)	257.5		0.94		4.63			0
Type 2ps															
2B					-2.4		2b(#22)	130.3		0.97		4.01			0
2A							2b(#23)	181		0.97					0
Type 3a															
5B	-64						3a(#23)	9.75		1			*47*		
1F	-66.1					na	3a(#19)	-34.7		1			*56*		
1H	-65.8					na	3a(#19)	-23.5		1			*56*		
1C	-68.9						3a(#39)	5.5		1			*69*		
1D	-69.7						3a(#39)	1.3		1			*72*		
Type 3b															
5C	-62.5						3b(#23)		21.4	1			*60*		
Type 2L															
2E					-4.5		3c(#18)	na	na	1		7.1			0
		Th(CO2)	Th(CO2)										Res	Bulk	
HORZ		l+v=l	l+v=l	Th(CO2)		Tm(clth)	incl					wt %	mol %	mol %	
Typ	Tm(CO2)	w/ clth	w/o clth	l+v=v	Tm(H2O)	CO2	type	Th(to l)	Th(to v)	F	Td	NaCl	CH4	CH4	D gas
1B	-62.9			24.9		7.2	1(#31)		311	0.73		5.4	np		
2B	-61.2	8.4			-5.25	8.7	1(#31)			0.91	181.8	4.1	25		0.48
2C	-60.7			12.2	-5.15	8.7	1(#31)			0.87	267.4	4.1	np		
3D	-60.6	9.55			-4.1	10.35	1(#31)			0.90	187.7		24.3		0.44
1E	-61.2					8.2	1(#26)			0.90					
2A	-60.4					8.7	1(#26)			0.76					
3C	-62.4		-9.85	-5.5		11.95	1(#27)			0.82	213		44		0.27
2A	-58.7	10.9			-4.25	8.9	1s(#25)			0.85	191.8	2.2	11.5		0.67
2C	-59.1	9.2			-4.55	9.6	1(#25)			0.82	234.2	0.7	13.5		0.71
2D	-58.2	9.7			-4.45	8.9	1(#25)	267.4		0.75		2.2	8.5		0.74
3C	-59.6	12.25			-4.7	9.65	1(#31)			0.90	187.7	0.7	17.4		0.55
4A	-56.8					10	1(#26)		323	0.76			*2*		0.87
2A	-61.2		-9.95			12.35	1(#27)			0.85	278				
3A	-57.2		20.1			11.15	1(#26)	257		0.81			*4*		0.86
3A	-63.2		-10.1	-6.3	-4.2	11.95	1(#27)			0.92	278		40		0.41
1A	-64.4	7.25				10.5	1(#27)	>323		0.93					
Type 2p															
1A					-6.15		2a(#31)			0.92	202	9.4			0
1D					-5.55		2a(#31)	222.1		0.88		8.6			0
1B					-8.35		2a(#25)	no		0.96		12.1			0
3E					-4.1		2a(#31)	325.5		0.86		7.5			0
1C					-4.1		2a(#26)	326		0.96		6.58			0
1D							2a(#26)	308		0.95					0
2B					-2.8		2a(#27)	274		0.91		4.63			0
Type 2ps															
2B				*17.9?*	-3.95		2b(#25)	157.1		0.88		6.4	?		0
2A					-4.35		2b(#31)			0.94	151.6	6.9			0
3C					-1.35		2b(#26)	175		0.92		2.3			0
3B					-3.05	*9.6?*	2b(#26)	236		0.80		0.7			
Type 3a															
3B	-59.3						3a(#31)	6.3		1			14		0.69
3B	-61.2						3a(#27)	-2.55		1			25		0.62
3D	-61.2						3a(#27)	2.85		1			26.6		0.51
1B	*-56.6*				-5.3		3a(#26)	-21.60		1		8.27			
Type 3b															
1C	-67.6						3b(#31)		-7.9	1			*80*		
Type 4															
1B	-57.4						4(#26)			?					

STATS BY VEIN TYPE														
		Th(CO2)	Th(CO2)									Res	Bulk	
SUB VERTICAL		l+v=l	l+v=l	Th(CO2)		Tm(clth)					wt %	mol %	mol %	
	Tm(CO2)	w/ clth	w/o clth	l+v=v	Tm(H2O)	CO2	Th(to l)	Th(to v)	F	Td	NaCl	CH4	CH4	Dbulk
Type 1 av	-62.47	-15.1	4.7	-15.3	-2.3	12.994	220.6	318.4	0.83	231.4		44		0.89
Type 1 sd	2.377		19.09	13.4209	1.3	1.6306	14.07	0.707	0.12	43.41		15.21		0.05
Type 1 low	-66		-8.8	-24.5	-3.8	11	210.6	317.9	0.58	192.5		28		0.83
Type 1 hi	-60.1		18.2	0.1	-1.5	15.25	230.5	318.9	1	287.8		57		0.94
n	7	1	2	3	3	8	2	2	8	4		4		4
Type 2 av					-2.278	11.817	175	308	0.90	249	3.25			0.96
Type 2 sd					1.466	0.5508	32.88		0.08	2.887	2.15			0.05
Type 2 low					-3.8	11.25	129		0.70	248	0			0.88
Type 2 hi					0	12.35	218		0.99	253	5.7			1.03
n					9	3	6	1	10	3	10			8
Type 3a av	-60.5						5.5		1			22.5		0.57
Type 3a sd														
Type 3a low														
Type 3a hi														
n	1						1		1			1		1
		Th(CO2)	Th(CO2)									Res	Bulk	
VERTICAL		l+v=l	l+v=l	Th(CO2)		Tm(clth)					wt %	mol %	mol %	
	Tm(CO2)	w/ clth	w/o clth	l+v=v	Tm(H2O)	CO2	Th(to l)	Th(to v)	F	Td	NaCl	CH4	CH4	Dbulk
Type 1 av	-62.6	6.07	-4.58	-14.814	-1.8	12.215	310.5	321.5	0.81	217.5		32.29	22.5	0.91
Type 1 sd	2.926	8.346	9.517	10.6371		2.3435	6.93	32.17	0.09	41.26		23.79	5.36	0.06
Type 1 low	-68.1	-19.6	-20.5	-30.4		7.5	305.6	274	0.59	102		8	15	0.79
Type 1 hi	-58.1	10.4	13.45	1.5		15.8	315.4	349.8	0.94	285		76	28	0.98
n	31	15	12	7	1	31	2	5	31	23		15	6	14
Type 2 av					-3.667		199		0.96	229.5	5.9			1
Type 2 sd					1.052		55.5		0.01	30.33	1.57			0.02
Type 2 low					-5.1		130.3		0.94	198	4.01			0.97
Type 2 hi					-2.4		257.5		0.97	258.5	8			1.02
n					6		4		7	3	6			6
Type 3a av	-66.9						-8.33		1			60		
Type 3a sd	2.351						19.6					10.32		
Type 3a low	-69.7						-34.7					47		
Type 3a hi	-64						9.75					72		
n	5						5		5			5		
		Th(CO2)	Th(CO2)									Res	Bulk	
HORIZONTAL		l+v=l	l+v=l	Th(CO2)		Tm(clth)					wt %	mol %	mol %	
	Tm(CO2)	w/ clth	w/o clth	l+v=v	Tm(H2O)	CO2	Th(to l)	Th(to v)	F	Td	NaCl	CH4	CH4	Dbulk
Type 1 av	-60.49	9.607	-2.44	6.325	-4.581	9.8	262.1	317	0.84	224.3	2.77	19.02		0.94
Type 1 sd	2.149	1.625	15.03	15.0418	0.429	1.484	7.531	8.415	0.07	40.86	1.81	14.31		0.03
Type 1 low	-64.4	7.25	-10.1	-6.3	-5.25	7.2	256.8	311	0.73	181.8	0.7	2		0.87
Type 1 hi	-56.8	12.25	20.1	24.9	-4.1	12.35	267.4	322.9	0.93	277.8	5.4	44		0.97
n	16	7	4	4	8	16	2	2	16	9	7	10		10
Type 2 av					-4.375		253		0.91	176.8	6.51			0.97
Type 2 sd					1.945		66.02		0.05	35.64	3.34			0.04
Type 2 low					-8.35		157.1		0.8	151.6	0.7			0.92
Type 2 hi					-1.35		326		0.96	202	12.1			1.05
n					10		8		11	2	10			9
Type 3a av	-59.58				-5.3		-3.75		1		8.27	21.87		0.69
Type 3a sd	2.176						12.44		0			6.86		0.07
Type 3a low	-61.2						-21.6		1			14		0.61
Type 3a hi	-56.6						6.3		1			26.6		0.75
n	4				1		4		4		1	3		3

APPENDIX G

Principle and Organic Gas Data

PROPORTIONS OF PRINCIPLE GASES BY GAS ANALYSIS (CRUSH)

	He %	CH4 %	H2O %	N2 %	H2S %	Ar %	CO2 %	CnHn %	SO2 %
18 5092A	0	13.60	42.45	16.29	0.00215	0.04426	27.15698	0.44147	0.00105
18 5092D	0	7.16	59.53	13.42	0.00318	0.02557	19.64339	0.19112	0.00105
18 5092F	0	4.79	68.96	9.88	0.00322	0.02149	16.13602	0.18806	0.00117
19 5093C	0	9.51	62.57	8.83	0.00123	0.01353	18.98916	0.06477	0.00137
19 5093E	0	9.31	58.71	9.34	0.00132	0.0145	22.54871	0.05859	0.0014
19 5093F	0	9.69	57.29	9.43	0.00218	0.01459	23.48513	0.06464	0.00215
19 5093G	0	8.84	61.47	9.63	0.00123	0.01395	19.97827	0.05567	0.00166
23 5094C	0	2.68	64.05	6.76	0.00097	0.01451	26.43424	0.0474	0.00144
23 5094D	0	1.94	62.18	8.32	0.00169	0.01578	27.49738	0.03004	0.00091
23 5094E	0	1.70	70.75	6.32	0.001	0.01069	21.16339	0.03941	0.00109
23 5094G	0	1.01	84.05	3.33	0.001	0.00712	11.55968	0.0223	0.00091
29 5095C	0	17.67	37.14	22.54	0.00086	0.05219	22.22765	0.34499	0.00121
29 5095D	0	17.24	37.57	25.34	0.0008	0.07008	19.30202	0.45119	0.00066
29 5095G	0	20.39	39.67	22.95	0.00049	0.04007	16.63655	0.28222	0.00069
31 5096B	0	3.65	66.32	9.05	0.00073	0.01629	20.76744	0.17235	0.00094
31 5096C	0	1.61	71.47	8.33	0.00109	0.01924	18.43734	0.11429	0.00078
31 5096D	0	1.56	64.84	7.64	0.00086	0.01231	25.87756	0.06437	0.00079
31 5096F	0	4.15	67.05	7.72	0.00068	0.01739	20.7838	0.26227	0.00095
38 5097B	0	1.08	78.01	4.73	0.0004	0.00665	16.16608	0.0074	0.0007
38 5097C	0	0.92	83.12	4.47	0.00019	0.00509	11.46856	0.01035	0.00088
38 5097H	0.00019	0.80	85.19	4.44	0.00024	0.00607	9.54747	0.01159	0.00098
16 5098E	0	2.22	60.35	7.53	0.00033	0.02116	29.73637	0.11754	0.00072
16 5098F	0	0.99	63.15	5.54	0.00032	0.01771	30.24496	0.04589	0.00042
16 5098H	0	3.40	54.87	12.89	0.00049	0.03218	28.6136	0.17457	0.00075
20S 5099A	0.03527	6.59	84.83	6.25	0.0001	0.01307	2.1939	0.07236	0.00011
20S 5099B	0.05177	5.17	88.27	5.35	0.00012	0.0081	1.11016	0.02239	0.00009
22 5100D	0	3.47	62.12	4.03	0.0009	0.01488	30.26258	0.07247	0.00073
22 5100G	0	2.16	77.56	1.85	0.0005	0.00567	18.3913	0.01977	0.00086
22 5100H	0	2.87	72.18	3.03	0.00078	0.01361	21.8417	0.05611	0.00104
25 5019A	0	1.58	58.31	11.08	0.00405	0.02368	28.86915	0.09092	0.00151
25 5019B	0	0.91	64.76	7.49	0.00263	0.01383	26.74065	0.05441	0.00057
25 5019C	0	0.75	63.85	7.20	0.00616	0.02161	28.06137	0.08359	0.00074
27 5020A	0	4.78	54.13	7.76	0.00212	0.01845	33.1911	0.08935	0.00076
27 5020B	0	3.83	51.48	7.17	0.00405	0.0216	37.3265	0.12174	0.0013
27 5020D	0	1.39	78.41	3.10	0.00085	0.00743	17.04063	0.03726	0.00052
34 5021A	0	0.57	70.41	5.76	0.00047	0.00713	23.19936	0.04701	0.00061
34 5021B	0	1.17	67.24	4.09	0.0005	0.00875	27.36183	0.11834	0.00067
34 5021C	0	0.43	83.47	2.29	0.00023	0.00421	13.76099	0.03605	0.00045
20 5025A	0	5.94	64.02	7.76	0.00254	0.04314	21.98483	0.21237	0.00109
20 5025B	0	9.93	56.30	13.08	0.00121	0.03399	20.46017	0.16792	0.00054
20 5025C	0	10.41	51.50	18.84	0.00116	0.04686	18.89505	0.29199	0.00042
20 5025D	0	9.39	60.35	13.21	0.00098	0.0343	16.7291	0.25986	0.00038
26 5026A	0	0.85	46.36	9.56	0.00195	0.02124	43.12492	0.06889	0.00079
26 5026B	0	1.29	37.98	12.50	0.00252	0.02914	48.05838	0.09949	0.00128
26 5026C	0	0.95	53.07	8.40	0.00105	0.01612	37.49129	0.05122	0.00086
26 5026D	0	1.29	44.28	8.73	0.00099	0.01976	45.5747	0.08158	0.00114
39 5027B	0	2.41	89.87	3.11	0.00035	0.00705	4.51906	0.06722	0.00036
39 5027C	0	4.82	76.10	8.02	0.00071	0.01833	10.93021	0.10289	0.0006
39 5027D	0	4.29	74.72	9.18	0.00054	0.01964	11.63835	0.13299	0.00054
39 5027E	0	2.92	76.69	6.44	0.00053	0.01682	13.78588	0.12794	0.00064
4 5124A	0.0019	12.81	70.14	5.35	0.00001	0.01252	11.06798	0.61288	0.00031
4 5124C	0.00393	14.45	72.08	8.29	0.00001	0.01735	4.28707	0.87395	0.0002
4 5124F	0.00316	19.18	50.30	18.93	0.00001	0.03829	9.93206	1.6112	0.00019
9A 5125B	0.00356	10.66	64.34	6.80	0.00008	0.01278	17.78825	0.39098	0.00044
9A 5125D	0	11.32	62.88	8.91	0.00009	0.01341	16.11285	0.75269	0.00045

		He %	CH4 %	H2O %	N2 %	H2S %	Ar %	CO2 %	CnHn %	SO2 %
6S	5220A	0.000529	3.41	94.26	1.57	0.00214	0.002602	0.456978	0.091957	0
6S	5220B	0	2.91	96.08	0.68	0	0.00104	0.09265	0.02540	0.00021
6S	5220C	0	5.03	92.12	1.84	0.00004	0.00235	0.21885	0.21372	0
6S	5220E	0.00017	5.35	90.11	3.15	0	0.00664	0.52839	0.24458	0.00001
10S	5221A	0.01920	10.36	79.41	6.60	0	0.01633	2.04738	0.43423	0
10S	5221C	0.00498	25.50	70.45	2.30	8.35E-05	0.016058	1.188004	0.198297	1.3E-05
10S	5221D	0.004394	37.14	57.54	3.49	0	0.012706	0.684503	0.600655	1.6E-05
10S	5221G	0.006532	48.37	46.50	2.53	0	0.005772	1.799483	0.313735	0
40	5255B	0	6.14	76.07	4.43	5.63E-04	1.32E-02	13.23819		4.57E-04
40	5255C	0	6.98	74.45	9.79	3.52E-04	2.75E-02	8.596962		3.97E-04
40	5255E	0	4.63	83.06	6.45	2.74E-04	1.37E-02	5.748191		6.54E-04

ORGANIC GAS PEAKS

		26	27	28	29	30	39	41	44	56	57	58	78
25	5019D	36825.45	179169.9	5806072	109820	11855.99	2564.999	14909.82	12351140	911.1536	796.6699	341.1536	0
27	5020E	25365	110709.4	4259804	77485.7	12543.47	1938	10165	8535594	496.6431	669.629	236.8349	0
34	5021D	6321.818	27420.46	1508496	18049.99	2242	398.9995	1855.091	3121993	153.2696	194.4734	66.82816	0
26	5026E	1727.273	13110	974406.1	9690	1007	188.2727	1065.728	2802216	44.90907	42.72409	22.23	0
39	5027F	17100	76189.99	2879027	50539.99	9500	2014	5416.727	3938225	327.5773	1197.708	232.2318	0
18	5092E	11951	13969.96	1774531	13515.74	8594.605	972.3856	2309.743	2778457	81.51	275.8385	91.78896	44.65864
19	5093D	1639.7	5452.792	504380.9	4781.79	1197.743	136.3336	434.2191	1043204	0.228	49.21	12.61773	5.694819
23	5094F	881.6	5811.927	512274.4	5233.084	724.5908	119.9245	667.8672	1676879	0.114	26.0775	11.01569	12.16518
29	5095E	1941.8	6249.273	368479.1	4010.753	1419.913	132.4214	236.3773	236342.7	*0.01*	27.65536	8.448088	3.42
29	5095F	2403.5	6338.598	376415.8	4709.496	1882.235	171.9845	306.66	326782.7	0.171	32.80782	9.53109	3.6955
31	5096E	6404.899	10462.33	1091257	9475.301	4616.032	952.0557	2562.668	2379431	67.64	232.5738	89.36132	46.03009
38	5097F	9.5	193.5927	16927.27	137.37	31.03045	3.817274	14.82	46714.09	*0.01*	0.8075	0.475	0.401591
16	5098G	689.7	2751.183	151499.1	1636.85	512.7409	123.4137	270.18	314139.1	0.152	28.05264	9.733183	3.097002
22	5100F	2409.2	7600	517162.6	6216.99	1508.375	239.0981	867.1945	1374805	5.851999	45.82714	19.45427	48.23063
4	5124M	155.8863	278.8765	2806.644	126.514	100.4753	34.43146	56.46281	20138.26	*0.01*	2.8063	3.908301	0
9A	5125K	974.8208	2621.578	98255.03	1162.42	778.1368	94.8428	161.6632	105173.7	0.40356	13.3969	9.006863	0.06574
6S	5220F	902.4481	4418.363	231212.7	2487.86	722.3109	78.87762	252.396	358357.3	*0.01*	8.4588	4.947599	0.28215
10S	5221F	142.6399	409.1736	11748.91	335.16	133.38	40.16255	61.332	3248.139	*0.01*	8.733696	4.67875	0.578365

APPENDIX H

Boiling Model

This program was developed on a Windows Excel spreadsheet for calculating fluid and gas separation in a boiling environment. It uses a model presented by Henley et al. (1984). Henry's Law constants were calculated for gases at each boiling step over a predicted range of 350° to 300° C. Henry's Law constants for CO_2 and H_2S were calculated from equations in Henley et al. (1984). Constants for CH_4, N_2, and Ar were calculated from equations in Prini and Crovetto (1989). Helium, C_mH_n, and SO_2 are of minor or trace quantities and their contributions were ignored during the calculations. Gas compositions of individual analytical results were chosen and liquid and gas separations from that initial fluid over a range of temperatures were calculated by the spreadsheet program.

In the shown program, step 1 normalizes initial composition analyses to 100%. Step 2 and 3 convert these mol % values to mmol/kg. These values are then inserted to step 4a and 4b, where liquid (C_l) and vapor (C_v) fractions of each gaseous species are determined over a specified temperature range. The format of the program does not allow for the determination of vapor fractions in ternary systems involving H_2O.

FLUID MODELING BASED ON GAS ANALYSIS DATA

STEP 2

	INIT %	liquid comp.	Initial comp.	gas comp.
H2O	57.34			
CH4	9.71		22.7556	
CO2	23.50		55.0827	
H2S	2.18E-03		0.00511	
N2	9.44		22.1222	
Ar	1.46E-02		0.03425	
		0.00	100.00	0.00

STEP 3

Conversions for initial mmol/kg values

	(mol %)		mmol/kg
H2O =	57.34	1032	23061.4
CH4 =	9.71	155.3	3904.618
CO2 =	23.50	1034	9451.59
H2S =	2.18E-03	0.074	0.877533
N2 =	9.44	264.3	3795.932
Ar =	1.46E-02	0.584	5.877053
		2.486	

STEP 1 - Suggested initial compositions (raw data)

H2O	78.4	56.3
CH4	1.393	9.93
CO2	17.04	20.46
H2S	0.00085	0.00121
N2	3.098	13.08
Ar	0.00743	0.043
	5020D	5025B
	27	20

STEP 4A - Single Step Separation for liquid phase (Cl)

T (C)	T (K)	Kh adj*	sum y	B(CO2)	Cl/Co-CO2	Cl(CO2)	B(CH4)	Cl/Co-CH4	Cl(CH4)	B(H2S)	Cl/Co-H2S	Cl(H2S)	B(N2)	Cl/Co-N2	Cl(N2)	B(Ar)	Cl/Co-Ar
300	573.15	0.28031	0.000	30.706	1.000	9452	73.67	1.000	3905	13.05	1.000	0.878	124.566	1.00	3796	130.7055	1
297	570.15	0.28782	0.012	33.017	0.739	6982	81.141	0.536	2094	13.93	0.875	0.767	138.608	0.405	1536	141.9754	0.393
294	567.15	0.29521	0.023	35.494	0.578	5466	89.332	0.354	1382	14.86	0.773	0.678	154.101	0.242	918	154.1596	0.237
291	564.15	0.30247	0.034	38.143	0.460	4351	98.3	0.250	976	15.84	0.680	0.597	171.168	0.161	612	167.3149	0.161
288	561.15	0.30961	0.044	41.005	0.378	3575	108.19	0.188	736	16.9	0.603	0.530	190.082	0.117	445	181.6388	0.120
285	558.15	0.31665	0.054	44.074	0.315	2981	119.03	0.147	573	18.03	0.537	0.471	210.925	0.089	337	197.1368	0.093
282	555.15	0.32358	0.064	47.394	0.266	2516	131	0.117	456	19.24	0.478	0.420	234.017	0.069	263	214.0288	0.074
279	552.15	0.33041	0.073	50.962	0.228	2157	144.13	0.095	373	20.53	0.429	0.377	259.466	0.056	211	232.3305	0.060
276	549.15	0.33714	0.082	54.79	0.196	1850	158.53	0.078	306	21.9	0.384	0.337	287.461	0.045	171	252.1304	0.050
273	546.15	0.34378	0.091	58.942	0.170	1607	174.45	0.065	255	23.38	0.345	0.303	318.486	0.037	141	273.7638	0.042
270	543.15	0.35033	0.099	63.402	0.148	1402	191.9	0.055	215	24.96	0.311	0.273	352.597	0.031	117	297.1849	0.036

STEP 4B - Single Step Separation for vapor phase (Cv)

T (C)	T (K)	Kh adj*	sum y	B(CO2)	Cl/Co	Cv(CO2)	B(CH4)	Cl/Co	Cv(CH4)	B(H2S)	Cl/Co	Cv(H2S)	B(N2)	Cl/Co	Cv(N2)	B(Ar)	Cl/Co-Ar
300	573.15	0.28031	0.000	30.706	1.000	-	73.67	1.000	-	13.05	1.000	-	124.566	1.00	-	130.7055	1
297	570.15	0.28782	0.012	33.017	0.739	214400	81.141	0.536	154227	13.93	0.875	10.015	138.608	0.405	191355	141.9754	0.393
294	567.15	0.29521	0.023	35.494	0.578	180472	89.332	0.354	112144	14.86	0.773	9.441	154.101	0.242	127275	154.1596	0.237
291	564.15	0.30247	0.034	38.143	0.460	154420	98.3	0.250	87148	15.84	0.680	8.862	171.168	0.161	94287	167.3149	0.161
288	561.15	0.30961	0.044	41.005	0.378	136343	108.19	0.188	72323	16.9	0.603	8.390	190.082	0.117	76148	181.6388	0.120
285	558.15	0.31665	0.054	44.074	0.315	122220	119.03	0.147	61968	18.03	0.537	7.961	210.925	0.089	64073	197.1368	0.093
282	555.15	0.32358	0.064	47.394	0.266	110873	131	0.117	54326	19.24	0.478	7.569	234.017	0.069	55457	214.0288	0.074
279	552.15	0.33041	0.073	50.962	0.228	102219	144.13	0.095	48820	20.53	0.429	7.247	259.466	0.056	49384	232.3305	0.060
276	549.15	0.33714	0.082	54.79	0.196	94302	158.53	0.078	44077	21.9	0.384	6.914	287.461	0.045	44265	252.1304	0.050
273	546.15	0.34378	0.091	58.942	0.170	88059	174.45	0.065	40474	23.38	0.345	6.635	318.486	0.037	40425	273.7638	0.042
270	543.15	0.35033	0.099	63.402	0.148	82655	191.9	0.055	37462	24.96	0.311	6.377	352.597	0.031	37254	297.1849	0.036

B(CO2) and B(H2S) from Henley, 1984

B(CH4), B(N2), and B(Ar) from Prini and Crovetto, 1989

								raw	normalized	
MC 8	MC 7	MC 6	MC 5	MC 4	MC 1	MC 2	MC 3	57.29	57.34	H2O
70.45	72.08	57.29	67.33	39.79	46.40	64.54	66.45	9.70	9.71	CH4
25.50	14.45	9.70	1.17	20.46	0.85	10.70	3.65	23.48	23.50	CO2
1.20	4.29	23.48	27.40	16.69	43.16	17.94	20.81	2.18E-03	2.18E-03	H2S
8.30E-05	1.00E-05	2.18E-03	5.01E-04	4.92E-04	1.95E-03	8.02E-05	7.31E-04	9.43	9.44	N2
2.30	8.29	9.43	4.10	23.03	9.56	6.82	9.07	1.46E-02	1.46E-02	Ar
1.61E-02	1.74E-02	1.46E-02	8.76E-03	4.01E-02	2.13E-02	1.28E-02	1.63E-02	5093F		
5221c	5124c	5093F	5021B	5095G	5026A	5125B	5096B	(19)		
(10S)	(4)	(19)	(34)	(29)	(26)	(9A)	(31)			

					Gas Content (mol)					% total gas	*mol %*	*Cl Gas Proportions (by %)*					
Cl(Ar)	Hv	Hl	D(v)		CO2	CH4	H2S	N2	Ar	remaining	*H2O left*	CO2	CH4	H2S	N2	Ar	T (C)
5.87705	2749	1344	21.67		23.4996	9.7081	2.18E-03	9.4379	0.0146	100	57.34	55	23	0.0051	22	0.034	300
2.310	2755	1327	22.78		17.3602	5.2051	1.91E-03	3.8194	0.0057	62	73.61	66	20	0.0072	14	0.022	297
1.396	2760	1311	23.94		13.5900	3.4363	1.69E-03	2.2830	0.0035	45	80.69	70	18	0.0087	12	0.018	294
0.947	2765	1294	25.15		10.8171	2.4255	1.48E-03	1.5213	0.0024	35	85.23	73	16	0.0100	10	0.016	291
0.703	2769	1278	26.43		8.8874	1.8293	1.32E-03	1.1061	0.0017	28	88.17	75	15	0.0111	9	0.015	288
0.544	2773	1262	27.77		7.4108	1.4241	1.17E-03	0.8381	0.0014	23	90.32	77	15	0.0121	9	0.014	285
0.434	2777	1246	29.19		6.2545	1.1347	1.04E-03	0.6537	0.0011	19	91.95	78	14	0.0130	8	0.013	282
0.356	2781	1231	30.68		5.3624	0.9266	9.37E-04	0.5247	0.0009	16	93.18	79	14	0.0137	8	0.013	279
0.294	2784	1215	32.24		4.6007	0.7603	8.37E-04	0.4242	0.0007	14	94.21	80	13	0.0145	7	0.013	276
0.247	2787	1200	33.9		3.9960	0.6348	7.53E-04	0.3496	0.0006	12	95.02	80	13	0.0151	7	0.012	273
0.210	2790	1185	35.64		3.4865	0.5339	6.78E-04	0.2908	0.0005	10	95.69	81	12	0.0157	7	0.012	270

					Gas Content (mol)							*Cv Gas Proportions (by mol %)*					
Cv(Ar)	Hv	Hl	D(v)		CO2	CH4	H2S	N2	Ar			CO2	CH4	H2S	N2	Ar	T (C)
-	2749	1344	21.67		0.0000	0.0000	0.0000	0.0000	0			0	0	0.0000	0	0	300
302	2755	1327	22.78		533.0644	383.4566	0.0249	#######	0.7507			38	28	0.0018	34	0.05	297
198	2760	1311	23.94		448.7081	278.8247	0.0235	#######	0.4927			43	27	0.0022	30	0.05	294
146	2765	1294	25.15		383.9362	216.6779	0.0220	#######	0.3630			46	26	0.0026	28	0.04	291
118	2769	1278	26.43		338.9896	179.8184	0.0209	#######	0.2924			48	25	0.0029	27	0.04	288
99	2773	1262	27.77		303.8758	154.0716	0.0198	#######	0.2457			49	25	0.0032	26	0.04	285
85	2777	1246	29.19		275.6638	135.0713	0.0188	#######	0.2125			50	25	0.0034	25	0.04	282
76	2781	1231	30.68		254.1467	121.3808	0.0180	#######	0.1892			51	24	0.0036	25	0.04	279
68	2784	1215	32.24		234.4631	109.5899	0.0172	#######	0.1696			52	24	0.0038	24	0.04	276
62	2787	1200	33.9		218.9411	100.6303	0.0165	#######	0.1549			52	24	0.0039	24	0.04	273
57	2790	1185	35.64		205.5047	93.1411	0.0159	92.6240	0.1428			53	24	0.0041	24	0.04	270

APPENDIX I

Mineral Equilibria

Analysis results were used to evaluate the ability of selected fluids to carry gold in solution. The mole percentages of gases and water were entered along with estimates of pH and salinity into the Geomod program. This program quantitatively determines the ability of the fluid to carry gold, using solubility equations presented by Shenberger and Barnes (1989). The program requires a value for concentration of H_2. This gas was not determined in gas analyses. To estimate the concentration of H_2, two equations were required. An equilibrium equation for the reaction $CO_2 + 4H_2 \equiv CH_4 + 2H_2O$ was calculated for the temperature of interest and partial pressures for the known gases were determined according to P(gas) = Kh*X(gas). The mole fraction of H_2 was the only remaining unknown in this equation, and determinations were made for each crush result. A similar procedure was undertaken for estimations of fO_2. Kh values were taken from Henley et al. (1984).

FLUID A		He %	CH4 %	H2O %	N2 %	H2S %	Ar %	CO2 %	(300 c)
18	5092A	0	13.59572	42.45157	16.28559	0.00215	0.04426	27.15698	
18	5092D	0	7.16297	59.53265	13.41794	0.00318	0.02557	19.64339	
18	5092F	0	4.79098	68.95544	9.88188	0.00322	0.02149	16.13602	
19	5093C	0	9.50976	62.56815	8.83216	0.00123	0.01353	18.98916	
19	5093E	0	9.30761	58.71135	9.34356	0.00132	0.0145	22.54871	
19	5093F	0	9.69254	57.28673	9.43361	0.00218	0.01459	23.48513	
19	5093G	0	8.83648	61.47309	9.62725	0.00123	0.01395	19.97827	
20	5025A	0	5.94398	64.018	7.76223	0.00254	0.04314	21.98483	
20	5025B	0	9.93369	56.29889	13.08064	0.00121	0.03399	20.46017	
20	5025C	0	10.40931	51.50141	18.83708	0.00116	0.04686	18.89505	
20	5025D	0	9.39237	60.34958	13.21235	0.00098	0.0343	16.7291	
29	5095C	0	17.66576	37.14356	22.54391	0.00086	0.05219	22.22765	
29	5095D	0	17.24107	37.56799	25.34228	0.0008	0.07008	19.30202	
29	5095G	0	20.39411	39.66582	22.95488	0.00049	0.04007	16.63655	
39	5027B	0	2.41124	89.87453	3.1146	0.00035	0.00705	4.51906	
39	5027C	0	4.82112	76.09937	8.01982	0.00071	0.01833	10.93021	
39	5027D	0	4.28932	74.7221	9.18441	0.00054	0.01964	11.63835	
39	5027E	0	2.92282	76.69361	6.44269	0.00053	0.01682	13.78588	
FLUID B		He %	CH4 %	H2O %	N2 %	H2S %	Ar %	CO2 %	(300 c)
31	5096B	0	3.64653	66.32416	9.05357	0.00073	0.01629	20.76744	
31	5096C	0	1.61167	71.46737	8.3259	0.00109	0.01924	18.43734	
31	5096D	0	1.55775	64.83511	7.64164	0.00086	0.01231	25.87756	
31	5096F	0	4.14961	67.05186	7.71993	0.00068	0.01739	20.7838	
38	5097B	0	1.08109	78.00591	4.72724	0.0004	0.00665	16.16608	
38	5097C	0	0.92355	83.119	4.46841	0.00019	0.00509	11.46856	
38	5097H	0	0.80424	85.19106	4.4361	0.00024	0.00607	9.54747	
23	5094C	0	2.679	64.05274	6.75595	0.00097	0.01451	26.43424	
23	5094D	0	1.93906	62.18054	8.32488	0.00169	0.01578	27.49738	
23	5094E	0	1.70152	70.75095	6.31915	0.001	0.01069	21.16339	
23	5094G	0	1.00719	84.05444	3.33474	0.001	0.00712	11.55968	
22	5100D	0	3.47296	62.12337	4.02952	0.0009	0.01488	30.26258	
22	5100G	0	2.15501	77.56343	1.85202	0.0005	0.00567	18.3913	
22	5100H	0	2.87082	72.17761	3.02906	0.00078	0.01361	21.8417	
26	5026A	0	0.84607	46.36115	9.5562	0.00195	0.02124	43.12492	
26	5026B	0	1.28968	37.98459	12.50041	0.00252	0.02914	48.05838	
26	5026C	0	0.95144	53.06947	8.40332	0.00105	0.01612	37.49129	
26	5026D	0	1.29073	44.28099	8.72789	0.00099	0.01976	45.5747	
25	5019A	0	1.57954	58.30814	11.08494	0.00405	0.02368	28.86915	
25	5019B	0	0.91464	64.76134	7.49417	0.00263	0.01383	26.74065	
25	5019C	0	0.75326	63.84539	7.2012	0.00616	0.02161	28.06137	
27	5020A	0	4.78388	54.12944	7.76194	0.00212	0.01845	33.1911	
27	5020B	0	3.83182	51.48446	7.17113	0.00405	0.0216	37.3265	
27	5020D	0	1.39364	78.41293	3.09826	0.00085	0.00743	17.04063	
16	5098E	0	2.22109	60.3547	7.53168	0.00033	0.02116	29.73637	
16	5098F	0	0.99307	63.14955	5.53965	0.00032	0.01771	30.24496	
16	5098H	0	3.39843	54.86765	12.89135	0.00049	0.03218	28.6136	
34	5021A	0	0.57253	70.40506	5.75835	0.00047	0.00713	23.19936	
34	5021B	0	1.17016	67.23532	4.09156	0.0005	0.00875	27.36183	
34	5021C	0	0.43226	83.46992	2.2907	0.00023	0.00421	13.76099	
FLUID C		He %	CH4 %	H2O %	N2 %	H2S %	Ar %	CO2 %	(300 C)
4	5124A	0	12.80722	70.14261	5.34638	0	0.01252	11.06798	
4	5124C	0	14.44765	72.07596	8.29103	0	0.01735	4.28707	
4	5124F	0	19.1786	50.29918	18.9281	0	0.03829	9.93206	
9A	5125B	0	10.66303	64.33549	6.79681	0.00008	0.01278	17.8825	
9A	5125D	0	11.31683	62.87744	8.91224	0.00009	0.01341	16.11285	

H2O Caculated as gas					*H2O Calculated as liquid*					
H2%	O2%	PO2 (bars)	PH2 (bars)	(300o)	H2%	PO2 (bars)	PH2 (bars)		m(H2S)*	(300o)
0.0021	8.56E-38	1.11E-35	0.25		0.0028	2.06E-35	0.34		0.0008	
0.0019	1E-37	1.3E-35	0.23		0.0026	2.41E-35	0.32		0.0013	
0.0018	1.11E-37	1.44E-35	0.22		0.0025	2.67E-35	0.30		0.0014	
0.0021	8.56E-38	1.11E-35	0.25		0.0028	2.06E-35	0.34		0.0005	
0.0020	9.43E-38	1.22E-35	0.24		0.0027	2.27E-35	0.33		0.0005	
0.0020	9.43E-38	1.22E-35	0.24		0.0027	2.27E-35	0.33		0.0009	
0.0020	9.11E-38	1.18E-35	0.24		0.0027	2.19E-35	0.33		0.0005	
0.0018	1.17E-37	1.51E-35	0.22		0.0024	2.8E-35	0.29		0.0010	
0.0020	8.7E-38	1.13E-35	0.25		0.0028	2.09E-35	0.34		0.0005	
0.0021	8.16E-38	1.06E-35	0.26		0.0029	1.96E-35	0.35		0.0005	
0.0021	8.09E-38	1.05E-35	0.26		0.0029	1.94E-35	0.35		0.0004	
0.0023	6.8E-38	8.82E-36	0.28		0.0031	1.63E-35	0.38		0.0003	
0.0024	6.41E-38	8.32E-36	0.29		0.0032	1.54E-35	0.39		0.0003	
0.0026	5.47E-38	7.1E-36	0.31		0.0035	1.32E-35	0.43		0.0002	
0.0021	8.29E-38	1.08E-35	0.25		0.0028	1.99E-35	0.35		0.0002	
0.0020	9.12E-38	1.18E-35	0.24		0.0027	2.19E-35	0.33		0.0003	
0.0019	9.98E-38	1.3E-35	0.23		0.0026	2.4E-35	0.32		0.0002	
0.0017	1.32E-37	1.71E-35	0.20		0.0023	3.16E-35	0.28		0.0002	
								ave =	0.0006	
H2O Caculated as gas					*H2O Calculated as liquid*					
H2%	O2%	PO2 (bars)	PH2 (bars)		H2%	PO2 (bars)	PH2 (bars)			
0.001584	1.45E-37	1.88E-35	0.19		0.0022	3.47E-35	0.26		0.0003	
0.001331	2.05E-37	2.66E-35	0.16		0.0018	4.92E-35	0.22		0.0005	
0.001212	2.47E-37	3.21E-35	0.15		0.0016	5.93E-35	0.20		0.0003	
0.001636	1.36E-37	1.76E-35	0.20		0.0022	3.26E-35	0.27		0.0003	
0.001245	2.34E-37	3.04E-35	0.15		0.0017	5.63E-35	0.21		0.0002	
0.001304	2.14E-37	2.77E-35	0.16		0.0018	5.13E-35	0.22		0.0001	
0.001318	2.09E-37	2.71E-35	0.16		0.0018	5.02E-35	0.22		0.0001	
0.001381	1.9E-37	2.47E-35	0.17		0.0019	4.57E-35	0.23		0.0004	
0.001261	2.28E-37	2.96E-35	0.15		0.0017	5.48E-35	0.21		0.0007	
0.001303	2.14E-37	2.77E-35	0.16		0.0018	5.14E-35	0.22		0.0004	
0.00133	2.05E-37	2.66E-35	0.16		0.0018	4.93E-35	0.22		0.0005	
0.001424	1.79E-37	2.32E-35	0.17		0.0019	4.3E-35	0.24		0.0003	
0.001432	1.77E-37	2.3E-35	0.17		0.0019	4.25E-35	0.24		0.0002	
0.001474	1.67E-37	2.17E-35	0.18		0.0020	4.02E-35	0.24		0.0003	
0.000916	4.33E-37	5.62E-35	0.11		0.0012	1.04E-34	0.15		0.0006	
0.000991	3.7E-37	4.8E-35	0.12		0.0013	8.89E-35	0.16		0.0008	
0.000977	3.8E-37	4.94E-35	0.12		0.0013	9.14E-35	0.16		0.0004	
0.001004	3.6E-37	4.67E-35	0.12		0.0014	8.65E-35	0.17		0.0003	
0.001184	2.59E-37	3.36E-35	0.14		0.0016	6.22E-35	0.20		0.0015	
0.001052	3.28E-37	4.25E-35	0.13		0.0014	7.87E-35	0.17		0.0010	
0.000991	3.7E-37	4.8E-35	0.12		0.0013	8.89E-35	0.16		0.0024	
0.001508	1.6E-37	2.07E-35	0.18		0.0021	3.84E-35	0.25		0.0008	
0.001385	1.89E-37	2.45E-35	0.17		0.0019	4.54E-35	0.23		0.0014	
0.001309	2.12E-37	2.75E-35	0.16		0.0018	5.09E-35	0.22		0.0004	
0.001279	2.22E-37	2.88E-35	0.16		0.0017	5.33E-35	0.21		0.0001	
0.001042	3.34E-37	4.34E-35	0.13		0.0014	8.04E-35	0.17		0.0001	
0.001437	1.76E-37	2.28E-35	0.18		0.0020	4.22E-35	0.24		0.0002	
0.00097	3.86E-37	5.01E-35	0.12		0.0013	9.27E-35	0.16		0.0002	
0.001113	2.93E-37	3.8E-35	0.14		0.0015	7.04E-35	0.18		0.0002	
0.00103	3.42E-37	4.44E-35	0.13		0.0014	8.22E-35	0.17		0.0001	
H2O Caculated as gas								ave =	0.0005	
H2%	O2%	PO2 (bars)	PH2 (bars)		H2%	PO2 (bars)	PH2 (bars)		m(H2S)*	(300o)
0.003479	8.07E-38	1.05E-35	0.42		0.0035	1.35E-35	0.42		0.00000	
0.004545	4.73E-38	6.14E-36	0.55		0.0045	7.93E-36	0.55		0.00000	
0.003954	6.25E-38	8.11E-36	0.48		0.0039	1.05E-35	0.48		0.00000	
0.002948	1.12E-37	1.46E-35	0.36		0.0029	1.89E-35	0.36		0.00003	
0.003071	1.04E-37	1.35E-35	0.37		0.0030	1.74E-35	0.37		0.00004	
			*m(H2S) calculation:							
				mol% H2S/100 (1000g/kg) (1/dfluid*18)						

H2S(g) % in pyrite/mag rxn			H2S(aq) with H2O(l)			H2S(aq) with H2O(g)	
w/ H2O(l)	w/ H2O(g)	d fluid	m	mol %	d fluid	m	mol %
0.029299	1.05E-05	1.4550	0.0011	0.0027	1.4550	1.00E-08	2.34E-08
0.028535	1.02E-05	1.3439	0.0011	0.0028	1.3439	9.76E-09	2.47E-08
0.02805	1E-05	1.2776	0.0011	0.0029	1.2776	9.59E-09	2.55E-08
0.029299	1.05E-05	1.3065	0.0011	0.0030	1.3065	1.00E-08	2.61E-08
0.028831	1.03E-05	1.3612	0.0011	0.0028	1.3612	9.86E-09	2.46E-08
0.028831	1.03E-05	1.3745	0.0011	0.0028	1.3745	9.86E-09	2.44E-08
0.028998	1.04E-05	1.3265	0.0011	0.0029	1.3265	9.92E-09	2.54E-08
0.027832	9.94E-06	1.3479	0.0011	0.0028	1.3479	9.52E-09	2.40E-08
0.029224	1.04E-05	1.3494	0.0011	0.0029	1.3494	1.00E-08	2.52E-08
0.029533	1.06E-05	1.3567	0.0012	0.0029	1.3567	1.01E-08	2.53E-08
0.02958	1.06E-05	1.2962	0.0012	0.0030	1.2962	1.01E-08	2.65E-08
0.030449	1.09E-05	1.4127	0.0012	0.0029	1.4127	1.04E-08	2.51E-08
0.030747	1.1E-05	1.3854	0.0012	0.0030	1.3854	1.05E-08	2.58E-08
0.031569	1.13E-05	1.3304	0.0012	0.0032	1.3304	1.08E-08	2.76E-08
0.029455	1.05E-05	1.0778	0.0012	0.0036	1.0778	1.01E-08	3.18E-08
0.028991	1.04E-05	1.1931	0.0011	0.0032	1.1931	9.92E-09	2.83E-08
0.02856	1.02E-05	1.2103	0.0011	0.0031	1.2103	9.77E-09	2.74E-08
0.027274	9.74E-06	1.2285	0.0011	0.0030	1.2285	9.33E-09	2.58E-08
H2S(g) % in pyrite/mag rxn			H2S(aq) with H2O(l)			H2S(aq) with H2O(g)	
w/ H2O(l)	w/ H2O(g)	d fluid	m	mol %	d fluid	m	mol %
0.026849	9.59E-06	1.3421	0.0011	0.0027	1.3421	9.18E-09	2.33E-08
0.025333	9.05E-06	1.3083	0.0010	0.0026	1.3083	8.67E-09	2.25E-08
0.024558	8.77E-06	1.4128	0.0010	0.0023	1.4128	8.40E-09	2.02E-08
0.027138	9.69E-06	1.3332	0.0011	0.0027	1.3332	9.28E-09	2.37E-08
0.024774	8.85E-06	1.2578	0.0010	0.0026	1.2578	8.47E-09	2.29E-08
0.02516	8.99E-06	1.1887	0.0010	0.0028	1.1887	8.61E-09	2.46E-08
0.025255	9.02E-06	1.1610	0.0010	0.0029	1.1610	8.64E-09	2.53E-08
0.025647	9.16E-06	1.4141	0.0010	0.0024	1.4141	8.77E-09	2.11E-08
0.024884	8.89E-06	1.4396	0.0010	0.0023	1.4396	8.51E-09	2.01E-08
0.025157	8.99E-06	1.3373	0.0010	0.0025	1.3373	8.61E-09	2.19E-08
0.025326	9.05E-06	1.1834	0.0010	0.0029	1.1834	8.66E-09	2.49E-08
0.025914	9.26E-06	1.4526	0.0010	0.0024	1.4526	8.86E-09	2.07E-08
0.025959	9.27E-06	1.2720	0.0010	0.0027	1.2720	8.88E-09	2.37E-08
0.026209	9.36E-06	1.3267	0.0010	0.0026	1.3267	8.96E-09	2.30E-08
0.022367	7.99E-06	1.6735	0.0009	0.0018	1.6735	7.65E-09	1.55E-08
0.022959	8.2E-06	1.7598	0.0009	0.0017	1.7598	7.85E-09	1.52E-08
0.022852	8.16E-06	1.5858	0.0009	0.0019	1.5858	7.82E-09	1.68E-08
0.023062	8.24E-06	1.7034	0.0009	0.0018	1.7034	7.89E-09	1.57E-08
0.024363	8.7E-06	1.4744	0.0010	0.0022	1.4744	8.33E-09	1.92E-08
0.023428	8.37E-06	1.4255	0.0009	0.0022	1.4255	8.01E-09	1.91E-08
0.022959	8.2E-06	1.4427	0.0009	0.0021	1.4427	7.85E-09	1.85E-08
0.026411	9.44E-06	1.5132	0.0010	0.0023	1.5132	9.03E-09	2.03E-08
0.025675	9.17E-06	1.5708	0.0010	0.0022	1.5708	8.78E-09	1.90E-08
0.025193	9E-06	1.2605	0.0010	0.0027	1.2605	8.62E-09	2.32E-08
0.025003	8.93E-06	1.4661	0.0010	0.0023	1.4661	8.55E-09	1.98E-08
0.023348	8.34E-06	1.4653	0.0009	0.0021	1.4653	7.99E-09	1.85E-08
0.025988	9.28E-06	1.4770	0.0010	0.0023	1.4770	8.89E-09	2.05E-08
0.022799	8.14E-06	1.3655	0.0009	0.0022	1.3655	7.80E-09	1.94E-08
0.023868	8.53E-06	1.4146	0.0009	0.0022	1.4146	8.16E-09	1.96E-08
0.023262	8.31E-06	1.2103	0.0009	0.0026	1.2103	7.96E-09	2.24E-08
H2S(g) % in pyrite/mag rxn			H2S(aq) with H2O(l)			H2S(aq) with H2O(g)	
w/ H2O(l)	w/ H2O(g)	d fluid	m	mol %	d fluid	m	mol %
0.031417	1.12E-05	1.1619	0.0012	0.0036	1.1619	1.07E-08	3.14E-08
0.034344	1.23E-05	1.0749	0.0013	0.0043	1.0749	1.17E-08	3.72E-08
0.032787	1.17E-05	1.2000	0.0013	0.0036	1.2000	1.12E-08	3.18E-08
0.029729	1.06E-05	1.2751	0.0012	0.0031	1.2751	1.02E-08	2.71E-08
0.030137	1.08E-05	1.2556	0.0012	0.0032	1.2556	1.03E-08	2.79E-08

Table B - Gas Calculations for H2 and O2 Determinations

Delta Gr:	350	300	250	200
H2O	-213	-215	-216.5	-221
CH4	-20.34	-25	-27	-35
CO2	-395.2	-395.1	-395	-394.82
H2S				

	log Keq 350	300	250	200
CO2 === C + O2	-31.33	-36.02	-39.45	-43.6
2H2 + C === CH4	1.71	2.32	3.04	3.89
2H2 + O2 === 2H2O(l)	31.56	35.62	40.46	46.36
2H2O(l) === 2H2O(g)	5.047895	4.403899	3.636769	2.707454
CO2+4H2===CH4+2H2O(g)	9725126	2108140	48614836	2.28E+09

(Keq from Henley, 1984)

	log Keq 350	300	250	200
C + O2 === CO2	31.33	36.02	39.45	43.6
CH4 === C + 2H2	-1.71	-2.32	-3.04	-3.89
2H2 + O2 === 2H2O(l)	31.56	35.62	40.46	46.36
2H2O(l) === 2H2O(g)	5.047895	4.403899	3.636769	2.707454
CH4+2O2===CO2+2H2O(g)	1.69E+66	5.3E+73	3.21E+80	5.99E+88

(Keq from Henley, 1984)

(b values (CH4, H2, O2) from Rini and Crovetto, CO2, H2S from Henley 1984)

Kh	CH4	CO2	H2	O2	H2O (Pp)	H2S
350	4374	2816	5527	6845	165	1355
300	8985	3980	12190	12982	86	1592
250	12536	5340	16871	17385	40	1872
200	31836	6620	38690	39118	15.5	2201

Experiment: Effects of CH4 on H2S(aq) content of fluid

CH4%	CO2%	mH2S(aq)
0.0001	20	0.0004
1	30	0.000916
10	10	0.001216
15	25	0.001166
2	7	0.001096

Experiment: Gas composition effects on equilibrium

			ilmenite to pyrite and rutile			magnetite to pyrite		
CO2 frac	CH4 frac	H2S frac	300	250	200	300	250	200
			0	0	0	**9.38E-05**	**4.84E-13**	**3.78E-25**
0.15	0.05	0.005	4.67E-08	1.33E-08	7.45E-09	8.60E+10	5.78E+11	1.97E+12
0.15	0.05	0.0005	4.668976	1.328254	0.745098	0.085987	0.577859	1.968552
0.15	0.05	0.00005	4.67E+08	1.33E+08	74509799	8.6E-14	5.78E-13	1.97E-12
0.15	0.05	0.000005	4.67E+16	1.33E+16	7.45E+15	8.6E-26	5.78E-25	1.97E-24
0.1	0.1	0.0005	14.00693	3.984763	2.235294	0.028662	0.19262	0.656184
0.1	0.1	0.00005	1.4E+09	3.98E+08	2.24E+08	2.87E-14	1.93E-13	6.56E-13
0.2	0.1	0.00031	320.7594	91.25129	51.18835	0.000185	0.001243	0.004234

Delta H							
350	300	250	200				
-244.8	-244.7	-244	-243.82				
-83.5	-82.2	-81.6	-79.7				
-393.82	-393.73	-393.7	-393.6				
			log Keq				
			350	300	250	200	
CO2 = = = C + O2			-31.33	-36.02	-39.45	-43.6	
2H2 + C = = = CH4			1.71	2.32	3.04	3.89	
2H2 + O2 = = = 2H2O(l)			31.56	35.62	40.46	46.36	
CO2+4H2= = =CH4+2H2O(l)			87.09636	83.17638	11220.18	4466836	
(Keq from Henley, 1984)							
			log Keq				
			350	300	250	200	
C + O2 = = = CO2			31.33	36.02	39.45	43.6	
CH4 = = = C + 2H2			-1.71	-2.32	-3.04	-3.89	
2H2 + O2 = = = 2H2O(l)			31.56	35.62	40.46	46.36	
CH4+2O2= = =CO2+2H2O(l)			1.51E+61	2.09E+69	7.41E+76	1.17E+86	
(Keq from Henley, 1984)							

Experiment: Effects of CH4 on H2S(g) content of fluid			
	CH4%	CO2%	H2S(g)
	30	20	0.0003
	1	30	0.00023
	5	10	0.00029
	20	2	0.00038
	4	19	0.00027

Table C1 - Sulfide Equilibrium for solving H2S(g) with H2O(l) factor				
	log Keq			
	350	300	250	200
12FeS + 12H2O(l) + 2O2 = = = 4Fe3O4 + 12HS- + 12H+	-76.68	-58.84	-48.32	-41.12
12HS- + 12H+ = = = 12H2S(aq)	-	96.6	91.2	86.04
12FeS2 + 12H2O(l) = = = 12FeS + 12H2S(g) + 6O2	-186.6	-215.76	-250.56	-292.8
12H2S(aq) = = = 12H2S(g)	-	31.30462	29.31018	26.89409
2CH4 + 4O2 = = = 2CO2 + 4H2O(l)	122.36	138.64	153.74	172.14
12FeS2 + 20H2O(l) + 2CH4 = = 2CO2 + 24H2S(g) + 4Fe3O4	-	-8.05538	-24.6298	-48.8459
6FeS2 + 10H2O(l) + CH4 = = CO2 + 12H2S(g) + 2Fe3O4		-4.02769	-12.3149	-24.423
Keq =		**9.38E-05**	**4.84E-13**	**3.78E-25**
(All from Henley, 1984 except H2S from Drever)				
Keq = ((X(H2S) * Kh(H2S))^12 * (X(CO2)) * (Kh(CO2)))/(X(CH4) * Kh(CH4))				
Table C2 - Sulfide Equilibrium for solving H2S(g) with H2O(g) factor				
	log Keq			
	350	300	250	200
12FeS + 12H2O(l) + 2O2 = = = 4Fe3O4 + 12HS- + 12H+	-76.68	-58.84	-48.32	-41.12
12HS- + 12H+ = = = 12H2S(aq)	-	96.6	91.2	86.04
12FeS2 + 12H2O(l) = = = 12FeS + 12H2S(g) + 6O2	-186.6	-215.76	-250.56	-292.8
12H2S(aq) = = = 12H2S(g)	-	31.30462	29.31018	26.89409
2CH4 + 4O2 = = = 2CO2 + 4H2O(l)	122.36	138.64	153.74	172.14
20H2O(g) = = = 20H2O(l)	-50.479	-44.039	-36.3677	-27.0745
12FeS2 + 20H2O(g) + 2CH4 = = 2CO2 + 24H2S(g) + 4Fe3O4	-	-52.0944	-60.9975	-75.9204
6FeS2 + 10H2O(g) + CH4 = = CO2 + 12H2S(g) + 2Fe3O4		-26.0472	-30.4988	-37.9602
Keq =		**8.97E-27**	**3.17E-31**	**1.1E-38**
(All from Henley, 1984 except H2S from Drever)				
Keq = ((X(H2S) * Kh(H2S))^12 * (X(CO2)) * (Kh(CO2))/((P(H2O)^10)) * (X(CH4) * Kh(CH4))				
Table C3 - Sulfide Equilibrium for solving H2S(aq) with H2O(l) factor				
	log Keq			
	350	300	250	200
12FeS + 12H2O(l) + 2O2 = = = 4Fe3O4 + 12HS- + 12H+	-76.68	-58.84	-48.32	-41.12
12HS- + 12H+ = = = 12H2S(aq)	-	96.6	91.2	86.04
12FeS2 + 12H2O(l) = = = 12FeS + 12H2S(g) + 6O2	-186.6	-215.76	-250.56	-292.8
12H2S(g) = = = 12H2S(aq)	-	-31.3046	-29.3102	-26.8941
2CH4 + 4O2 = = = 2CO2 + 4H2O(l)	122.36	138.64	153.74	172.14
12FeS2 + 20H2O(l) + 2CH4 = = 2CO2 + 24H2S(aq) + 4Fe3O4	-	-70.6646	-83.2502	-102.634
6FeS2 + 10H2O(l) + CH4 = = CO2 + 12H2S(aq) + 2Fe3O4		-35.3323	-41.6251	-51.317
Keq =		**4.65E-36**	**2.37E-42**	**4.82E-52**
(All from Henley, 1984 except H2S from Drever)				
Keq = ((m(H2S)^12) * (X(CO2)) * (Kh(CO2))/(X(CH4) * Kh(CH4))				

Table C4 - Sulfide Equilibrium for solving H2S(aq) with H2O(g) factor									
					log Keq				
					350	300	250	200	
12FeS + 12H2O(l) + 2O2 = = = 4Fe3O4 + 12HS- + 12H+					-76.68	-58.84	-48.32	-41.12	
12HS- + 12H+ = = = 12H2S(aq)					-	96.6	91.2	86.04	
12FeS2 + 12H2O(l) = = = 12FeS + 12H2S(g) + 6O2					-186.6	-215.76	-250.56	-292.8	
12H2S(g) = = = 12H2S(aq)					-	-31.3046	-29.3102	-26.8941	
2CH4 + 4O2 = = = 2CO2 + 4H2O(l)					122.36	138.64	153.74	172.14	
20H2O(g) = = = 20H2O(l)					-50.479	-44.039	-36.3677	-27.0745	
12FeS2 + 20H2O(g) + 2CH4 = = 2CO2 + 24H2S(aq) + 4Fe3O					-	-114.704	-119.618	-129.709	
6FeS2 + 10H2O(g) + CH4 = = CO2 + 12H2S(aq) + 2Fe3O4						-57.3518	-59.8089	-64.8543	
				Keq =		**4.45E-58**	**1.55E-60**	**1.4E-65**	
(All from Henley, 1984 except H2S from Drever)									
	Keq = ((m(H2S)^12)*(X(CO2))*(Kh(CO2))/(X(CH4)*Kh(CH4))								
Table D - H2S adjustment for Table C1,C3									
H2S(aq) = = = H2S(g)		300	250	200	Temp				
Gr(298) =	-5.73								
Hr(298) =	19.07								
lnK(298) =	2.312748								
Keq		406.1797	277.0227	174.2506					
logK		2.608718	2.442515	2.241174					
(Values from Drever)									
Table E - H2O adjustment for Table C2,C4									
H2O(g) = = = H2O(l)		350	300	250	200	Temp			
Gr(298) =	-8.56								
Hr(298) =	-44.01								
lnK(298) =	3.454995								
Keq		0.002993	0.006281	0.015192	0.044287				
logK		-2.52395	-2.20195	-1.81838	-1.35373				
(Values from Drever)									

APPENDIX J

Raman Microprobe Results

(Analyses by C. Broman, Institutionen för Geologi och Geokemi, Stockholms Universitet, Stockholm, Sweden)

Prof. David Norman
Department of Geosciences
New Mecxico Tech
Socorro
New Mexico 87 801
USA

Regarding Raman analyses of gas phases in fluid inclusion in samples from gold-bearing quartz veins hosted by a granitoid in the Birimian sediments in Ghana, W. Africa.

Analyses made by: Curt Broman
Department of Geology and Geochemistry
Stockholm University, S-106 91 Stockholm, Sweden

Carbon dioxide and methane

Photos of four of the largest fluid inclusions from your samples are shown in Figs. 1 to 4. The volume % gas phase of the total inclusion volume range from 10 to 100. Raman spectra of the analyzed carbonic phases are displayed in Figs. 5 to 8. Almost all the "CO_2 spectra" (left part in Figs 5 to 8) have an increased background due to the presence of minor graphite and graphite-like solid matter within the inclusions. The graphite-like matter can be seen in the upper part of the inclusion in Fig. 1. Raman spectra for this solid is presented in Fig. 10 and graphite together with quartz and CO_2 peaks in Fig. 11. In general no liquid or gaseous hydrocarbons heavier than methane was detected in the CO_2-bearing inclusions, there are no other peaks than the methane peak in the "CH_4 spectra". One exeption was an inclusion in sample #29A (incl. II in Fig. 9) where some hydrocarbon (n-Alkenes) was found. Unfortunantly, the laser beam disturbed the original hydrocarbon so it became impossible to repeat the analyse because of an increasing fluorescence that masked the signal. No indication of nitrogen was noted (see below). Calculated mole % CO_2 and CH_4 are given in Table 1 and in Fig. 12 the mole % CH_4 has been plotted versus the volume % gas phase.

Nitrogen

No nitrogen was detected in any of the analyzed fluid inclusions in Table 1. However, in sample #18A, one inclusion, that was monophase (gas) at room temperature (Fig. 13), displayed two phases (liquid and gas) below -150°C (Fig. 14). This fluid inclusion homogenized to the gas phase at -139°C. Such a low temperature indicates the presence of N_2 with minor amounts of CH_4. No solid CO_2 was formed during cooling. It may well be that most of the nitrogen liberated during crushing comes from this inclusion type that seems to outline former quartz grain boundaries. No Raman signal was obtained from this inclusion, because of the low density of the inclusion and possibly also due to its position relatively deep down in the thin section.

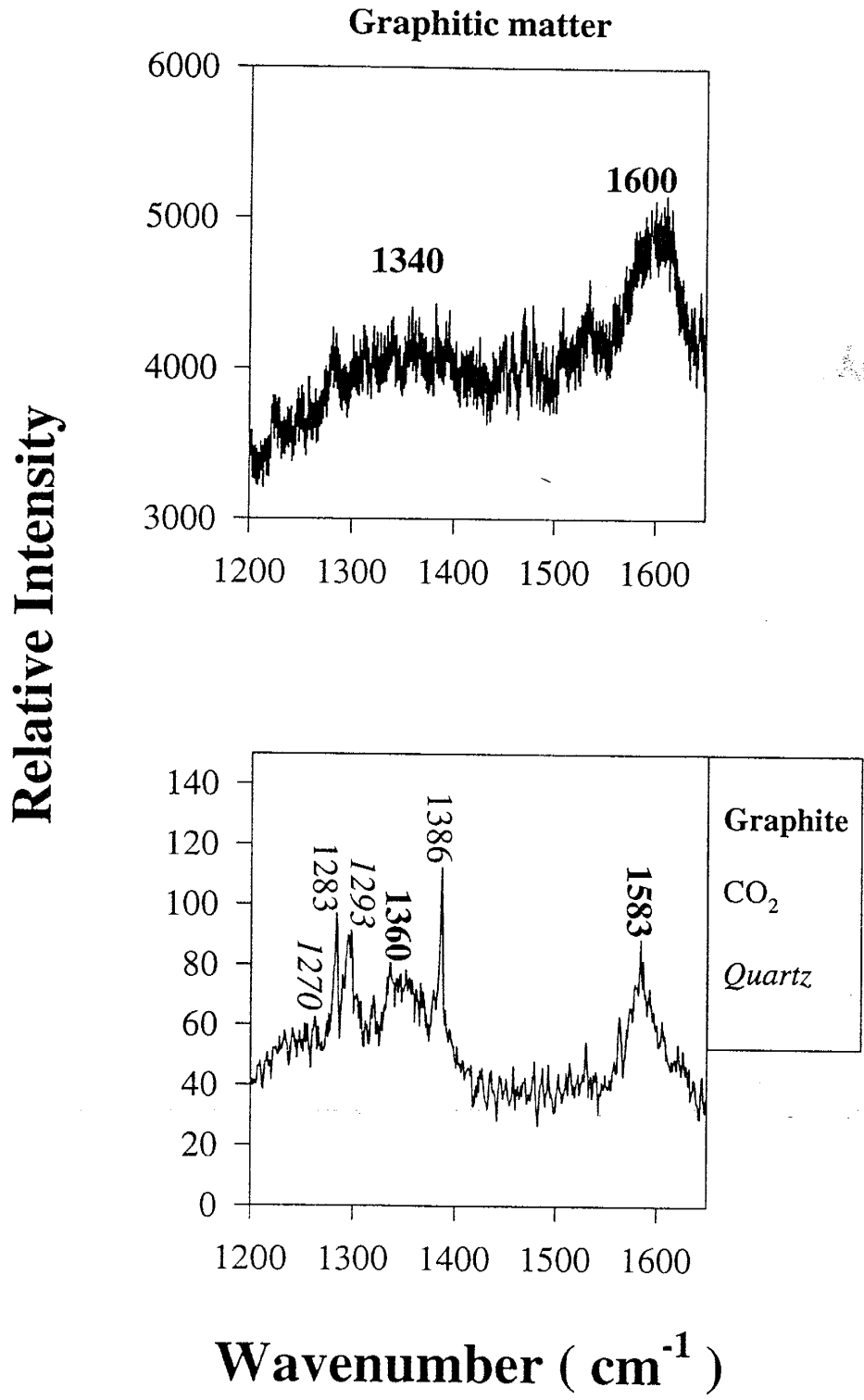
Graphitic matter
6000
5000
4000
3000
1340
1600
1200 1300 1400 1500 1600
Relative Intensity
140
120
100
80
60
40
20
0
1283
1270
1293
1360
1386
1583
Graphite
CO_2
Quartz
1200 1300 1400 1500 1600
Wavenumber (cm^{-1})

Sample # 18 A

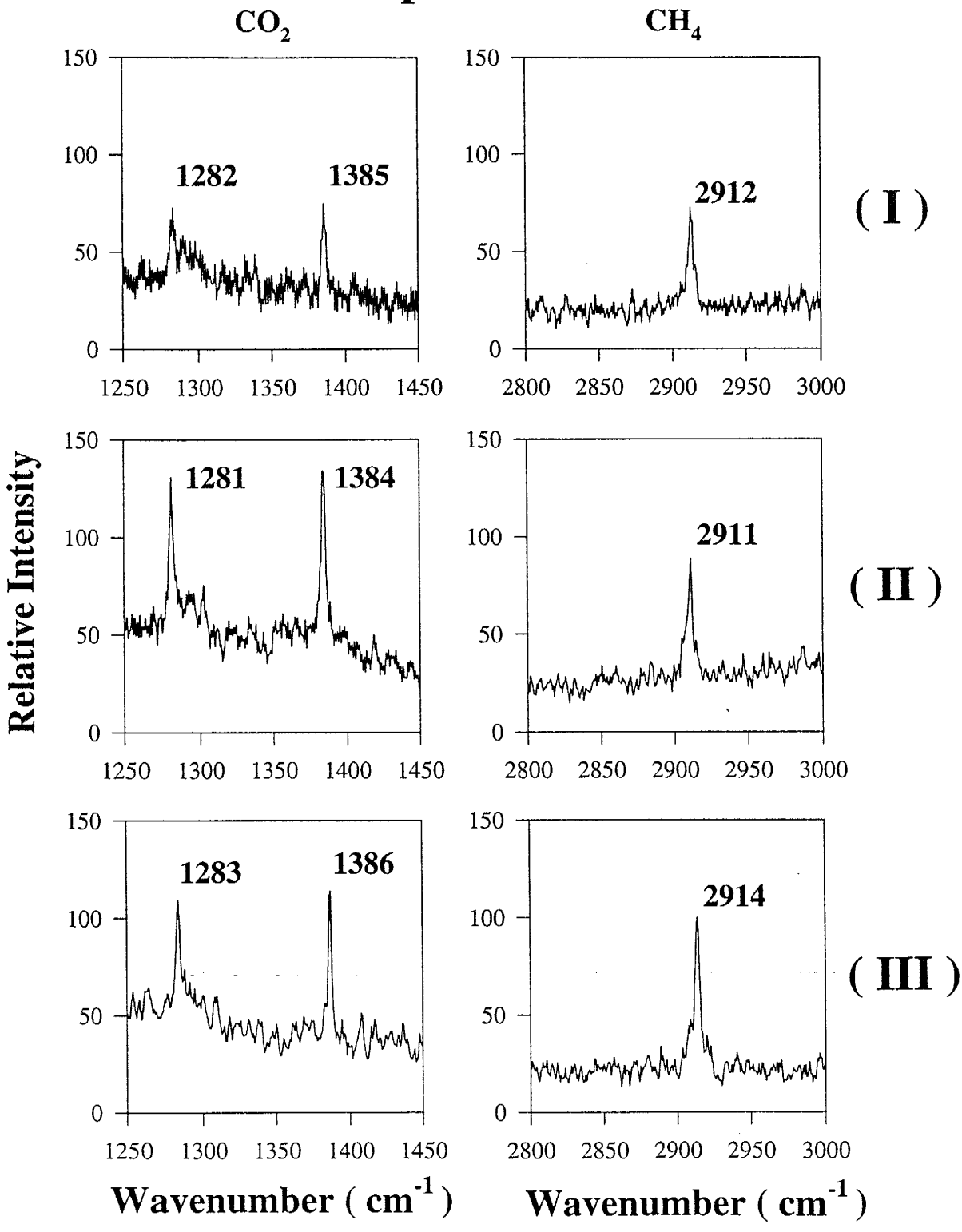
CO2
CH4
1282
1385
2912
(I)
1281
1384
2911
(II)
1283
1386
2914
(III)
Relative Intensity
Wavenumber (cm-1)
Wavenumber (cm-1)
150
100
50
0
1250
1300
1350
1400
1450
2800
2850
2900
2950
3000

Sample # 20 A

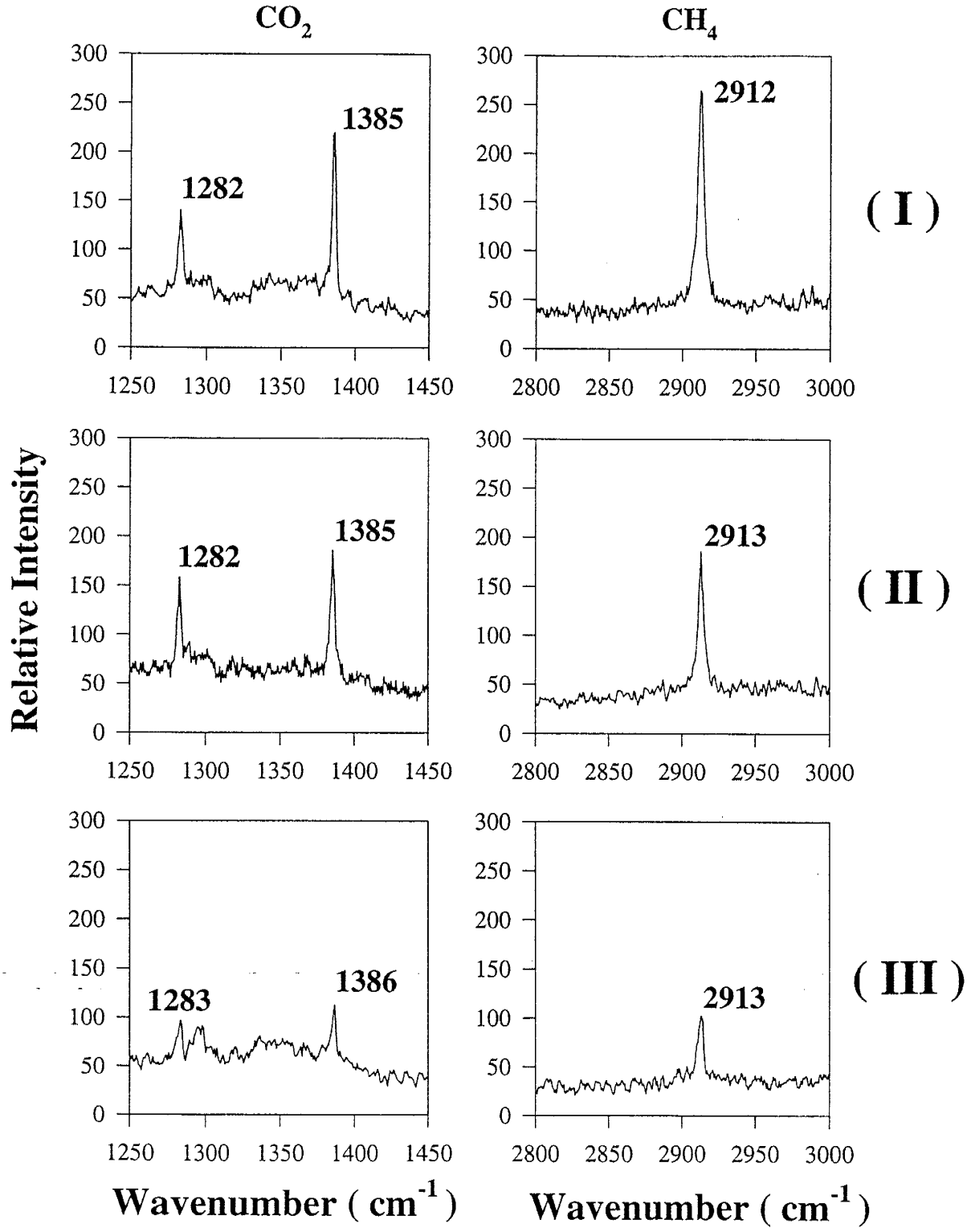
CO2
CH4
1282
1385
2912
(I)
1282
1385
2913
(II)
1283
1386
2913
(III)
Relative Intensity
Wavenumber (cm-1)
Wavenumber (cm-1)

Sample # 27 A

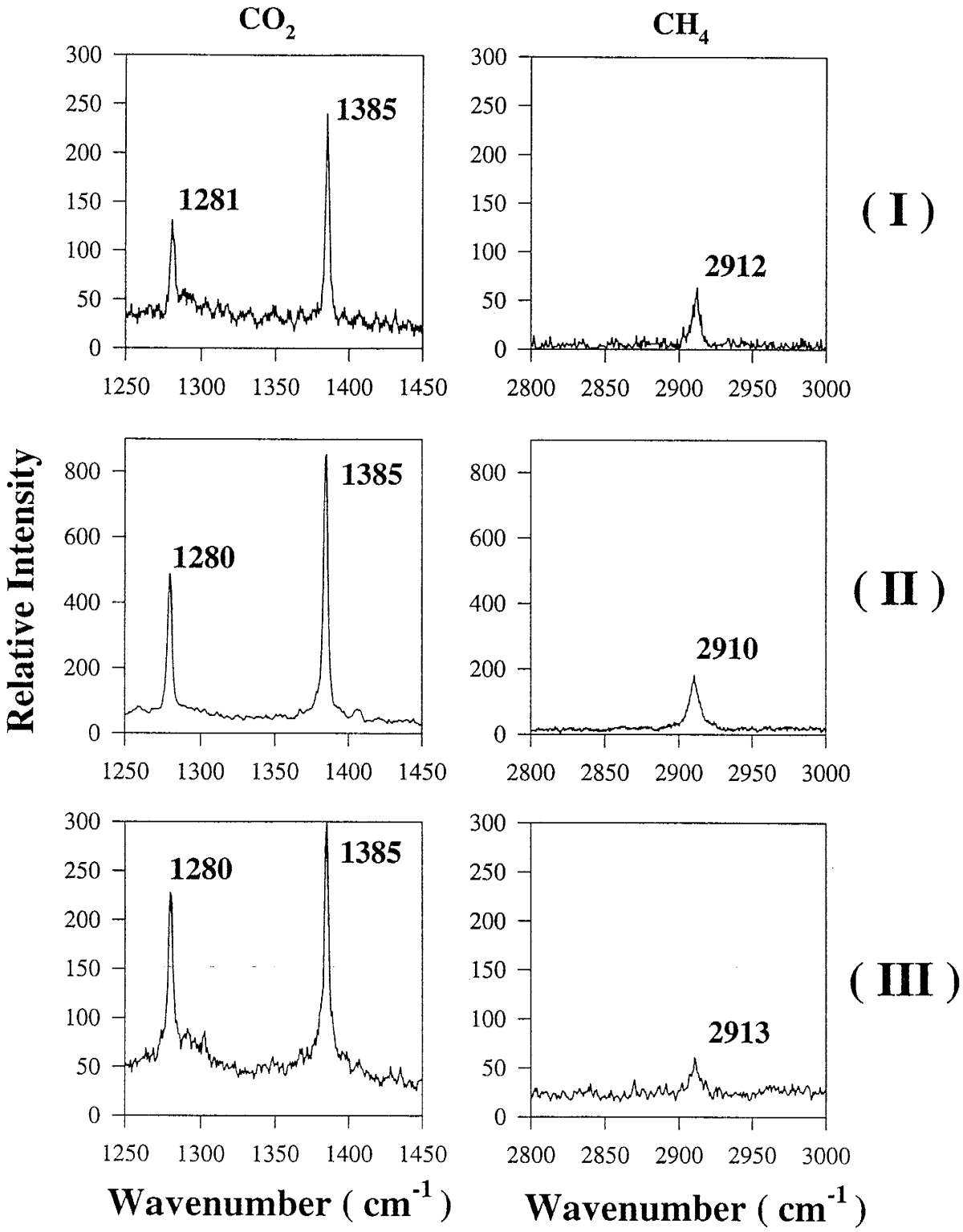
CO2
CH4
1281
1385
2912
(I)
1280
1385
2910
(II)
1280
1385
2913
(III)
Relative Intensity
Wavenumber (cm-1)
Wavenumber (cm-1)

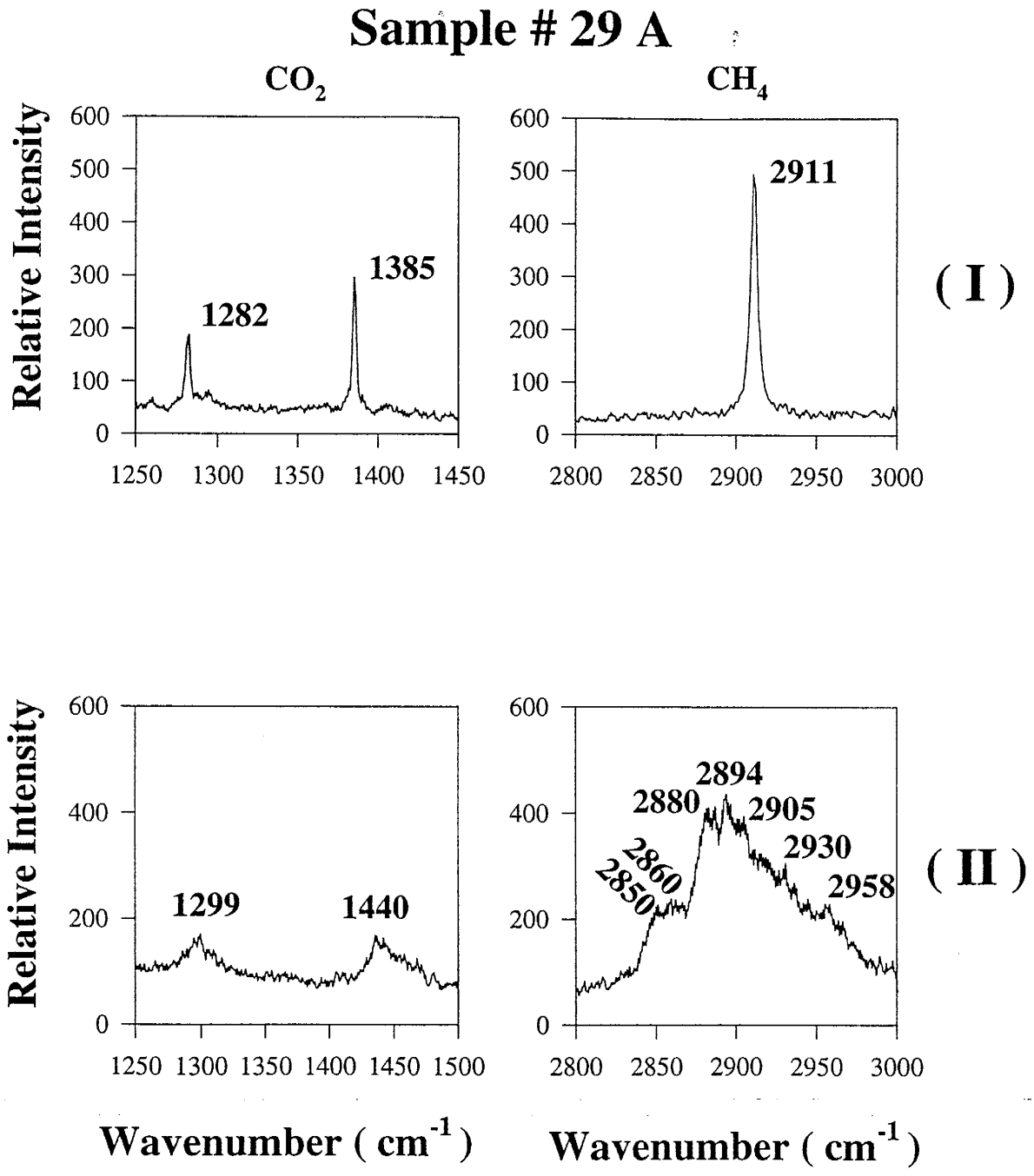
Sample # 29 A
CO2
CH4
Relative Intensity
1282
1385
2911
(I)
1299
1440
2850
2860
2880
2894
2905
2930
2958
(II)
Wavenumber (cm-1)
Wavenumber (cm-1)

(Fig 8 and 9)

GAS ANALYSES OF SAMPLES SENT FOR RAMAN MICROPROBE										
CHIP	run #	CH4 %	H2O %	N2 %	H2S %	Ar %	CO2 %	CnHn %	SO2 %	CH4/CO2
18	5092A	13.60	42.45	16.29	0.00215	0.04426	27.16	0.44147	0.00105	1.9975
18	5092D	7.16	59.53	13.42	0.00318	0.02557	19.64	0.19112	0.00105	2.7424
18	5092F	4.79	68.96	9.88	0.00322	0.02149	16.14	0.18806	0.00117	3.368
	ave	*8.52*	*56.98*	*13.20*	*0.00285*	*0.03044*	*20.98*	*0.27355*	*0.00109*	2.4633
29	5095C	17.67	37.14	22.54	0.00086	0.05219	22.23	0.34499	0.00121	1.2582
29	5095D	17.24	37.57	25.34	0.0008	0.07008	19.30	0.45119	0.00066	1.1195
29	5095G	20.39	39.67	22.95	0.00049	0.04007	16.64	0.28222	0.00069	0.8158
	ave	*18.43*	*38.13*	*23.61*	*0.000717*	*0.054113*	*19.39*	*0.35947*	*0.00085*	1.0518
27	5020A	4.78	54.13	7.76	0.00212	0.01845	33.19	0.08935	0.00076	6.9381
27	5020B	3.83	51.48	7.17	0.00405	0.0216	37.33	0.12174	0.0013	9.7412
27	5020D	1.39	78.41	3.10	0.00085	0.00743	17.04	0.03726	0.00052	12.227
	ave	*3.34*	*61.34*	*6.01*	*0.00234*	*0.015827*	*29.19*	*0.08278*	*0.00086*	8.7477
20	5025A	5.94	64.02	7.76	0.00254	0.04314	21.98	0.21237	0.00109	3.6987
20	5025B	9.93	56.30	13.08	0.00121	0.03399	20.46	0.16792	0.00054	2.0597
20	5025C	10.41	51.50	18.84	0.00116	0.04686	18.90	0.29199	0.00042	1.8152
20	5025D	9.39	60.35	13.21	0.00098	0.0343	16.73	0.25986	0.00038	1.7811
	ave	*8.92*	*58.04*	*13.22*	*0.001473*	*0.039573*	*19.52*	*0.23304*	*0.00061*	2.1881
MICROPROBE RESULTS										
	Vol gas	CO2%	CH4%		CO2/CH4					
18a	20	76	24		3.17					
18b	15	88	12		7.33					
18c	25	72	28		2.57					
				ave	*4.36*					
20a	15	70	30		2.33					
20b	20	80	20		4.00					
20c	10	80	20		4.00					
				ave	*3.44*					
27a	20	90	10		9.00					
27b	40	90	10		9.00					
27c	35	95	5	ave	19.00					
					12.33					
29	100	64	36		1.78					
FLUID INCLUSION RESULTS										
								CO2/CH4		
20		Tm(CO2) = -69o C. Tm(clth) = 11.8o C								
		% CH4 cannot be determined								
27a		Tm(CO2) = -61o C. Tm(clth) = 11o C.								
		Results in 7 % CH4 in vapor phase.						14.2857		

APPENDIX K

System Equilibrium

A stability field diagram at 300° C was created to check the equilibrium conditions for sulfur species, iron sulfides, iron oxides, arsenic sulfides, gas species, and gold complexes (Fig. 38). This spreadsheet program was created for calculation of equilibria involving gas species, iron, arsenic, sulfides, and iron oxides. Equilibrium constants were taken from Drever (1988), Garrels and Christ (1965), Barnes (1979), and Kolonin et al. (1988). The results are plotted on a stability field diagram (see discussion section), along with the solubility of gold complexes determined from equations by Shenberger and Barnes (1989).

WORKSHEET FOR SULFUR ACTIVITY DIAGRAM

(T = 300 C)

I =	0.02	log g(HS-) =	-0.146
TOT S =	0.0007 m	log g(SO4) =	-0.581
T =	300 C	log g(HSO4-) =	-0.146
TOT As =	0.01	log g(Ca+ +) =	-0.532

CH4-CO2-C:

X(CH4) =	0.1
m(Ca+) =	0.0015
X(CO2) =	0.25

H2S(aq) = HS- + H+

pH =	7.904	-31.9
and pH =	7.904	-50

Kh(CH4) =	10476
Kh(CO2) =	3748
Kh(H2) =	12890.6

H2S(aq) + 2O2 = SO4 + 2H+

If log fO2	-30	then pH =	6.0445
If log fO2	-31.9	then pH =	7.9445

CaCO3 + H2O + 2H+ = Ca+ + CH4 + 2O2

If logf(O2)	-29.8	pH =	0.017857
If logf(O2)	-36.4	pH =	6.617857

H2S(aq) + 2O2 = HSO4 + H+

If logfO2	-29.8	then pH =	6.044
if logfO2	-26.8	then pH =	0.044

CH4 + 2O2 = CO2 + 2H2O

If X(CH4) = X(CO2), logfO2 =	-34.8832	when pH =	0
	-34.8832	when pH =	12
If 5X(CH4) = X(CO2), logfO2	-34.5337	when pH =	0
	-34.5337	when pH =	12

HS- + 2O2 = SO4 + H+

If logfO2	-31.9	then pH =	7.985
if logfO2	-33.8	then pH =	11.785

C + 2H2O = CH4 + O2

log f(O2) =	-36.3202	at pH =	6.6
log f(O2) =	-36.3202	at pH =	12

CO2 = C(gr) + O2

log f(O2) =	-33.0483	at pH =	0
log f(O2) =	-33.0483	at pH =	12

FeS + H2S(aq) + 1/2O2 = FeS2 + H2O

log fO2 =	-34.87	pH =	0
log fO2 =	-34.87	pH =	7.9

3FeS + 3H2O + 1/2O2 = Fe3O4 + 3HS- + 3H+

If log fO2	-37.9	then pH =	7.9191
If log fO2	-50	then pH =	9.93576

3FeS + 3H2O +1/2O2 = Fe3O4 +3H2S(g)

log fO2 = -37.8094

CaCO3 = C(gr) + 3/2O2 + Ca+

log f(O2) =	-30.9349	at pH =	1.2
log f(O2) =	-30.9349	at pH =	12

3FeS + 3H2O + 13/2O2 = Fe3O4 + 3SO4 + 6H+

If log fO2	-30	then pH =	5.39372
If log fO2	-32	then pH =	7.56038

300aq determined using NEW estimate of deltaH for FeAsS(s)

	log Keq py-aspy	log Keq pyo-aspy	log Keq mag-aspy
300g	-86.9327	-84.0447	-194.234
300aq	*-85.67*	-84.0447	-194.234
350g	-77.9081		
350aq	-83.7059		

The following values for H3AsO3 were taken from a table in Garrels and Christ (1965). Values for FeAsS were taken from Kolonin et al. (1988).

2FeS2 + 2H3AsO3 = 5/2O2 + 2FeAsS + 2H2S(g or aq) + H2O(l)

	H2Sg	*H2Saq*		
log fO2	-33.849	-33.3441	at pH =	0
log fO2	-33.849	-33.3441	at pH =	7.95

$2FeS + 2H_3AsO_3 = 3/2O_2 + 2FeAsS + 3H_2O(l)$

log fO_2 -58.696

$2Fe_3O_4 + 6H_3AsO_3 + 6HS^- + 6H^+ = 11/2O_2 + 6FeAsS + 15H_2O(l)$

If log fO_2 -50 then pH = 8.16012
If log fO_2 -55 then pH = 12.7435

Further reactions concerning FeAsS:

logKeq(300) = -23.1283

	log Keq	
$2FeS_2 + 2H_3AsO_3 = 5/2O_2 + 2FeAsS + 2H_2S + H_2$	-92.4483	If X(CH4) = X(CO2): logf(O2) = -40.7
$CH_4 + 2O_2 = CO_2 + 2H_2O(l)$	69.32	If 10X(CH4) = X(CO2): logf(O2) = -42.7

$2FeS_2 + CH_4 + 2H_3AsO_3 = CO_2 + 2FeAsS + 2H_2S(aq) + 3H_2O(l) + 1/2O_2$

$2FeS + 2H_3AsO_3 = 3/2O_2 + 2FeAsS + 3H_2O(l)$	-84.0447
$CH_4 + 2O_2 = CO_2 + 2H_2O(l)$	69.32

log Keq(300) = -14.7247

$2FeS + 2H_3AsO_3 + CH_4 + 1/2O_2 = CO_2 + 5H_2O(l) + 2FeAsS$

If X(CH4) = X(CO2): logf(O2) = 36.5
If 10X(CH4) = X(CO2): logf(O2) = -26.9

logKeq(300) = -42.9

$2FeS_2 + 2H_3AsO_4 = 7/2O_2 + 2FeAsS + 2H_2S + H_2O$		If X(CH4) = X(CO2): logf(O2) = -26.7
$CH_4 + 2O_2 = CO_2 + 2H_2O(l)$	69.32	If 10X(CH4) = X(CO2): logf(O2) = -27.4

$2FeS_2 + CH_4 + 2H_3AsO_4 = CO_2 + 2FeAsS + 2H_2S(aq) + 3H_2O(l) + 3/2O_2$

[redacted] - WORKSHEET FOR CALCULATIONS FOR Na2O-K2O-Al2O3-H2O ACTIVITY DIAGRAM

(T = 300 C)

compound	Delta G (kJ/mol)	Reaction	Delta Gr	log Kr
Qtz	-872.4	Kspar-ser	-83	7.563204
Albite	-3787.8	Alb-ser	-115.7	10.54292
Kspar	-3827.5	ser-kaol	-37.7	3.435335
Sericite	-5706.1	cc	92.5	-8.42887
Kaolinite	-3872.3			
Na-mont				
Calcite	-1164.4			
H+	0			
Na+	-283.7			
K+	-312.5			
Ca++	-535.6			
H2O(l)	-264			
CO2(g)	-457.3			

Albite - NaMont:

7ALB + 6H+ = 3 NaMONT + 6Na+ + 10SiO2 Gr =

log K = 22.6

3.76667 = log(aNa+/aH+)

Kspar - Sericite:

3KSPAR + 2H+ = SER + 6SiO2 + 2K+ Gr = -83

log K = 7.56

3.78 = log(aK+/aH+)

Sericite - Kaolinite:

2SER + 3H2O + 2H+ = 3KAOL + 2K+ Gr = -37.7

log K = 3.44

1.72 = log(aK+/aH+)

Albite - Sericite:

3ALB + 2H+ + K+ = SER + 3Na+ + 6SiO2 Gr = -115.7

log K = 10.54

10.54 = 3log(aNa+/aH+) - log(aK+/aH+)

Sericite - NaMont:

7/3SER + Na+ + 4SiO2 + 4/3H+ = 3NaMONT + 7/3K+ log K = 1.47

1.47 = 7/3log(aK+/aH+) - log(aNa+/aH+)

Albite - Kspar:

Will be 1:1 exchange between Na+ and K+ (slope of 1)

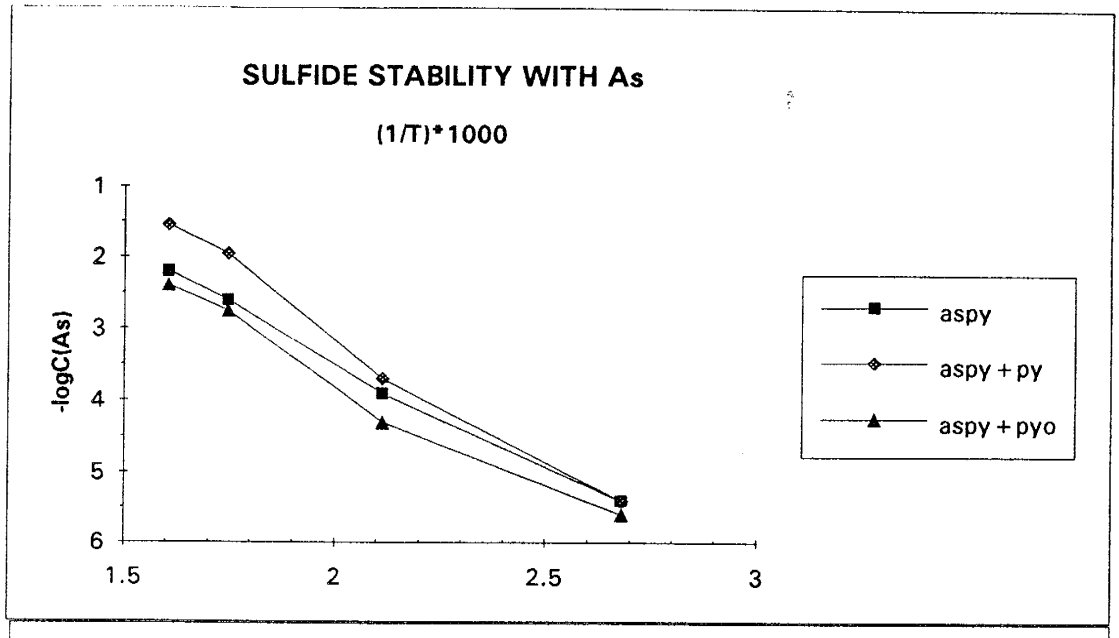
SULFIDE STABILITY WITH As
(1/T)*1000
-logC(As)
1
2
3
4
5
6
1.5
2
2.5
3
aspy
aspy + py
aspy + pyo

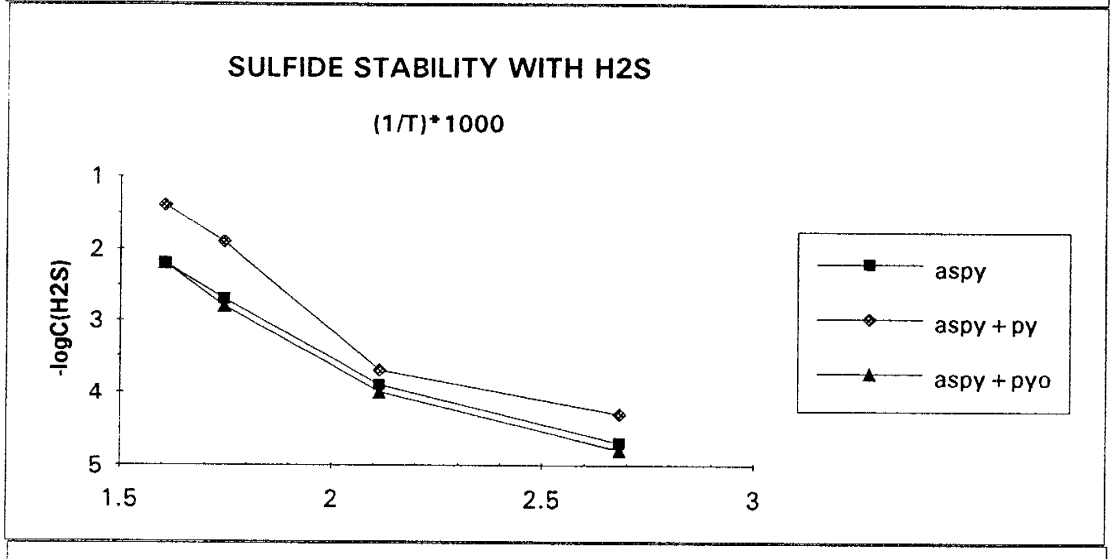
SULFIDE STABILITY WITH H2S
(1/T)*1000
-logC(H2S)
1
2
3
4
5
1.5
2
2.5
3
aspy
aspy + py
aspy + pyo

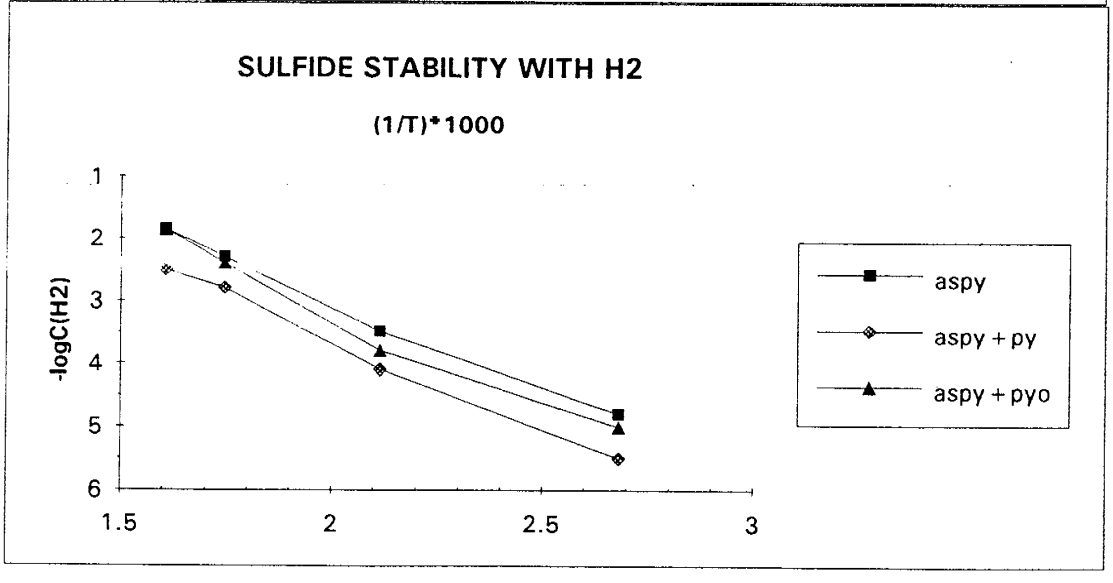
SULFIDE STABILITY WITH H2
(1/T)*1000
-logC(H2)
1
2
3
4
5
6
1.5
2
2.5
3
aspy
aspy + py
aspy + pyo

This thesis is accepted on behalf of the faculty

of the institute by the following committee:

Advisor

26 May, 1996

Date